Developing Carbon-based Electrocatalysts for Highly Efficient Oxygen Reduction Reaction

Kuang-Hsu (Tim) Wu

Doctor of Philosophy

A thesis submitted for the degree of Doctor of Philosophy at

The University of Queensland in 2015

School of Chemistry and Molecular Biosciences

Abstract

The oxygen reduction reaction (ORR) is an important cathode process in fuel cells and metal-air batteries which promises enormous energy storage and conversion capability for portable electronics and electric vehicles. However, this reaction is quite sluggish and therefore requires a highly effective electrocatalyst, such as the state-of-the-art platinum materials, to drive the energy storage devices. The main obstacle for commercial applications lies in the poor electrocatalytic activity of non-platinum materials and the high cost (and scarcity) of platinum-based electrocatalysts. To achieve an ideal combination of high performance and low cost, functional carbon materials like graphene and carbon nanotubes have become more and more predominant in the field of research for their numerous advantages. However, it is essential that the origin of activity in ORR electrocatalysis is understood and the electrode configuration optimized before an effective electrocatalytic cathode can be rationally designed. In this thesis, there are three major sections covering the topics of the optimized structure for a porous carbon electrode, the ORR on metal-free heteroatom-doped carbons and the ORR on metal oxide/carbon hybrid electrocatalysts.

In the first section, a study of the electrode configuration of graphene-chitosan composites for ORR is reported. Graphene nanosheets, a two-dimensional carbon allotrope, can gather into various assemblies depending on the amount of introduced chitosan binder. In particular, the assembled composite configuration can have substantial impact on the ORR overpotential. The mass and charge transport inside the graphene-chitosan composite was shown to be most influenced by the assembled structure, due to the distant separation of individual graphene nanosheets in a chitosan medium. Furthermore, a minimal amount of chitosan binder can ensure efficient transport

for both mass and charge, provided that the active material itself is electrically conductive.

The second part focuses on the ORR performed on oxygen and halogen-doped carbons (and sulfur) as important metal-free electrocatalysts. These attempts were aiming to provide information about the activity origin of metal-free nitrogen-doped carbons; direct study on N-doped carbon was thus not part of the focus. In the study of oxygen-doped carbons, limited activity improvement was found for most of the oxidized carbon nanotubes, although it was determined that the basal plane epoxides could be the most active of the common oxygen functional groups. Other surface oxygen groups (carboxyls and carbonyls) are also responsible for the improved ORR activity. Halogen-doping on reduced graphene oxide showed some small activity improvement for bromine and iodine doping, but not for chlorine. The electronegativity contrast of the dopant does not seem to be a crucial factor for highly efficient ORR. An accidental doping of sulfur in the form of sulfide did not seem to encourage the ORR on the doped graphene.

Metal oxide/carbon hybrids have recently attracted attention for their synergistic effect in ORR electrocatalysis. By combining spinel manganese oxide and graphene oxide nanoribbons (GONR), the covalently bound Mn_3O_4-GONR interface was structurally resolved and determined to be the origin of the synergistic effect. In addition, the functional roles of each electrocatalytic component in the hybrid are really what govern the apparent four-electron ORR. A further study on amorphous manganese-oxygen nanoclusters attached to partially impaired carbon nanotubes showed that the amorphous nanoclusters act like a fully exposed covalent C–O–Mn junction in the Mn_3O_4-GONR hybrid and can deliver similar activity to crystalline Mn_3O_4-GONR hybrid. Importantly,

these manganese-oxygen nanoclusters are the direct active sites for both catalytic O_2 and

H_2O_2 electro-reduction.

Declaration by author

This thesis is composed of my original work, and contains no material previously published or written by another person except where due reference has been made in the text. I have clearly stated the contribution by others to jointly-authored works that I have included in my thesis.

I have clearly stated the contribution of others to my thesis as a whole, including statistical assistance, survey design, data analysis, significant technical procedures, professional editorial advice, and any other original research work used or reported in my thesis. The content of my thesis is the result of work I have carried out since the commencement of my research higher degree candidature and does not include a substantial part of work that has been submitted to qualify for the award of any other degree or diploma in any university or other tertiary institution. I have clearly stated which parts of my thesis, if any, have been submitted to qualify for another award.

I acknowledge that an electronic copy of my thesis must be lodged with the University Library and, subject to the policy and procedures of The University of Queensland, the thesis be made available for research and study in accordance with the Copyright Act 1968 unless a period of embargo has been approved by the Dean of the Graduate School.

I acknowledge that copyright of all material contained in my thesis resides with the copyright holder(s) of that material. Where appropriate I have obtained copyright permission from the copyright holder to reproduce material in this thesis.

<u>Publications during candidature</u>

Peer-reviewed papers:

1. Wu, K. H.; Wang D. W.; Gentle, I. R., "The value of mixed conduction for oxygen electroreduction on graphene–chitosan composites", *Carbon,* **2014**, 73, 234-243.

2. Wu, K. H.; Wang D. W.; Gentle, I. R., "Revisiting oxygen reduction reaction on oxidized and unzipped carbon nanotubes", *Carbon,* **2014**, 81, 295-304.

3. Wu, K. H.; Wang D. W.; Zeng, Q. C.; Li, Y.; Gentle, I. R., "Solution phase synthesis of halogenated graphene and the electrocatalytic activity for oxygen reduction reaction", *Chin. J. Catal.,* **2014**, 35, 884-890.

4. Wang, D. W.; Wu, K. H.; Gentle, I. R.; Lu, G. Q., "Anodic chlorine/nitrogen co-doping of reduced graphene oxide films at room temperature", *Carbon,* **2012**, 50, 3333-3341

Conference abstracts (as published in conference booklets):

1. Wu, K.-H., Wang, D.-W. & Gentle, I. R. in International conference on nanoscience and nanotechnology 2012 "*Graphene-based metal-free oxygen reduction electrocatalysts*" (Perth, Western Australia, 2012).

2. Wu, K.-H., Wang, D.-W. & Gentle, I. R. in 5th International Conference on Carbon for Energy Storage and Environmental Protection "*The Role of Oxygen Functionalities on Carbon Nanotubes for Oxygen Reduction Reaction*" (Mulheim an der Ruhr, Germany, 2013).

3. Wu, K.-H., Wang, D.-W. & Gentle, I. R. in OzCarbon Conference "*Elucidating Oxygen Reduction Reaction Active Sites on Oxidized Carbon Nanotubes*" *(Graduate House, The University of Melbourne, Australia, 2013).*

4. Wu, K.-H., Wang, D.-W. & Gentle, I. R. in Carbon2014: The World Conference on Carbon "*Oxidized Carbon Nanotubes as Metal-free Electrocatalytic Platforms for Oxygen Reduction Reaction*" (Jeju, Korea, 2014).

5. Wu, K.-H. *et al.* in 1st Future Energy Conference "*Synergistic Coupling of Mn_3O_4 and Graphene Oxide Nanoribbons for Promoted Oxygen Reduction Electrocatalysis*" (The University of New South Wales, Sydney, Australia, 2014).

Publication included in this thesis

1. Wu, K. H.; Wang D. W.; Gentle, I. R., "The value of mixed conduction for oxygen electroreduction on graphene–chitosan composites", *Carbon,* **2014**, 73, 234-243. – KHW was responsible for 100% of data collection, 70% of data interpretation and analysis, 70% of drafting and writing and 40% of conception and design; DWW was responsible for 30% of data interpretation and analysis, 60% of conception and design, 30% drafting and writing; IRG helped with drafting and writing.

2. Wu, K. H.; Wang D. W.; Gentle, I. R., "Revisiting oxygen reduction reaction on oxidized and unzipped carbon nanotubes", *Carbon,* **2014**, 81, 295-304. – KHW was responsible for 100% of data collection, 80% of data interpretation and analysis, 80% of drafting and writing and 60% of conception and design; DWW was responsible for 10% of data interpretation and analysis, 40% of conception and design, 20% drafting and writing; IRG was responsible for 10% of data interpretation and analysis and helped with drafting and writing.

3. Wu, K. H.; Wang D. W.; Zeng, Q. C.; Li, Y.; Gentle, I. R., "Solution phase synthesis of halogenated graphene and the electrocatalytic activity for oxygen reduction reaction", *Chin. J. Catal.,* **2014**, 35, 884-890. **2014**, 35, 884-890. – KHW was responsible for 90% of data collection, 80% of data interpretation and analysis, 80% of conception and design and 80% of drafting and writing; DWW was responsible for 20% of data interpretation and analysis, 20% of conception and design, 20% drafting and writing; QCZ and LY were each responsible for 5% of data collection; IRG helped with drafting and writing.

Contribution by others to the thesis

Dr Da-Wei Wang and Prof. Ian R. Gentle had significant and substantial input into the concept and design of the project, as well as critical revision of this thesis so as to contribute to the interpretation.

Statement of Parts of the Thesis Submitted to Qualify for the Award of Another Degree

None.

Acknowledgements

Completing a PhD degree is never an easy task and it took more than three years of my life, but I must admit that it is a worthwhile experience. I could made it this far, not only because I have ideals in science, but also the supports I have received from my family, colleagues and friends in their academic, professional and personal roles.

Firstly, I would like to give my sincere thanks to Prof. Ian Gentle and Dr Da-Wei Wang for taking me on over the past four years. Together they have provided comprehensive supervision during the journey so that I could go through it without much hustle. Firstly to Ian, who encouraged me to pursue on research higher degree (RHD) after completing my Honours course, thank you for all the time you have devoted to my education and development. You have always been encouraging when I face unsuccessful situations and be very supportive (especially financially) for my academic developments. Secondly to Da-Wei, thank you for all your time you have spent at guiding my work. Your suggestions on my research has always been explicit and inspiring, and very importantly, you are always approachable. I did enjoy the times when we were having discussions on some wild research ideas. Also, I have to say that reading and revising my manuscripts from scratch in multiple loops must be a hard time, particularly when you need to provide continuous guidance for four PhD students at the same time while carrying out your own research topic. Here, I have to thank you once more for being considerate for my future in academia and provide specific assistance for the prospect. I am grateful for all the opportunities and experiences that you and Ian have offered me.

Financial support throughout the years was primarily provided by The University of Queensland in the form of a UQ Research Scholarship (UQRS). In addition, the School of Chemistry and Molecular Biosciences (SCMB) has offered a RHD fund to cover the majority of my travel cost. Other travel bursaries, in the form of direct funds or free

PhD life.

Finally, my family is always the fundamental support throughout my life. They have been an endless source of care and concern throughout these turbulent years. To my parents, you have always been my shelter, with all the necessities I may possibly need in any occasion. I can remember you have always prepared warm dinner when I got back home after late experiments. To my brother Tom, I know you have mitigated several financial burdens for me that I may possibly deal with, without asking for return. I can feel the care and love from all of you, thank you.

Kuang-Hsu (Tim) Wu

Brisbane, January 2015

Table of Contents

List of Figures

Chapter I

Chapter II:

Chapter III

Chapter IV

Chapter V-A

Chapter V-B

Chapter VI

List of Tables

Chapter I

Chapter II

Chapter VI

List of Abbreviations

2D	Two-dimensional
CNT	Carbon nanotube
CPA	Constant potential amperometry
CV	Cyclic voltammetry
DPV	Differential pulse voltammetry
EDX	Energy dispersive X-ray spectroscopy
EELS	Electron energy loss spectroscopy
EIS	Electrochemical impedance spectroscopy
EXAFS	Extended X-ray absorption fine structure
FTIR	Fourier-transform infrared (spectroscopy)
FWHM	Full-width at half-maximum
G/Chit ratio	Graphene/chitosan (weight-to-volume) ratio
GC	Glassy carbon
GDE	Gas-diffusion electrode
GO	Graphene oxide
GONR	Graphene oxide nanoribbon
HAADF	High-angle annular dark-field (TEM mode)
HER	Hydrogen evolution reaction

K–L analysis	Koutecky–Levich analysis
Li-air	Lithium-air (battery)
LSV	Linear sweep voltammetry
OCNT	Oxidized carbon nanotube
ORR	Oxygen reduction reaction
RGO	Reduced graphene oxide
RDE	Rotating disk electrode
rpm	Revolution per minute (rotation rate)
RRDE	Rotating ring-disk electrode
SCV	Stair-case voltammetry
SEM	Scanning electron microscopy
TEM	Transmission electron microscopy
UV–Vis	Ultraviolet–visible (spectroscopy)
X-RGO	Halogenated RGO
XANES	X-ray absorption near-edge structure
XAS	X-ray absorption spectroscopy
XPS	X-ray photoelectron spectroscopy
XRD	X-ray powder diffraction

List of Symbols

Raman

I_D	Intensity of D (defective) band
I_G	Intensity of G (graphitic) band
I_{2D}	Intensity of second-order D band

Electrochemistry

$\%HO_2^-$	Percentage of HO_2^- production for a given flux of ORR (%)
A	Electrode surface area (cm^2)
C_b	Bulk concentration of reactant (mol L^{-1})
D	Diffusion coefficient ($cm^2\ s^{-1}$)
E_{pa}	Anodic peak potential (V)
E_{pc}	Cathodic peak potential (V)
F	Faraday constant (96,485 C mol^{-1})
i_d	Disk current on a RRDE (mA)
i_r	Ring current on a RRDE (mA)
j	Current density (mA cm^{-2})
j_{O2}	j for the first two-electron transfer reaction in ORR (mA cm^{-2})
j_{HO2}	j for the second two-electron transfer reaction in ORR (mA cm^{-2})

N	Collecting efficiency
n	Number of electrons transferred per defined reaction
σ	Disk-to-ring current (i_d/i_r) ratio
v	Kinematic viscosity ($cm^2\ s^{-1}$)
χ	Electronegativity
ω	Electrode rotation rate (rpm)

Reaction Mechanism

ΔE_{ad}	Activation overpotential for O_2 adsorption
ΔE_{ET}	Activation overpotential for electron transfer

Chapter I.

Literature Review on the Oxygen Reduction Reaction

and the Electrocatalyst Development

&

Thesis Outline

1.1 Introduction

Electrochemical energy storage and conversion systems are anticipated to dominate in our future electrical energy grid.[1,2] Our modern society has a growing demand for sustainable power sources in order to implement next generation portable multimedia and communication technologies, and fully electrified transportation.[2,3] Although fossil fuels remain an effective power source, their non-renewable nature means that they will inevitably become exhausted, and the use of fossil fuels is considered a major cause of global warming.[4,5] In order to replace fossil fuels, there is an urgent need to develop high-capacity electrochemical power sources. In this respect, both fuel cells and metal-air batteries are highlighted in this category of electrochemical devices.[1-3,6,7]

Unlike internal combustion engines, these electrochemical devices directly convert chemical energy to electrical energy through electrochemical reactions between a light-weight anode (e.g., hydrogen, hydrocarbons or metals) and a cathode of gaseous oxygen (O_2). Featured examples are hydrogen (H_2) fuel cells,[1] and lithium-air (Li-air) rechargeable batteries,[2] in which the devices possess enormous energy-storing capability as given by the very high specific energies (33,500 Wh kg^{-1} for H_2 fuel cell and 11,700 Wh kg^{-1} for Li-air battery) and the high cell voltage.[1,3] Figure 1.1 shows a direct comparison of the specific energy of H_2 fuel cells and Li-air batteries (indicated by red arrows) with other types of conventional batteries and fuel cells. It is important to recognize that the essential element in these devices is the use of virtually unlimited O_2 from the air in the cathode process.[6,8,9] Without the need to carry the air (which is therefore "weightless"), both fuel cells and metal-air batteries are able to deliver the massive energy storage capacities.
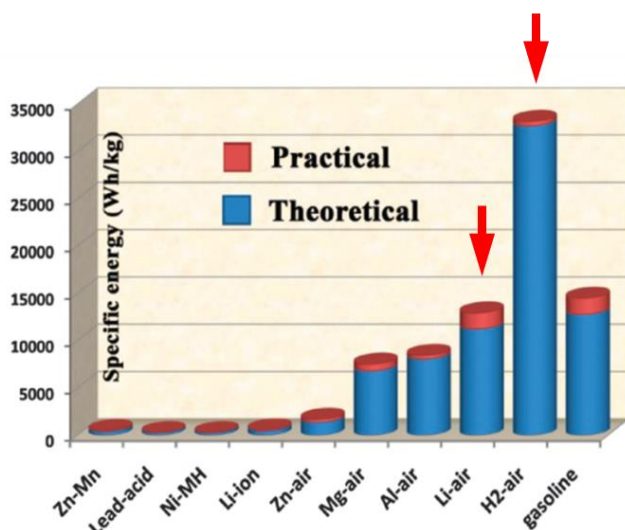
Figure 1.1 Expected specific energies of conventional batteries and fuel cells.[2]

The oxygen reduction reaction (ORR) is a central process in fuel cells and metal-air batteries and its capability essentially governs the device performance. However one complication associated with the use of these technologies is the sluggish reaction kinetics that requires an appropriate electrocatalyst to promote the ORR for a practically workable cell.[6,10-13] Unfortunately, such electrocatalysts are usually very expensive and scarce in nature; they are not likely to be commercially available for consumer devices. Moreover, the electrocatalytic activity of these precious materials is still unsatisfactory to meet the power demand for massive machines. Therefore the development of high performance electrocatalysts at an affordable cost is a most urgent task.

The search for excellent ORR electrocatalysts has been ongoing for almost two centuries.[14] Until now, precious Pt-class materials remain as the state-of-the-art standards for ORR electrocatalysis and current research strives to find a low-cost alternative to replace the precious materials.[6,14] A general overview of the progression of electrocatalyst development is illustrated in Figure 1.2.[15] Non-precious materials such as transition metal compounds (metal oxides and chalcogenides) and transition

metal macrocycle complexes had been exploited as potential candidates, although none of them could transcend the activity of Pt-class electrocatalysts and there were other problems with bringing them into application.[16-20] Recently, carbon-based materials have emerged as superior candidates for their low-cost and versatility of physical forms and chemical properties.[15,21-24] The high specific surface area and the satisfactory electronic conductivity of particular graphitic carbon materials (e.g., graphene, carbon black and carbon nanotubes) are bonuses for their use in electrocatalysis.[25-28] In particular, the ability to adopt specific bonding and electronic configurations with heteroatoms, especially nitrogen, has granted the carbon-based materials decent electrocatalytic activity for the ORR, together with excellent tolerance against poisoning chemicals.[21,29-33] All these advantages certainly raise the hope for the use of carbon-based materials as low-cost, high-performance ORR electrocatalysts.
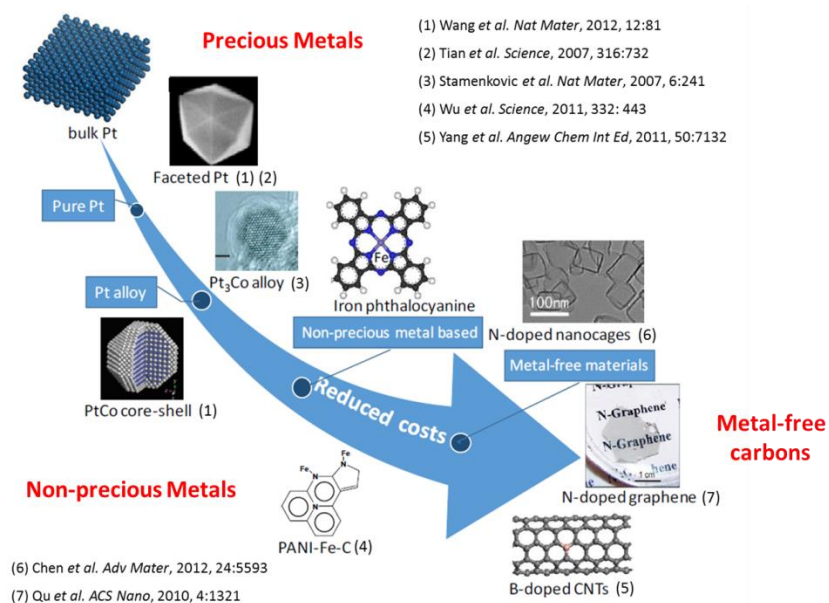
Figure 1.2 An overview of the progression of ORR electrocatalyst development.[15]

Like other potential materials under research and development, the exploitation of carbon-based materials suffers from a series of scientific problems. The most

challenging obstacles are associated with the unclear origin of the electrocatalytic activity and the unclear reaction mechanism on the modified carbons.[6,33] Still, the research has progressed by the use of beneficial empirical elements (e.g., high temperature and nitrogen-containing precursors) without an explicit understanding backed up by experimentally-validated theory.[17,30,33-41] The ORR mechanism on modified carbons remains controversial due to the lack of knowledge of the active site structure and this has significantly hampered the rational development of high performance ORR electrocatalysts.[15,22,33] For example, nitrogen doping was known to greatly improve the electrocatalytic activity of carbons at high temperatures, although the reason behind this fact remains open to conjecture even after a few decades of effort. Another major issue comes with the appropriate selection of electrode structure (and composition) for the ORR. Unlike simple solution electrochemistry, the ORR involves complex charge-transfer reactions and mass transport conditions at the electrocatalytic surfaces.[2] This requires a suitable electrode configuration for both participating processes in order to support the overall reaction kinetics. In this context, much effort has been dedicated to resolving the origin of the electrocatalytic activity and the mechanism, with a view to optimizing the electrode structure.

In this review, we provide an overview of current understanding of the ORR electrocatalysis and the recent development of carbon-based electrocatalysts. Since the use of aqueous electrolytes is the norm in fuel cells and metal-air batteries,[8,14] the discussions will be based on ORR in these systems. A general introduction on the ORR processes and current opinions for improving the electrocatalytic activity will be delivered in the first section. Next, three major categories of carbon-based ORR electrocatalysts under intensive development will be highlighted: structurally engineered porous carbon electrodes, heteroatom-doped carbons and metal

oxide/carbon hybrid electrocatalysts. In each section, an overview of the research and the current understanding of the origin of the improved electrocatalytic activity will be presented, together with critical discussions on the conclusions that have been drawn.

1.2 Fundamentals of ORR electrocatalysis

1.2.1 Basic ORR and the reaction pathways

In general, the ORR represents the cathode reactions that reduce an O_2 molecule into water and various oxides, depending on their reaction pathway and the electrolyte system.[6,42,43] Table 1.1 provides a summary of the ORRs in aqueous electrolyte systems and their corresponding reaction potentials.[6] Simplistically, the ORR can proceed through two different reaction pathways. When a total of four electrons are inserted into an O_2 molecule at once to form two water molecules in acid solution or four hydroxide ions under alkaline conditions, the ORR process is said to be a direct four-electron (4e) pathway. If an O_2 molecule only receives two electrons at first, followed by a delayed gaining of two additional electrons, then a two-step two-electron ([2+2]e) pathway is dominant.[6] The generation of peroxide intermediates is the main characteristic that distinguishes the stepwise mechanism from the 4e pathway.

Table 1.1 A list of ORRs and their reaction potentials in aqueous electrolytes.[6]

Electrolyte	Reaction pathway	Reaction potential
Alkaline	*4e pathway:*	
Aqueous	$O_2 + 2H_2O + 4e^- \rightarrow 4OH^-$;	+0.401 V (NHE)
Electrolyte	*[2+2]e pathway:*	
	$O_2 + H_2O + 2e^- \rightarrow HO_2^- + OH^-$;	–0.065 V (NHE)

	$HO_2^- + H_2O + 2e^- \rightarrow 3OH^-$	+0.867 V	(NHE)
Acidic	*4e pathway:*		
Aqueous	$O_2 + 4H^+ + 4e^- \rightarrow 2H_2O;$	+1.229 V	(NHE)
Electrolyte	*[2+2]e pathway:*		
	$O_2 + 2H^+ + 2e^- \rightarrow H_2O_2;$	+0.70 V	(NHE)
	$H_2O_2 + 2H^+ + 2e^- \rightarrow 2H_2O$	+1.76 V	(NHE)

From a device perspective, it is always preferable to drive the ORR in a 4e pathway for maximum utilization of transferred electrons. Although the [2+2]e ORR also involves a total of four electrons, there exist three major drawbacks when the generation of intermediate peroxides is highly probable.[19,38,44-47] Firstly, the peroxide intermediates are usually quite stable against further electrochemical reduction; this causes additional reaction overpotential for the peroxide reduction.[6,48] Secondly, the peroxides can easily leave the electrode surface (since they are quite stable) and lead to an overall two-electron yield per O_2 molecule. This can result in a reduced current flux and therefore less efficient energy conversion. Thirdly, the accumulated peroxide species can react with the electrode causing degradation to the electrocatalyst and the membrane separator through chemical oxidation.[49-51] To circumvent these adverse consequences, the peroxide generation should be inhibited through careful selection of the reaction pathway.
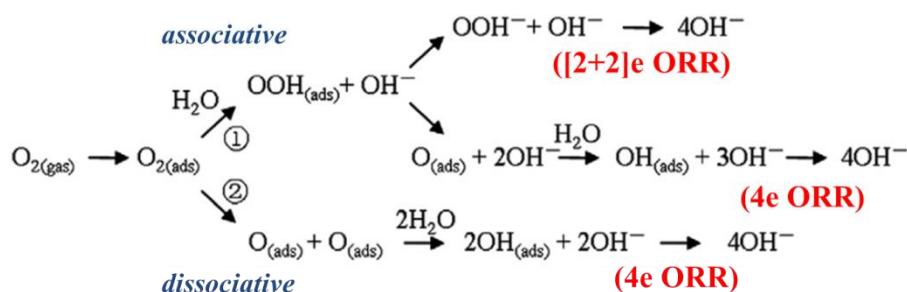
Figure 1.3 The associative (①) and dissociative (②) ORR mechanism in alkaline electrolyte.[52]

Unfortunately, the mechanism is in fact much more complicated in realistic situations, where the ORR has to occur at an electrode surface. As an inner-sphere reaction, the ORR in either pathway involves multiple interactive processes with a heterogeneous electrode surface including O_2 adsorption, charge transfer and product dissociation.[53-55] In this respect, the boundary between the 4e and the [2+2]e pathway can become ambiguous when the transitional states on O_2 adsorption (e.g., adsorbed peroxides) are concerned. Hence, a refined classification has employed "dissociative" and "associative" descriptions based on the initial adsorbed O_2 configurations to distinguish between the different mechanisms for 4e ORR.[54] Figure 1.3 presents a schematic diagram of the associative and dissociative reaction mechanisms.[52] Basically the dissociative mechanism can only go through the 4e pathway where two oxygen atoms of an O_2 molecule simultaneously attach to electrocatalytic sites (i.e., side-on mode) and the O–O bond is cleaved as the first elementary step. In contrast, the associative mechanism refers to the single attachment at one end of an O_2 molecule (i.e., end-on mode; an adsorbed peroxide), while the cleavage can be either at the first attachment (generates a free peroxide) or at the O–O bond (the 4e ORR). Note that the [2+2]e pathway can only undergo the associative mechanism.[54] Again, this classification relies on the production of peroxide species to differentiate the two pathways, except this time the "peroxide" may be a temporary intermediate attached on the electrode surface. Importantly, the application of the refined definition of reaction pathways not only relates to the ORR processes occurring on a physical surface, it also allows computational input to help determine the mechanism on a particular electrocatalyst.

Beside these conventional electrochemical pathways, the occurrence of peroxide intermediates has introduced an alternative pathway in the associative mechanism.

Since peroxides are meta-stable in nature, they can spontaneously self-decompose into O_2 and H_2O (acid)/OH^- (base) through the disproportionation reaction, as shown in Eq. 1.1.[55,56]

$$2\,H_2O_2/HO_2^- \rightarrow O_2 + 2\,H_2O/OH^- \qquad \text{(Eq. 1.1)}$$
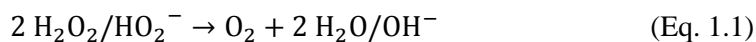
This means that any as-produced peroxides, being free or adsorbed, are prone to decompose and regenerate the reactant. As such, the electrochemical reduction is terminated with a total yield of two electrons, and this process is not advantageous if the regenerated O_2 molecule is not bound to the electrode surface. Fortunately, this chemical reaction typically requires a good catalyst to accelerate the decomposition in order to be important.[57,58] However, under circumstances where this reaction can be highly favoured, it may be considered as a plausible ORR pathway.

Table 1.2 Summary of possible ORR pathways through different mechanisms.

Pathways	Mechanism of O_2 adsorption
4e (side-on attachment)	Dissociative
4e (end-on attachment)	Associative
[2+2]e	Associative
2e (+ peroxide decomposition)	Associative

From this discussion it can be seen that there are various mechanistic pathways for the ORR, rather than a simple discrimination between direct or serial reaction pathways. A summary of the ORR pathways and mechanisms are given in Table 1.2. Although there are sharp differences among the ORR pathways from a theoretical point of view, there is no simple method to distinguish between them in a practical system. This is because accurate *in-situ* detection of all forms of intermediate peroxides is very challenging.[59] In this case, one cannot differentiate among the dissociative and the associative mechanisms for a 4e ORR in a real experiment. If the

surface peroxide in the [2+2]e pathway can be reduced so rapidly that no peroxide can be detected, the result would be an apparent "4e ORR".[56,60,61] In another situation where an electrode can rapidly reduce O_2 into peroxide while providing an excellent catalytic platform for peroxide decomposition, the large current flux and the absence of detectable peroxide also resemble an apparent 4e ORR.[60,61] It is worthy of note that all of above examples can deliver an apparent 4e ORR behaviour in voltammetry experiments, implying that unravelling the true mechanism, especially for highly efficient ORRs, is very difficult. One outstanding attempt by Jaouen and co-workers has demonstrated a direct 4e ORR on a Fe/N/C electrocatalyst by the elimination of other possible mechanisms through a series of comparative experiments coupled with mathematical modelling.[60,61] Still, it is almost impossible to explicitly resolve the ORR mechanism on an electrocatalyst. This is the main obstacle holding back rational development of ORR electrocatalysts.

1.2.2 Fundamental ORR processes and electrocatalysis

There are three fundamental processes in ORRs, regardless of their mechanistic pathways: (1) the diffusion of O_2 molecules through the bulk of the electrolyte to the proximity of electrode surface, (2) O_2 adsorption to the electrode surface (or active site) and (3) electron transfer to an adsorbed O_2 molecule.[56] For an efficient ORR, all three processes should be facilitated or any of them could become rate-determining. This section will discuss their importance towards the ORR performance.

The diffusion of reactant molecules is usually the first obstacle for reactions occurring in a solution. Once dissolved in the electrolyte, the O_2 molecules must diffuse across the bulk to near the Helmholtz plane for the surface adsorption and subsequent reaction activation.[62] In this process, the movement of reaction species follows Brownian behaviour and the net displacement of a particular species is driven

by the concentration gradient. Once an ORR is activated, the O_2 concentration will quickly deplete around the electrode and this creates a gradient of O_2 concentration. The distant O_2 molecules will then diffuse towards the electrode as a feeding current. At the same time, the accumulated products (e.g., peroxides and hydroxides) also need to escape from the electrode or they could hinder the reactant diffusion. If the electrokinetics is much faster than the reactant supply, the ORR can be greatly retarded by the diffusion process.[63] For a maximal feeding current, the mass transport for both the reactant and products must be facilitated in order to support the ORR kinetics. However, this is less serious when the diffusion processes take place in a low-viscosity aqueous electrolyte. In fact, the main problem arises in a non-ideal electrode for which the ORR occurs at the electrode/electrolyte boundaries within a porous composite electrode. The diffusion within the porous electrode is usually limited by the dense binder matrix and can be modulated by the electrode structure. Mass transport within a porous composite electrode will be covered in the next section.

The adsorption of an O_2 molecule to an electrode surface is a necessary step before any ORR could occur, as binding is necessary for the following intermolecular charge transfer.[64-68] Therefore, the preferential sites for O_2 adsorption are often considered as the ORR active sites. Since the adsorbed configuration will determine the ORR pathway, it is not difficult to imagine that the factors enabling the chemisorption would have important roles for the subsequent ORR.[54,56,69,70] For instance, an O_2 molecule arriving in a side-on mode will undergo a dissociative mechanism (definitely a peroxide-free 4e ORR), whereas in an end-on mode the O_2 molecule may go through an associative mechanism.[54,71] However, the factors desired for O_2 adsorption cannot directly predict the primary adsorbed configuration, at least

not with current computational methods. At present, there are two major postulates on the beneficial elements for preferential adsorption, either based on a quantum chemical approach,[11,68,71,72] or a classical theory of O_2 reactivity.[53,73-76] Since the concepts are best exemplified with carbon-based models, the below discussion will employ carbon materials as the principal system.

From recent quantum chemical calculations, it was suggested that the spin and charge density distributions across a heteroatom-modified (especially nitrogen-doped) carbon surface govern the O_2 adsorption.[11,68] A density functional theory (DFT) simulation by Zhang *et al.* suggests that the carbon atoms near a nitrogen group in a graphene plane with high spin density or positive charge density are the electrocatalytic active sites because they are energetically favourable for O_2 adsorption.[11] Another DFT study by Okamoto has introduced geometrical parameters to the functional group, where more than one nitrogen atom in different arrangements were incorporated in a graphene lattice.[77] His results suggested that the polarization of a C–N moiety in a graphitic basal plane can lower the adsorption barrier of O_2 in a side-on mode (typically side-on adsorption has a larger barrier than end-on adsorption), and the adsorption can be fairly favourable when there are more than three nitrogen atoms in a structural moiety, in which each nitrogen atom is separated by the lattice carbon atoms as shown in Figure 1.4a. Further, Kim *et al.* showed that the adsorption of an O_2 molecule in an end-on mode is more favourable than in a side-on mode and suggested that that the edge carbon atom adjacent to a valley-type graphitic nitrogen atom may be the most probable active site for ORR with fast kinetics (N0 configuration in Figure 1.4b).[78] In general, many calculation-based results agree that the positive charge in the carbon atom next to an electron-withdrawing nitrogen atom is a crucial factor for preferential O_2 adsorption.

However, one flaw in the quantum chemical calculations is the absence of an applied electric field to the model carbon structure. When an electrode potential is applied, the expected charge distribution on the model nitrogen structure may be disrupted. In a different viewpoint, Wang *et al.* suggested the positively charged sites on a carbon surface efficiently extract electrons from the anode thereby facilitating the O_2 adsorption and the reduction.[79]
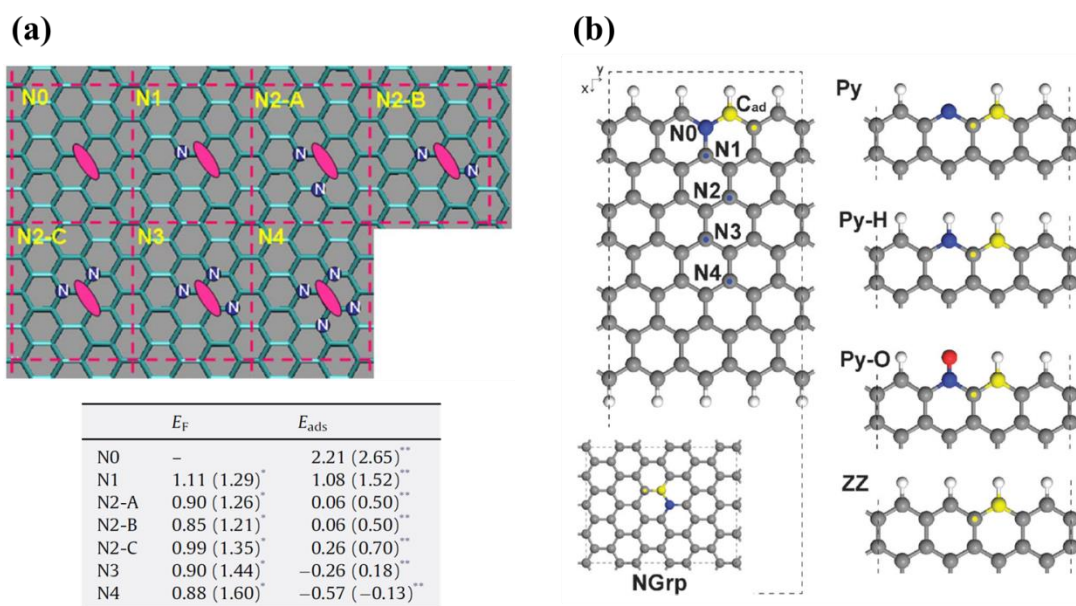
Figure 1.4 (a) Nitrogen-containing structural moieties for O_2 adsorption (top), and the related formation energy of the N-doping (E_F) and the adsorption energy of O_2 (E_{ads}) in units of eV (bottom); the values in parentheses are the energies including the correction of Gibbs free energy in the corresponding standard states.[77] (b) Nitrogen structures (blue) and the model O_2 adsorption sites (yellow) employed in the calculation by Kim *et al.*.[78]

In the view of classical chemical reactivity, preferential O_2 adsorption is a type of chemisorption that is equivalent to a chemical oxidation.[80] This suggests that an electrophilic O_2 molecule would adsorb to a nucleophilic site with labile electrons to be donated, rather than to electron-deficient carbon atoms or stable electronegative

13

nitrogen atoms.[80] In short, the basic sites on an N-doped carbon surface, by the Lewis definition, are the potential adsorption sites. An example using a carbonyl moiety as the model (also generates similar basic sites as N-doped carbons) demonstrates that it is the second or the third carbon neighbour to the doubly bonded oxygen atom (Figure 1.5).[80] Analogously, the second or third carbon neighbour to an imine group would be the adsorption site. This creates the principal difference from the results of DFT calculation, which suggests that the first carbon neighbour (with positive charge) to a nitrogen atom is the candidate adsorption site.
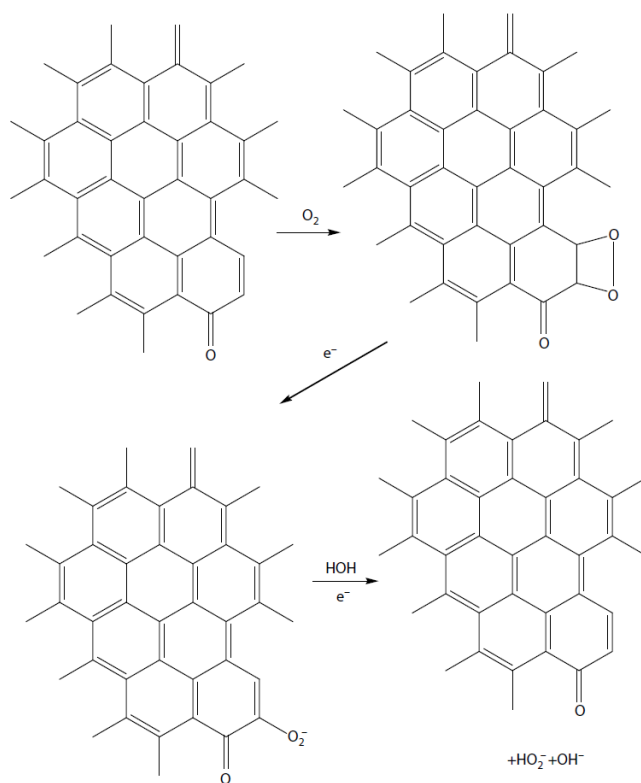
Figure 1.5 Garten and Weiss mechanism for ORR on quinone-functionalized graphitic carbon surface.[80]

Alongside these models that focus on the beneficial factors for O_2 adsorption, a complementary theory has been brought up by Nørskov *et al.*, which describes the desired binding strength for O_2 and its possible transitional intermediate in order to

facilitate the ORR in a dissociative mechanism.[54] In their consideration, an efficient catalytic surface cannot bind O_2 and its intermediate so strongly to prevent further chemical change upon reduction. Thus there must be an optimal binding energy for the reaction species, especially for the O_2 binding. An important outcome of the work is the construction of a volcano plot, which provides a direct correlation of the ORR activity of various transition metals with their O_2 binding energies.

There is more to be done to verify the correct mechanism of O_2 adsorption, especially at identifying the adsorbed configuration of O_2 on an active site. Nonetheless, these inferences and predictions have offered useful clues towards the probable ORR active site structure from first-principles to guide the design of ORR electrocatalysts.

Lastly, the charge transfer to an adsorbed O_2 molecule is probably the simplest yet the most difficult process to study. It is the simplest because it involves a simple transfer of electrons from an electrode to an adsorbed O_2 molecule. However, it can be the most difficult to study when the adsorbed configuration is not known; there could be a vast number of possbilities with all kinds of proposed reactant-substrate complex.[73] To accurately investigate the charge transfer process requires knowledge of the adsorbed O_2 configuration (and therefore the energy state), the reaction complex and the effective physical properties of the electrode under an applied electric potential. As stated earlier, the actual adsorbed O_2 configuration is typically not accessible, let alone a correct prediction of the complex structure. Added to that, the physical properties of electrode, such as the electrode structure, the conductivity and the diffusion within the electrode, cannot be simply measured. As a result the study of the charge transfer process has not been very successful to date.

1.2.3   Mass transport within a porous composite electrode

When a porous electrode is used in an ORR, the reaction process can become complicated as the mass transport within such an electrode has to also be considered in addition to the simple diffusion process in the electrolyte.[81-84] Typically, a porous electrode is in a composite material consisting of a powdered active material and a polymeric ion-conducting binder (Figure 1.6).[81,83] In this situation, the ORR occurs at the new phase boundaries inside the porous electrode and the mass transport within the binder matrix will be hindered in both inward and outward directions as compared to diffusion in the aqueous electrolyte.[81,82] It is worth mentioning that the charge transport is also important in a porous electrode when the electron now needs to be transported to the active material surface through the narrow, interconnected conductive path.[62] An efficient ORR will require facilitated kinetics for all transport processes.
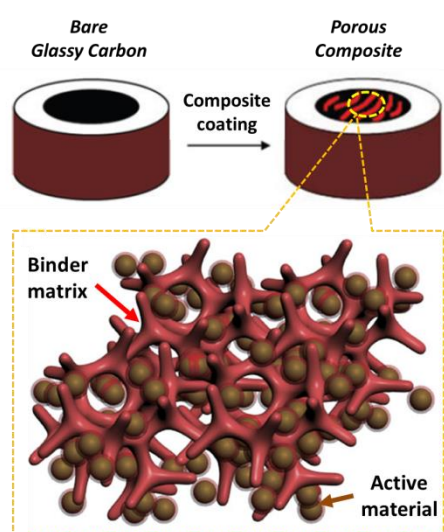
Figure 1.6 An illustration of a porous composite electrode. The enlarged view describes the active material (brown) and the binder (red) in a composite matrix; the empty portion may be filled with electrolyte and is the path for reactant diffusion.

In a porous composite electrode, the mass transport can be separated into two processes: the O_2 diffusion to the electrode for reactant feed and the ion conduction to remove the accumulated ionic products (in an alkaline electrolyte).[6] In this case the

ORR will take part at new phase boundaries at the surfaces of electrically connected active material within the composite matrix. Therefore, diffusion of reactants must occur across the binder portion in order to reach the reaction surface. One direct consequence is the slowdown of the movement of neutral O_2 molecules towards the active material, depending on the density of the composite and the binder content.[85] Yet, this situation may be circumvented if the composite can be made highly porous (therefore less dense) for efficient electrolyte intake and with a high content of active material so that the diffusion path to reach the active materials is shorter. Additionally, the outward diffusion of ionic products (e.g., OH^-) requires an efficient ion-conductor because the diffusion of charged particles is easily influenced by the charged surfaces and the spectator ions in the electrolyte.[86] In such cases, the binder is usually carefully selected to possess good ionic conductivity to relieve the concentration stress within the porous composite electrode. Without a capable ion conductor, the absorbed electrolyte will have to transport two streams of reaction species within the narrow porous channels at the same time; this would certainly hinder the mass transport kinetics.

Not all of the active material surfaces are considered as reaction surfaces, but the situation is in fact more complicated. Other than the two mass transport mechanism, one must also consider the charge transport from the current collector to the active material.[85] Without an electron conduction path, the active materials cannot collect electrons for the ORR and thus are not useful for the cathode reaction. Hence, the new complex phase boundaries inside the composite electrode have to satisfy the transport conditions for both charge and reaction mass in order to facilitate the ORR. From this, it should be clear that the structure and composition of a porous composite electrode must be firstly optimized before the electro-kinetics can be promoted.

1.2.4 Improving the ORR activity

The understanding of the fundamental ORR processes provides useful insights into the design of electrocatalytic active site and the desired electrode structure, though it is also important to recognize that there are practical aspects that can improve the ORR activity. In general, the ORR activity is defined by the magnitude of reaction overpotential (the extra energy required to activate a reaction) and the reaction current when performed on an electrocatalyst. For an efficient electrocatalyst, the ORR would deliver a low reaction overpotential and a large reaction current throughout the reaction potential range.[6] To achieve these reaction features with respect to a given electrolyte system, there are six key aspects that need to be taken into account. The first three aspects are associated with the fundamental processes (diffusion, adsorption and charge transfer) while the charge transport resistance, the ORR pathway and the active electrode surface area also have significant impact on the overall performance.[62]

As discussed, the three fundamental processes basically regulate the ORR activation. Consequently, the potential barriers for the diffusion, adsorption and charge transfer processes will hinder the reaction activation and increase the reaction overpotential. To reduce the reaction overpotential, the diffusion process must be facilitated, and the ORR active sites should be properly designed for preferential O_2 adsorption and efficient charge transfer.

Electrode resistance also retards the electrochemical O_2 reduction by creating a direct potential barrier.[62] This resistance can be intrinsic to the electrode material or can originate from poor electrical contacts within a porous composite electrode. When this resistance is significant, the applied electrode potential will have to overcome such barrier (as an ohmic drop) by raising the potential in order to promote the

reaction to a similar flux on a fully conductive electrode. Thus it is important to ensure that the electrode is electrically conductive for charge transport.

Apart from the reduction of reaction overpotential, there are two common strategies to increase the reaction current.[6] Firstly is by restricting the ORR to a 4e pathway. In this way, the fundamental current per reaction would be double that of the ORR in a 2e pathway. This is the main reason why researchers strives to design electrocatalysts that have the ability to perform a 4e ORR. Secondly, electrode surface area is another key contributor to the reaction current.[87] Eq. 1.2.4.1 is a general mathematical description of an electrochemical reaction current, which also works for the ORR.[62]

$$i_k = nFAkC_b \qquad \text{(Eq. 1.2.4.1)}$$

In the equation, the reaction kinetic current (i_k, reaction-based current) is the product of average electron-transfer number (n), Faradaic constant (F), electrode surface area (A), kinetic rate constant (k) and bulk reactant concentration (C_b). It can be seen that the electrode surface area plays an important role in determining the level of current response. Since the larger the surface area, the more probable the reaction can initiate at rising of electrode potential (reactions do not instantly start to its maximum capability due to limited contact area and inhomogeneous surface) and therefore the faster the reaction activation. Certainly, increasing the electrode surface area per given weight of electrocatalyst can derive a larger reaction current at low applied overpotential, if the reaction is not limited by the sluggish diffusion.

1.2.5 Analytical techniques for measuring the ORR activity

Analytical methods for the ORR activity measurement are essential for the examination of electrocatalysts, in order to provide a platform for cross-laboratory

comparison of electrocatalyst performance and also for understanding of the reaction mechanism.[88-91] In the following, we will briefly describe conventional electrochemical techniques for the assessment of ORR activity.

As the most common technique in electrochemistry, cyclic voltammetry (CV) has been widely used for preliminary screening for reaction potentials by sweeping the electrode potential back and forth. This includes the ORR and other side reactions (e.g., metal contamination and electrolyte reactions). CV is typically performed under stationary reaction conditions and the system is controlled by natural diffusion. Since the diffusion behaviour and the electric double layer at electrode surface can complicate the mathematical description of the situation, CV does not provide valuable information for the reaction mechanism.

Rotating electrode techniques are very popular for the measurement of ORR activity. One obvious advantage of using a rotating electrode is the creation of a laminar flow of electrolyte fluid, perpendicular to a planar electrode. This can significantly suppress the double layer capacitance and facilitate the exchange of reactant and product at the electrode surface. In this kind of hydrodynamic environment, the diffusion process in the electrolyte can be accurately described by mathematical models and therefore useful mechanistic parameters can be calculated for an ORR. Typically, linear sweep voltammetry (LSV) is employed on a rotating electrode for a first examination on the current propagation behaviour by a single linear sweep of the electrode potential. This can determine the ORR onset potential and, in some cases, the participation of multiple reaction steps. The current density also provides information about the efficacy of an ORR process. These are the basic pieces of information obtainable from a simple LSV experiment on a rotating electrode.

Based on the analytical approach and setup, rotating electrode techniques can be categorized into the rotating disk electrode (RDE) and rotating ring-disk electrode (RRDE) methods. Both methods are able to provide the average electron transfer number (n) as an important mechanistic parameter in an ORR. In the RDE method, the analysis relies on the Koutecky-Levich equation (K–L equation, Eq. 1.2.5.1) in order to calculate the n number from a double reciprocal plot of the measured current (i) and the square root of the electrode rotation rate (ω) at a given reaction potential.[92] The K–L equation describes a partially diffusion-controlled electrochemical process, in which the current contributions come from the Levich current (i_L, Eq. 1.2.5.2) and a kinetic current (i_k, as in Eq. 1.2.4.1). The Levich current is a mathematical solution to a disk reaction under a linear diffusion field generated by electrode rotation, in which F is the Faraday constant, A is the electrode area, C_b is the bulk reactant concentration, v is the kinematic viscosity and ω is the electrode rotation rate in rpm.

$$\frac{1}{i} = \frac{1}{i_L} + \frac{1}{i_k} \qquad\qquad \text{(Eq. 1.2.5.1)}$$

$$i_L = 0.2nFAC_b D^{2/3} v^{-1/6} \omega^{1/2} \qquad\qquad \text{(Eq. 1.2.5.2)}$$

By knowing the system constants (F, A, C_b, D, v and ω), the n number can be calculated from the slope of the double reciprocal plot.

The RRDE method employs a current feedback system at the ring electrode for simultaneous detection of the reaction intermediates.[93] The working principle is illustrated in Figure 1.7.[94] Basically, an ordinary LSV is carried out to scan the potential at the disk electrode, while a constant oxidising potential is held at the ring electrode to oxidize any possible labile intermediates. If we assume that an ORR simply follows the reactions as shown in the figure, then the n number can be calculated from both the disk (i_d) and ring (i_r) currents and a known value of

collecting efficiency (N) following Eq. 1.2.5.3.[93,95] In addition, the ring current is a direct reflection of the amount of generated peroxide and hence it makes possible the calculation of percentage production of peroxide, as expressed in Eq. 1.2.5.4.[93,95]

$$n = \frac{4i_d}{i_d + i_r/N} \qquad \text{(Eq. 1.2.5.3)}$$

$$\%HO_2^- = \frac{200 \cdot i_r/N}{i_d + i_r/N} \qquad \text{(Eq. 1.2.5.4)}$$

Both n number and $\%HO_2^-$ represent important criteria for assessing the ability of an electrocatalyst to deliver 4e ORR and to suppress peroxide production.
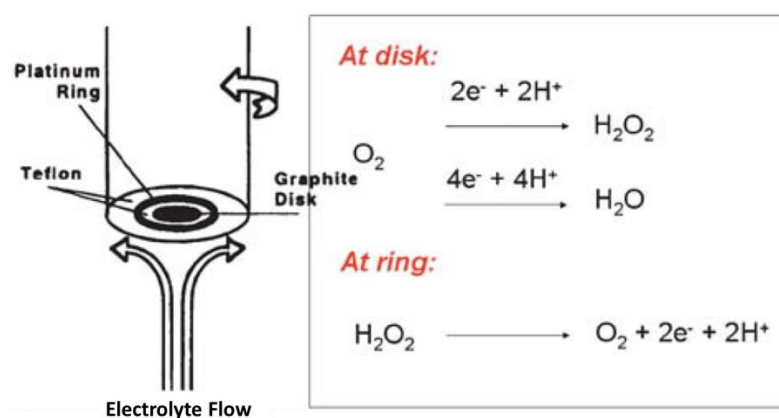
Figure 1.7 The working principle of RRDE method and the expected reactions.[94]

Tafel analysis is another useful method for understanding the reaction mechanism. This analysis employs a simplified form of the Butler-Volmer equation, the so-called Tafel equation, to evaluate the rate-determining step in an ORR. The Tafel equation is shown in Eq. 1.2.5.5, where i_0 is the exchange current, β is the symmetry factor, R is the ideal gas constant, T is the temperature and η is the applied overpotential.[96,97]

$$\ln(i) - \ln(i_0) = \frac{\beta F}{RT} \eta \qquad \text{(Eq. 1.2.5.5)}$$

From a plot of $\ln(i)$ versus η, the slope of the linear region can provide the reaction

mechanism about the rate-determining step.[96] For a rate-determining single-electron transfer, the Tafel slope is typically close to 120 mV dec^{-1}. However, when a chemical step following the charge transfer is rate-determining, then a Tafel slope of 60 mV dec^{-1} should be obtained. This enables identification of the rate-retarding processes in an ORR.

Lastly, the stability of electrocatalysts on operation and the tolerance against chemical poisoning are also common criteria for assessing the applicability of an electrocatalyst.[29,30] Constant potential amperometry (CPA) is a technique which monitors the current response over a time period at a constant applied reaction potential.[29,30] When there is a gradual decrease in reaction current within a short period, the electrocatalyst is very likely unstable under the given conditions. In another situation where there is a sharp drop in current when a poisoning chemical (e.g., CO and methanol) is introduced, then the electrocatalyst is certainly incompatible with the poisoning chemicals. Although CPA cannot quantify the activity of an electrocatalyst, it is nevertheless useful to help foresee potential shortcomings before bringing a class of materials into application.

1.3 Recent development of ORR electrocatalysts

1.3.1 A brief history of ORR electrocatalyst development

The history of the development of ORR electrocatalysts is perhaps centred around two classes of materials: precious metals and biological molecules.[14,98] Both catalysts are considered to be derived from nature, given that precious metals like Pt are simply extracted from natural ores and particular peptide entities occur naturally

in living organisms. As the archetypes of most artificial electrocatalysts, they are capable of delivering highly efficient 4e ORR at a very fast rate and are still used as the standard models for activity evaluation.[99]

Ever since Pt demonstrated excellent ORR performance in the very first fuel cell invention in 1839, extensive research effort has been invested in advancing this category of electrocatalyst by alloying and modifying the nanostructures.[14] Due to the lack of versatile chemistry, there has been only limited improvement. More recently, the expensive market price and the low abundance of Pt have driven the investigation of into non-precious metal oxides (and chalcogenides).[15] However, there have not been major breakthroughs on pure metal oxide materials because of their high intrinsic resistances. In addition, most metal oxides can only work in alkaline media as they are prone to dissolution in acidic electrolytes. This remains one of the major limitations for this family of materials.[100-102]

Alternatively, the focus has shifted to the active sites of biomolecules after the bottleneck was encountered for Pt-based electrocatalysts. In particular, the O_2-binding ability of haemoglobin and the efficient ORR catalyzed by cytochrome *c* oxidase (CcO).[18,98,103] have stimulated researchers to imitate their active sites for developing superior ORR catalysts. This eventually led to studies of various small molecules based on non-precious transition metal macrocycles for better ORR activity, for example, the phthalocyanine- and porphyrin-based transition metal complexes.[16,17] One distinguished example was demonstrated by Collman *et al*. in which a rationally designed dicobalt face-to-face porphyrin complex can effectively promote 4e ORR in an acidic electrolyte.[20] Despite this, only a few combinations of transition metal and macrocycle structure can successfully facilitate 4e ORR in this group of materials.[17,18,104] Because of this, the past research was directed to metal-containing

nitrogen-doped (N-doped) carbons after the discovery of the unusual activity enhancement by high temperature pyrolysis of the macrocycles under an inert atmosphere.[17,105] Following this, an explosion of N-doped carbon materials for ORR has taken place in the literature. Initially it was believed that metal-coordinated nitrogen-containing moieties that emerged after high temperature treatment, especially in the range of 700–900 °C, were reported for the improved activity.[33,34] In 2009, Gong *et al.* reported that vertically-aligned N-doped carbon nanotubes (CNTs) after the removal of metal impurity can offer superior ORR activity to that of a commercial Pt/C catalyst in an alkaline electrolyte.[29] This strongly encouraged the research direction of metal-free carbons for high-performance ORR. Since then, significant effort has been devoted to resolving the activity origin in N-doped carbons and this has promoted the screening of various non-metal heteroatom-doped carbons.

Other recent research has followed up the transition metal oxide materials by incorporating carbon materials to reduce the material resistance as a whole. Typically, carbons have been used as a conductive filler in a composite electrode to reduce the high resistance of metal oxides. This simple strategy can deliver much improved reaction performance for semiconducting metal oxides. In 2011, Dai and co-workers discovered a possible synergistic effect in a metal oxide/carbon hybrid through covalent connection.[95] This has caused a burst of interest in the field and motivated researchers to screen other combinations of metal oxides and carbon. Similar to N-doped carbons, current research in the area focuses on unravelling the origin of the improved ORR activity.

As an emerging research emphasis, recent studies have started to recognize the benefit of porous carbon electrodes for generally improved ORR. Apart from the high surface area, the porous structure of such carbon materials may have an important role

in facilitating ORR. One research highlight demonstrated by Chen and co-workers was the demonstration that a porous carbon with high pore surface area can more efficiently facilitate the ORR.[106] Indeed, this is one of the few examples that exploited the physical electrode structure to promote the observed ORR.[106,107] There is an increasing number of papers published now that take advantage of this concept.

To this point, there are three main directions of ORR electrocatalysts: (1) structurally engineered porous carbon electrodes, (2) metal-free, heteroatom-doped carbons and (3) synergistic metal oxide/carbon hybrids. The next section will touch on the chemistry and current understanding of each category of materials.

1.3.2   Structurally engineered porous carbon electrodes

Structurally engineered porous carbon electrodes have been widely used for the purpose of facilitating mass transport and increasing the reaction surface area. The aspect of mass transport within a porous composite electrode has been discussed in Section1.2.3. On the other hand, a large reaction surface area could merely provide a higher Faradaic current, according to Eq. 1.2.4.1. In this regard, it would be quite intriguing if a physically modified porous carbon electrode could direct the ORR pathway.

As widely known, the high surface area in carbons often comes from highly porous three-dimensional (3D) structures; a large surface area would typically mean a higher pore density and smaller pores.[108-111] Interestingly, the ORR turned out to be more selective towards an apparent 4e pathway when the reaction is performed in low-density, highly porous carbons.[106,112,113] In the work of Choi *et al.*, two high surface area Ketjen Black carbons of different micropore surface areas were decorated with pyrolyzed metal-nitrogen catalysts under the same reflux treatment

(FeCo-EDA-300R and FeCo-EDA-600R).[106] Their results show that the carbon with a higher micropore surface can provide a slightly higher onset potential and a much smaller ring current density, demonstrating an efficient 4e ORR (Figure 1.8). Zheng *et al.* also reported a similar result for ORR carried out in the mesopores with a diameter of ~3.0 nm when the pore walls were decorated with N-doped electrocatalysts.[112] Furthermore, Liang *et al.* demonstrated that improved ORR activity can also be found in 3D ordered macroporous carbons decorated with g-C_3N_4 catalysts.[113] If the ORR electrocatalysis is purely of a chemical basis, then it is very interesting that the ORR can operate at a higher onset potential through an alternative reaction pathway with identical material chemistry.

(a)

TABLE 1: Summary of Physical Properties of Ketjen Black EC300J and EC600JD

	KJ300	KJ600	FeCo-EDA-300R	FeCo-EDA-600R
BET surface area (m^2/g)	822.7	1416.2	298.1	483.7
pore volume (cm^3/g)	1.048	2.279	0.292	0.541
area from micropores (m^2/g)	154.23	591.89	28.42	136.11
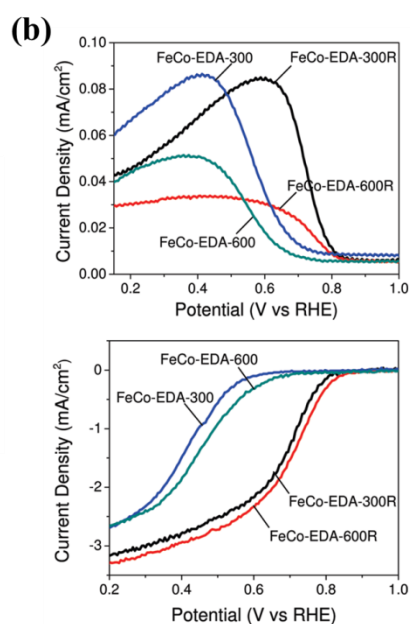
Figure 1.8 (a) A table of the physical properties of the unmodified Ketjen Black carbons and the catalyst-decorated carbons after a reflux treatment. (b) LSV-RRDE profiles of the carbon materials performed in O_2-saturated 0.5 M H_2SO_4 with an electrode rotation rate of 900 rpm; the top is the ring current densities and the bottom is the disk current densities.[106]

An explanation of these phenomena may be related to transport effects in spatially confined porous carbons.[63] The transport hindrance in the limited space could restrict the escape of peroxide intermediates from the surface proximity of the surface. In such situations, the promotion of reduction of the peroxides can eventually lead to a 4e-like ORR behaviour. If this particular aspect of ORR can be directly confirmed in porous carbons, it may be a new approach towards more efficient ORR.

1.3.3 Metal-free heteroatom-doped carbons

1.3.3.1 Nitrogen-doped carbons

Since the discovery of the beneficial effect of high temperature treatment on transition metal macrocycles, a huge amount of literature on N-doped carbons for ORR has been documented.[33,114-119] However, not all of the metal-free N-doped carbon exhibits excellent ORR activity in respect of the onset potential and the reaction current. There are in fact only a small number of reports that demonstrated Pt-level performance of their N-doped carbons.[29,120,121] In most cases, the as-claimed highly active N-doped carbons display an inferior performance to that of commercial Pt/C,[114,115] although they are superior in the tolerance against chemical poisoning by carbon monoxide and methanol.[30] This has raised an interesting question: what is the origin of such exceptional ORR activity in the metal-free N-doped carbons? Two aspects related to the materials are relevant to this discussion: (1) trace metal impurities and (2) the configuration of nitrogen groups.

The contribution of trace metal impurities in doped carbons to the ORR activity has been brought to wide attention by two separate groups very recently.[122,123] In most N-doped carbons, it is very challenging to completely remove the transition metal residues that are introduced at early stages of the preparation by washing with acids.

Interestingly, it is a common observation that the presence of both metal and nitrogen in the carbon source at high temperature treatment can lead to a better ORR activity than when only one is present alone.[36,124] In an experiment by Masa *et al.*, it was shown that enhanced ORR activity in linear sweep voltammetry on a rotating ring-disk electrode (LSV-RRDE) could result from a trivial amount of iron residue that remained in a polypyrrole-derived carbon (Figure 1.9a,b).[122] In a highlight on the significance of trace metal impurities in the commonly claimed "metal-free" doped carbons, Wang *et al.* demonstrated that the metal residues in the form of metal oxides, especially MnO_2, can also give rise to the superior activity in reduced graphene oxide (Figure 1.9c,d).[123] As such, the debate as to whether the metal participates in the active site (or is the active site) or merely facilitates the formation of the active site remains unsettled, although it is clear that the presence of metal residues in many forms is beneficial for the ORR activity.
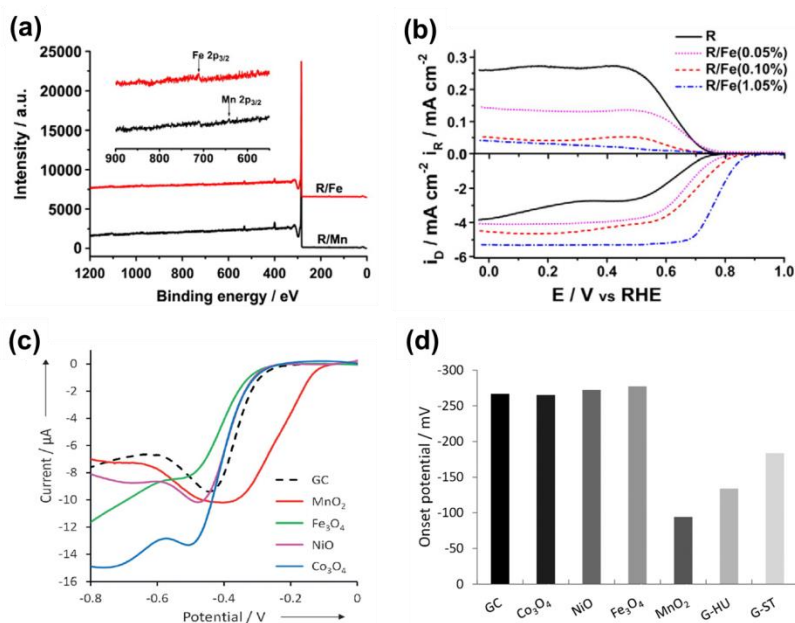
Figure 1.9 (a) XPS survey spectra of a polypyrrole-derived carbon (R) incorporated with 0.10% Fe (red) and Mn (black), pyrolyzed at 800 ℃ under He gas; (b) LSV-RRDE profiles of the pyrolyzed carbons at different Fe content in an

O$_2$-saturated 0.1 M KOH electrolyte, rotated at 1600 rpm.[122] (c) LSV profiles of various transition metal oxides located on a glassy carbon (GC) electrode in an O$_2$-saturated 0.1 M KOH electrolyte; (d) the recorded ORR onset potentials for the metal oxides and hydrazine-reduced graphene oxide by Hummer's method (G-HU) and Staudenmaier's method (G-ST).[123]

Indeed, metal incorporation can have a profound influence on the chemistry of N-doped carbons in the synthesis and make it inseparable with the carbon counterpart. During pyrolysis, the impregnated metals in the form of organometallic complexes or salt nanoparticles can coordinate with nitrogen groups, act as catalysts for carbon graphitization and also direct the morphology of the graphitic structures.[125] The positive consequences of this are the enriched active sites, and the improved degree of graphitization. On the other hand, the embedded metal nanoparticles are usually protected by the graphitic shells and can be quite difficult to remove.[34] This has complicated the understanding of the activity origin in N-doped carbons.

If we accept that the highly active N-doped carbons can be completely metal-free, then the nitrogen functional groups (N-groups) in appropriate configuration must be the origin of the high ORR activity. In the early studies, the formation of coordinated metal-nitrogen moieties, typically in a N$_4$-M configuration, has been credited as the active sites in macrocycle-derived N-doped carbons.[16,126,127] Later supported by the degradation of N$_4$-M complex and the formation of inactive metallic particles at high temperatures (> 550 °C),[128] there is a school of belief that the nitrogen functionalities without a coordinated metal centre are the ORR-active sites. In general, there are four types of nitrogen functional groups that have been frequently endorsed in metal-free nitrogen doped carbons: pyrrolic, pyridinic, quaternary types and pyridinic N-oxide, based on X-ray photoelectron spectroscopy (XPS) characterization (Figure 1.10).[129]
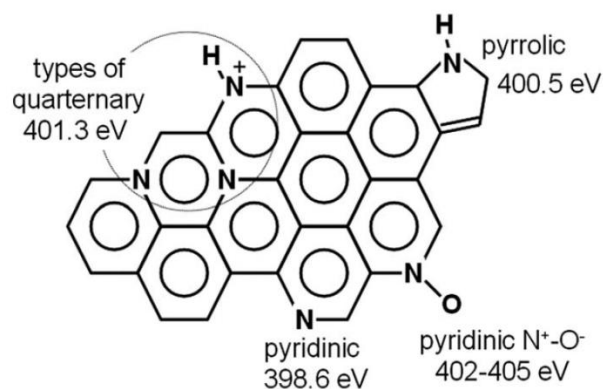
Figure 1.10 (a) A structural model of possible nitrogen groups on N-doped carbon after pyrolysis and their binding energies.[129]

Of the four types of conventional nitrogen groups, only the pyridinic and quaternary types have been suggested as the ORR active sites for their regular occurrence in active N-doped carbons. This is also supported by the results of quantum chemical calculations.[11,78,130] Owing to the difficulty of selectively doping a single type of nitrogen to carbon over the course of thermal treatment, the ascription of active sites to pyridinic and quaternary nitrogen groups remains a hypothesis.[115,131] In an attempt to verify this hypothesis, Luo *et al.* employed a chemical vapour deposition (CVD) method to synthesize a neat pyridinic N-doped graphene for the study of ORR active sites.[132] Unfortunately, the pyridinic N-doped graphene did not show the anticipated ORR activity; the voltammetry behaviour displayed a low onset potential and a low reaction current with a two-step ORR mechanism.[132] The focus of the active site studies has therefore been directed towards the quaternary nitrogen groups.

The category of quaternary nitrogen includes the graphitic type (in sp^2 configuration) and the ammonium type (in sp^3 configuration) structures.[64] At the moment, there is no selective method to dope either quaternary group into carbon, and their investigation has been a challenge. Despite this, in numerous reports there has

been general agreement on the active nitrogen groups and attribution of the good ORR activities of their N-doped carbons by the existence of quaternary nitrogen groups as observed in the XPS results.[115,121,133-135] This does not help the elucidation of ORR activity on quaternary nitrogen groups. Clearly, alternative methods must be sought. In an ingenious approach, Wang *et al.* demonstrated an effective strategy to study the ammonium type nitrogen by adsorbing an ammonium-containing polyelectrolyte to graphene as a conductive support.[79] The outcome was quite encouraging in the enhancement of reaction current and the reduced peroxide generation, even though the improvement in the onset potential was not very impressive (Figure 1.11). These characteristics indicate a 4e ORR-like mechanism, like that of active N-doped carbons. This partly supports the hypothesis of active quaternary nitrogen groups. On the other hand, the evaluation of graphitic nitrogen structure usually relies on the existence of graphitic type nitrogen in N-doped carbons, which always involves a mixture of other nitrogen groups. A solution to this is by transforming the population of non-graphitic nitrogen into graphitic type in the N-doped carbon, which does not have any graphitic nitrogen structure before the reaction.[136] In this way, the change in ORR behaviour may be reasonably ascribed to the increased amount of graphitic nitrogen. This approach was used by Zheng *et al.* who showed that a hydrothermally derived N-doped graphene containing only pyridinic and pyrrolic nitrogen, can be converted into a N-doped graphene with a moderate population of graphitic nitrogen.[136] However, the weakness in this method is the change in the carbon chemistry upon the thermal treatment; the reduced level of oxygen may have granted the pyrolyzed graphene better conductivity. Nonetheless, their result was also quite encouraging in that a higher onset potential and slightly higher reaction current could be achieved.[136] On top of this, Sharifi *et al.* further put forward that the graphitic nitrogen at valley (edge) positions is more active than that

within the basal plane.[134] From these remarks, simple quaternary nitrogen groups appear to be active for ORR although maybe not to an extent that is comparable with typical active N-doped carbons.[79,134,136]
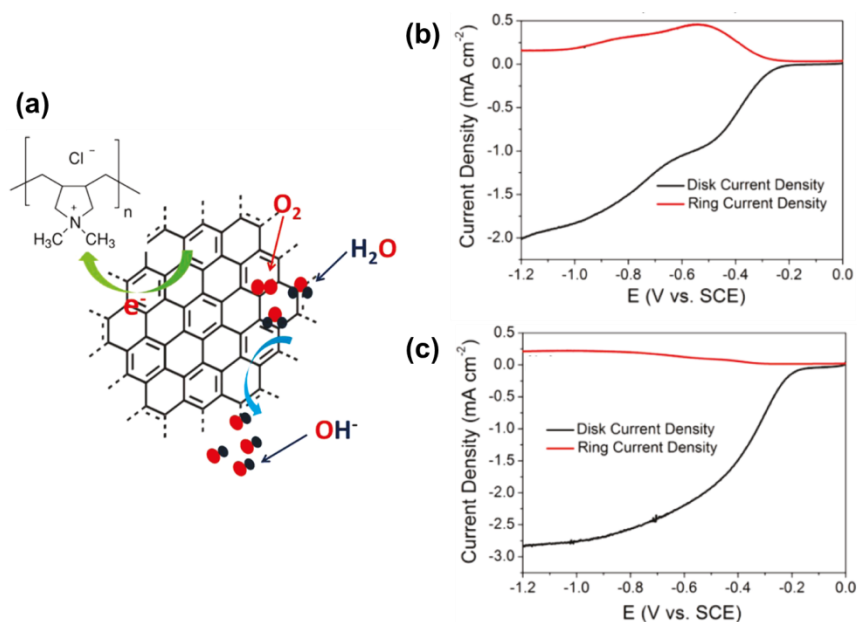
Figure 1.11 (a) Schematic diagram of the ORR performed on graphene with adsorbed polydiallyldimethylammonium (PDDA) chloride. (b) The LSV-RRDE profiles of graphene and (c) PDDA-graphene in an O_2-saturated 0.1 M KOH electrolyte.[79]

In a recent highlight of N-doped carbon research, an amine-functionalized holey graphene was prepared at a low temperature (180 ℃) by a hydrothermal method.[114] This means that the nitrogen functional groups do not necessarily fall into the conventional assignment and allows the reasonable existence of amine-type nitrogen in the "N-doped" carbon. Jiang *et al.* demonstrated that, with a negligible amount of graphitic type nitrogen, the amine-rich graphene can display a one-step ORR behaviour with a very high current and a much higher onset potential than typical chemically derived graphene.[114] The authors admitted that the reaction onset potential was still lower than that of a pyrolyzed metal-free N-doped graphene reported elsewhere.[121] Despite this, their result suggests a direction for low temperature

nitrogen structures as potential ORR active sites.

Until now, the explicit structure of the active site in N-doped carbons is still controversial within the scientific community, although there is no doubt that we have learnt much of the material chemistry with the help of conventional characterization tools. Since N-doped carbons have been very thoroughly exploited over the past few decades, further insights will require strategic experiment design and advanced spectroscopic methods for resolving the active site configuration.

1.3.3.2 Other non-metal heteroatom-doped carbons

Inspired by the excellent activity of N-doped carbons, researchers in the field have expanded the scope to other non-metal heteroatom-doped carbons.[21] The principal theory is based on the breaking of electro-neutrality in a pristine carbon lattice.[21] Because nitrogen is highly electronegative relative to carbon, there is a widely renowned hypothesis that the electronegativity contrast can induce particular changes in the electronic configuration thereby give rise excellent electrocatalytic activity. In this regard, doping with other electronegative elements such as oxygen, phosphorus, sulfur, and halogens, or even electron-deficient boron may result in a similar activity to N-doped carbons. The following reviews recent research into single-type heteroatom-doped carbons.

Although being quite thoroughly investigated in the past, oxygen-doped carbons are not currently the subject of such intensive focus as other heteroatom-doped carbons. As compared to nitrogen, oxygen is more electronegative and possesses less complicated bonding configurations with carbon (only up to double bonds). Previous studies on oxidized carbons have demonstrated that the introduction of oxygen into graphitic carbons can lead to a slight reduction in the ORR

overpotential and promote peroxide reduction at high overpotential.[137] However, these studies did not explicitly elucidate the origin of the improved activity – whether it came from the defects or the oxygen functional groups created during oxidation. A recent highlight in oxidized carbon research is on the use of graphene oxide (GO) in a composite with conductive carbon nanotubes (CNTs).[138] One interesting chemical aspect associated with GO is the emergence of uncommon epoxide groups upon severe oxidation by a modified Hummer's method.[139] In the report by Wang *et al.*, their GO/CNT composite exhibited a 4e ORR-like current behaviour with an *n* number of ~3.5 as compared to the two-step reaction behaviour in the heat-treated, oxygen-containing RGO with an *n* number below 2.5.[138] Since the epoxide groups in GO are usually the first to be removed at elevated temperature (~110 °C),[140] the improved ORR activity in GO/CNT may be attributed to the conductivity-enhanced epoxide groups. Therefore, the category of oxidized carbons should be revisited for a better understanding of the origin of activity.

Phosphorus-doped (P-doped) carbons have quickly attracted attention soon after the rise of N-doped carbons since phosphorus and nitrogen are within the same periodic group.[35,141-143] Both elements can easily adopt complex bonding configurations and may be incorporated into a graphitic lattice, except that phosphorus is bigger in size and less electronegative than nitrogen.[21] Therefore, P-doped carbons were expected to provide a somewhat similar result to N-doped carbons. Unfortunately in most cases, there was only a slight improvement in the ORR onset potential and the reaction current exhibited a multi-plateau behaviour, which indicates the ORR on the P-doped carbons is a non-4e ORR pathway, unlike that of N-doped carbons.[35,141,142] In a recent report, the P-doped graphene nanosheets prepared from a hexafluorophosphate salt demonstrated a Pt-level activity and good

tolerance against poisoning chemicals.[143] Although the P-doped product showed negligible nitrogen content from their XPS characterization, the fact that the carbon precursor contained an imidazole group is suspected to be the cause of the superior activity.

Sulfur-doped (S-doped) carbons have also been investigated.[144-147] Sulfur is in the same periodic group as oxygen and has an electronegativity close to carbon (χ = 2.58). As such, it is not expected that there will be a large electronegativity contrast in the C–S moiety. In the studies of S-doped carbons, just like most P-doped carbons, there is only limited enhancement in the ORR onset potential while the reaction clearly shows two-plateau behaviour. That is, the ORR follows a [2+2]e reaction pathway. Despite these reports highlighting the improvement in the reaction potential, S-doped carbons do not have promising properties for ORR electrocatalysis.

Halogen-doped (X-doped) carbons should be the most suitable form of heteroatom-doped carbons for the investigation of the hypothesis on the breaking of electro-neutrality. Common halogen group elements (F, Cl, Br and I) can only accept one covalent bond with another element and have decreasing electronegativity down the periodic table. Such properties have made halogen group elements an excellent system for studying the activity origin in heteroatom-doped carbons. However, doping halogen into carbon from halide precursors is very challenging and usually requires high temperature treatment or other harsh conditions.[148-150] Since halogens are also good leaving groups, it is very hard to keep them on conductive carbon at quantitative amounts; usually the halogen content is < 2 at.%.[148,149,151] Owing to this, there are very few studies on X-doped carbons.[151,152] In a study of iodine-doped (I-doped) graphene, there was an improvement in overall performance with a two-step ORR behaviour, despite that the fact that the iodine content is much less than 1.0 at%. So

far, it is difficult to affirm that the observed activity is the result of a low-level halogen doping.

Boron-doped (B-doped) carbons are a unique group of heteroatom-doped carbons since boron is electron-deficient and has a low electronegativity relative to carbon (χ = 2.04). In principle, this can still cause an imbalance of charge in a C–B moiety, in which the electron density will be attracted towards the carbon atom instead of to the dopant. However, the results from the past studies were not encouraging.[11,153-155] Like other non-nitrogen heteroatoms, B-doping does not lead to excellent ORR performance and the reaction pathway remains a [2+2]e ORR.[11,153-155]

In the end, non-nitrogen heteroatom-doped carbons generally cannot provide highly efficient ORR as can N-doped carbons, according to recent studies. Upon doping with electronegative elements and boron, there is merely a slight enhancement in the reaction onset potential, while the ORR cannot be as efficient as in a 4e pathway. Despite this, there are still opportunities for detailed investigation of each category of heteroatom-doped carbons in order to reveal the activity origin.

1.3.4   *Synergistic metal oxide/carbon hybrids*

Interest in the synergistic metal oxide/carbon hybrid came about after the discovery of improved ORR activity in a hybrid electrocatalyst of Co_3O_4 nanocrystals and a graphene substrate.[95] This type of hybrid electrocatalyst is characterized by the covalent connection between the metal oxide nanocrystals and the carbon substrate through a C–N–M or a C–O–M bridge. The synergistic consequence of this covalent linkage has triggered screening of different combinations of metal oxide/carbon hybrids, for which the metal oxide can be Co_3O_4, Mn_3O_4, Fe_3O_4 or their combinations.[95,108,156-158] Since it has become a common observation that hybrid

electrocatalysts can exert improved ORR activity as compared to their individual components, researchers have recently started to explore the cause of the synergistic effect.
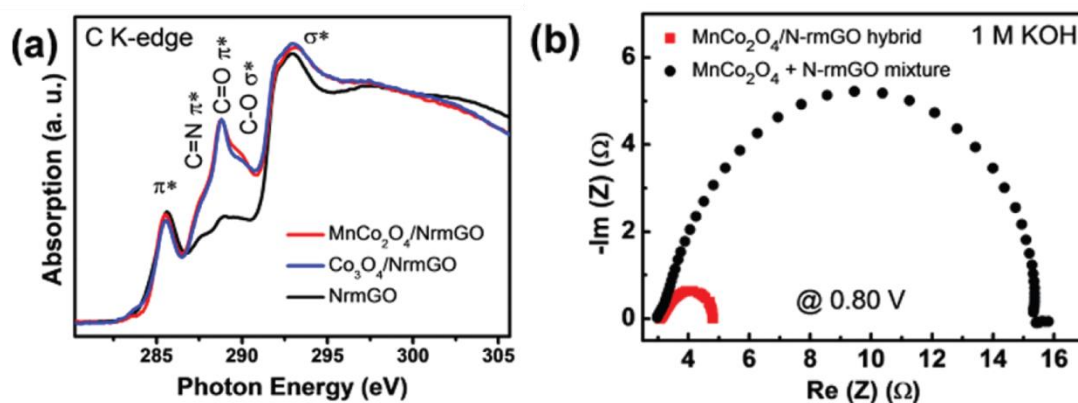
Figure 1.12 (a) Carbon *K*-edge X-ray absorption near-edge spectra for the N-doped reduced, mildly oxidized GO (NrmGO) and the hybrid with Co_3O_4 and $MnCo_2O_4$; (b) the Nyquist plot from EIS measurement for the $MnCo_2O_4$/N-rmGO hybrid and the blended mixture of the hybrid components.[156]

The first attempt to uncover the cause of the synergistic effect was done by Liang *et al.*, in which they have associated an uncommon spectral feature in the carbon *K*-edge X-ray absorption spectrum of the hybrid with the reduced material conductivity measured by electrochemical impedance spectroscopy (EIS), as shown in Figure 1.8.[156] From this, they believed that the change in the electronic structure at the hybrid interface is responsible for the facilitated charge transport across the metal oxide/carbon interface to the catalytic surface of metal oxide nanocrystals. In other words, the reduced charge transport resistance was suggested as the origin of the reduced ORR overpotential and the enhanced reaction current. However, a flaw in their approach is that their EIS measurement is not a direct probe for the charge transport across the subtle molecular interface. In addition, there is a lack of a recognized theory on the improved charge transport across a covalently bridged C–O–

M or C–N–M interface. For this reason, perhaps, Wang *et al.* further exploited the chemical interaction between the covalently connected Co_3O_4 nanocrystals and N-doped graphene.[159] Their results endorse the presence of C–O–M and C–N–M bridges at the interface and they have successfully identified a partial chemical change to the Co species at the octahedral sites in the nanocrystal. In this case, a change in the electronic structure at the Co_3O_4 catalytic surface may be expected and the ORR activity on this hybrid catalyst would not be simply explained by the reduced charge transport resistance. Yet, there is still no satisfactory explanation for the improved ORR activity in synergistic metal oxide/carbon hybrids. It will require further scientific effort to unravel the origin of the unusual synergistic effect.

1.4 Thesis Outline

This research project aims to investigate the structural and chemical origins of the improved ORR activity in carbon-based materials, for the purpose of developing low-cost high-performance ORR electrocatalysts. In this regard, this thesis is comprised of three important aspects to the understanding of the electrocatalytic activity in carbon-based materials.

● *The structure-property relationship of self-assembled graphene/binder composite electrode.*

● *The verification of the hypothesis on the breaking of electro-neutrality as the origin of ORR activity in metal-free, heteroatom-doped carbons.*

● *The origin of the improved activity in metal oxide/carbon hybrid electrocatalyst.*

In Chapter II, the structure-property relationship of a self-assembled graphene/ chitosan composite electrode is investigated. The structure of the composite matrix was tailored by tuning the composition of the electrode. Particular attention was paid to the mixed conduction of electrons and ions in the graphene/chitosan composite matrix. The influences on the ORR activity are described with supporting evidence and an empirical trend. Recommendations on the preparation of electrode composite are also provided for reducing the impact of electron/ion transport resistance on the intrinsic activity measurement.

Chapter III and IV focus on two important classes of heteroatom-doped carbons: oxidized carbon and halogenated carbons. In addition, a sulfur-doped carbon is discussed in Chapter IV. Chapter III aims to unravel the electrocatalytic origin on oxidized carbons as well as to examine the electrocatalytic activity of an uncommon oxygen group: epoxide. Systematic experiments were conducted to validate that the introduced oxygen groups are the origin of the improved activity, apart from the lattice defects in the graphitic framework. Epoxide, as an uncommon oxygen group, was also investigated. Collectively, conclusions are drawn on the capability of oxygen-doped carbons for the ORR electrocatalysis. Chapter IV explores chlorine-, bromine- and iodine-doped reduced graphene oxide (RGO) using a solution synthesis in both acid and organic media. The compositions of the halogenated materials were carefully characterized for the efficiency of doping and the configuration of the doped elements; an unusual sulfur-doping was identified. The ORR activity of all the materials was inspected and compared for a conclusion on the dependence of the ORR activity on the electronegativity of the doping element.

Chapter V and VI elucidate the origin of the synergistic effect and the ORR mechanism in manganese oxide/carbon hybrid electrocatalysts. Chapter V is separated

into two parts, where part A demonstrates that the uncovered portion of the hybrid interface should the origin of the synergistic effect, and part B elaborates the electrocatalytic roles of the manganese oxide nanocrystals and the graphene oxide substrate, by a series of spectroscopic and electrochemical techniques. Further, Chapter VI focuses on the hybrid interface to scrutinize the capability in ORR electrocatalysis, by imitating the covalent interface in a manganese oxide/graphene oxide hybrid. Amorphous manganese-oxygen nanoclusters were decorated on mildly oxidized carbon nanotubes to replicate the covalently linked C–O–Mn configuration. Comparative experiments were carried out to reveal the electrocatalytic role of the fully uncovered hybrid interface.

Finally Chapter VII concludes the thesis by providing a consolidated summary of the findings presented and discusses the future prospects of carbon-based materials as high-performance ORR electrocatalysts for fuel cells and metal-air batteries.

Chapter II.

The Importance of Mixed Conduction in Oxygen Reduction Electrodes

2.1 Abstract

Graphene-based electrocatalysts have been widely investigated for their excellent performance in electrocatalytic oxygen reduction. The surface chemistry of graphene-based electrocatalysts is important for developing more efficient fuel cells and metal-air batteries. In addition, the nanostructured gas-diffusion electrode (GDE) on which the electrocatalysts are loaded needs to be carefully tailored to facilitate mass transport (reactants and products). A polymer binder is often used to fabricate the GDE which means there is a need to optimize the ratio of binder to electrocatalyst. Herein we demonstrate the impacts of graphene-based GDE nanostructures on the efficiency of oxygen electro-reduction by comparing a series of graphene/chitosan composites with varying compositions. In these nanostructured GDEs graphene acts as the electrocatalyst and chitosan as the binder. Our results illustrate a critical ratio of graphene to chitosan for enhanced electrocatalytic surface area and facilitated mass transport, while a continuous network for electron conduction is effectively established. We believe this work is an important piece of the puzzle to better understand the electrode behaviour of electrocatalysts consisting of graphene-like two-dimensional materials in oxygen reduction reaction.

2.2 Introduction

The oxygen reduction reaction (ORR) is an important topic in research on fuel cells and metal-air batteries.[2,34] These energy conversion devices are capable of delivering a much higher specific energy that potentially outperforms conventional energy storage devices, such as lithium-ion batteries and supercapacitors.[1,9] Unfortunately the anticipated performance is largely limited by the sluggish ORR

kinetics at the cathode, which degrades the energy efficiency. Significant research effort has thus been devoted to developing low-cost and robust ORR electrocatalysts to tackle this problem. Two vital bottlenecks being intensively investigated are the large onset reaction overpotential and the low reaction current density.[1,6,160] Both limitations are the combined consequences of poor intrinsic electrocatalytic activity, limited electron conductivity, slow mass transfer for reactant and product molecules and low electrocatalytic surface area.[54,161,162] Clearly, ORR electrocatalysis can only become efficient if all the influential structural factors are optimized.

Intensive research has focused on the (i) heteroatom doping or surface functionalization,[30,163-168] and (ii) hybrid modification,[169] of graphene nanosheets. Nitrogen-containing functional groups or dopants were observed to be very active towards direct 4-electron reduction of dioxygen.[30,164,165] Other heteroatoms, such as O,[163] S,[167,168] and B,[166] also demonstrate superior ORR activity compared to an unmodified graphene electrocatalyst. Covalently bonded metal oxides even exhibit a synergy with a graphene matrix for oxygen reduction, typically when N heteroatoms are introduced.[169] The robust surface chemistry of graphene and of its derivatives is clearly of significance for understanding and developing advanced ORR electrocatalysts. In spite of this, however, the nanostructures of gas-diffusion electrodes (GDE) consisting of graphene-based electrocatalysts and a binder can affect the processes of electron conduction and mass transfer and can change the accessible electrocatalytic surface area. These effects will eventually impact on the overall ORR efficiency, but they have often been overlooked in studies of graphene-based ORR electrocatalysts.

GDEs usually take the form of a composite which incorporates an active electrocatalyst and a polymer binder at certain mass ratios. The morphology and

physical properties of the GDE composite can affect the mass transfer and electron conduction which in turn alters the catalytic properties of the electrocatalyst. For example, the electron conduction network may not develop effectively if the active electrocatalyst particles (which are usually conducting) are isolated by the polymer binder. This may in turn suppress the reaction by generating resistance to charge transport. It is therefore important to understand how the structure of a composite electrocatalyst influences ORR behavior.

We have fabricated a nanostructured GDE consisting of chemically-derived graphene nanosheets as the electrocatalyst and chitosan as the binder to demonstrate the significance of optimization of GDE nanostructures for ORR. The graphene nanosheet is used as a two-dimensional (2D) electrocatalytic platform with high surface area and excellent electron conductivity, while chitosan is a polysaccharide which exhibits satisfactory ion conductivity and stability as a binder in alkaline electrolytes.[170] Compared to the widely-used Nafion, chitosan is a much cheaper natural product derivative which is highly hydrophilic and facilitates hydroxide ion conduction in an alkaline electrolyte.[170] While graphene nanosheets are 2D anisotropic materials, they are known to exhibit enormous surface area and can self-assemble into versatile structures. With the goal of investigating the structure-performance relationship, graphene and chitosan were blended in various ratios to tune the GDE nanostructures. We have employed several techniques to provide a relatively complete picture of the composite structure and the electrocatalytic ORR performance.

2.3 Experimental Section

2.3.1   Materials

Graphene nanosheets were prepared by thermal exfoliation and reduction of graphite oxide through a short insertion into a 1000 °C Ar-filled furnace. The graphite oxide was synthesized by a modified Hummer's method from expandable graphite (see Appendix A). Chitosan (>75% deacetylated, from shrimp shell) was purchased from Sigma-Aldrich and used as received.

2.3.2   Preparation of graphene/chitosan composite electrode

A saturated chitosan solution was prepared by dissolving excessive chitosan in a given volume of purified water at 50 ^{o}C and stirring overnight. This solution was allowed to settle and maintained under ambient conditions for more than a day before extracting the chitosan-saturated supernatant. Since this supernatant is chitosan saturated, we have used the solution volume to represent the chitosan content in the composite. In a typical preparation of graphene/chitosan (G/Chit) suspension, a quantity of graphene nanosheets was dispersed in the supernatant at a certain weight-to-volume ratio with the help of ultrasonic probe treatment for at least 2 hours to achieve a uniform suspension; the same treatment was applied for graphene nanosheets in 1% Nafion solution and purified water for comparison purposes.

A circular glassy carbon (GC) working electrode (ALS Co., Ltd.) with a diameter of 3.0 mm was adopted for electrochemical measurements. The vigorously shaken aqueous G/Chit suspension was loaded onto the electrode by drop-casting. 12 L of each suspension was applied onto the GC electrode which was then dried in an oven at 60 °C. A platinum reference (Pt/C) using 20 wt% platinum on carbon was used directly as purchased (Sigma-Aldrich). The Pt/C electrode was prepared in a similar way to G/Chit composite at 1.0 mg/mL in a chitosan-saturated supernatant.

2.3.3 Characterizations and measurements

Scanning electron microscopy (SEM, JEOL6610) was employed for imaging the composite morphology at a working distance of 12 mm. The acceleration voltage was 4.0 kV and no conductive coating was applied to the samples. Transmission electron microscopy (TEM) was operated on a FEI Tecnai G2 F20 microscope at an acceleration voltage of 200 kV. X-ray photoelectron spectroscopy (XPS) was performed on a Kratos Axis Ultra spectrometer using Al K radiation (15 kV, 150 W). The survey spectra were recorded from 0 to 1200 eV at an energy interval of 1 eV/step. The high resolution C 1s spectra were collected at an interval of 0.05 eV/step. Raman spectroscopy (Renishaw Raman spectrometer) was performed with a red laser of 785 nm wavelength. Fourier-transform infra-red (FTIR, Perkin Elmer Spectrum 2000) spectra were collected from 4000 cm^{-1} to 650 cm^{-1} by an attenuated total reflection (ATR) technique, at a resolution of 4.0 cm^{-1}.

All electrochemical measurements were performed on a CHI-440B potentiostat-galvanostat instrument in a 0.1 M KOH electrolyte, saturated with oxygen (O_2) bubbling for at least 30 min. A three-electrode system consisting of a working electrode, a Pt wire counter electrode and an HgO/Hg reference electrode (0.1 M KOH) was used. The as-described setup was employed for cyclic voltammetry (CV) and linear sweep voltammetry on a rotating disk electrode (LSV-RDE).

2.4 Results and Discussion

2.4.1 Self-assembled nanostructures of graphene/chitosan composite GDE

The self-assembly behaviour of graphene nanosheets is determined by the solvent and the type and concentration of dispersant. In an aqueous medium, the hydrophobic graphene nanosheets tend to quickly aggregate into multilayer stacks, probably in a loose manner. This assembly process can alter when the hydrophobic surfaces are stabilized with amphiphilic molecules. Chitosan has worked well with these hydrophobic carbon surfaces as a functional binder.[171] In Figure 2.1, SEM micrographs display the morphology of self-assembled G/Chit composite films on a glassy carbon substrate; the films were prepared at different weight-to-volume (w/v) ratios of graphene nanosheets in chitosan-saturated liquid supernatant (samples are labelled as: G/Chit w:v; mg:mL). Our reference chitosan film shows a non-porous flat surface when no graphene nanosheets were incorporated (Figure 2.1a). When a small quantity of graphene sheets was introduced (G/Chit1:10, Figure 2.1b), significant roughness emerged across the film without visible open cavities. This suggests that the graphene nanosheets are evenly distributed in random orientations throughout the composite rather than being stacked into thick layers. Increasing the graphene content (G/Chit1:1, Figure 2.1c) enhances this roughness and establishes a dense, grass-like film of uniformly distributed sheets; the estimated chitosan content of the film is only about 15 wt% (see Appendix A). By further increasing the graphene content, there resulted in a rapid precipitation of graphene particulates in the suspension which subsequently led to uneven localization of graphene aggregates in the drop-cast film; this was visible to the naked eye. The graphene film without chitosan exhibits strongly aggregated sheets with large open voids (Figure 2.1d). Interestingly the graphene units appear to be larger than those in the composites, despite the fact that an identical source of graphene nanosheets was used and the same treatment method was employed. The small size of the raw nanosheets was confirmed by TEM, as shown in Figure A1 in Appendix A. It is plausible that the large sheets came from a

rapid oriented stacking of smaller nanosheets, followed by a secondary assembly into the observed morphology.
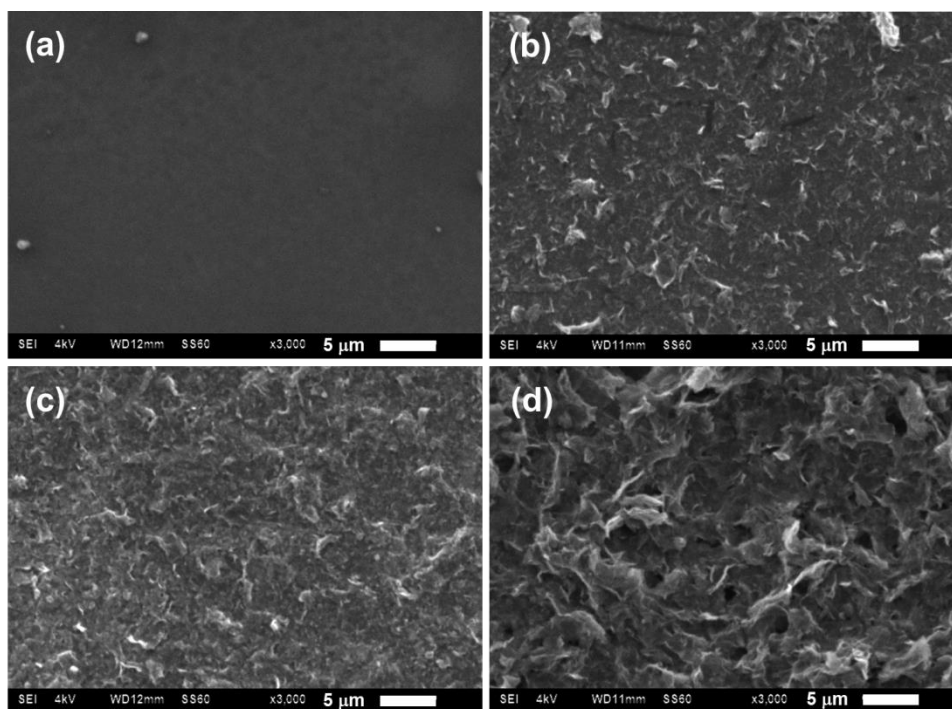
Figure 2.1 SEM micrographs of chitosan, G/Chit composite and graphene films cast on a glassy carbon substrate; (a) chitosan film, (b) G/Chit1:10 (0.1 mg/mL), (c) G/Chit1:1 (1.0 mg/mL) and (d) graphene film. The scale bar is 5 µm.

A proposed mechanism for the evaporation-induced self-assembly of the graphene/chitosan composites or graphene sheets is illustrated in Figure 2.2. In the absence of chitosan, graphene nanosheets quickly stack by hydrophobic interactions, likely in a loose manner, and this leads to an apparent size coarsening in the aqueous dispersion. During drying, these large graphene aggregates further arrange themselves to form a highly rough film with large voids. On the other hand, chitosan acts similarly to a surfactant, preventing the stacking of graphene sheets through surface attachment. We have observed a more stable suspension of graphene nanosheets in a chitosan-saturated solution compared to the segregated aggregates in purified water

(Figure A2, Appendix A). These dispersed nanosheets eventually organize themselves into a homogeneous grass-like film in the chitosan matrix.
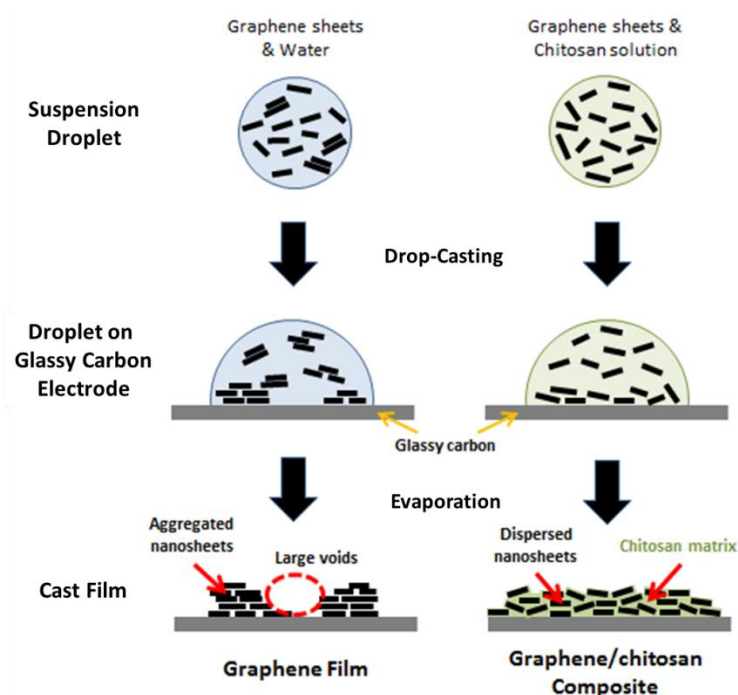
Figure 2.2 A schematic diagram illustrating the film formation for the composite films.

2.4.2   Composition and structural properties

Composition analysis is crucial to verify the content of the composites that gave rise to the differently assembled morphologies. We have employed XPS to study the composition of the films. In Figure 2.3a, the presence of chitosan in the G/Chit1:1 composite was directly confirmed by the nitrogen signature and the slightly increased oxygen content. A reasonable level of oxygen (11.4 at. %) was present in our graphene sample prepared through thermal exfoliation and reduction of graphene oxide. This amount of oxygen could be due to the short exposure to high temperature. This oxygen presence is beneficial for dispersion in chitosan solution as well as for ORR catalysis, as oxidized carbons usually exhibit improved activity compared to

oxygen-free pristine carbons.[137,138] Figure 2.3b to 2.3d are the high-resolution C $1s$ spectra for G/Chit1:1 composite, graphene and chitosan films, respectively; these spectra were calibrated to the carbon-carbon peak at 284.8 eV. Quantitative analysis of the spectra reveals five different types of carbons in the composites, which are commonly found in reduced graphene oxides:[172] graphitic/aliphatic carbon (C–C, 284.8 eV), carbon linked to hydroxide (C–OH, 286.0 eV), carbon in epoxide (C–O–C, 286.9 eV), carbon in carbonyl group (C=O, 288.2 eV) and carbon in carboxylic acid (COOH, 290.0 eV). The numerical values from the analysis are tabulated in Table 2.1. The carbonyl presence in chitosan is due to the amide groups remaining from the incomplete deacetylation of chitin. We did not attempt to resolve for the possible amine group (C–NH$_2$) from chitosan due to its insignificant concentration and the overlapping binding energy with hydroxide/epoxide functionalities. Clearly, the oxygen content in the graphene was dominated by both hydroxides and epoxides. The incorporation of chitosan is also evident, given by a noticeable increase of hydroxide amount from the polysaccharide.
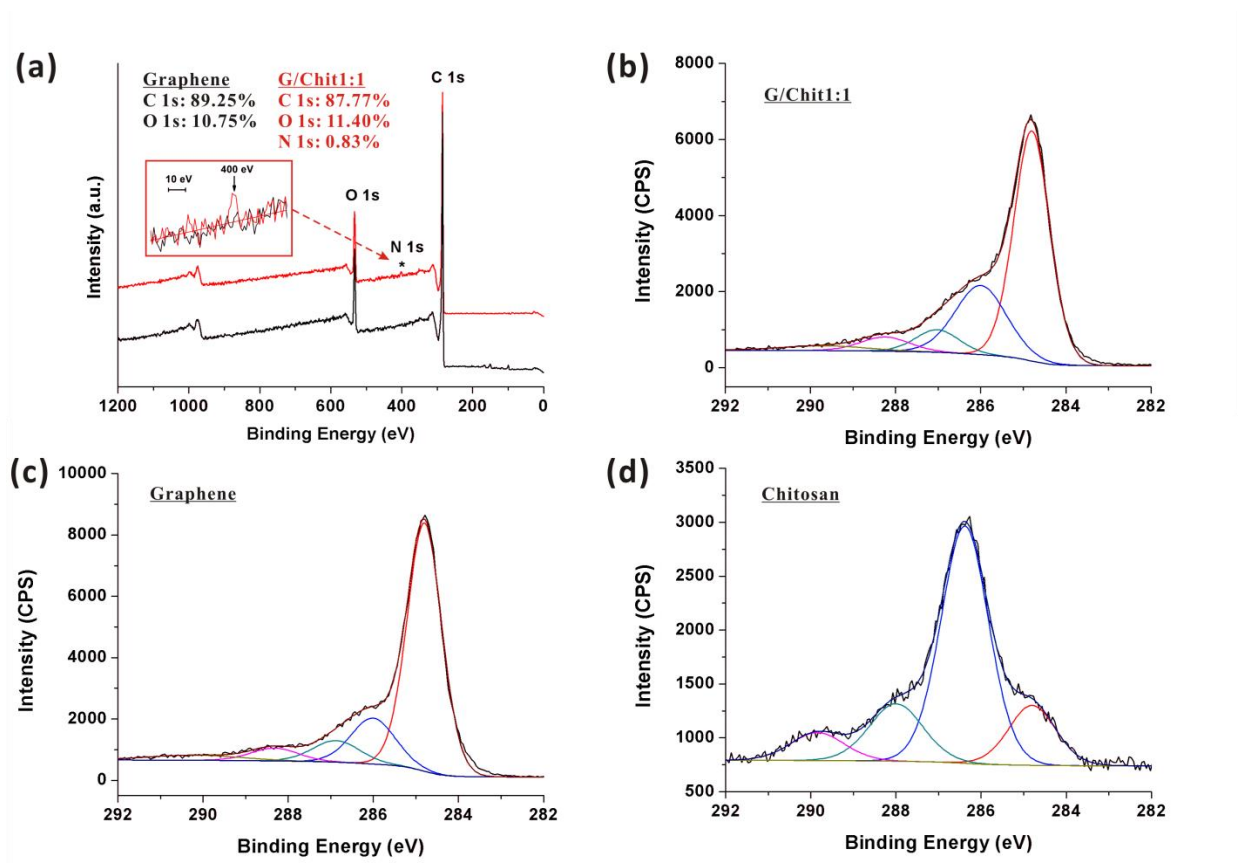
Figure 2.3 XPS (a) survey spectra for G/Chit1:1 composite and graphene nanosheets;

C *1s* spectra for (b) G/Chit1:1 composite, (c) graphene film and (d) chitosan film.

Table 2.1. Statistical composition analysis of the XPS C *1s* spectra.

C *1s*	G/Chit1:1 composite film		Graphene film		Chitosan film	
Functional Groups	*B.E. (eV)*	*Conc. (at.%)*	*B.E. (eV)*	*Conc. (at.%)*	*B.E. (eV)*	*Conc. (at.%)*
C–C	284.8	59.48	284.8	67.65	284.8	15.09
C–O	286.0	25.51	286.0	15.87	286.4	60.46
C–O–C (epoxide)	287.0	7.03	286.9	7.97	N/A	N/A

C=O	288.2	4.94	288.3	4.77	288.0	16.46
COOH	289.8	3.04	290.2	3.74	289.8	7.99

In order to better understand the overall chemical structure of G/Chit composites, we have employed Raman spectroscopy to look for any chemical linkages that could disrupt the phonon vibration in the graphitic lattice. Figure 2.4a shows the intensity-normalized Raman spectra for G/Chit1:1 composite, graphene and chitosan films. Both D band (1320 cm^{-1}) and G bands (1589 cm^{-1}) were observed for graphene-containing samples, signifying the presence of sp^3 defects in a sp^2 carbon lattice, and the in-plane vibration in a graphitic network, respectively.[172,173] The intensity ratio of the D and G bands (I_D/I_G) provides information about the degree of structural disorder for a graphene sample. For both graphene film and the G/Chit1:1 composite, an I_D/I_G value of 1.33 was measured, indicating the significant presence of sp^3 defects in the original graphene source. This is not surprising for an exfoliated graphene whose structure has been vigorously distorted by harsh chemical oxidation and high-temperature thermal shock.[172,174] In addition, the oxygen content in the graphene sheets could contribute to the high number of sp^3 defects. The absence of 2D band (~2700 cm^{-1}) in the graphene sample further suggests that the restacking occurred was not in a close-packing configuration over a fair range, although the high doped amount of oxygen may also diminish the 2D vibration.[175] In comparison to graphene-containing samples, chitosan only exhibits a weak fluorescence background, which accounts for the slightly enhanced background in the G/Chit1:1 composite. There is no change in the ratio and the position of the peaks, indicating that chitosan molecules are not chemically connected with the graphitic lattice, at least not in a way

that interrupts the electronic conjugation. This suggests that the mode of interaction is probably physical adsorption and hydrogen bonding with the oxygen functionalities.

FTIR spectroscopy also reveals the chemical structures of the composite through vibrational signals. From Figure 2.4b, the G/Chit1:1 composite shares common features with that of graphene (C–H stretching, 2920 cm^{-1} and 2847 cm^{-1}; C=O stretching, 1721 cm^{-1}; graphitic C=C skeletal vibration, 1546 cm^{-1}).[106] These signatures are mainly attributed to the defects in the graphitic lattice. The undulating feature at ~2100 cm^{-1} is due to the CO_2 contamination. The presence of chitosan is seen by the aliphatic amine and hydroxyl signatures (N–H bending of primary amine, 1629 cm^{-1}; CH_3 symmetrical deformation, 1363 cm^{-1}; C–O skeletal stretching vibration, 1067 cm^{-1}).[176] No extra peak was found for possible bridging functional groups, which again suggests no chemical interaction was established between graphene sheets and chitosan. In summary, chitosan in the G/Chit1:1 composite acts as a physically adsorbed spacer and separates graphene nanosheets.
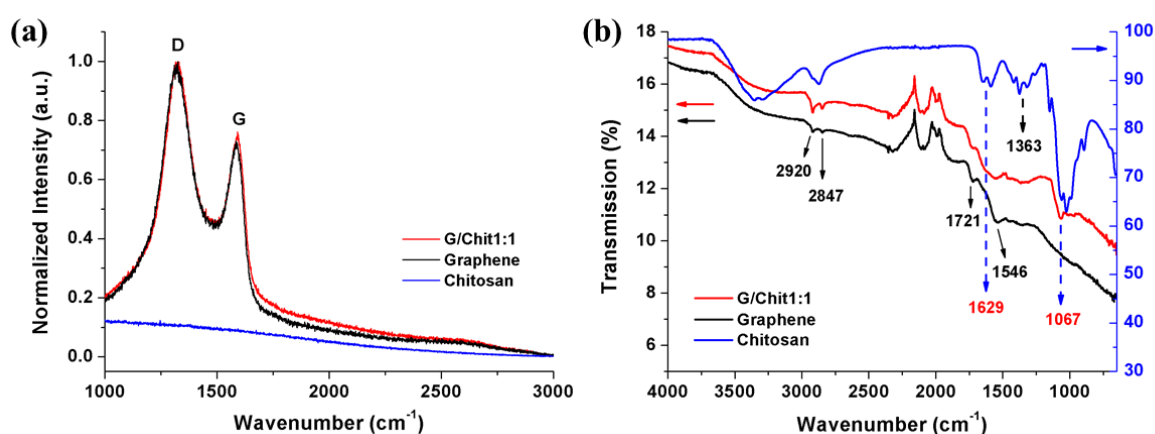
Figure 2.4 (a) Raman spectra and (b) FTIR spectra for G/Chit1:1 composite, graphene and chitosan films.

2.4.3   ORR electrocatalysis on graphene/chitosan composite GDE

Oxygen reduction reactions (ORR) are electrochemical reactions which consume O_2 and produce either peroxide ions (HO_2^-) or hydroxide ions (OH^-) in an alkaline medium. The principal reactions are expressed as follows.[6]

$$O_2 + H_2O + 2\,e^- \rightarrow HO_2^- + OH^- \qquad -0.065\ \text{V, NHE} \qquad (2.1)$$

$$HO_2^- + H_2O + 2\,e^- \rightarrow 3OH^- \qquad +0.867\ \text{V, NHE} \qquad (2.2)$$

Basically, the aim of electrocatalysis is to promote ORR by reducing the reaction overpotential for both reactions and facilitating the kinetics of the HO_2^- decomposition to achieve an apparent four-electron (4e) reaction at low overpotential.[177] With the intention of investigating the structural effect of the electrocatalyst on ORR, we only focus on the change of the first reaction overpotential rather than to strive for an efficient 4e ORR at low overpotential. Since the determination of theoretical reaction potential for O_2/HO_2^- couple for a non-ideal system is not trivial, we have taken the first peak potential of G/Chit1:1 composite as a reference potential for later calculations. Note that G/Chit1:1 composite shares an identical reaction potential with neat graphene as a better control reference (Figure 2.5a); G/Chit1:1 composite was therefore chosen for a better visual comparison. CV and LSV-RDE were employed to examine the structure-activity relationship of G/Chit composites.
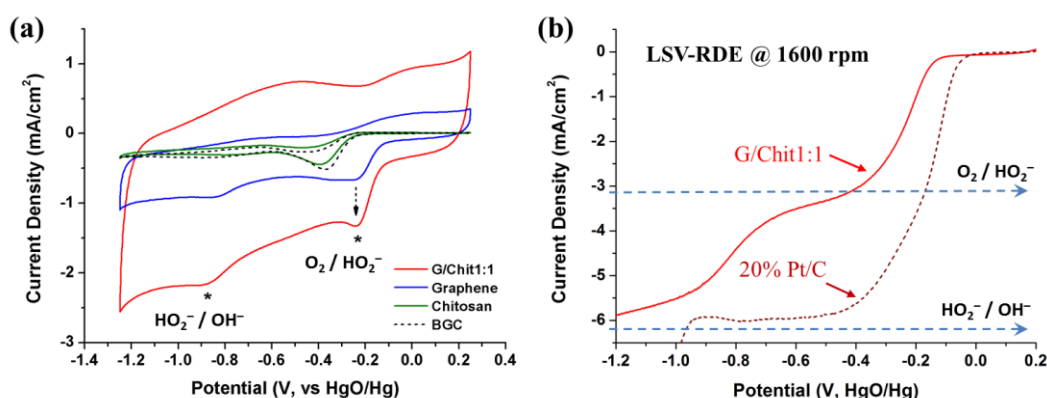
Figure 2.5. (a) CV profiles for G/Chit1:1 composite, graphene, chitosan and BGC at a sweep rate of 50 mV s^{-1}; (b) LSV-RDE profile for G/Chit1:1 composite (at 10 mV s^{-1}). All measurements were carried out in an O$_2$-saturated 0.1 M KOH electrolyte.

Figure 2.5a displays the cyclic voltammograms of G/Chit1:1 composite, graphene and chitosan films as well as the bare glassy carbon (BGC) substrate in an O$_2$-saturated 0.1 M KOH electrolyte. Two electrochemical reactions associated with ORR can be observed at –0.24 V and –0.86 V for G/Chit1:1 composite and the graphene film. They are confirmed to be the reduction reactions of the dissolved oxygen in contrast to the capacitive background profile in a deoxygenated environment (Figure A3, Appendix A). These processes occurred in a successive manner according to the LSV-RDE profile (Figure 2.5b), and can be assigned to the two-electron reduction of O$_2$ (Eq. 2.1) and the subsequent reduction of HO$_2^-$ intermediate (Eq. 2.2), respectively.[35] This is unlike the behaviour of Pt/C, which performs a direct 4e ORR at a less negative onset potential. Furthermore, there is an obvious current density enhancement in CV for G/Chit1:1 composite in contrast to the graphene film, even when compare to a graphene composite blended with Nafion as the binder (Figure A4, Appendix A). Note that same amount of graphene (12 g) was applied onto the electrode for both G/Chit1:1 composite and the graphene film. This suggests that the uniformly dispersed graphene nanosheets in G/Chit1:1 composite developed a higher electrocatalytic surface area. It is important to also point out that a certain amount of chitosan was required to reinforce the composite integrity, from the observation that pure graphene or composites with a G/Chit ratio > 1.0 could easily fall from the electrode surface when immersed in the electrolyte. This result is a clear demonstration of the importance of composite structure for enhancing ORR activity.

We have also performed Koutecky–Levich analysis on G/Chit1:1 composite to evaluate the average electron transfer (n) number as a reference for the ORR activity. The n number was determined to be 2.94 at a potential of –0.50 V from LSV-RDE at various rotation rates, provided in Appendix A. This corresponds to the parallel occurrence of 2e and 4e transfer processes. Although this can suggest improved activity in oxygen-functionalized graphene, the large effective electrode surface area may have influenced the accuracy of the analysis.[87,178]

On the other hand, the reference BGC and chitosan film did not show satisfactory activity towards ORR. The first reaction peaks were found at more negative potentials for BGC (–0.38 V) and chitosan film (–0.40 V). In addition, a lower current density of chitosan film relative to BGC probably indicates an imposed hindrance by the insulating layer to O_2 mass transport. Since there is a lack of chemical interaction between chitosan and graphene nanosheets, the fact that G/Chit1:1 composite exhibited a better ORR activity in the presence of chitosan must come from the favourable composite structure for both efficient electrolyte diffusion and electron conduction.

The manner in which the composite structure affords an optimal ORR activity was the motivation for the study of the structure-activity relationship. For this reason, we have varied the G/Chit ratios to tune the composite structure and optimize the reaction behaviour. From the CV profiles in Figure 2.6a, the first ORR peak shifted progressively towards a more negative potential with the decreasing of the graphene content; the reduction in the current density was clearly due to the lower overall content of graphene nanosheets in the composite. In a plot of the G/Chit ratio against the peak potential (ΔE_p, in reference to G/Chit1:1 composite) on a semi-logarithmic scale (Figure 2.6b), a two-stage quasi-linear relationship is evident below a G/Chit

ratio of ~0.45 mg/mL, and beyond which is a plateau for an optimal composite structure (no additional overpotential compared to G/Chit1:1 composite). The two stages suggest there are two major contributions to the reaction overpotential in addition to the intrinsic reaction potential for graphene nanosheets, although the exact reason for the linear relationship remains unclear. As discussed previously, the composite components do not chemically interact with each other, so that the reaction overpotential is essentially the result of subtle structural differences in the composite. Such alterations in structure may have obstructed the aqueous O_2 mass transport.[161] Because chitosan exhibits insulating properties, the electronic conductivity across the composite may have been degraded with high loadings of chitosan. As a result of this, we have attributed the first stage (Stage 1, from 0.13 mg/mL to 0.45 mg/mL) to the diffusion-related overpotential, and the second stage (Stage 2, < 0.13 mg/mL) to the combined overpotentials due to the hampered mass transport and poor electron conduction.
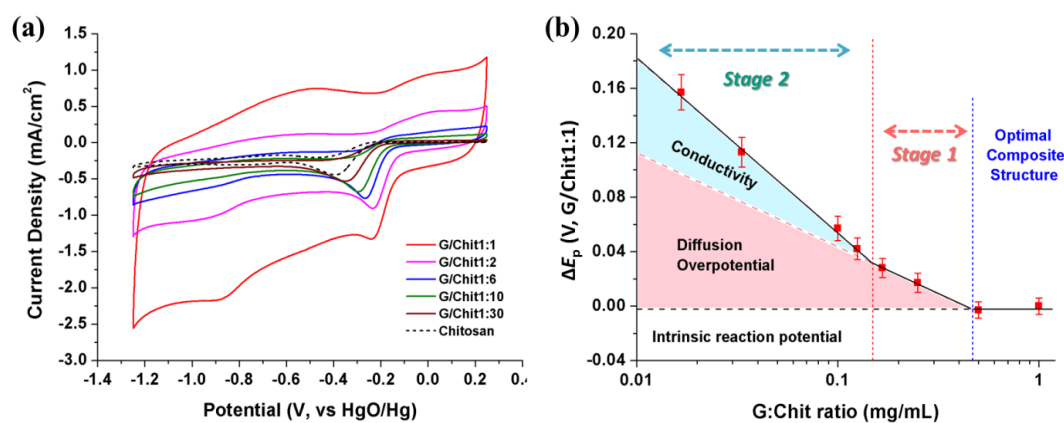
Figure 2.6. (a) CV profiles of G/Chit composites at various composition ratios in an O_2-saturated 0.1 M KOH electrolyte, swept at 50 mV s^{-1}. (b) A semi-logarithmic plot of ΔE_p against the weight-to-volume (w/v) ratios of G/Chit composites.

In order to verify our hypothetical assignments, we have employed an aqueous electrolyte system containing $K_3Fe(CN)_6$ to study the electron transfer reaction. In

principle, electrons can only be transported to the reaction sites through a conducting network. When this network is not properly established, electron conduction paths can be blocked and reaction overpotential can develop. The redox couple $Fe(CN)_6^{4-}/Fe(CN)_6^{3-}$ delivers a very fast charge transfer process and this reaction typically serves as a benchmark quasi-reversible reaction that is close to an ideal system, particularly for carbon-based electrodes.[179] This eliminates the problem of reacted and unreacted reactants and products bound to the carbon surface. Moreover, the system only requires an electrically conducting surface rather than an electrocatalytic surface to perform the reaction, which mitigates the requirement for diffusion to specific reaction sites. A much higher bulk reactant concentration was employed to ensure a minimal participation of diffusion interference.[117] Hence, any resistance should correspond to inefficient charge transport in the composite matrix; this can be examined by the peak separation ($E_{pa} - E_{pc}$) of the reversible couple in a CV experiment.[179]

Figure 2.7a shows the CV profiles for various G/Chit composites. The two characteristic peaks correspond to the anodic and cathodic reaction of the $Fe(CN)_6^{4-}/Fe(CN)_6^{3-}$ couple. Clearly, the peak separation values stay approximately constant until a G/Chit ratio of 0.033 mg/mL (G/Chit1:30) is reached. The subsequent rapid change in the peak separation likely indicates the breakdown of electron conduction in the composite and therefore induced reaction overpotential in both directions. By directly plotting the peak separation against the G/Chit ratio, we find a sigmoidal-type relationship and a very sharp boundary occurring at a G/Chit ratio of 0.061 mg/mL (Figure A6, Appendix A). This suggests a threshold for electron conduction, which is often noticed in carbon-polymer composites at various volume fractions.[180,181] To compare with Figure 2.6b, we have transformed the plot into a

semi-logarithmic scale, as shown in Figure 2.7b. Interestingly, we find that the rising point of the peak separation (0.15 mg/mL) is very close to the start of Stage 2 (0.13 mg/mL) in Figure 5b, where the conductivity overpotential begins to participate. This strongly supports our hypothesis that poor electron conduction is the secondary element in creating reaction overpotential. This is best illustrated in the proposed composite structure of Figure 2.7b. By reducing the graphene content, the packing density of the nanosheets gradually decreases until a threshold value where individual nanosheets become disconnected or aggregated into isolated domains and the electron conduction paths are disrupted.
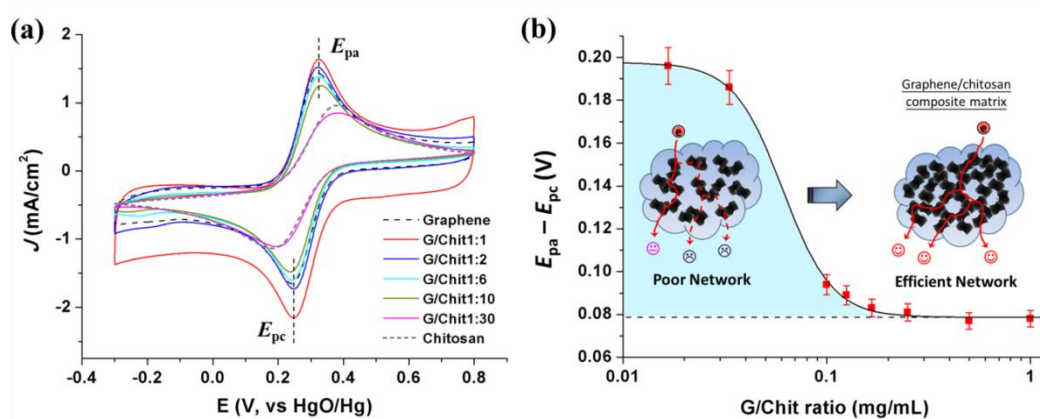
Figure 2.7 (a) CV profiles of G/Chit composites at various w/v ratios in 10 mM $K_3Fe(CN)_6$/1.0 M KNO_3 electrolyte; (b) a graph of peak separation ($E_{pa} - E_{pc}$) against the w/v ratios, fitted with a sigmoidal function as a guide to the eye. The inset figures are proposed matrix structures for electron transport.

Returning to the discussion of reaction overpotential due to diffusion hindrance and poor electron conduction, it is now obvious that the increase of the overpotential in Stage 1 (from Figure 2.6b) is not attributable to the electronic conductivity. Since electrolyte diffusion can occur in various forms and the behaviour is dependent on the structure and composition of the composite, we did not endeavour to solve for a diffusion expression since numerous assumptions must be made. Nevertheless, the

hindrance of mass transport has been commonly recognized to be a substantial issue in gas diffusion electrodes.[161] Here we rationalize this fact based on the G/Chit composite structure. From our SEM result, the graphene nanosheets appear to be loosely covered by a layer of chitosan molecules to prevent severe aggregation. In this case, O_2 molecules have to diffuse through the liquid channels in the chitosan medium to arrive at the active surface, and so do the reaction products in the opposite direction. This would be the primary resistance for ORR. If we view the chitosan medium surrounding an individual nanosheet as a diffusion sphere, then increasing the chitosan content would enlarge the diffusion radius and thus generate transport hindrance for an enhanced overpotential. Fortunately, this diffusion hindrance only becomes influential beyond a certain threshold value (0.45 mg/mL) and an enhanced current density can be achieved with an effective binary composite system.

Putting together all the information, we are now able to construct a scheme to illustrate the particular contributions towards ORR overpotential for G/Chit composites. As shown in Figure 2.8, both diffusion and electron conduction issues are the main sources of ORR overpotential arising from the composite structure. When the density of graphene nanosheets is reduced in a composite matrix, the nanosheets become farther separated and the inter-diffusion distance for O_2 and the reaction products (OH_2^- in the present case) would be increased. As this diffusion radius is extended, an extra potential driving force would be required to facilitate ORR thus generating overpotential. However, this may not have an impact on the electronic conductivity as long as the majority of nanosheets stay connected. As the average diffusion radius increases, the nanosheets (or the aggregates) are separated from each other and break down the electron conduction network. From this point, the ORR overpotential is dominated by both limited diffusion and electron conduction.

Ultimately all of these adverse effects are the result of the poorly assembled structure of the binary composite matrix.
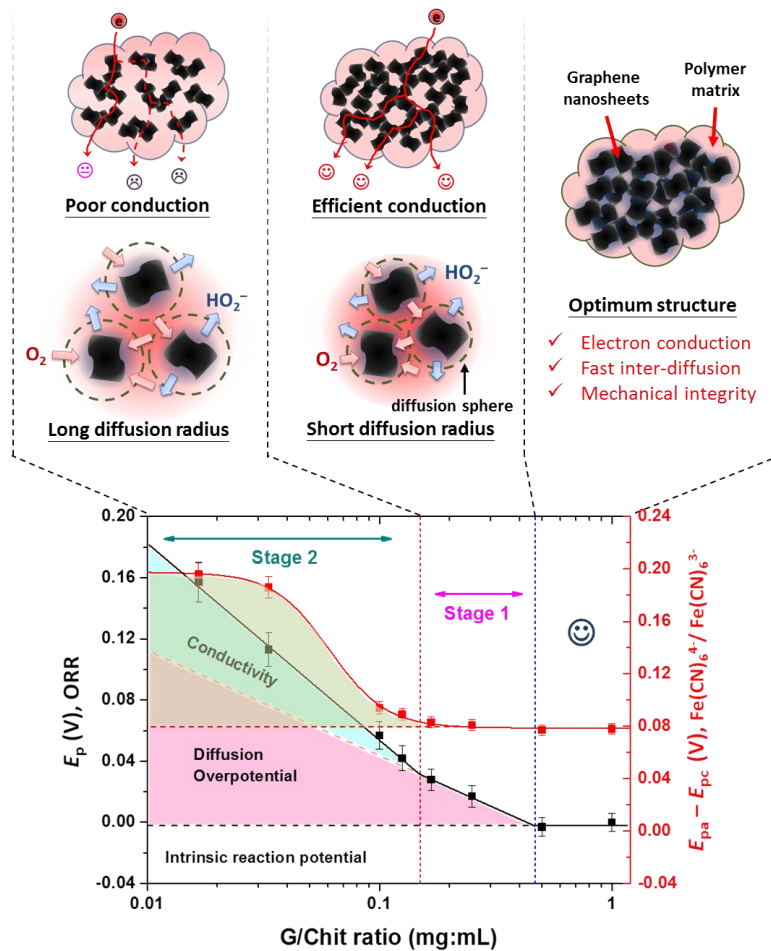
Figure 2.8 Structural influences on ORR overpotential in a graphene/binder matrix.

Structural optimization of graphene-based binary composites is necessary to attain the intrinsic electrocatalytic performance of the active material. An optimal composite composition is one in which the assembled structure can deliver efficient mass and charge transport within the composite matrix and provide a high reaction current density from the large electrocatalytic surface area. As a general guide towards the optimal structure, we recommend a high weight content of conductive active material with a satisfactory binder that can facilitate electrolyte transport within a composite matrix.

63

2.5 Conclusion

The self-assembled structure of graphene-based composites has a significant impact on ORR performance, due to significant hindrances in both mass and charge transport. We have demonstrated in this work that a graphene-based binary composite in the absence of chemical interactions can deliver an improved reaction current density without additional overpotential at an optimal configuration. Furthermore, our results suggest that ORR performed on a G/Chit composite is sensitive to diffusion hindrance and that electron conduction within the composite matrix makes a significant impact on the reaction onset potential. For efficient ORR, we recommend an optimal composite configuration at a high loading of active material should be employed.

Chapter III.

Metal-free ORR Electrocatalysts:

Oxygen Reduction Reaction on Oxidized Carbons

3.1 Abstract

Metal-free carbon electrocatalysts are potentially effective in delivering robust and efficient oxygen reduction if the active sites are covalently located on a conductive support. In this report, we demonstrate that carbon nanotube, as a framework carbon, can create active sites upon oxidation for efficient oxygen reduction to peroxide, whereas the saturation of oxygen groups at graphitic basal planes leads to the loss of electron conduction thereby worsens the electrocatalytic activity. Importantly, oxygen groups at different locations and with different structures have a significant impact on the oxygen reduction activity. In particular, epoxide bound oxidized carbon shows superior activity among other oxidized carbon nanotubes.

3.2 Introduction

The electro-reduction of oxygen has been a fundamental part of the function of hydrogen fuel cells and metal-air batteries for almost two centuries [14]. Since the recent discovery of highly efficient metal-free electrocatalysts for the oxygen reduction reaction (ORR), researchers have striven to develop a superior replacement for platinum.[17,105] Unfortunately, there is still little understanding of the origin of the activity in these metal-free electrocatalysts, such as nitrogen-doped carbons.[15,21,22] Although suggestions have been made that the electronegativity of doped heteroatoms,[145] and particular dopant-incorporated "defective" structures,[182] may be the origin of active sites, there is still a lack of experimental evidence to verify these hypotheses. In addition, good electron transport across the support structure of active sites is crucial for the overall activity,[85] although the macroscopic origin of the prohibited transport by chemical modification has not been clearly elucidated. It has been shown that chemical and thermal treatment of carbon-based materials can

change both the active sites and the electron conductivity.[183-185] To better understand the origin of activity of the electrocatalysts, we therefore need a model system in which the non-metal dopants are finely controlled in content, location and type, supported on a tuneable framework of a carbon substrate.

Among non-metal dopants, oxygen is the most common heteroatom in carbons and has been investigated for many decades.[53,137] This element exhibits stronger electronegativity than nitrogen while still allowing sufficient complexity in the bonding configuration for a variety of local structures. Past research has shown that graphitic carbons can perform more efficient ORR after being slightly oxidized,[137] and that the quinone groups are responsible for the lowering of reaction overpotential.[53,186] Although these studies have looked at oxygen functionalities at the graphitic edges or by physically adsorbing oxygen-containing small molecules to the carbons, cases with of high oxygen content on the carbons, different oxygen groups at various locations, and the integrity of the carbon framework for electron conduction were not clearly addressed. Fortunately, years of development in carbon processing have led to methods for fine tuning of the content, location and type of oxygen functionalities in carbons. One recent study has shown that graphene oxide as an oxygen-enriched carbon exhibits improved ORR activity when carbon nanotubes (CNTs) were incorporated as the electron conductor [138]. For this reason we have selected multi-walled CNTs as a framework carbon substrate for oxidation with the aim of understanding the ORR behaviour on oxidized carbons.

In this report, we demonstrate controlled oxidative modifications of CNTs and study the oxidized CNTs (OCNTs) with variations in content, location and type of oxygen groups to provide a deeper understanding of the active oxygen functional groups for ORR as well as the structural origin of activity loss due to the damage of

conductive carbon framework.

3.3 Experimental Section

3.3.1 Materials

Multi-walled CNTs (purity $\geq$ 95%) were commercially purchased. All other chemicals (36% hydrochloric acid, 70% nitric acid, 98% sulfuric acid, 30% hydrogen peroxide solution, potassium hydroxide and potassium permanganate) were used as purchased from Sigma-Aldrich.

3.3.2 Preparation of OCNTs

CNTs used in this work were purified before use with extensive washing and sonication in 5.0 M HCl, ethanol and water, separately and repeatedly. No metal traces were identified and a C/O ratio of 70 was found based on X-ray photoelectron spectroscopy (XPS) analysis; an O *1s* spectrum of purified CNT is provided in Appendix B for reference. OCNTs were prepared using a modified Hummer's oxidation at different $KMnO_4$:CNT mass ratios, and H_2SO_4-catalyzed HNO_3 oxidation (1:2 v/v for H_2SO_4/HNO_3) for different periods. Detailed experimental procedures including the further thermal treatment can be found in Appendix B. All OCNTs were purified before characterization and electrochemical measurements.

3.3.3 Characterizations

Transmission electron microscopy (TEM) of CNTs and OCNTs was performed on a JEOL1010 transmission electron microscope at an accelerating voltage of 100 kV. XPS was performed on a Kratos Axis Ultra XPS spectrometer using a monochromated Al Kα source. The survey scan and high-resolution scan were

measured at an energy-sweeping rate of 160 eV s^{-1} and 20 eV s^{-1}, respectively. All spectra were corrected against the C–C peak at 284.8 eV as a reference and the full-width at half-maximum (FWHM) values were held constant for all peaks. X-ray diffraction (XRD) was carried out on a Bruker D8 Advance X-ray diffractometer with a Cu Kα source; the step rate was 0.02 degrees per second. Raman spectra were collected on a Renishaw inVia Raman spectrometer from 1000 cm^{-1} to 3000 cm^{-1} using an argon green excitation laser (514 nm) with 1% of the maximum power (50 mW).

3.3.4   Electrochemical measurements

A three-electrode system was employed for the measurement: a rotating Pt ring/glassy carbon (GC) disk working electrode (ALS Co., Ltd.; GC diameter: 4.0 mm, Pt ring inner diameter: 5.0 mm and outer diameter: 7.0 mm), a Pt wire counter electrode and an HgO/Hg reference electrode stabilized in 0.1 M KOH. A total of 75 μg of the catalyst material with Nafion was drop-cast onto the working electrode. A RRDE-3A apparatus (ALS Co., Ltd.) coupled with CHI920D bipotentiostat instrument was set up for the experiment. The reaction was conducted in an O$_2$-saturated 0.1 M KOH electrolyte; the gas saturation was performed by purging O$_2$ gas at a flow rate of 10 mL min^{-1} for at least 30 min before the measurements. Linear sweep voltammetry on a rotating ring-disk electrode (LSV-RRDE) was performed in the electrolyte at an electrode rotation rate of 1600 rpm, scanned at a sweeping rate of 10 mV s^{-1} and the ring potential was held at +0.5 V versus the reference electrode.

3.4 Results and Discussion

The   controlled   oxidation   of   CNTs   has   been   undertaken   using   two

well-recognized methods: modified Hummer's oxidation and oxidative acid etching. Starting with purified CNTs, we have selectively impaired the nanotube by either piercing through the CNT walls with aggressive oxidation,[187] or caustically etching from the surface.[188] By such methods, oxygen groups can either be spread throughout the carbon framework (unzipped and oxidized) or confined at the surface (surface etched). Furthermore, the content of oxygen and the degree of damage of the CNT framework can be modulated by the extent of oxidation. Since there are various possible oxygen groups in the OCNTs, we have used high-resolution XPS analysis to provide information about the types of oxygen groups present. Figure 3.1 illustrates the predicted outer-shell structures of multi-walled CNTs and their oxidized derivatives following the two oxidation methods. When acid-promoted oxidative etching is employed, the nitric acid attacks and oxidizes the carbon from the surface and leads to carboxylic acid groups as the major species.[187] In the Hummer's oxidation method, the reagents not only cut through CNTs in the longitudal direction, but typically introduce ether-type oxygen groups on carbon (e.g., epoxide and 1,3-ether) as the major products when a high mass ratio of $KMnO_4$:CNT is used.[183]
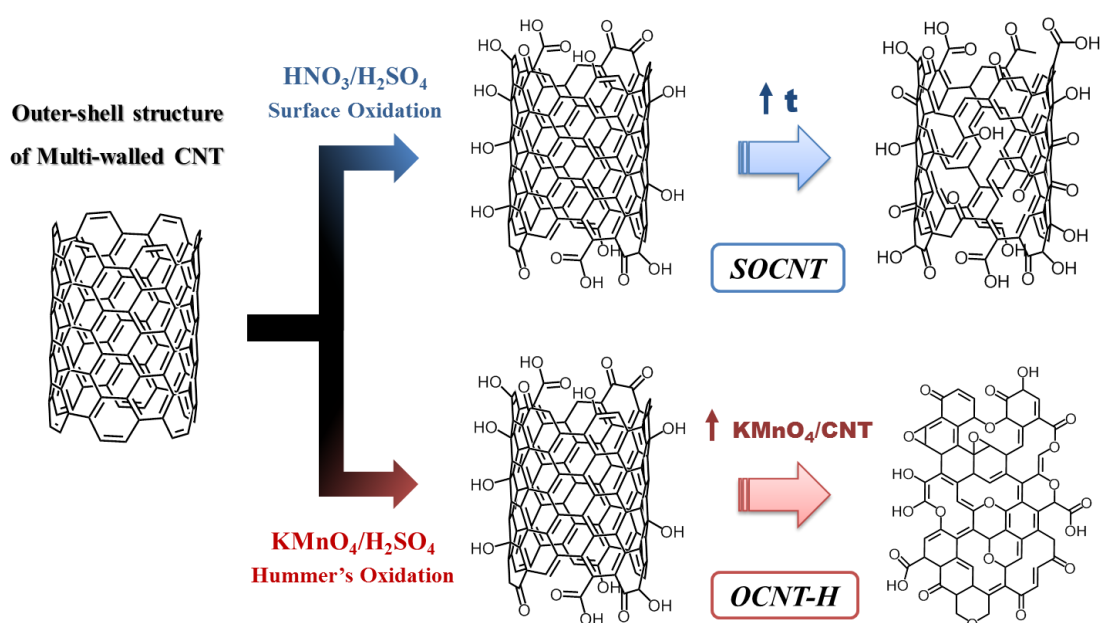
Figure 3.1 Outer-shell structure of CNT and the structural evolution of the OCNTs during Hummer's oxidation and oxidative acid etching.

Figure 3.2a shows the XPS survey spectra of CNT and OCNTs after particular oxidation conditions. The OCNTs are labelled according to their modification methods and experimental conditions, namely SOCNT-xh and OCNT-Hy for the acid etching and the Hummer's method, respectively, where x is the reaction period in hours and y is the KMnO$_4$:CNT mass ratio. Only C $1s$ and O $1s$ peaks were observed, without any trace of other elemental impurities. The varying ratios of the peak intensity indicate the change in the oxygen content of the OCNTs. Through quantitative analysis, we have plotted the oxygen content and the C/O atomic ratios of the OCNTs, as shown in Figure 3.2b. Clearly, both systems display an increase in the oxygen content (or a decrease in C/O atomic ratio) as the respective reaction conditions as intensified. Of the two methods, the Hummer's oxidation appears to be a much more effective strategy in attaining high oxygen content in the CNTs. Overall this result demonstrates that the oxygen content on OCNTs can be tuned from 4.0 at.% up to 28 at.%, combining both methods.
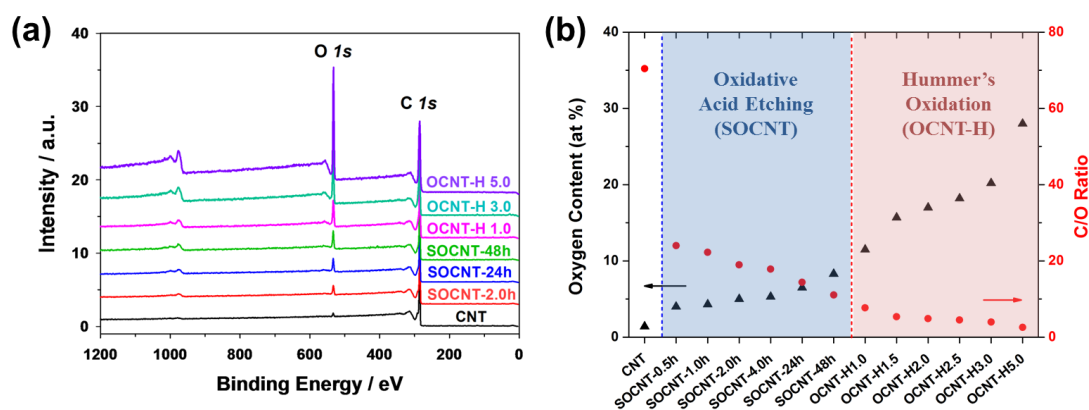
Figure 3.2 (a) XPS survey spectra of CNTs and the OCNTs prepared from different methods; (b) the evaluated oxygen contents and C/O ratios of the CNTs following oxidation by acid etching (blue shading) and Hummer's oxidation (red shading),

based on XPS results.

One typical reference to structural damage of carbon framework is by looking at the graphite interlayer crystallinity using XRD method. When a multi-layered nanotube is exposed to penetrative chemical damage, the unzipping and intercalation by the intruding molecules can cause expansion and exfoliation of the graphite layers.[189] This leads to the disappearance of characteristic (002) diffraction peak at around 26° (2θ), signifying the typical 0.34 nm graphite interlayer spacing. Figure 3.3a and 3.3b are the diffraction patterns of the OCNTs prepared by different methods. The characteristic pattern reveals that the source CNTs has a graphite-type crystal structure in an AB stacking configuration.[190] In line with the nature of oxidative etching, the (002) peaks of surface-oxidized CNTs do not experience a change in the intensity even after 48 hours of reaction time; this means the majority of graphite interlayer remains intact and only the surface layers have undergone acid oxidation. The slight decrease in the (101) diffraction can be rather complicated, which is probably attributed to some displacement of the graphitic multilayers. In another case, the (002) peak drops progressively for OCNTs prepared by a modified Hummer's method upon increasing the $KMnO_4$ amount in the reaction (Figure 3.3b). This suggests layer expansion and exfoliation processes have occurred during Hummer's oxidation, accompanied with oxidation at the inner layers. Such result is not surprising since Kosynkin *et al.* have demonstrated the unzipping of CNTs into graphene oxide nanoribbons (GONRs) by using a modified Hummer's method.[187] Note that there retains a fair level of (002) crystallinity at a $KMnO_4$:CNT ratio of 3.0 and this feature completely vanishes at a ratio of 5.0. This is an important indication that some undamaged graphite domains are preserved even for OCNT-H3.0; this will be discussed in a later section to reveal the route of electron transport. In further

evidence to the unzipping process, the TEM images shown in Figure 3.3c provide a significant morphological change from CNTs to GONRs in OCNT-H5.0. This directly suggests the unzipping of CNTs through penetrative oxidation. As a summary to the structural evolution of multi-walled CNTs during Hummer's oxidation, a simple diagram is illustrated in Figure 3.3d. Essentially, the multi-walled CNTs must have undergone an aggressive unzipping in order to allow exposure of the interlayers to oxidative damage and intercalation. In a consequence, layer expansion and exfoliation subsequently take place and determine the final morphology of GONRs. This is a physical change of the nanotube morphology; additional information about the basal plane structure is required to resolve for a more complete picture of the graphitic framework configuration.
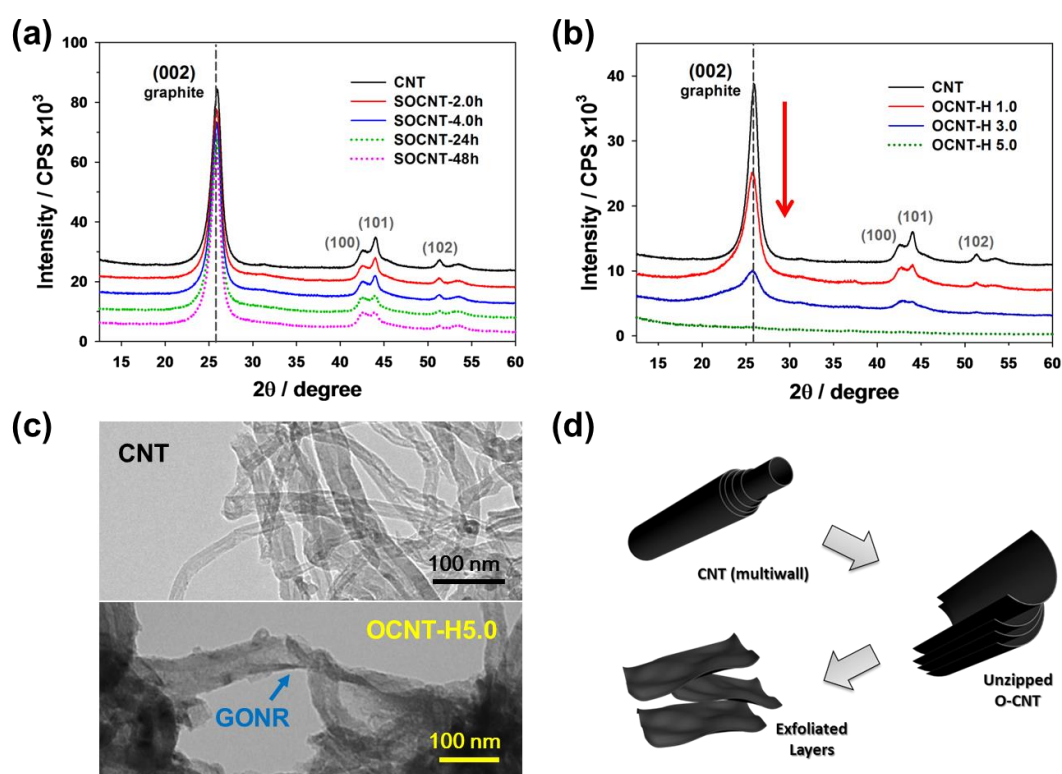
Figure 3.3 XRD patterns of OCNTs in (a) SOCNT and (b) OCNT-H systems; (c) TEM micrographs of CNT (top) and OCNT-H5.0 (bottom); (d) the morphological change of CNT upon Hummer's oxidation.

In order to study the basal plane framework of OCNTs, Raman spectroscopy was employed to observe the changes in the spectral features of the OCNTs. Figure 3.4 displays the Raman spectra for SOCNT and OCNT-H systems. Basically there are three major peaks for the OCNTs, which can be assigned to D (1354 cm^{-1}), G (1584 cm^{-1}) and 2D (2707cm^{-1}) bands; a small shoulder (~1614 cm^{-1}) affiliated to the G band is labeled as D' band. In simple terms, the G band signifies the phonon stretching mode of the sp^2 carbon atoms in an aromatic ring and the D band results from the breathing mode of sp^2 carbons in a ring (although it is typically forbidden in perfect graphene lattice), while the 2D band is the second order overtone of the D peak and is originated from the two-phonon scattering on a continuous graphene domain.[175] Generally, the D band is only present when there is some structural disorder in the sp^2 carbon lattice. The weak D' band is also a disorder-induced peak, indicative of lattice disorder in the carbon.[191] From the D and weak D' bands, it is clear that all the samples including the unmodified CNTs contain some disorder in the carbon lattice. Moreover, the relative intensity of 2D band to G band is inversely associated with the doping level on the graphene basal planes.[175] In Figure 3.4a, which shows the results for the SOCNT samples, neither the I_{2D}/I_G intensity ratios nor the spectral profiles of the G band show obvious change. This suggests that the majority of the graphitic basal planes remain intact throughout the surface-oxidized CNTs, despite of the oxygen doping at the very outer surfaces. Likely, the acid focally attacks at the graphitic edges through oxidation once a holey defect is occasionally created at surface basal planes; in this way, large area continuous graphene domains can be preserved or regenerated at the surface. Using the Hummer's oxidation method, we can see in Fig. 3.4b that the I_{2D}/I_G ratio reduces significantly and the $I_{D'}$ increases such that the G band appears to be up-shifted by ~20 cm^{-1} along with increasing KMnO$_4$:CNT ratio. This is a direct indication of the penetrative oxidation and the

damage on the graphitic basal planes. Importantly, the decrease in the I_{2D}/I_G ratios suggests a reduced continuous sp^2 domain size due to the occupation of doped oxygen groups on the basal planes. When the value of this ratio becomes stabilized at small intensities, the graphitic basal planes, especially at the outer surfaces, are majorly saturated by the oxygen groups and left with only narrow sp^2 domains. Therefore, most graphitic planes of Hummer's OCNTs are saturated with oxygen groups at high $KMnO_4$:CNT ratios.
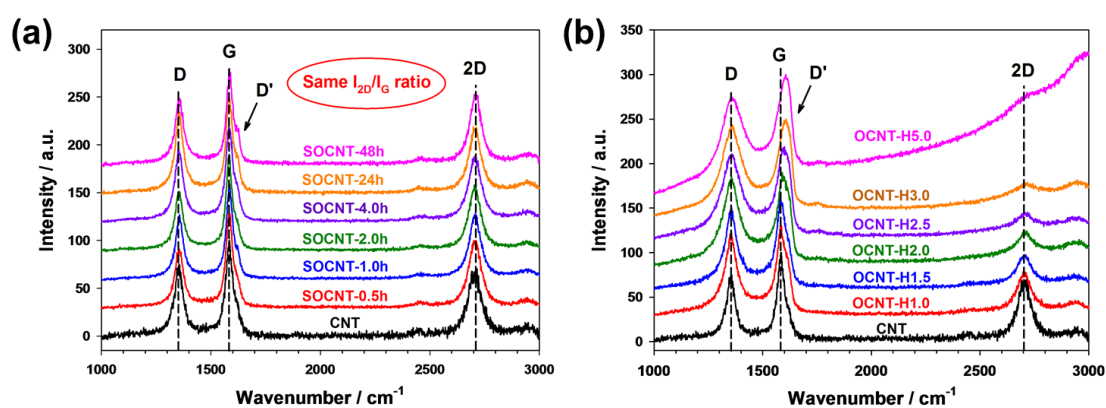
Figure 3.4 Raman spectra of (a) surface-oxidized CNTs (SOCNT) by the acid etching method and (b) OCNTs by the Hummer's method (OCNT-H).

From both XRD and Raman data, it is clear that the OCNTs of SOCNT system maintain their bulk graphitic quality and large continuous sp^2 domains without distinctive difference over the extended reaction time. The introduced oxygen groups basically locate at the graphitic edges, likely loosely scattered over the outer surface. In contrast, the OCNTs of OCNT-H system experience a progressive oxidative penetration such that the interlayer crystallinity gradually degrades and the average sp^2 domain size becomes smaller along with increasing $KMnO_4$:CNT ratio. The distribution of oxygen groups should be spread throughout the OCNTs, particularly for those at high precursor ratios.

3.4.1 The ORR activity of OCNTs and their structural correlations

With the structural information, we are able to investigate the influences of the content, location and type of oxygen groups in OCNTs and the impact of framework damage on the ORR electrocatalysis. Figure 3.5 is the LSV-RRDE profiles for the SOCNT and OCNT-H systems, respectively; the small arrows point to the primary onset potential of the curves. As a common reaction feature, all OCNTs exhibit a predominant two-electron ORR mechanism, which reduces O_2 into HO_2^- as shown in Eq. (3.1);[6] this can be read from the large ring current (i_r) and the lower disk current (i_d) between the onset potential and -0.6 V. At more negative potentials, a moderate drop of i_r and an increase of i_d suggest that the ORR partially proceeds through a further reduction of HO_2^- to the final OH^- product, following Eq. (3.2).

$$O_2 + H_2O + 2\ e^- \rightarrow HO_2^- + OH^- \qquad \text{Eq. (3.1)}$$

$$HO_2^- + H_2O + 2\ e^- \rightarrow 3\ OH^- \qquad \text{Eq. (3.2)}$$
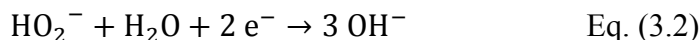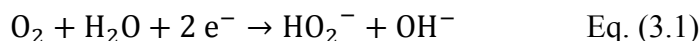
Since ORR activity can be defined alternatively by the reaction pathway, reaction current density or reaction overpotential depending on the field of argument, our discussion have focused on the primary reaction onset for ORR activation activity and the relative reaction current to unmodified CNT for the conversion activity.
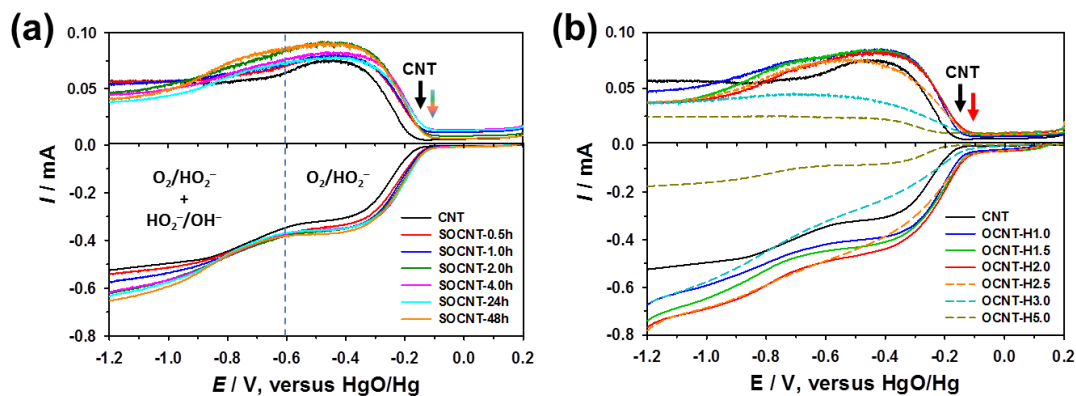
Figure 3.5 LSV-RRDE profiles of (a) OCNTs prepared by using H_2SO_4-catalyzed

HNO$_3$ oxidation, (b) OCNTs by using modified Hummer's oxidation.

The concentration and location of active sites in any type of catalyst are known to be crucial factors for the activity. For our OCNTs, we have introduced the oxygen groups specifically at the surface or penetrate into the inner graphitic layers. From our XPS analysis (Figure 3.2), we can simply find a progressive increase of oxygen content for both cases. This allows us to examine if the general inferences are strictly followed for the case of ORR electrocatalysis. In Figure 3.5a, all surface-oxidized CNTs show a higher onset potential and reaction current than that of CNT. The onset potentials arrive at an identical potential and there shows only a slight current enhancement with increasing oxygen content (from 4.0 at.% to 8.3 at.%, Figure 3.2b). In contrast, Hummer's OCNTs show a higher onset potential until a KMnO$_4$:CNT ratio of 2.0, above which the potentials start to drop noticeably (Figure 3.5b). Similar behaviour can be observed for the reaction current where the current markedly improves up to the critical point, followed by a dramatic drop in the reaction current at higher precursor ratios. If we overlay the best OCNTs among each system, Figure 3.6a can be obtained for comparison. Despite of the capacitive background in OCNT-H2.0, it is clear that both SOCNT-48h and OCNT-H2.0 initiate the ORR at the same onset potential from both i_d and i_r profiles and express a +50 mV difference as compare to the unmodified CNT. This implies that the chemical nature of the active sites can be quite similar. Note that the ORR current for OCNT-H2.0 is only somewhat greater than that of SOCNT-48h, although it contains about double of the oxygen content of SOCNT-48h (17.0 at.% for OCNT-H2.0). Also remember that all surface-oxidized CNTs activate ORR at an identical potential. In other words, the OCNTs with only the surface oxidized can give rise an almost equivalent ORR activity as the deeply oxidized CNTs. Furthermore, we notice that SOCNT-48h, which

has double the oxygen content of SOCNT-0.5h, only shows a shallow improvement in the reaction current; note that both samples have similar XPS O $1s$ spectral profile (Figure B2, Appendix B). Firstly this result provides that the reaction activation can be effectively initiated by the surface oxygen groups at a low concentration down to 4.0 at.%. Moreover, it suggests that much of the surface oxygen groups on SOCNT-48h stay inert for the ORR. This entails an important scientific question on how to increase the surface active site density while keeping these structures catalytically active.

To verify the prediction of similar chemistry for SOCNT-48h and OCNT-H2.0, high resolution XPS O $1s$ spectra for both OCNTs were collected in Figure 3.6b. Clearly both OCNTs share a comparable spectral envelope, which suggests they may be similar in the chemical nature. For simplicity, we only resolved the spectra into singly and doubly bonded oxygen groups. The peaks at 533.5 eV and 532.0 eV respectively correspond to the hydroxyl/carboxyl C–OH, and carbonyl/carboxyl C=O groups, indicating there is a combination of hydroxyl, carbonyl and carboxyl groups on the carbon surface.[192,193] Therefore, the improved onset potential likely originates from any of the possible oxygen groups at the carbon surface. The resolution of these oxygen groups is provided in the next section. Nevertheless, the above results deliver two key messages: (1) oxygen groups located on CNT surface facilitate the O_2 reduction to HO_2^-, probably by providing favourable adsorption and conversion sites for O_2 molecules and (2) only partial surface oxygen groups are catalytically functional as high oxygen content does not seem to boost reaction current.
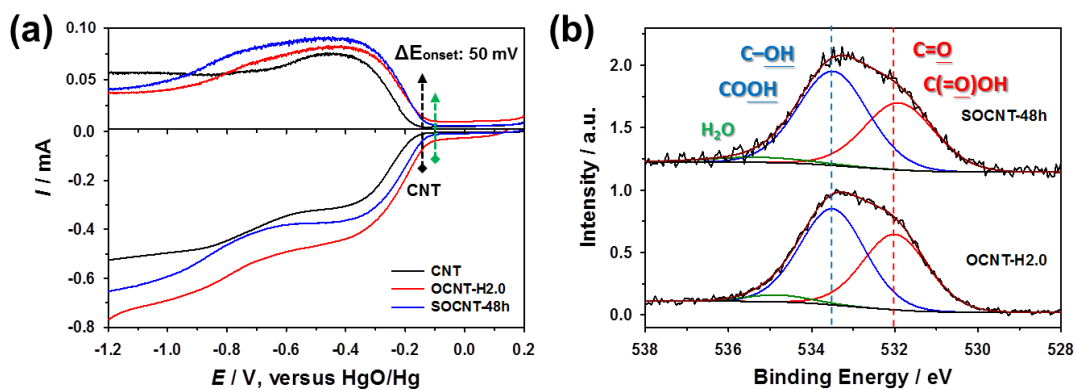
Figure 3.6 (a) LSV-RRDE profiles of the superior OCNTs among each of the oxidation methods and (b) their high-resolution XPS O *1s* spectra.

During chemical oxidation, both oxygen groups and structural defects are simultaneously introduced to the carbon framework. It has been shown that the graphite edges show better activity than the graphitic basal planes, without incorporating any oxygen.[137] Note that most relevant studies only look at oxidation in one direction without clarifying the contribution of the edge defects (sp^3 edges without oxygen) to the ORR activity. To distinguish the ORR activity of the surface oxygen groups from the edge defects in continuous graphene planes, we have thermally treated the SOCNT-48h and OCNT-H2.0 at 800 °C in a 5% H_2-containing inert gas atmosphere for 2 hours to remove the majority of the oxygen and to saturate labile dangling bonds to prevent subsequent oxidation by the air. After treatment, the surface oxygen should be largely removed, leaving mainly saturated defects at the nanotube surfaces. The oxygen content reduced to ~2.9 at.% for both samples, according to XPS analysis (Figure B3, Appendix B). Figure 3.7a is the LSV-RRDE profiles of the thermally treated OCNTs. The result shows that when the surface oxygen is largely removed, leaving only saturated (sp^3) edges on the framework, the OCNTs express poor ORR activity. Both the onset potentials and the reaction currents of the OCNTs have become significantly worse, and the behaviour of the ring currents

suggest that the thermally treated OCNTs no longer promote effective consecutive conversion of HO_2^- to OH^- at more negative potentials. Clearly, it must be the oxygen groups on the carbon promote the ORR activation.

For a better understanding of the active oxygen groups on SOCNT-48h and OCNT-H2.0, high-resolution XPS O *1s* spectra were again recorded on the thermally treated OCNTs to resolve the oxygen functional groups by their thermal stability. According to the O *1s* spectra of SOCNT-48h and OCNT-H2.0, there is a mixture of hydroxyl, carbonyl and carboxyl oxygen groups present in the samples, although it can be any combination of these groups that results in a comparable spectral envelope. From Figure 3.7b, the population of the oxygen groups in SOCNT-48h and OCNT-H2.0 are in fact quite different. On the reminder oxygen groups on SOCNT-48h-800, the population of carbonyl/carboxyl C=O groups mostly vanishes and left with only hydroxyl groups. This indicates that the 532.0 eV peak for SOCNT-48h was mainly attributable to thermally unstable carboxyl groups.[194] This agrees with the result of oxidized carbons after treatment with nitric acid.[188] Since the same peak remains for OCNT-H2.0-800, the oxygen groups on OCNT-H2.0 should be dominated by carbonyl and hydroxyl groups as they have much better thermal stability.[194] Now, it is apparent that the surface of SOCNT-48h is dominated by carboxylic and hydroxyl group, whereas carbonyl and hydroxyl groups mainly occupy in OCNT-H2.0. A plausible explanation to their identical ORR activation potential is the presence of C=O groups in both cases, regardless of being carbonyl or carboxyl group. This aspect of preferential O_2 chemisorption has been well discussed in a book section by Radovic.[73]
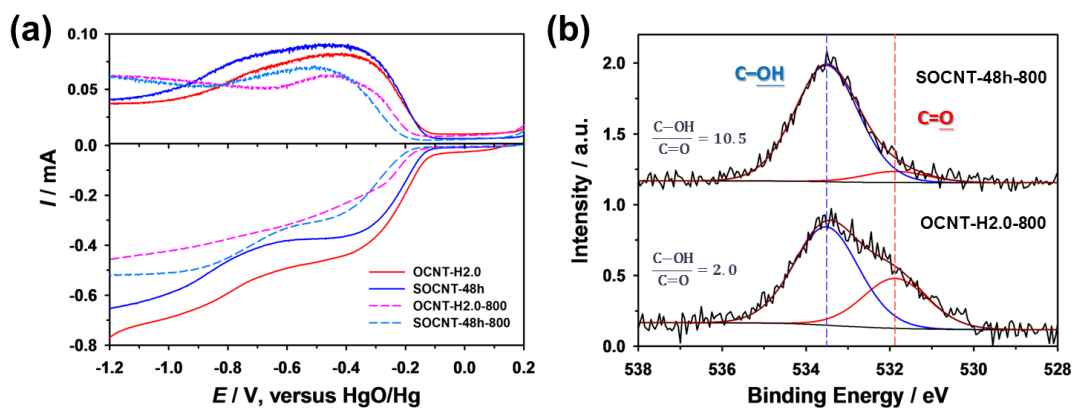
Figure 3.7 (a) LSV-RRDE profiles and (b) XPS O *1s* spectra of thermally treated OCNT-H2.0 and SOCNT-48h; the OCNTs prior to thermal treatment are included in the voltammogram for comparison.

Next question to be elucidated for OCNTs is the origin of activity loss when Hummer's OCNTs is prepared at high $KMnO_4$:CNT ratios. The solution can be as simple as the obstruction of electron conduction channels (through physical contacts) by oxidative damage in the OCNT electrodes. From the XRD profiles of the OCNTs (Figure 3.3b), some graphite crystallinity is preserved up to a precursor ratio of 3.0, even though the ORR activity started to degrade after a ratio 2.0. This suggests that graphite crystallinity is not an appropriate index for the loss of ORR activity. A rather intuitive parameter is the I_{2D}/I_G ratio in the Raman spectra (Figure 3.4b), which signifies the saturation of oxygen groups or sp^3 domains on graphitic framework as previously discussed. From a structural point of view, it is expected that the electron conduction across Hummer's OCNTs can be prohibited if the introduced oxygen groups predominantly saturate the accessible surfaces at both graphitic edges and basal planes, even if some conductive graphitic structures are preserved within the nanotubes. Figure 3.8 displays the reduction profile of the I_{2D}/I_G ratio of each OCNT against the $KMnO_4$:CNT ratio. If a transition point is taken where the curve starts to plateau from a rapid saturation, we can find the critical point (between a $KMnO_4$:CNT

ratio of 2.0 and 2.5) actually corresponds to what is observed for the ORR activity (Figure 3.5b). In addition, the I_{2D}/I_G ratio at the critical point is about 25% of the extrapolated minimum value. This may suggest the oxygen saturation at below 75% level can be considered in the "unsaturated" regime where the electron conduction remain satisfactory for ORR, if the ratio is directly proportional to the degree of saturation in an opposite direction. Also note that it has not reached a full saturation right after the critical point and therefore the activity for OCNT-H2.5 and OCNT-H3.0 is not completely deprived. As a consequence, the structural origin for the loss of ORR activity in the oxidized carbons can be ascribed to the hindrance of electron conduction due to the saturation of insulating oxygen functionalities and sp^3 domains on the carbon framework.
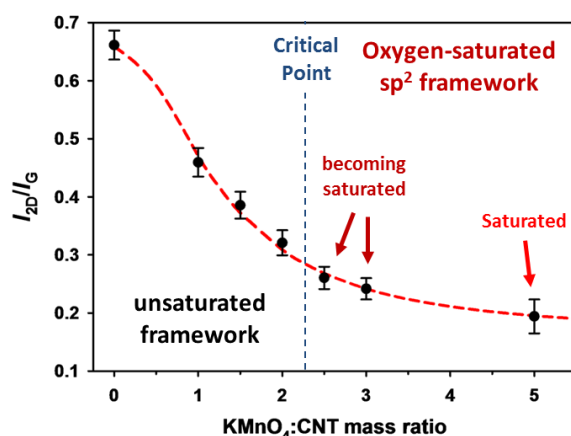
Figure 3.8 A graph of I_{2D}/I_G ratio versus $KMnO_4$:CNT mass ratio from the Raman spectra for Hummer's OCNTs.

3.4.2   The ORR activity of epoxide group

Lastly, we have explored an uncommon type of oxygen that emerges on extensively oxidized graphitic carbons using Hummer's method: the epoxide group.[195] To ensure the CNTs were extensively oxidized and effectively turned into GONR, we have employed a $KMnO_4$:CNT ratio of 10 with an extended reaction period; the final

oxygen content of GONR is 31 at.% by XPS analysis. The presence of epoxide is verified from the evolution of oxygen group on Hummer's OCNTs, based on the XPS O *1s* spectra in Figure 3.9a. The carbonyl/carboxyl C=O is presented as peak A at a binding energy of 532.0 eV. The down-shift in the binding energy from peak B at 533.7 eV to peak C at 532.8 eV clearly indicates a change in the C–O groups from hydroxyl/carboxyl C–OH to ether C–O–C group.[192] In addition, Hontoria-Lucas and the co-workers have shown that the epoxide oxygen in graphite oxide has a binding energy at ~533.0 eV.[196] Therefore, we believe the oxygen group responsible for peak C is the epoxide group. A structural evolution of oxygen groups on Hummer's OCNTs is displayed in Figure 3.9b, according to analysis of the XPS result. It is noteworthy that both GONR and OCNT-H5.0 are dominated by epoxide groups and the only difference is the high concentration of carbonyl groups (peak A) in OCNT-H5.0. A simple comparison of the onset potentials may reveal the relative ORR activation activity.

LSV-RRDE technique was again employed to examine the ORR activity of the electrocatalysts. For a sensible activity assessment for GONR and OCNT-H5.0, both active materials were blended with CNTs at 20 wt.% to support electron conduction. Figure 3.9c shows the LSV-RRDE profiles for the raw materials and their CNT blends. As expected, the insulating raw materials exhibit poor overall activity. Remarkably, with only 20 wt.% of the oxidized carbons, the blended composites can deliver an equivalent performance to the OCNTs with partially impaired graphitic framework for satisfactory electron conduction. This suggests that electron conduction channels do not have to present in a single phase material, but in a well-blended mixture. In a careful comparison, it can be seen that our GONR/CNT blend has a slightly higher onset potential than the OCNT-H5.0/CNT blend by +20 mV. That is, the GONR/CNT

blend can activate ORR at +70 mV with respect to CNT, which is the highest among the OCNTs with common oxygen groups. We have also compared the activity with OCNT-H2.0 as the best-performing OCNTs and found that the OCNT-H5.0/CNT blend has an identical onset potential to that of OCNT-H2.0 (Fig. B4, Appendix B). This indicates the presence of carbonyl groups dominates the apparent ORR activation and the epoxide groups may further lower the activation barrier. This is quite an interesting result that the epoxide groups can facilitate ORR more efficiently than the commonly known carbonyl groups.[73]

Since both GONR and OCNT-H5.0 are dominated by epoxide groups, it is a challenge to explain the reason behind the activity interference by the carbonyl groups. We have proposed a potential energy diagram in Figure 3.9d to provide a possible explanation to the observation; ΔE_{ad} and ΔE_{ET} represents the activation potential energy required for the adsorption and the electron transfer step. At a fundamental level, the process of O_2 reduction to HO_2^- has to go through an adsorption step follow by an electron transfer step. Although many studies have focused on the preferential O_2 adsorption sites, the adsorbed configuration for conversion should be the most critical step for an observable current. Carbonyl groups are known to possess nucleophilic sites at adjacent carbons for electrophilic attack by O_2;[73] this promotes the adsorption of O_2 to the sites. However, how favourable the adsorbed configuration is in accepting two electrons and restoring the structure with respect to other sites is still unclear. In a reason of our observation, we propose that the epoxide groups may be less favourable for O_2 adsorption but facilitate the charge transfer at the adjacent carbon as labelled with an asterisk. The mechanism may involve reversible ring-opening and reformation, like that in the epoxide diffusion on a graphite basal plane,[74] to generate nucleophilic reaction sites. On the other hand, the carbonyl groups

(i.e., at the alpha-carbons) favour O_2 adsorption and the adsorbed state is perhaps stable enough to require extra potential to drive the electron transfer. In this way, most of the free O_2 at the OCNT surface may preferentially adsorb to and be stably trapped at the carbonyl groups instead of the epoxides. Therefore, the apparent onset potential will replicate that of the OCNTs which contain reasonable carbonyl group concentrations. As a consequence, the activity of epoxide can be masked by the carbonyl groups present by preferential adsorption even though the epoxide groups may deliver more efficient electron transfer.
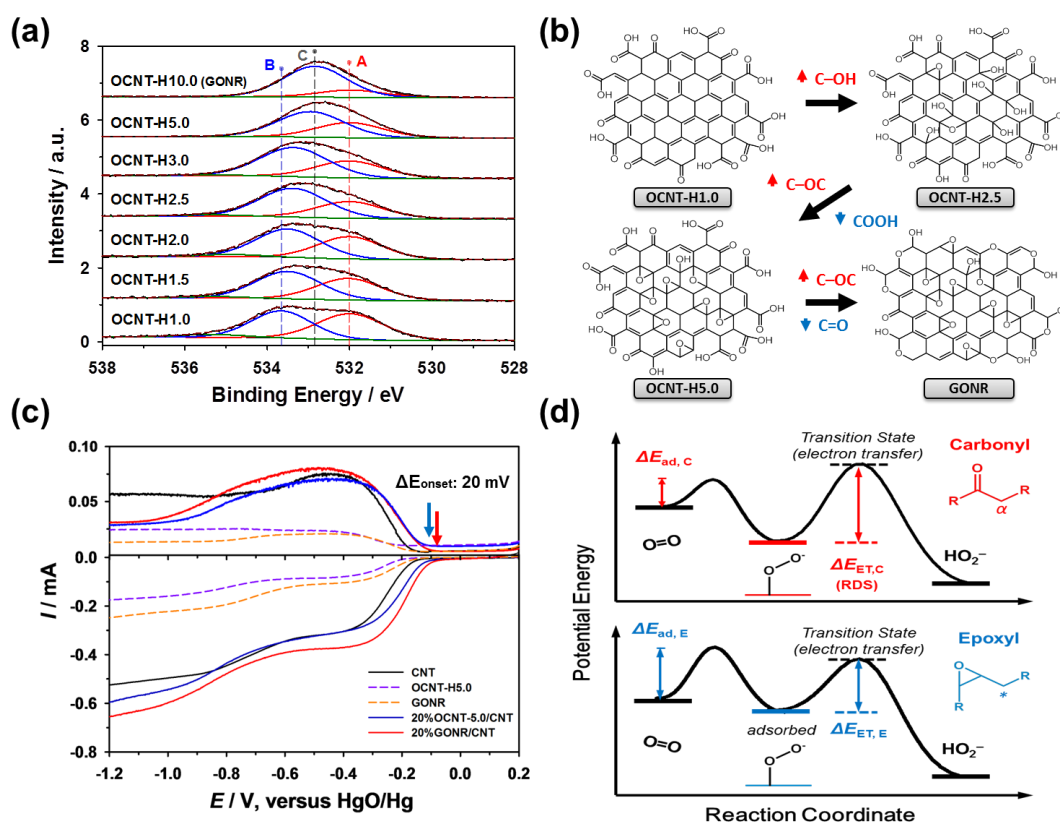
Figure 3.9 (a) XPS O *1s* spectra of Hummer's OCNTs at different CNT:KMnO$_4$ ratios; (b) The evolution of oxygen-functionalities on the OCNTs. (c) LSV-RRDE profiles of OCNT-H5.0, GONR and their 20 wt.% blends with CNT. (d) A proposed potential energy diagram for ORR on carbonyl group and epoxide on carbon.

3.5 Conclusions

In closing, we have demonstrated that metal-free OCNTs with a partially impaired carbon framework are satisfactory catalytic platforms for ORR. In particular, only a portion of the oxygen functional groups at the carbon surface work efficiently for O_2 electro-reduction into HO_2^- intermediate; the overall oxygen content is less important. We have confirmed that the presence of surface oxygen groups is necessary for the ORR activity rather than the edge defects in sp^3 configuration. Moreover, the saturation of oxygen groups on the carbon framework determines the effective electron conduction across the OCNT electrode for the ORR activity, rather than the level of preserved graphite crystallinity. Finally, we have identified that the surface epoxides exhibit the best activity amongst the oxygen groups of interest; they enabled ORR at an onset potential of +70 mV higher than unmodified CNTs, in the absence of interfering carbonyl groups.

Chapter IV.

Metal-free ORR Electrocatalysts:

Halogen and Sulfur-doped Carbons

4.1 Abstract

Metal-free carbon electrocatalyts for the oxygen reduction reaction (ORR) are attractive for their high activity and economic advantages. However, the origin of the activity in nitrogen-doped carbons with highly asymmetric charge density has never been clearly elucidated in a systematic manner. Halogen group elements are good candidates for elucidating the effect, although it has been a difficult task due to safety issues. In this report, we demonstrate the synthesis of Cl-, Br- and I-doped reduced graphene oxide through two solution phase syntheses. We have evaluated the effectiveness of doping and performed electrochemical measurements of the ORR activity on these halogenated graphene materials. Our results suggest that the high electronegativity of the dopant is not the key factor for high ORR activity; both Br- and I-doped graphene promoted ORR more efficiently than Cl-doped graphene. Furthermore, an unexpected sulfur-doping in acidic conditions suggests that a high level of sulfide can degrade the ORR activity of the graphene material.

4.2 Introduction

Since the invention of the hydrogen fuel cell in 1838, the electrocatalysis of the oxygen reduction reaction (ORR) has emerged as an attractive research topic, for it potentially allows enormous energy to be delivered for small mass.[197] The ORR reaction is critical for various types of fuel cells and metal-air batteries. Nowadays, much of the research focus is on developing a low cost and robust ORR electrocatalyst with Pt-grade activity while being environmentally benign.[2,16] Metal-free nitrogen-doped (N-doped) carbon materials, in particular, have been discovered to offer the above advantages while delivering almost equivalent

90

performance to Pt after thermal treatment.[29] However, the origin of electrocatalytic activity on N-doped carbons remains unclear due to a lack of understanding about the role that the dopant plays in the active site. This has prevented further development of metal-free ORR electrocatalyst and a solution should be actively pursued.

Recent research has established a hypothesis that the breaking of electro-neutrality in the graphitic carbon lattice is responsible for forming active centres for ORR.[198] In order to validate this concept, an experiment would require a simple system which allows the dopant electronegativity to be tuned from the level of nitrogen down to a level close to carbon. To achieve this, halogen group elements are perhaps the ideal candidates since the electronegativity difference versus carbon ($\Delta\chi$) for chlorine, bromine and iodine are 0.61, 0.41, 0.11, respectively, by the Pauling scale ($\Delta\chi$ for nitrogen is 0.49). Unfortunately, current methods of halogen doping into carbon typically require harsh reaction conditions (e.g., high temperature treatment or laser ablation) and the direct use of highly toxic gases.[149,199-201] It would certainly be desirable to make a solution phase halogenation method for carbon materials under ambient conditions available.

In this report, we demonstrate two solution phase preparations of chlorine-, bromine- and iodine-doped reduced graphene oxide in different solvent systems and compare the effectiveness of the two doping procedures. Importantly, the electrocatalytic activity for ORR is carefully evaluated for each halogenated graphene material. The effect of an unexpected sulfur-doping is also evaluated on the ORR activity.

4.3 Experimental Section

4.3.1 Materials

Reduced graphene oxide (RGO) was prepared by a thermal exfoliation method on graphite oxide, which was synthesized according to a reported modified Hummer's method [202]. All other chemicals (potassium chloride (KCl, ≥99%), potassium bromide (KBr, ≥99%) and potassium iodide (KI, ≥99%), sodium hypochlorite (NaClO, 12.5% in water), concentrated sulfuric acid (H_2SO_4, ≥98%) and carbon tetrachloride (CCl_4)) were purchased from Ajax Finechem Pty Ltd and Sigma-Aldrich, and used as received.

4.3.2   Preparation of X-RGO in concentrated H_2SO_4

Halogen-containing solutions were firstly prepared by adding 0.1 M equivalent amount of NaClO, KBr and KI into 10 mL of 10 M H_2SO_4 in a 20 mL glass bottle. Note that NaClO was used instead of KCl because the chloride anion is too stable to be oxidized by the concentrated acid. In a typical preparation of halogenated RGO (X-RGO), 2.0 mg of RGO was introduced into the halogen-containing acid solution and dispersed in an ultrasonic bath for 30 minutes. With the bottle capped, the solution was stirred at ambient conditions overnight. The modified RGO was then filtered and washed with water and ethanol, and finally dried at 40 °C for collection.

4.3.3   Preparation of X-RGO in halogen-dissolved CCl_4

The procedure for RGO modification in halogen-dissolved CCl_4 was similar to that in sulfuric acid except a halogen gas (X_2) extraction step was involved. Basically, 15 mL of CCl_4 and 2.0 mL of concentrated H_2SO_4 was placed in a capped glass bottle and 0.1 M equivalent of a halide salt was added into the two-phase mixture and shaken vigorously to dissolve the X_2 gas into the organic phase. Since KCl cannot be oxidized by the acid, an equivalent amount of NaClO was used instead to generate Cl_2

gas. The X_2-dissolved CCl_4 was then extracted and transferred to another bottle for RGO modification. The modification procedure was as described previously.

4.3.4   Characterizations

The materials were characterized mainly by X-ray photoelectron spectroscopy (XPS) and Fourier-transform infrared (FTIR) spectroscopy. XPS was performed with a Kratos XPS spectrometer using a monochromated Al Kα source. The survey scan and high-resolution scan were measured at a pass energy of 160 eV s^{-1} and 20 eV s^{-1}, respectively. All spectra were corrected against the C $1s$ (C–C) peak at 284.8 eV as a reference and the full-width at half-maximum (FWHM) values were held constant for all peaks. Transmission electron microscopy (TEM) was carried out on a JEOL 1010 microscope and the micrographs were taken at an accelerating voltage of 100 kV. Ultraviolet-Visible (UV-Vis) spectroscopy was used to confirm the identity of a particular halogen dissolved in CCl_4 solvent. This was performed on an Agilent Technologies Cary 60 UV-Vis spectrophotometer.

4.3.5   Electrochemical measurements

The electrochemical measurements of ORR activity were carried out using a CHI920D bipotentiostat instrument coupled with a RRDE-3A electrode rotor (ALS Co., Ltd.). In a typical cell, a rotating Pt ring/glassy carbon (GC) disk electrode, a Pt wire counter electrode and a HgO/Hg reference electrode stabilized in 0.1 M KOH were employed in a three-electrode system. All electrochemical reactions were performed in an O_2-saturated 0.1 M KOH electrolyte; the O_2 saturation was done by purging with the gas for at least 30 minutes before the measurements. Linear sweep voltammetry on a rotating ring-disk electrode (LSV-RRDE) was performed using the above setup at a sweep rate of 10 mV s^{-1}, the electrode was rotated constantly at 1500

rpm and the ring potential was held at +0.5 V versus the reference electrode. All the potentials were quoted with respect to the reference electrode. The collecting efficiency of the RRDE was determined by using a bare glassy carbon disk in an Ar-saturated standard ferricyanide electrolyte (5 mM potassium ferricyanide in 0.1 M potassium nitrate solution) under a rotation rate of 1500 rpm. The collecting efficiency was found to be ~0.32 by calculating the ratio of the ring current (at oxidizing potential) and the disk current (at reducing potential) for the one-electron transfer reaction.

4.4 Results and Discussion

In the preparation of X-RGO, concentrated sulfuric acid was employed to generate X_2 gases at laboratory scale from the various halide sources. Each reaction follows one of the chemical equations shown below:

$$2\ NaClO + 2\ H_2SO_4 \rightarrow 2\ NaSO_4 + Cl_{2(g)} + 2\ H_2O \qquad (4.1)$$

$$H_2SO_4 + 2\ H^+ + 2\ Br^- \rightarrow Br_{2(g)} + SO_{2(g)} + 2\ H_2O \qquad (4.2)$$

$$H_2SO_4 + 8\ H^+ + 8\ I^- \rightarrow 4\ I_{2(g)} + H_2S_{(g)} + 4\ H_2O \qquad (4.3)$$
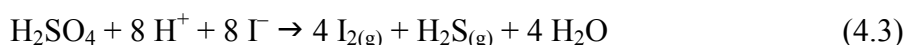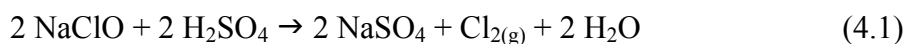
In this way, the highly oxidative X_2 gases can react with RGO in the solution phase and introduce the desired carbon-halogen (C–X) species. Since halogens in their gaseous form are typically unstable in an aqueous medium, we have examined the effectiveness of this chemical modification in both sulfuric acid and carbon tetrachloride. Figure 4.1a is the schematic diagram of the X-RGO preparation procedures in the two media. The typical sheet-like morphology of the raw RGO material was confirmed by TEM and is shown in Figure 4.1b. The presence of X_2

gases in CCl$_4$ after the solvent extraction was also identified by their characteristic absorption bands in the UV−Vis spectra as shown in Figure 4.1c; the excitation wavelengths for Cl$_2$, Br$_2$ and I$_2$ are respectively 346 nm, 414 nm and 512 nm, which are in agreement with the reported values.[203,204]
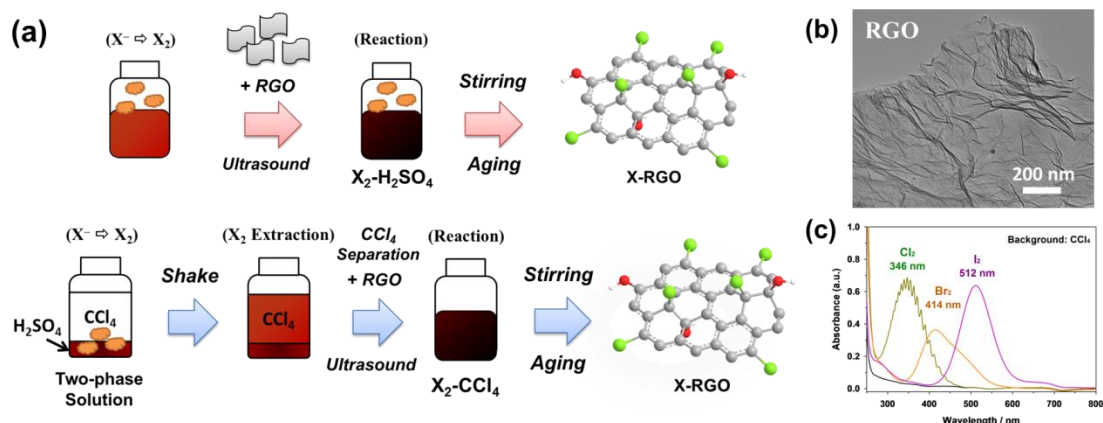
Figure 4.1 (a) A schematic diagram of the preparation procedures of X-RGO in sulfuric acid (top) and CCl$_4$ (bottom). (b) A typical TEM image of the RGO used in the synthesis. (c) UV−Vis spectra of halogen gases dissolved in CCl$_4$.

Composition analysis of the surface of the modified X-RGO requires a highly sensitive analytical technique and XPS was hence selected for this purpose. Figure 4.2 displays the survey spectra of the X-RGO prepared in both aqueous acidic and organic media; all spectral intensity was normalized according to the C *1s* peaks. At the first glance, there is a fair amount of oxygen (8.0 ~ 9.0 at.%) observed in the raw RGO and this is found to be unchanged after the halogenation. No other impurities except for sulfur and the halogens could be identified in the spectra. In 10 M sulfuric acid (Figure 4.2a), the product X-RGO shows almost negligible halogen content after the reaction. Interestingly, a notable amount of sulfur was unexpectedly incorporated into the I-RGO; this is probably due to the presence of H$_2$S after the iodide reduction of H$_2$SO$_4$ (Eq. 4.3). In contrast, the reactions performed in CCl$_4$ demonstrated a much improved effect of raising the halogen content in the X-RGO. In Figure 4.2b, the Cl

2p and the Br *2p* features display pronounced signals for the Cl-RGO and the Br-RGO, respectively, although the iodine signature in the I-RGO remains at a very weak intensity. The quantitative results are tabulated in Table 4.1. For clarity, the X-RGO samples prepared in 10 M sulfuric acid are denoted X-RGO-A and those prepared in CCl_4 are labelled X-RGO-CT.
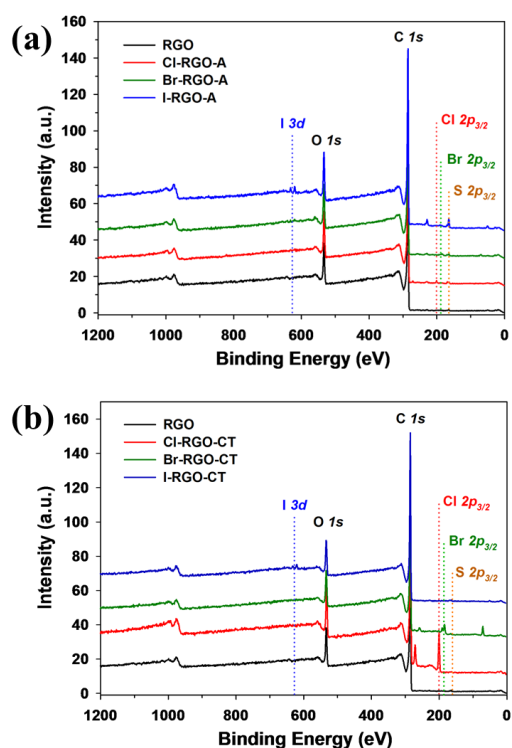
Figure 4.2 XPS survey spectra for X-RGO prepared in (a) 10 M sulfuric acid and (b) CCl_4 media; the quantitative analysis of each element is given in Table 4.1.

The quantitative analysis shows that the sulfur content in the original RGO is only around 0.40 at.%, which arises from both sulfide and sulfate groups after the thermal exfoliation process (data not shown here). This low amount of sulfur is likely to come from the Hummer's method of graphite oxide synthesis and it is therefore not surprising to find sulfur traces in the RGO. For the same reason, the reactions performed in sulfuric acid show slightly increased sulfur contents in the modified

X-RGO; the special case of I-RGO-A will be discussed later. Furthermore, the remarkably high amount of incorporated chlorine at 8.10 at.% in Cl-RGO-CT has shown that the reaction system is very effective when performed in an organic solvent, even under ambient conditions. However, it was not clear about the origin of the marginally increased oxygen level, given the fact that the NaClO salt was insoluble in CCl$_4$. Similarly, Br-RGO-CT also yielded a fair amount of bromine in the product, but the results were less encouraging for I-RGO-CT. This is likely because I$_2$ gas is quite unreactive and the iodine groups are excellent leaving groups compared to other halogen elements. By all accounts, sulfuric acid does not seem to be a suitable medium for the halogen modification of RGO, although the side reaction with iodide ion has effectively facilitated the sulfur doping of the graphene material.

Table 4.1 Composition analysis of the X-RGO prepared from the two methods.

Sample	Composition (at.%), ±0.2%			
	C	X	O	S
RGO	91.58	0.0	8.02	0.40
Cl-RGO-A	90.19	0.31 (Cl)	8.78	0.72
Br-RGO-A	90.46	0.28 (Br)	8.60	0.66
I-RGO-A	88.72	0.14 (I)	8.40	2.74
Cl-RGO-CT	82.00	8.10 (Cl)	9.60	0.30
Br-RGO-CT	89.86	1.70 (Br)	8.07	0.37
I-RGO-CT	91.68	0.13 (I)	7.71	0.48

Of course it is not assured that all incorporated halogen species are in the desired C–X configuration. We thus employed high-resolution XPS spectroscopy to examine

the particular elements of interest. Figure 4.3 shows the high-resolution XPS spectra of the halogen and the sulfur peaks in X-RGO prepared in the acid system. Although the samples after modification were extensively rinsed with water and ethanol to remove possible impurities, the deconvoluted spectra show that a low to moderate level of halide species was present together with the covalently bonded halogen groups. In the Cl $2p$ spectrum for Cl-RGO-A (Figure 4.3a), the spin-orbit splitting between $2p_{3/2}$ and $2p_{1/2}$ was found to be 1.6 eV. The $2p_{3/2}$ peaks of the two Cl species are located at 200.5 eV and 197.9 eV, corresponding to C–Cl and NaCl, respectively.[149,205] The halide may be sourced from the Cl_2 decomposition in water and the reaction by-products. Clearly, the majority of the doped chlorine is in the form of C–Cl groups. The Br $3d$ spectrum for Br-RGO-A (Figure 4.3b) also has two bromine species at 70.6 eV and 67.9 eV of the $3d_{5/2}$ feature, corresponding to C–Br and KCl, respectively.[206,207] The spin-orbit splitting for Br $3d$ is about 1.4 eV. In this sample, the amount of C–Br was only about 66.5% of the total Br content. For I-RGO-A, the two peaks in I $3d$ spectrum are associated with $3d_{5/2}$ and $3d_{3/2}$, with a spin-orbital splitting value of 11.6 eV (Figure 3c). Again, the C–I and KI species can respectively be found at 620.2 eV and 618.6 eV,[208,209] and only 41.2% out of the total I content is the C–I group.

In an attempt to understand the reason behind the unexpected increase of sulfur content in I-RGO-A, the high-resolution S $2p$ spectra of all X-RGO prepared in the acid system were carefully compared. In the spectra of X-RGO-A, two dominant types of sulfur can be identified, which are sulfide (C–S, 164.0 eV) and sulfate/sulfonate groups (SO_x, 168.2 eV) at the $2p_{3/2}$ positions.[210,211] In the case of Cl-RGO-A and Br-RGO-A, the C–S and SO_x level were roughly in equal amounts. As aforementioned, these sulfides should come from the raw RGO material. In contrast,

the sulfur in I-RGO-A is predominantly in the form of sulfide as shown in the S *2p* spectrum (Figure 4.3c). Since there is no direct sulfide source in the starting reagents, the excessive sulfide must be the consequence of additional reactions occurring during the RGO modification process, likely by the H_2S from the sulfate reduction. This result has confirmed that I-RGO-A is really a sulfide-doped material and H_2S is perhaps an excellent reactant for sulfur doping.
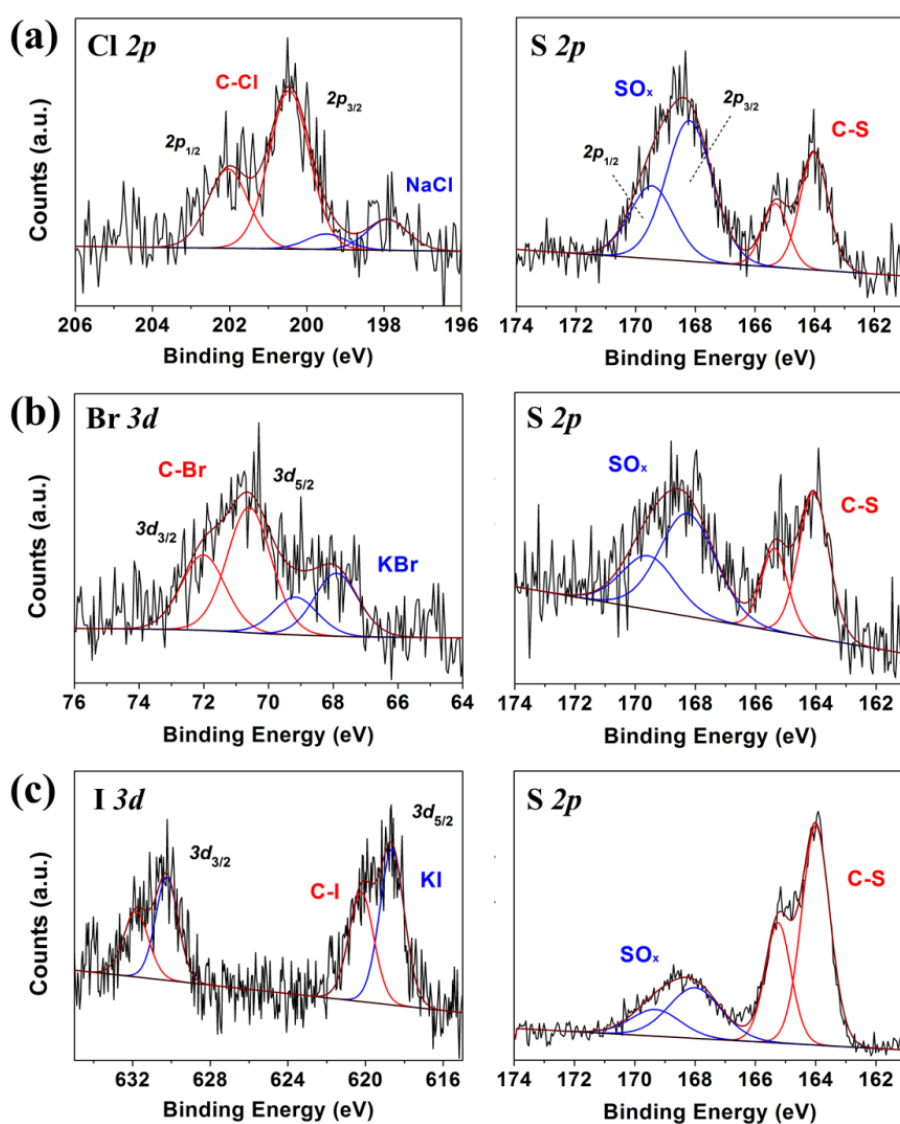
Figure 4.3 XPS high-resolution spectra of the halogen and sulfur species for (a) Cl-RGO, (b) Br-RGO and (c) I-RGO prepared in 10 M sulfuric acid.

The high-resolution XPS spectra of the halogens in X-RGO-CT are presented in

Figure 4.4. As the reactions were carried out in a non-polar electrolyte, the problem of salt deposition on the materials was entirely avoided. In the Cl *2p* spectrum of Cl-RGO-CT (Figure 4.4a), the neat spectrum with a *2p₃/₂* peak positioned at 200.3 eV directly indicates the introduction of C–Cl into RGO by Cl_2. The Br *3d* spectrum for Br-RGO-CT reveals one bromine type at 70.4 eV, suggesting the presence of C–Br group (Figure 4.4b). The I *3d* spectrum for I-RGO-CT is shown in Figure 4.4c. The position of the $3d_{5/2}$ peak is at 620.0 eV, signifying the presence of C–I group despite of the broader peak width. This may be due to the minor contamination by I_2 given that the binding energy for C–I (620.2 eV) and I_2 (619.9 eV) is too close to be distinguished.[208,212] Nonetheless, all of the X-RGO-CT samples have definite C–X signatures and are free from halide contamination.
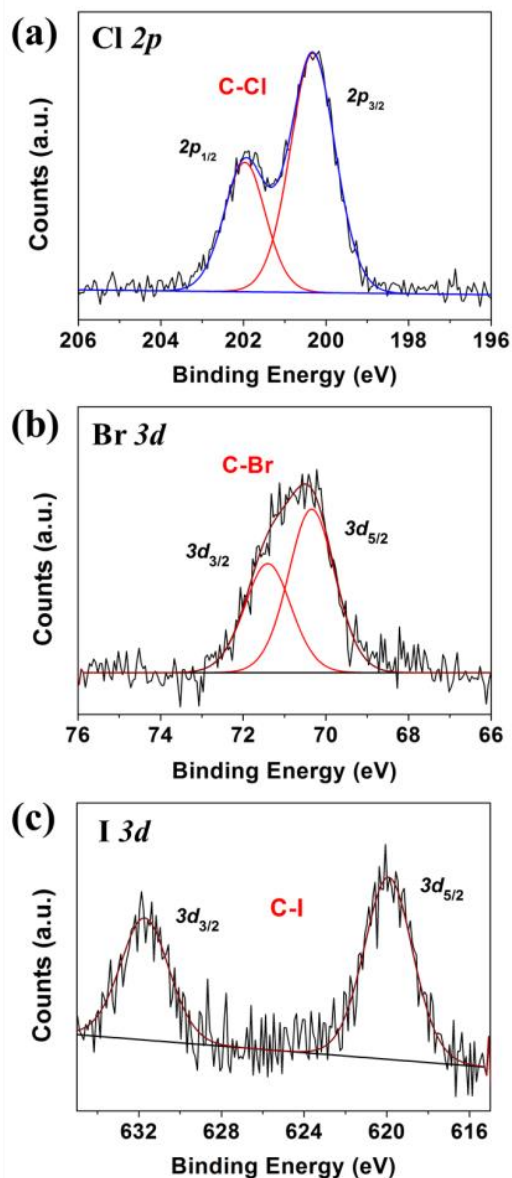
Figure 4.4 XPS high-resolution spectra of the halogen species for (a) Cl-RGO, (b) Br-RGO and (c) I-RGO prepared in CCl_4.

With the above data, we are able to summarize the C–X and C–S contents in the modified RGO, as shown in Figure 4.5. Briefly, the C–Cl content in Cl-RGO and the C–Br content in Br-RGO are probably the most pronounced differences for the acid and organic systems. The minor amount of the water-soluble halide salts that present in a non-covalently bonded fashion should have no influence on the electrocatalytic activity in an aqueous electrolyte system. I-RGO-CT can be regarded as a true

iodine-modified RGO, whereas the considerable number of C–S groups in I-RGO-A means that it is in fact better described as a sulfur-modified RGO. By using electrochemical methods, we shall be able to clarify the influence of each dopant on oxygen reduction electrocatalysis.
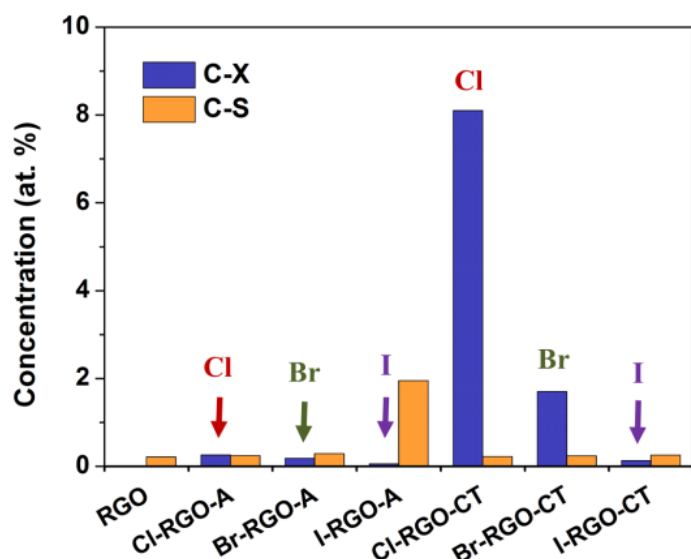
Figure 4.5 The C–X and C–S content in the X-RGO from two solution methods derived semi-quantitatively from XPS.

To study the electrocatalytic activity of the modified graphene materials, the ORR was carried out in an oxygen-saturated 0.1 M KOH electrolyte. In general, ORR propagates through a two-step reaction in which each individual step is a two-electron reduction process.[6] The following chemical equations describe the elementary steps of ORR:

$$O_2 + H_2O + 2\ e^- \rightarrow HO_2^- + OH^- \quad\quad (4.4)$$

$$HO_2^- + H_2O + 2\ e^- \rightarrow 3\ OH^- \qu\quad\quad (4.5)$$
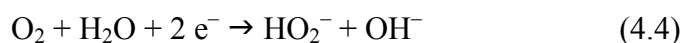
An efficient ORR process would initiate the reaction at low reaction overpotential (i.e., towards positive onset potential) and deliver a large reaction current.[2] In an ideal

scenario, an apparent four-electron ORR can be attained when the secondary reaction is sufficiently fast that the escape of the peroxide intermediate from the electrode surface can be prevented.[6] By incorporating halogen group elements into graphene, we are able to investigate the effect of increasing dopant electronegativity on ORR electrocatalytic activity using a metal-free carbon platform.

We have employed a linear sweep voltammetry technique using a rotating ring-disk electrode (LSV-RRDE) to study the electrocatalytic behaviour of X-RGO. This technique basically creates a hydrodynamic environment which promotes the introduction of fresh reactant and the removal of reaction products from the electrode surface. Any meta-stable intermediate such as peroxide anion, if generated, will be detected at the ring electrode generating a ring current. Figure 4.6 is the LSV-RRDE profiles of X-RGO from the two preparation conditions; the unmodified RGO was used as a reference for comparison. In the voltammogram of the raw RGO, a two-step profile starting from –0.15 V can be read from the disk current, suggesting the occurrence of the two-step consecutive reaction mechanism. The consistent initial increase and the decrease of the ring current at approximately –0.80 V support the view that the reaction mechanism is in agreement with equation (4.4) and (4.5). On this basis, it is clear that the Cl-RGO-A in Figure 4.6a shows similar reaction behaviour while starting at an almost identical onset potential to RGO. This means the Cl-doping does not affect RGO in a way that alters the ORR property of the electrocatalyst. Similar reaction features can be observed for Cl-RGO-CT (Figure 4.6b). This affirms that the doped Cl does not participate in the ORR, even at a much higher concentration. Br-doping, on the other hand, displays less negative reaction onset potential at –0.12 V, as can be read from Br-RGO-A and Br-RGO-CT. This suggests the doped Br promotes the O_2 reduction into HO_2^- at a lower energy cost. In

addition, Br-RGO-CT shows an improvement in the reaction current as compared to Br-RGO-A; this could simply be a direct result of increased Br content. Looking at I-RGO-CT as a real I-doped RGO as shown in Figure 4.6b, the improved reaction behaviour in the onset potential and the reaction current has also suggested the I-doping of RGO is beneficial for ORR, despite the low iodine concentration in the sample. Yet, it is not clear why Br-doped and I-doped RGO share a similarly improved reaction behaviour when there is a difference in the dopant electronegativity. Nevertheless, both Br- and I-doped RGO demonstrate a better ORR activity in terms of the onset potentials and the reaction currents over the entire reaction potential range, as compared to Cl-doped RGO. Therefore, it is suggested that the difference in electronegativity between the dopant and the neighbouring carbon atom is not the crucial factor in providing excellent activity for ORR.

As a practically sulfur-doped graphene material, I-RGO-A in Figure 4.6a exhibits a poor reaction current with a strongly negative onset potential of around –0.20 V. Moreover, the ring current shows a steady increase instead of a reduction at low potential. This suggests that the reaction is producing multiple intermediate species which can be easily oxidized at the Pt ring. This will reduce the electron gain per reaction and lead to poor energy efficiency in a fuel cell. Clearly the incorporated sulfide groups in I-RGO-A have an adverse effect on the general ORR activity of the electrode. Although there are reports about the beneficial effects of doping sulfur by a high temperature treatment,[144] our results of doping sulfur at ambient temperature do not support this conclusion.
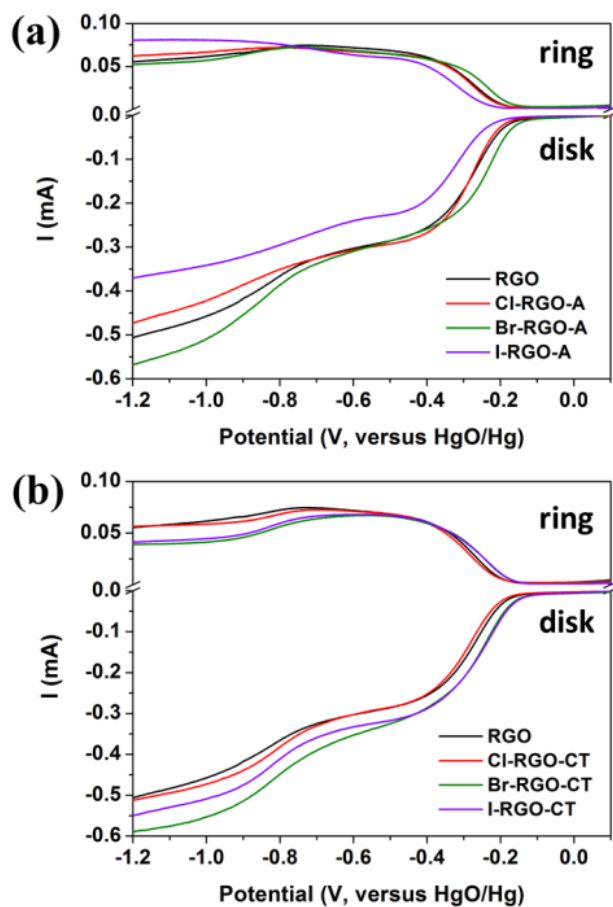
Figure 4.6 LSV-RRDE profiles of the X-RGO (a) in acid system and (b) in CCl$_4$ system, in O$_2$-saturated 0.1 M KOH electrolyte.

In an evaluation of ORR performance for each doped RGO material, we have calculated the average electron transfer (n) number based on the following equation,[213] where i_d is the disk current, i_r is the ring current and N denotes the collecting efficiency at the ring electrode.

$$n = \frac{4i_d}{i_d + \frac{i_r}{N}} \qquad (4.6)$$

As shown in Figure 4.7, all modified RGO materials except for I-RGO-A have n numbers of less than 2.5 at low negative potential that increase at approximately −0.80 V. The sulfur-doped RGO (I-RGO-A) performs ORR at an electron transfer number of around 2.0, suggesting that the secondary reduction of the peroxide

intermediate is inhibited. In other words, the sulfide groups at the electrode surface likely repel the intermediate species as soon as they are formed. The Cl-RGO samples produced by both doping methods share similar n number profiles across the potential range and both are similar to the reference RGO. The n numbers are around ~2.8 at − 1.0 V, which indicates that only a small portion of peroxide intermediate has been consumed for a full reduction of O_2. Next, both Br-RGO show a clear improvement in n number over the reaction potential range. This means a higher percentage of the intermediate is utilized, especially for Br-RGO-CT; a n number of ~3.2 can be reached at −1.0 V. A similar n number profile is also found for I-RGO-CT, which may suggest that the ORR activity by the electron transfer efficiency is at a comparable level with Br-RGO-CT. We are unable to distinguish between Br-doped and I-doped RGO in terms of which really has a superior activity from the limited sample size.
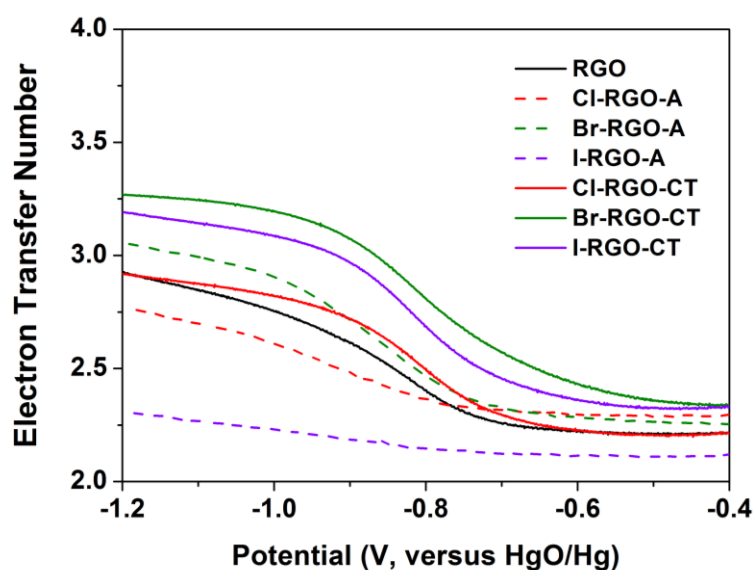
Figure 4.7 The electron transfer number evolution on X-RGO across the ORR potentials range.

Overall our results have established an understanding of the impact of doping highly electronegative elements into carbon on ORR performance. The ORR activity

in the view of general performance (i.e., onset potential, reaction current and n number) of the heteroatom modified RGO can be ranked approximately as: Br-RGO $\approx$ I-RGO > Cl-RGO $\approx$ RGO > S-RGO. Clearly, a highly electronegative dopant does not necessarily create ORR active sites as in the case of nitrogen-doped carbons. Firstly, none of the doped halogen elements led to an apparent four-electron ORR. Secondly, chlorine exhibits the highest electronegativity among the halogen group elements studied in this report, but it does not provide an enhanced electrocatalytic activity. Hence, the origin of ORR activity is perhaps rather related to the local electronic and bonding configuration around the dopant in the carbon lattice.[21] Yet, the dopant electronegativity may still have a role in tuning the electronic configuration. For instance, our Br-RGO has yielded improved activity, noting that the electronegativity value of bromine is very close to that of nitrogen ($\chi_{Br} = 2.96$ and $\chi_N = 3.04$). How such a level of electronegativity affects the electronic configuration will require further research. Overall, we believe that this report has solved an important piece of the puzzle about the origin of ORR activity on metal-free carbon electrocatalysts.

4.5 Conclusions

We have successfully demonstrated the preparation of halogenated graphene in both sulfuric acid and carbon tetrachloride media and addressed the effects of doping RGO with Cl, Br, I and S elements on the ORR activity. In 10 M sulfuric acid, the reaction yield of carbon-halogen groups was very poor (less than 0.5 at.%) and a considerable amount of sulfide was incorporated into I-RGO-A by a side reaction involving H_2S. For reactions performed in non-polar CCl_4 medium, the halogen introduction was highly effective and free of possible halide impurities; the chlorine

content in Cl-RGO-CT was as high as 8.1 at.%. The electrochemical experiments revealed that both Br-RGO and I-RGO facilitated a more efficient ORR than Cl-RGO and the undoped RGO at a higher reaction onset potential. The sulfide-containing I-RGO-A delivered the worst general ORR activity among all the modified RGO materials. The level of activity can be approximately rated in the order: Br-RGO ≈ I-RGO > Cl-RGO ≈ RGO > S-RGO. It is clear that high electronegativity of a dopant is not the key factor for a superior ORR electrocatalyst.

Chapter V.

Graphene-supported Metal Oxide Hybrid as High Performance ORR Electrocatalysts: The Synergism and The Dual Functionality

(Separated into two parts)

V-Part A

The Synergistic Consequence at the Covalently Coupled Metal Oxide/Graphene Oxide Interface

A manuscript has been submitted

5A.1 Abstract

Non-precious carbon/metal oxide hybrid electrocatalysts are of increasing importance in oxygen reduction reaction (ORR) in basic solutions. A synergistic effect is commonly used to explain the superior ORR activity exerted by the electrocatalytic hybrids, and is attributed to the carbon-metal interfaces. However the structure and the activity of the interface are unclear. We observed the site-specific growth of spinel Mn_3O_4 nanocrystals on graphene oxide nanoribbons and revealed the superior ORR activity of the hybrid electrocatalyst that was facilitated by the site-dependent interface structure. By combining X-ray photoelectron spectroscopy with synchrotron far-infrared spectroscopy, we elaborated the interface structure ($>C–O–Mn^{3+}$) and identified its electrocatalytic activity. The activity of the interface is illustrated by a ~60 mV decrease in overpotential. We expect the elucidation of the structure and the role of the $>C–O–Mn^{3+}$ interfaces in ORR can inspire the mechanistic insights into other carbon/metal oxide catalysts and computational studies.

5A.2 Introduction

The oxygen reduction reaction (ORR) is a central process in fuel cells and metal-air batteries for the next generation sustainable energy technologies.[1,2,7] Owing to the sluggish reaction nature, high-performance electrocatalysts such as platinum is required to promote the ORR kinetics. However, the very high cost and scarcity of Pt have limited the commercial applicability.[15] Enormous research effort has therefore been devoted to developing highly efficient electrocatalysts at an affordable cost.[16,22,34] The emerging research trends involve the metal oxide-functionalized nanocarbons,[95,108,156,157] and the heteroatom-doped nanocarbon

electrocatalysts.[11,12,21,35,214,215] A synergistic effect has been commonly claimed for the improved activity in the hybrid electrocatalyst consisted of spinel metal oxides and graphene.[95,108,156,157] A theory suggested that the interfacial oxygen or nitrogen atoms may reduce the charge transfer resistance,[156] but there is a lack of explicit mechanistic insight into the origin of the broadly accepted synergistic effect. In particular, the subtle interface structure and its electrocatalytic activity in the carbon/metal oxide hybrids have been neither clearly resolved nor directly correlated. New mechanistic insight into these remaining questions is important to assist in unravelling the origin of the synergistic effect in ORR.

Here, we aim to further elucidate the structure of the interface between spinel metal oxide nanoparticles and oxygen-rich graphene-based substrates, and its role in the synergistic ORR process. We employed spinel manganese oxide (Mn_3O_4) and graphene oxide nanoribbon (GONR) in the form of a synergistic hybrid, as an expedient system to advance the understanding of the covalent interface.

5A.3 Experimental Section

5A.3.1   Materials

Multi-walled CNTs (purity $\geqq$ 95%) were provided by Institute of Metal Research, Shengyang and were purified through extensive washing alternately in 20% HCl solution and 1.0 M KOH solution several times, to dissolve away possible metal residues. This was followed by rinsing in water, ethanol and weak HCl solution to remove any remaining impurities. Other reagents (36% HCl solution, KOH pellets, $KMnO_4$, 30% H_2O_2 in H_2O and ethanol) were purchased from Sigma-Aldrich and Ajax Chemicals and used as received.

The Mn$_3$O$_4$-GONR hybrid material was prepared by a modified Hummer's oxidation and unzipping of CNTs,[187] followed by a pH-controlled co-precipitation. Typically, 1.0 g of purified CNTs was mixed with 10 g of KMnO$_4$ in 120 mL of concentrated sulfuric acid. The temperature of the solution was then raised to 60 ℃ and maintained for 4 hours under stirring. After that, the reaction mixture was cooled to room temperature and 150 mL of water containing 30% H$_2$O$_2$ was added. Under stirring, this mixture was aged under ambient condition for two days to allow stabilization of GONRs and development of Mn clusters on the GONR surface. The solid product was separated by centrifugation in 50 mL Falcon tubes at 4400 rpm for 30 min; this solid contained a thick layer of white MnSO$_4$ salt and a layer of dark green GONRs. By discarding the supernatant, the product was purified with water using centrifuging an additional two times to remove the large excess of salt residues (i.e., until the white solid in the centrifuged product were removed). Next, the dark green product was re-suspended in 100 mL of water and the solution was carefully neutralized with 2.0 M KOH solution to pH 9.0 to precipitate Mn$_3$O$_4$-GONR hybrid. Finally, the black product was harvested by filtering and washing with water using a large pore-size cellulose filter paper (Whatman, Grade 1) to allow removal of free-standing Mn$_3$O$_4$ nanoparticles.

The synthesis of GONRs and Mn$_3$O$_4$ nanoparticles basically employed the same procedure as the synthesis of Mn$_3$O$_4$-GONR hybrid. For GONRs, extensive washing with water was applied until a neutral pH has been reached, instead of proceeding to the co-precipitation procedure. For Mn$_3$O$_4$ nanoparticles, the same Hummer's method was again followed, but without adding CNTs; this is to ensure a similar synthesis environment. The final reaction solution was diluted in proportion according to the

original procedure, and then the Mn_3O_4 nanoparticles were precipitated using 2.0 M KOH. Extensive washing was also applied to harvest the nanoparticles.

The preparation of the Mn_3O_4/GONR composite was done through direct blending of Mn_3O_4 nanoparticles and GONRs. In a mass ratio of 1:4 and 1:2 for Mn_3O_4:GONR, the as-prepared materials were firstly ground in a mortar for a good mixing, then were placed into a small volume of ethanol and ultrasonicated for a uniform suspension and finally were dried in an oven for a well-mixed composite.

5A.3.3   Characterizations

Transmission electron microscopy (TEM) was performed on a Tecnai G2 F20 transmission electron microscope at an acceleration voltage of 200 kV and an extraction voltage of 4,500 V. X-ray photoelectron spectroscopy (XPS) was carried out on a Kratos Ultra XPS spectrometer using a monochromated Al Kα source under ultra-high vacuum. The survey spectra were measured from 0–1200 eV at a resolution of 1.0 eV and a pass energy of 160 eV. The high-resolution spectra were collected at a resolution of 0.05 eV and a pass energy of 20 eV over an appropriate spectral range. All spectra were corrected based on the C *1s* position (284.8 eV). The peak deconvolution in O *1s* spectra involved constraining both the characteristic binding energies and the full-width at half-maximum (FWHM, 1.15 eV) at ±0.05 eV tolerance. The X-ray diffraction (XRD) profiles were collected using a Bruker Diffractometer X8 with a Cu K*α* source from 10° to 70° (2*θ*). The step size was 0.02 degrees and each step was recorded per second. Raman spectroscopy was performed on an inVia Renishaw Raman spectrometer using an Argon green excitation laser (514 nm) with 1% of the maximum power (50 mW). The spectra were recorded from 100 cm^{-1} to 3000 cm^{-1} at a resolution of 1 cm^{-1}. No background correction was performed except for the GONR sample; the large fluorescence background was corrected by

extrapolation and subtraction of an exponential background function. Fourier-transform infrared (FTIR) spectroscopy experiments were conducted in transmission mode using Australian Synchrotron facilities and the samples were prepared using a pellet-pressing method. For mid-infrared (MIR) spectroscopy, 1 wt% of sample and KBr was used as the mulling agent to form a uniform disc pellet. Each spectrum was collected at ambient temperature in vacuum using a Globar light source and MCTm detector and the data was averaged over a total of 1000 runs. For far-infrared (FIR) spectroscopy, a 10 wt% sample with polyethylene (PE) to obtain a white pellet was used. The experiment was performed in the same environment except a synchrotron light source and a Si-bolometer detector were employed for the measurement. All spectra were corrected against a background spectrum for particular IR ranges. (MIR = pure KBr and FIR = pure PE)

5A.3.4   *Electrochemical measurements*

All electrocatalysts for electrochemical measurements were prepared into appropriate electrodes with CNTs as conductive filler and Nafion as binder. Typically, a target electrocatalyst and purified CNTs were mixed at a weight ratio of 1:4 (20%) in a total mass of 5.0 mg. The solid was then dispersed in 1.0 mL of 0.5 wt% Nafion solution (Sigma-Aldrich) with the help of ultrasonication. Onto a glassy carbon electrode (RRDE Pt ring/GC disk electrode, ALS Co., Ltd.), 15 μL of the dispersion was drop-cast and dried in an oven to obtain a uniform composite film (0.6 mg cm^{-2}). This electrode was then used directly for electrochemical experiments.

Electrochemical experiments were performed in an O_2-saturated (flow rate: 10 mL min^{-1}, saturated for at least 1 h) 0.1 M KOH electrolyte using a three-electrode system: Pt ring/GC disk working electrode (ALS Co., Ltd., GC diameter: 4.0 mm, Pt ring inner diameter: 5.0 mm and outer diameter: 7.0 mm), a Pt wire counter electrode and

a HgO/Hg reference electrode stabilized in 0.1 M KOH. A RRDE-3A apparatus (ALS Co., Ltd.) for the electrode rotation control coupled with a CHI920D bipotentiostat instrument was installed for the measurement.

Differential pulse voltammetry (DPV) was carried out on a rotating electrode at a constant rotation rate of 1600 rpm. The potential range covered from 0.0 V to –0.6 V to study the reactions at ORR activation potentials. The data was recorded at an equivalent scan rate of 8 mV s^{-1} with a pulse width of 0.2 s for every 0.5 s. Linear sweep voltammetry on a rotating ring-disk electrode (LSV-RRDE) was measured from 0.2 V to –1.0 V at a scan rate of 10 mV s^{-1}, also under a constant rotation rate of 1600 rpm; the ring potential was held at +0.5 V.

The calculation of the average number of transferred electrons (n) was performed using an analytical equation as follows:

$$n = \frac{4\, i_\mathrm{d}}{i_\mathrm{d} + i_r/N}$$

, where i_d is the disk current, i_r is the ring current and N is the collecting coefficient. The value of N was experimentally determined to be 0.37 by using a standard ferricyanide system (5 mM $K_3Fe(CN)_6$ in 1.0 M KNO_3 electrolyte solution).

5A.4 Results and Discussion

The morphology of the Mn_3O_4-GONR hybrid was characterized by transmission electron microscopy (TEM). Figure 5A.1a shows the crystalline Mn_3O_4 nanoparticles supported by GONRs. The TEM image in Figure C1 shows the width of 50–100 nm for GONRs (Appendix C). The high-resolution TEM (HRTEM) image displays the (101) plane of Mn_3O_4 nanoparticles. Free-standing nanoparticles were not observed.

This result suggests the Mn_3O_4 nanoparticles are tightly adhered to the GONRs in the Mn_3O_4-GONR hybrid. It is worthwhile to point out that most of the visible Mn_3O_4 nanoparticles are attached to the basal plane of the GONRs; very few particles are seen on the edge sites. This indicates the tendency of in-plane growth for the Mn_3O_4 nanoparticles on the GONRs, which is believed relevant to the different chemistry at basal and peripheral sites of GONRs. The size of the GONR-supported Mn_3O_4 nanoparticles is 10–30 nm, which is very similar in size to the separately prepared Mn_3O_4 nanoparticles (Figure C1, Appendix C). Both the X-ray diffraction pattern (Figure C2, Appendix C) and the Raman spectra (Figure 5A.1b) confirm the expected constituents in the Mn_3O_4-GONR hybrid. In the Raman spectra, the peak at 655 cm^{-1} corresponds to Mn_3O_4 and those at 1358 cm^{-1} (D band) and 1605 cm^{-1} (G band) relate to GONRs. These characteristic peaks remain at the same positions compared to the spectra of the individual constituents which suggest that these components in the hybrid maintain similar bulk structures to their individual forms.
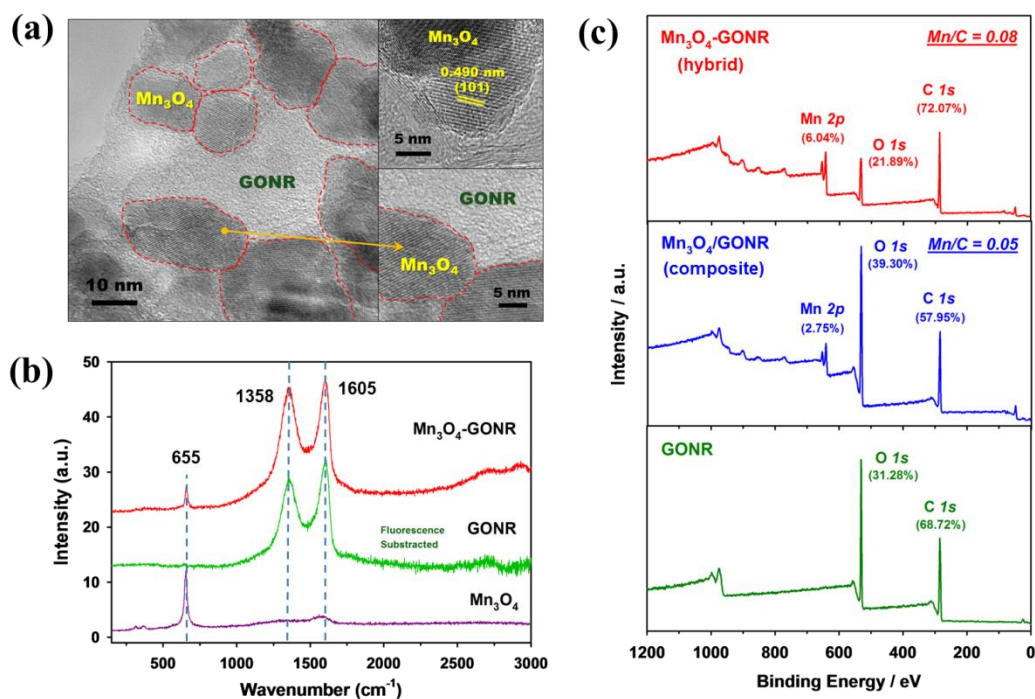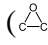
Figure 5A.1 (a) TEM micrographs of the Mn_3O_4-GONR hybrid. (b) Raman spectra of the hybrid, Mn_3O_4 nanoparticles and GONRs (fluorescence background subtracted). (c) XPS survey spectra for Mn_3O_4-GONR hybrid, Mn_3O_4/GONR composite and GONRs.

The XPS results are consistent with the expected composition and impurities were not observed (Figure 5A.1c). The oxygen content of Mn_3O_4-GONR hybrid was lower than that of GONRs, suggesting that the pH-stimulated Mn_3O_4 growth may induce some chemical reactions that removed some oxygen groups from the pristine GONRs. Since deoxygenation helps with repairing the damaged sp^2 network, we adopted electron energy loss spectroscopy (EELS) to probe the local structural differences between the pristine GONRs and the one in the hybrid. Figure C2 (Appendix C) reveals a much sharper π^* peak at the carbon absorption edge in the EELS spectrum of the GONRs in the hybrid compared with the pristine GONRs. This coincides with the observed lower oxygen content from XPS and confirms the carbon lattice being repaired in the Mn_3O_4-decorated GONRs. In contrast the XPS for the Mn_3O_4/GONR composite demonstrates a much-pronounced O *1s* peak that is similar to that of the pristine GONRs, indicating no dramatic impact of ultrasonic agitation on the oxygen groups. According to the atomic population of Mn (2.75 at. %), about 3.66 at. % oxygen in the composite can be assigned to Mn_3O_4, and the content of oxygen from GONRs is about 35.64 at. %. Hence the O/C ratio of GONRs in the composite approximates 0.62, which is relatively close to the ratio of 0.45 for the pristine GONRs compare to that for the hybrid (O/C=0.19).

In order to correlate interface structure with the surface oxygen on GONRs, we investigated the structural evolution of oxygen functionalities on GONRs by using high-resolution XPS. The high-resolution O *1s* and C *1s* spectra for Mn_3O_4-GONR

hybrid, Mn_3O_4/GONR composite and pristine GONRs are compared in Figure 5A.2a. The basal plane chemistry of GONRs is dominated by epoxides ($\triangle$) as depicted by the peaks at 287.0 eV and 532.8 eV in the C $1s$ and O $1s$ spectra, respectively, with a reasonable amount of carboxyl/carbonyl groups on the peripheral sites.[193,216] After the growth of Mn_3O_4 nanoparticles, the epoxides on basal planes of GONRs in the hybrid were mostly removed, leaving only a small amount of hydroxyl groups (C–OH, 286.3 eV in the C $1s$ spectrum). However, the peripheral carboxyl/carbonyl groups remained in a similar quantity to that in the pristine GONRs. Combining the TEM and XPS results, it is believed that the basal plane epoxides are probably the sites on which the Mn_3O_4 nucleated and grew. It has been shown that divalent cations can cross-link graphene oxide sheets via the interactions with the oxygen groups on basal planes.[217] We presume that the Mn ions in the solution preferentially attacked the relatively reactive epoxide groups and developed into Mn_3O_4 nanoparticles.[123,139] In contrast, the population of peaks due to epoxides in the Mn_3O_4/GONR composite remained similar to that of the pristine GONRs. This provides a straightforward clue that the interface structure in the Mn_3O_4/GONR composite is distinct from that in the Mn_3O_4-GONR hybrid, where the two constituents in the composite are likely spatially separated by the epoxide groups instead of being covalently connected. The slight decrease in epoxide population and the variation in the relative content of carboxyl, C=O and C–OH groups may be a sign of some weak interaction between Mn_3O_4 nanoparticles and GONRs in the composite.
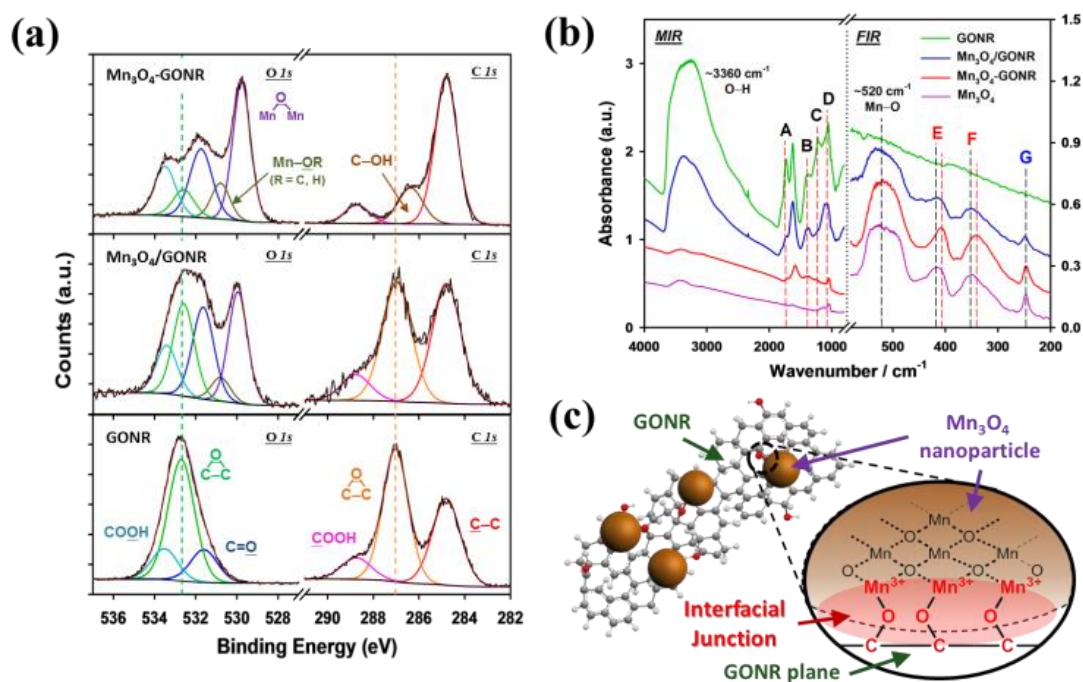
Figure 5A.2 (a) High-resolution XPS C *1s* and O *1s* spectra for Mn_3O_4-GONR hybrid, Mn_3O_4/GONR composite and GONR. (b) FTIR spectra for the hybrid, the composite and the individual constituents. (c) An illustrative diagram of the interfacial junction between a Mn_3O_4 nanoparticle and a GONR, based on collective information from XPS and FTIR spectroscopy.

The different surface chemistry of GONRs in those samples was examined by a synchrotron Fourier-transform infrared (FTIR) spectroscopy (Figure 5A.2b). Carbon-associated vibrations are found in the mid-infrared (MIR) region (4000 cm^{-1} to 800 cm^{-1}). In the MIR spectrum, significant amounts of C–O functionalities (carboxylic C=O (A, 1727 cm^{-1}), hydroxyl C–O (B, 1387 cm^{-1}), carboxylic C–O (C, 1227 cm^{-1}) and epoxy C–O (D, 1057 cm^{-1}) are depleted in the hybrid as are the O–H groups (~3360 cm^{-1}), as compare to the GONR spectrum.[218,219] It is unlikely that the Mn ions reacted with the hydroxyl to form Mn hydroxides based on the XRD result (Figure C3, Appendix C). The loss of O–H groups should be mainly due to the removal of water intercalate in graphene oxide as reflected by the disappearance of

121

the low-angle XRD peak (Figure C3, Appendix C).[123,140] This could be the case as the Mn_3O_4 nanoparticles tend to nucleate firstly on the epoxide sites and then to grow, which could concurrently break down the hydrogen bonding between water and epoxides, and expand the interlayer space of GONRs, resulting in the removal of intercalate water. In the composite, most C–O groups remain unchanged except for some loss in the epoxyl C–O and the carboxylic features (peaks A and C). This outcome agrees with the XPS results in that there was a considerable reduction in the oxygen groups of GONRs in the hybrid, and some relatively weak interaction has occurred between GONRs and Mn_3O_4 nanoparticles in the composite during the ultrasonic agitation. The distinct surface chemistry of GONRs in the three samples suggests the possibly different interface structures between the hybrid and the composite.

Since the Mn_3O_4 in the hybrid grows from the epoxide groups, O-bridged interface structure should be expected similar to our observation in a graphene-nickel oxide composite.[220] Therefore there should be two structures: Mn–O–Mn and Mn–O–C. The sharp peak at 529.8 eV in O $1s$ (Figure 5A.2a) is attributable to the structural oxygen (Mn–O–Mn) in the Mn_3O_4 crystal lattice while the peak at 530.8 eV is typically ascribed to the surface oxygen groups connected to non-metal elements (for example, Mn–O–C in this case).[221] It can be noticed that the relative peak intensity of Mn–O–C to Mn–O–Mn for the hybrid is higher than that for the composite. This implies the relative abundance of Mn–O–C in the hybrid.

There are both Mn^{2+} and Mn^{3+} in Mn_3O_4 lattice; thus it is uncertain which Mn cation links with O atom. To identify this subtle interface structure is critical for acquiring new mechanistic insight into the interface effect in synergistic ORR process, and for computer-aided simulation. In the far-IR region (600 cm^{-1} to 200 cm^{-1}), only

Mn$_3$O$_4$-related signals present (Figure 5A.2b). The four characteristic peaks signify the Mn–O bond vibrations at particular locations in the crystal structure. As compare to free-standing Mn$_3$O$_4$ nanoparticles, one substantial difference in the Mn$_3$O$_4$-GONR hybrid is the red-shift of the peaks at 415 cm^{-1} (E) and 351 cm^{-1} (F) by ~10 cm^{-1} for Mn$_3$O$_4$-GONR hybrid, with respect to the peak at 247 cm^{-1} (G), the Mn^{2+} bond vibration at the tetrahedral sites in Mn$_3$O$_4$ crystal lattice.[222] Such shifting is not observed in the Mn$_3$O$_4$/GONR composite. Interestingly, both shifted features are associated with the Mn^{3+}–O bond stretching at the octahedral sites of Mn$_3$O$_4$ crystal.[222] A red-shift in an IR spectrum typically means that the particular vibration was restricted in space or attached to a bulky neighbouring mass. It is believed that the Mn$_3$O$_4$ nanoparticles are connected to the bulky GONRs through >C–O–Mn^{3+} linkages, where the Mn^{3+} stays at the octahedral site on the spinel surface.

Combining the above findings, the coupled interface between Mn$_3$O$_4$ nanoparticle and GONRs in the hybrid is illustrated in Figure 5A.2c. Basically, the Mn$_3$O$_4$ nanoparticles are covalently connected to the GONR basal plane through >C–O–Mn^{3+} bridges at the original epoxide sites on GONRs. As a result of epoxide ring-opening, the bridging oxygen should be singly bonded to both a carbon atom and a Mn^{3+} ion. Recalling that most epoxide groups were consumed for the development of Mn$_3$O$_4$ nanoparticles at an alkaline pH; it is somewhat straightforward that the initially formed >C–O–Mn^{3+} moieties can be the seeds for crystal growth. During the growth, the Mn^{3+} ion in the moiety may be incorporated into the Mn$_3$O$_4$ crystal structure at the octahedral site of the lattice while being connected with GONRs. Since the >C–O–Mn^{3+} junction bridges between the Mn$_3$O$_4$ nanoparticles and GONRs in the hybrid, its electrocatalytic nature at the exposed interfacial periphery must be important for

understanding the origin of the synergistic effect in carbon/metal oxide hybrid electrocatalysts.

We used differential pulse voltammetry (DPV) to identify the electrocatalytic nature of the $>C–O–Mn^{3+}$ interface at the exposed peripheries in ORR. Multi-walled carbon nanotubes were used to support the three samples for the purpose of reducing resistance. The weight ratio of the samples to nanotubes was fixed at 1:4. The loading density of the samples is 0.6 mg/cm^2. Figure 5A.3a is the DPV profiles of the hybrid, GONRs and Mn_3O_4 nanoparticles, showing the characteristic reaction peaks at activation potentials. As already known, an apparent four-electron ORR could be an overall result of two highly efficient elementary processes as below:

$$O_2 + H_2O + 2\ e^-\ \rightarrow\ HO_2^- + OH^- \tag{5A.1}$$

$$HO_2^- + H_2O + 2\ e^-\ \rightarrow\ 3\ OH^- \tag{5A.2}$$

$$O_2 + 2\ H_2O + 4\ e^-\ \rightarrow 4\ OH^- \tag{5A.1+2}$$
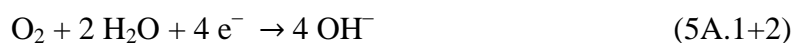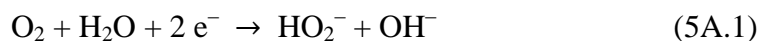
The peak for GONRs is attributable to the O_2 reduction into HO_2^- according to the established theory of the ORR performed on oxidized carbons,[73,137,223] while the peak for Mn_3O_4 nanoparticles should be associated with the simultaneous reduction of O_2 and HO_2^- into their corresponding products.[157] Interestingly, the Mn_3O_4-GONR hybrid result shows a broad envelope comprising of two deconvoluted peak features (solid lines in brown and in red), in close relation to the two individual reaction courses related to Mn_3O_4 and GONRs respectively. The peak of the red solid line is associated with the O_2/HO_2^- reduction and is up-shifted by about 60 mV in comparison with that of GONRs (green dotted line), whereas the feature corresponding to the ORR on Mn_3O_4 nanoparticles (brown peak) remains unchanged. It is likely that the $>C–O–Mn^{3+}$ junction preferentially promotes the first-step

two-electron reduction of O_2 into HO_2^- by reducing the activation barrier for oxygen adsorption, electron transfer, or both. The unchanged reduction peak in brown for the formation of OH^- suggests that the interface coupling does not affect the electrocatalytic processes on Mn_3O_4 nanoparticles. It is worth mentioning that Mn_3O_4 nanocrystals also function to accelerate the consumption of HO_2^- through either electrocatalytic reduction or catalytic decomposition.[224] In such a situation, it is suggested that the second-step two-electron reduction of HO_2^- is dominated by Mn_3O_4 nanocrystals and is less relevant to the $>C-O-Mn^{3+}$ interface. It is believed that the commonly observed synergistic effect is a combined result of the facilitated first step reaction catalysed by the peripheral $>C-O-Mn^{3+}$ moieties, coupled with the rapid HO_2^- consumption by Mn_3O_4 nanoparticles.
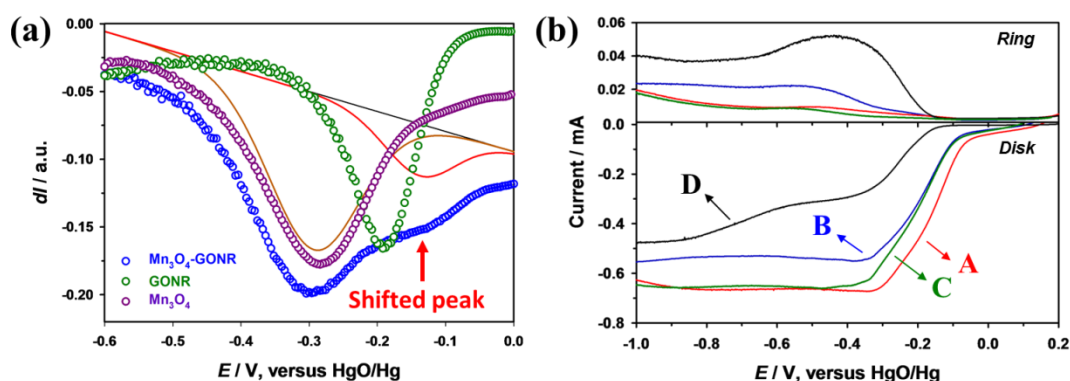
Figure 5A.3 (a) DPV profiles of Mn_3O_4-GONR hybrid, GONRs and Mn_3O_4 at ORR activation potentials on a rotating disk electrode; the solid lines represent the deconvoluted features for the hybrid. (b) LSV-RRDE profiles of Mn_3O_4-GONR hybrid (Mn/C=0.08) (A), Mn_3O_4/GONR composite (Mn/C=0.05) (B), Mn_3O_4/GONR composite (Mn/C=0.12) (C), and pristine CNT (D). Measurements were performed in an O_2-saturated 0.1 KOH electrolyte and at an electrode rotation rate of 1600 rpm.

Linear sweep voltammetry experiments were conducted on a rotating ring-disk electrode (LSV-RRDE) in 0.1 M KOH electrolyte to verify whether the

electrocatalysis at the interfacial periphery is indeed significant. We use the manganese-to-carbon (Mn/C) atomic ratio as an index to represent the relative amount of Mn_3O_4 nanoparticles and GONRs (Figure 5A.1c). Note that the Mn_3O_4-GONR hybrid has a Mn/C ratio of 0.08, which is higher than that of the composite (Mn/C=0.05). The ORR performance of the samples are compared in Figure 5A.3b; the relevant values for Mn_3O_4-GONR hybrid is listed with the values for the Mn_3O_4/GONR composite (Mn/C=0.05) in parentheses. The Mn_3O_4-GONR hybrid exhibits a more positive onset potential of –0.045 V (–0.068 V), a more positive half-wave potential of −0.159 V (−0.195 V), a larger diffusion-limiting current of 0.664 mA (0.538 mA), and an electron transfer number of 3.9 (3.6) at −0.6 V. The small ring current of the hybrid (9 µA at −0.6 V), in contrast to that of the composite (Mn/C=0.05, 22 µA), indicates that a negligible amount of peroxide was produced on the Mn_3O_4-GONR hybrid. This is typical of the synergistic consequence from hybrid electrocatalysts.[108,112,156,157] To determine the effect of Mn_3O_4 content in the composite on ORR, we prepared a composite with a higher Mn_3O_4 content (Mn/C=0.12). As shown in Figure 3b, the green curve (C, Mn/C=0.12) demonstrates nearly identical onset potential and half-wave potential compared with the blue curve (B, Mn/C=0.05). This indicates that the activation barrier does not reduce as the amount of Mn_3O_4 in the composite increases, which reflects the determinant role of the $>C–O–Mn^{3+}$ interface in activating dioxygen molecules. Note that the red curve in Figure 5A.3c (Mn_3O_4-GONR hybrid, Mn/C=0.08) with a smaller Mn content has a similar limiting current to that of the green curve (Mn_3O_4/GONR composite, Mn/C=0.12). The facilitated electron transport through the interface is likely to be responsible for the improved utilization efficiency of Mn_3O_4 in the hybrid.[156] Additionally, the freshly formed HO_2^- molecules at the peripheral $>C–O–Mn^{3+}$ sites can immediately reach the uncoupled Mn_3O_4 surfaces with a very short diffusion path, which may increase the

reaction current by preventing the intermediate loss (Figure 5A.4).
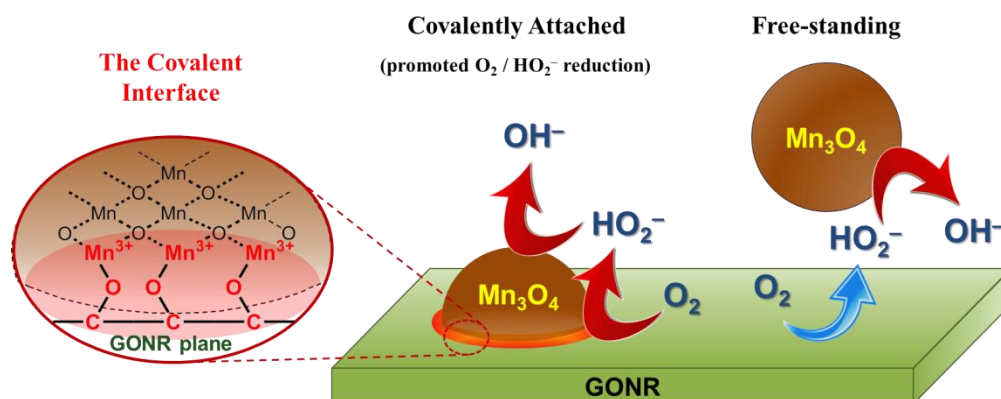
Figure 5A.4 An illustrative summary of the coupled interface (the highlighted boundary) in Mn_3O_4-GONR hybrid and its electrocatalytic role for ORR in comparison to the uncoupled composite.

5A.5 Conclusions

In conclusion, we devised two approaches (pH-stimulated precipitation and ultrasonic agitation) to tune the interface structure between spinel Mn_3O_4 nanoparticles and GONRs. By combining XPS and far-IR spectroscopy, the interface structure of the Mn_3O_4-GONR hybrid was explicitly determined, to be in the form of $>C–O–Mn^{3+}$ with Mn^{3+} ions selectively bound to single-bonded oxygen atoms on GONRs. Based on the comparative voltammetry studies, the coupled interface at the periphery is found to accelerate the initial O_2/HO_2^- reduction leading to a reduced ORR activation barrier. Moreover, the interface assists the utilization of Mn_3O_4 nanoparticles in the whole ORR process. We expect that recognition of the interface structure in the Mn_3O_4-GONR hybrid could advance research in interfacial modification in carbon/metal oxide hybrid electrocatalysts for high performance ORR-related applications.

V-Part B

Dual Electrocatalytic Roles in Metal Oxide Bound Graphene Oxide Nanoribbon Hybrid Promote Highly Efficient Oxygen Reduction Reaction

A manuscript to be submitted

5B.1 Abstract

The integration of multiple electrocatalytic functions can lead to highly efficient oxygen reduction reaction (ORR). We report on the two key electrocatalytic roles carried out by Mn_3O_4 nanoparticles and graphene oxide nanoribbons (GONR) in a hybrid configuration. Our results show that the GONR effectively facilitates the peroxide production and the Mn_3O_4 component promotes the peroxide electro-reduction. The results suggest that the dual electrocatalytic roles carried by the GONRs and Mn_3O_4 nanoparticles are the direct origin of the efficient four-electron ORR, in conjunction with the synergistic particle-substrate coupling for a further reduced ORR activation barrier. We further highlight the superior peroxide reduction activity of Mn_3O_4 nanoparticles in supporting the immediate consumption of the intermediate peroxide. As a successful example of functional integration, our Mn_3O_4-GONR hybrid demonstrated a highly efficient ORR that is close to the activity of Pt/C with good chemical robustness against methanol poisoning.

5B.2 Introduction

The electrocatalysis of oxygen reduction reaction (ORR) has great industrial importance in energy storage and conversion.[1,2,7,9] Since the invention of the fuel cell, platinum has been considered as the state-of-the-art electrocatalysts for the sluggish ORR, despite its very high cost.[15] For practical application, alternative cost-effective electrocatalysts are highly desired. Recently, transition metal oxide nanoparticles (e.g., Co_3O_4 and Mn_3O_4) supported on a conductive carbon substrate have been highlighted for their superior electrocatalytic activity due to the synergistic coupling between the nanoparticle and the graphitic carbon substrate.[108,112,156,157,225] However, the role of

each catalytic component (i.e., the metal oxide nanoparticle, the carbon substrate and the covalent junction) in the metal oxide-carbon hybrid has not been clearly addressed. A complete ORR process can proceed through two consecutive electron transfer reactions in an alkaline electrolyte such that (1) an oxygen molecule is reduced to a peroxide intermediate, followed by (2) a rapid reduction or decomposition of peroxide into hydroxide ions.[6,224,226] When effective electrocatalysts for each reaction are carefully selected and combined, a functionally integrated electrocatalyst can be sensibly devised for excellent activity. For proof-of-concept, we intend to highlight the dual electrocatalytic roles in a hybrid electrode combining the catalytic materials that promote ORR almost as efficiently as a commercial Pt/C electrocatalyst.
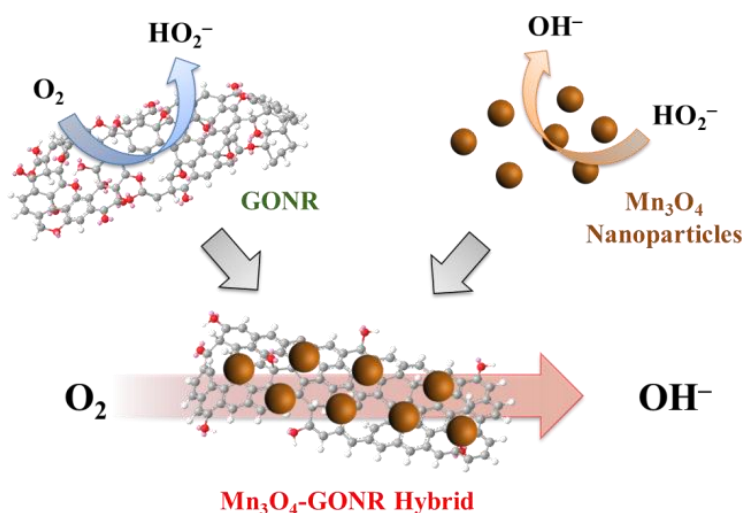
Figure 5B.1 An illustration of the design rationale for the functionally integrated Mn_3O_4-GONR hybrid electrocatalyst for highly efficient four-electron ORR by combining GONR and Mn_3O_4 nanoparticles for the respective ORR elementary processes.

In this work, we demonstrate that a functional combination of catalytic components for each elementary reaction can lead to highly efficient four-electron ORR. We have employed graphene oxide nanoribbons (GONRs) as an

oxygen-enriched graphitic carbon for initial oxygen reduction into a stable peroxide intermediate,[223] and Mn_3O_4 nanoparticles as excellent electrocatalysts for rapid peroxide reduction. The design rationale and the configuration of our Mn_3O_4-GONR hybrid are illustrated in Figure 5B.1. Note that Mn_3O_4 nanoparticles were deliberately decorated on GONR to ensure a uniform distribution of nanoparticles throughout the hybrid as well as to allow beneficial covalent coupling for a further suppressed activation barrier for peroxide generation.[227]

5B.3 Experimental Section

5B.3.1   Materials & Preparations

The preparation of graphene oxide nanoribbons (GONRs) employed a modified Hummer's method according to the literature.[187] Extensively purified multi-walled carbon nanotubes (CNTs; commercially obtained, purity > 95 %) were mixed with $KMnO_4$ (Sigma, reagent grade), at a mass ratio of 1:10, in 120 mL of sulfuric acid, concentrated (Sigma, reagent grade). The reaction temperature was kept at 60 °C for 4 hours under stirring. After that, the mixture was cooled to ambient temperature and 200 mL of purified water containing 10 mL of 30% H_2O_2 was added. The yellow-green solution was allowed to stand and the dark green GONR product obtained through extensive washing with water by centrifugation.

For the growth of Mn_3O_4 nanoparticles on GONR, the purified GONRs were suspended in a 60 mM $MnSO_4$ solution containing 2% H_2O_2 and the mixture allowed to stabilize before the addition of 2.0 M KOH solution to simultaneously precipitate the Mn_3O_4-GONR hybrid product. The solution pH was carefully controlled until a pH of 9.0 was attained. The hybrid materials was then separated from the solution by

vacuum filtration, washed extensively with water and dried in an oven.

For individual Mn_3O_4 nanoparticles, the same procedure for the simultaneous precipitation was used, except that purified GONRs were not added.

To prepare the materials into composite electrocatalysts, each material was mixed with purified CNTs at 20% of electrocatalyst content. In a small volume of ethanol, a mixture was dispersed using a probe ultrasound apparatus to ensure homogenous mixing. Finally the liquid portion was dried to collect the well-mixed composite.

5B.3.2   *Characterization*

The morphology of the hybrid composite was investigated by transmission electron microscopy (TEM, Tecnai G2 F20 transmission electron microscope) at 200 kV. The crystalline properties of the materials were characterized by powder X-ray diffraction (XRD, Bruker Diffractometer X8) using a Cu Kα source from 5° to 70° (2θ). The diffraction profiles were recorded at a step size of 0.02 degrees per second.

5B.3.3   *Electrochemical measurements*

Each composite electrocatalyst was prepared by making dispersion at a concentration of 5.0 mg/mL in 0.5 wt% Nafion solution (Sigma), with ultrasound treatment. 15 μL of the dispersion was loaded onto a glassy carbon electrode (RRDE Pt ring/GC disk electrode, ALS Co., Ltd.; GC diameter: 4.0 mm, Pt ring inner diameter: 5.0 mm and outer diameter: 7.0 mm) through drop-casting technique and dried in an oven for a uniform electrode film. This electrode was then used directly for electrochemical experiments.

Electrochemical experiments were carried out in either an O_2-saturated or

Ar-deaerated 0.1 M KOH electrolyte using a three-electrode setup: Pt ring/GC disk working electrode, a Pt wire counter electrode and a HgO/Hg reference electrode stabilized in a 0.1 M KOH; the solution was purged with O_2 gas for at least 30 min before the measurement to ensure oxygen saturation, while Ar gas was used to purge the solution for more than 1 hour before the measurement when an O_2-free environment was required. An RRDE-3A apparatus (ALS Co., Ltd.) for the electrode rotation control coupled with a CHI920D bipotentiostat instrument was installed for the measurement.

Cyclic voltammetry (CV) was performed in an undisturbed electrolyte. The voltammograms were collected from 0.2 V to -1.2 V, at a scan rate of 50 mV s^{-1}. In a hydrodynamic environment, linear sweep voltammetry on a rotating ring-disk electrode (LSV-RRDE) was measured from 0.1 V to -1.0 V at a scan rate of 10 mV s^{-1}, and under a constant electrode rotation rate of 1600 rpm; the ring potential was held at $+0.5$ V. LSV on a rotating disk electrode (LSV-RDE) for H_2O_2 reduction activity assessment was measured from 0.0 V to -0.8 V in an Ar-deaerated electrolyte with added 15 mM H_2O_2 under a rotation rate at 1600 rpm at a scan rate of 10 mV s^{-1}. Stair-case voltammetry (Tafel plot) was measured from 0.1 V to -0.3 V in an O_2-saturated electrolyte with a rotation rate of 1600 rpm at a step size of 20 mV. For each step, a dwell time of 10 s was allowed and the data points were collected at the end of each step. Constant potential amperometry (methanol-poisoning test) was performed in an O_2-saturated electrolyte at an electrode potential of -0.5 V, under a rotation rate at 800 rpm over a total duration of 2000 s. The first 100 s was allowed for current stabilization and hence was not recorded. Methanol (MeOH) was carefully injected into the electrolyte 200 s after the measurement was initiated.

5B.3.4   The calculation of electrochemical properties

The calculation of the theoretical diffusion-limiting ORR current was done using the Levich equation:

$$i_L = 0.2\ nFAC_bD^{2/3}v^{-1/6}\omega^{1/2}$$

where i_L is the Levich diffusion-limiting current (A), n is the electron transfer number, F is the Faraday constant (96,485 C mol^{-1}), A is the electrode surface area (cm^2), C_b is the bulk reactant concentration (mol cm^{-3}), D is the diffusion coefficient (cm^2 s^{-1}), v is the kinematic viscosity (cm^2 s^{-1}) and ω is the electrode rotation rate (rpm). For the calculation of i_L the values: $n = 4$, $A = 0.1257$ cm^2, $C_b = 1.2\times10^{-6}$ mol cm^{-3}, $D = 1.9\times10^{-5}$ cm^2 s^{-1} , $v = 0.01$ cm^2 s^{-1} and $\omega = 1600$ rpm were used; these system values for 0.1 M KOH electrolyte can be found in the literature.[117]

The calculation of the average number of electron transferred (n) and the percentage production of peroxide ($\%HO_2^-$) was performed using analytical equations as follows:

$$n = \frac{4i_d}{i_d + i_r/N}$$

And

$$\%HO_2^- = \frac{200\ i_r}{i_dN + i_r}$$

where i_d is the disk current, i_r is the ring current and N is the collection coefficient. Both equations were applied over the potential range after the reaction activation. The value of N was experimentally determined to be 0.37 by using a standard ferricyanide system (5 mM $K_3Fe(CN)_6$ in 1.0 M KNO_3 electrolyte solution).

5B.4 Results and Discussion

Transmission electron microscopy (TEM) was employed to examine the morphology of the Mn_3O_4-GONR hybrid composite with CNTs. The TEM micrographs are shown in Figure 5B.2a. In the hybrid composite, the Mn_3O_4 nanoparticles were decorated on GONRs through intimate connection, while the CNTs merely maintained physical contact with the Mn_3O_4-GONR hybrid.[227] The Mn_3O_4 nanoparticles bound to GONRs are typically of size 10–30 nm. The high-resolution TEM image on the right hand side shows the spinel crystalline phase of the nanoparticles; the interplanar distance of 0.491 nm of the lattice fringes is in agreement with that of the Mn_3O_4 (101) crystal plane (d_{101} = 0.492 nm). TEM micrographs of the hybrid components are provided in the Supplementary Information.
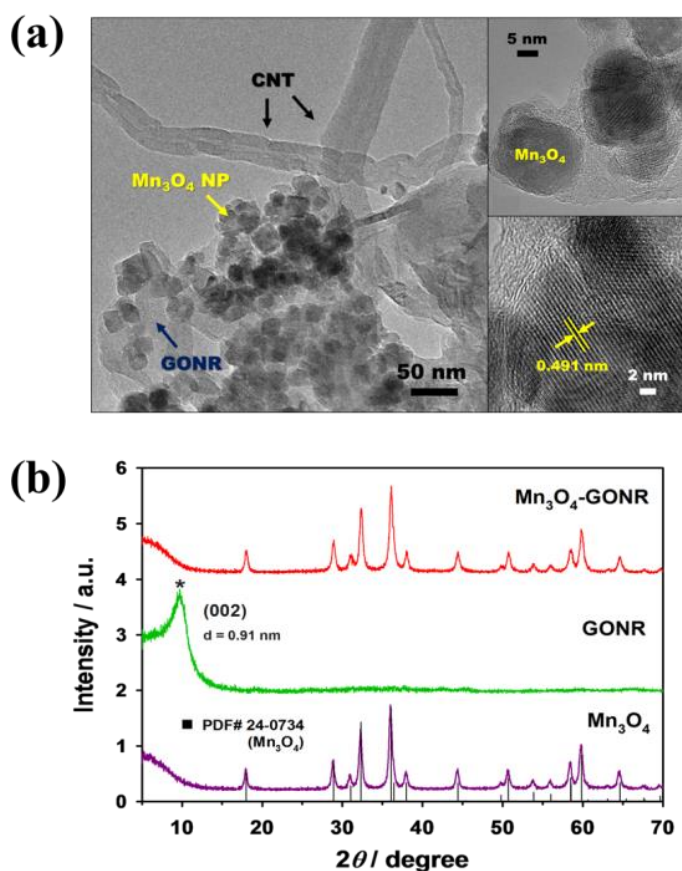
Figure 5B.2 (a) TEM images of the Mn_3O_4-GONR hybrid composite with CNTs; (b) XRD patterns for the Mn_3O_4-GONR hybrid, GONRs and Mn_3O_4 nanoparticles.

The spinel crystal phase was further confirmed by powder X-ray diffraction (XRD). The diffraction patterns of the hybrid and its components are provided in Figure 5B.2b. Both GONR and Mn_3O_4 nanoparticles exhibited the expected diffraction profiles, where GONR shows an expanded graphite (002) interlayer distance at ~10 ° (d_{002} = 0.91 nm) and the pattern of Mn_3O_4 nanoparticles directly matches the literature values (JCPDS Card# 24-0734). Interestingly, the Mn_3O_4-GONR hybrid shows a pattern that exactly matches that of Mn_3O_4 nanoparticles without any features from GONRs. This suggests there was a penetrative growth of Mn_3O_4 nanoparticles into the GONR layers which distorted the layered stacking. Nevertheless, it is clear that the Mn_3O_4-GONR hybrid is in a desired structural configuration and the Mn_3O_4 nanoparticles, either attached or free-standing, have their expected crystalline phase.
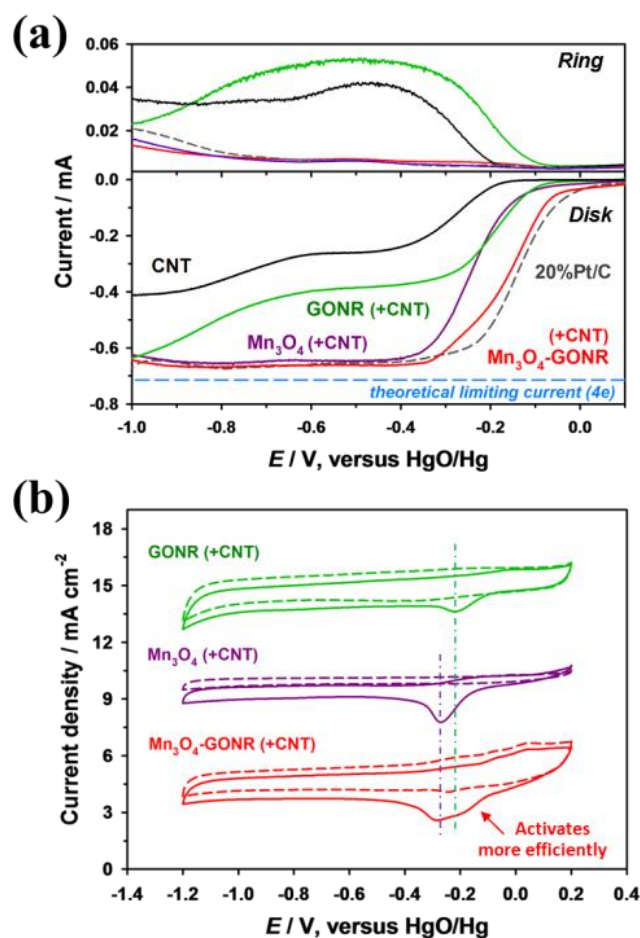
Figure 5B.3 (a) LSV-RRDE profiles of all composite electrocatalysts including 20% Pt/C and purified CNT in O_2-saturated 0.1 M KOH electrolyte; (b) CV profiles of the hybrid and its components in composites with CNTs in both Ar-deaerated (dashed lines) and O_2-saturated electrolytes (solid lines).

The electrocatalytic activity of the hybrid and its components, in composite forms with CNTs, were studied by linear sweep voltammetry on a rotating ring-disk electrode (LSV-RRDE) in an O_2-saturated 0.1 M KOH electrolyte. The results are displayed in Figure 5B.3a. Clearly, there is appreciable ORR activity in the Mn_3O_4-GONR hybrid composite. As a conductive filler, CNTs alone do not perform efficient ORR. The onset potential of the hybrid composite is around –0.05 V, which is very close to that of the Pt/C electrocatalyst. The reaction current approaches the

138

theoretical limiting current described by the Levich relation for a four-electron ORR, while the ring current remained negligible. These indicate promoted ORR completion at a low energy cost, regardless of the reaction pathway. On the other hand, the GONR composite exhibited a two-step current behaviour with a significant ring current within the potential range. While the Mn_3O_4 composite also showed a four-electron ORR-like current performance, a more negative onset potential and retarded activation behaviour (in that the system lacks a sharp increase in current) could be observed. It was noticed that the GONR composite has a more efficient ORR activation than the Mn_3O_4 composite, although the ORR does not proceed to completion. Moreover, the GONR composite showed larger disk and ring currents than the CNT and initiated ORR at a more positive potential. This suggests that the GONR in the hybrid likely functions to facilitate O_2 reduction to stable peroxide intermediates without further reducing them, while the Mn_3O_4 nanoparticles promoted the consumption of the intermediate after the initial reaction was effectively activated. Evidence for these conclusions can also be found from experiments using the hybrid and its components when not supported with CNTs; a short discussion is provided in Appendix D.

Cyclic voltammetry (CV) experiments further support the cooperative ORR mechanism. Figure 5B.3b shows the CV profiles for the hybrid and its components, in composites with CNTs, in both Ar-deaerated and O_2-saturated electrolytes. All composites exhibit neat voltammograms and the reduction peaks are associated with ORR. It can be observed that the reduction feature of the hybrid composite somewhat resembles an envelope of the reduction peaks of its individual components. This suggests that the components in the hybrid mainly carry out their own electrocatalytic roles while working together for efficient ORR. Note also that the reduction envelope

of the hybrid composite activated the ORR more efficiently than the GONR composite, given by the enhanced current increment relative to GONR composite. This is attributable to the consequence of the synergistic coupling between the Mn_3O_4 nanoparticles and GONRs, since this was not found in the individual components alone. Nevertheless, it is clear that the efficient ORR performed on the hybrid composite is the consequence of two complementary electrocatalytic functions.
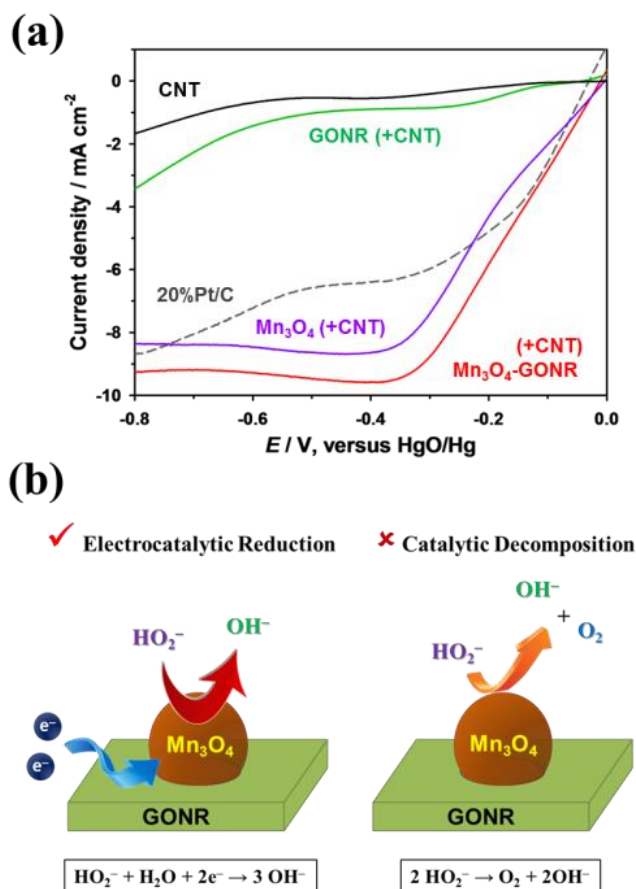
Figure 5B.4 (a) LSV-RDE profiles of the composite electrocatalysts in Ar-deaerated 0.1 M KOH containing 5 mM H_2O_2. (b) A diagram illustrating possible mechanisms for peroxide consumption on the Mn_3O_4 nanoparticles in Mn_3O_4-GONR hybrid, indicating that the electrocatalytic reduction is the dominant pathway.

Following the design principle discussed above, Mn_3O_4 nanoparticles must perform efficient electrocatalysis of peroxide reduction to support the overall

four-electron ORR, as distinguished from the catalytic disproportionation of peroxide into oxygen ($2\ HO_2^- \rightarrow O_2 + 2\ OH^-$).[61] Next, we studied H_2O_2 electro-reduction on the composite electrocatalysts in an Ar-deaerated alkaline electrolyte as a reaction analogue to the peroxide reduction using LSV on a rotating disk electrode (LSV-RDE). In Figure 5B.4a, both GONR composite and CNT are obviously inactive for H_2O_2 electro-reduction; this is in agreement with the previous discussion. Remarkably, the Mn_3O_4-containing composites displayed excellent H_2O_2 reduction activity that is even superior to the Pt/C electrocatalyst. Note that the Pt/C is considered a good electrocatalyst for H_2O_2 reduction, and this suggests that peroxide reduction is very likely an elementary step in the ORR.[228] The reason that the hybrid composite has an enhanced reduction current remains unclear, although it could be a facilitated H_2O_2 adsorption on the GONR surface or a synergistically promoted H_2O_2 reduction activation at the hybrid interface.

From the above, we can conclude that Mn_3O_4 nanoparticles play a crucial electrocatalytic role in the four-electron ORR apart from the synergistic effect. Figure 5B.4b is an illustration of two possible mechanisms for the peroxide removal in the associative ORR pathway. Very likely, the electrocatalytic reduction, rather than the catalytic decomposition, dominates the process since excellent H_2O_2 reduction activity can be expressed by the Mn_3O_4-containing composites. Overall, it appears quite straightforward that the excellent ORR activity in the hybrid composite is the combined consequence of (1) the dual electrocatalytic role of both GONR and Mn_3O_4 nanoparticles, and (2) the synergistic coupling at the interface between Mn_3O_4 nanoparticle and GONR resulting in a reduced activation barrier.[227]
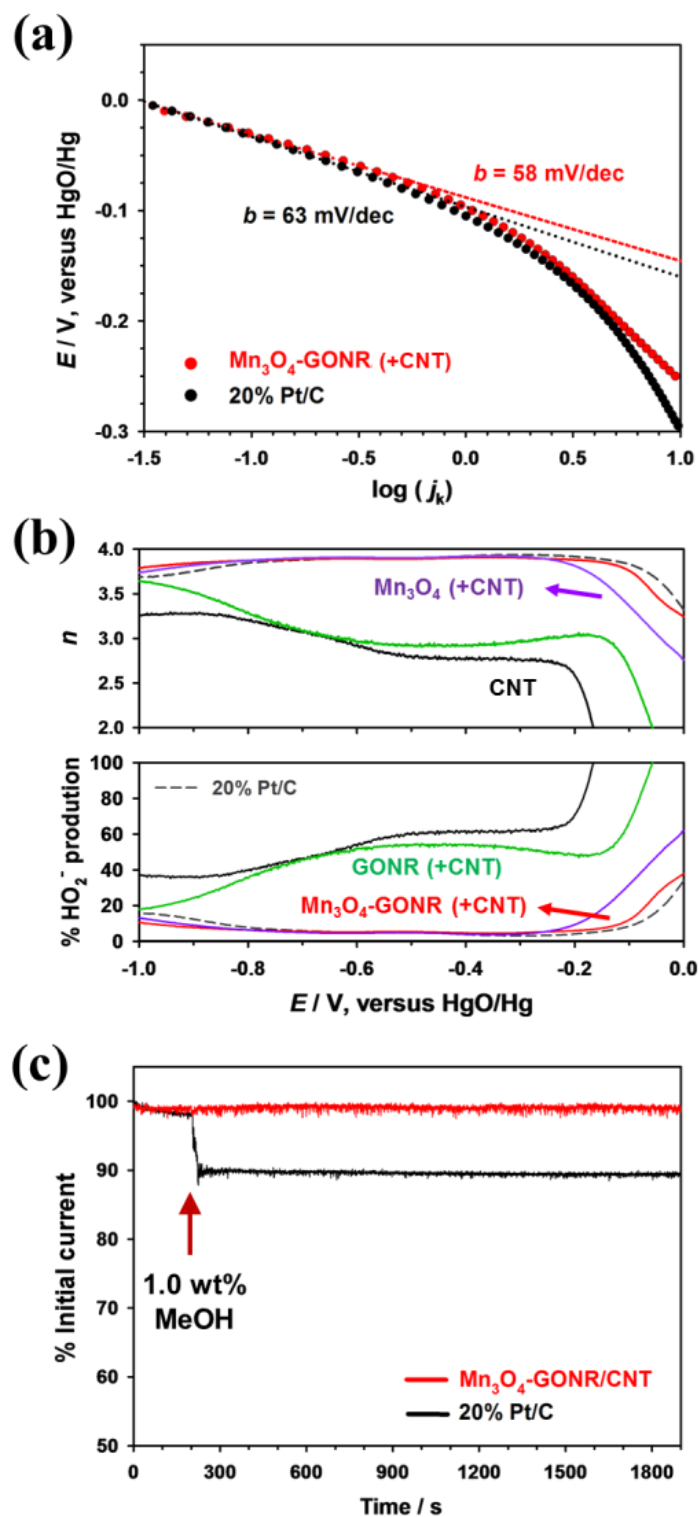
Figure 5B.5 (a) Tafel plots for Mn$_3$O$_4$-GONR hybrid composite and 20% Pt/C. (b)

The calculated *n* number and percentage peroxide production on the composite

electrocatalysts along the ORR potential. (c) The methanol-poisoning test on the

hybrid composite and 20% Pt/C in O_2-saturated 0.1 M KOH; 1.0 wt.% methanol was injected to the system at 200th second (red arrow).

In the last section, we address the reaction properties performed on the Mn_3O_4-GONR hybrid composite. Figure 5B.5a displays the Tafel plots of the hybrid composite and Pt/C electrocatalyst, measured using stair-case voltammetry (SCV). Both materials showed a linear relation at low overpotential region and the hybrid composite exhibited a slope of 58 mV dec^{-1}, which was very close to that of Pt/C (63 mV dec^{-1}). This suggests the rate-determining step of the electrocatalysts may be a two-electron transfer process, for which could be the peroxide generation process.[96] Such resemblance in the reaction mechanism implies that the hybrid composite may share similar elementary reactions with the Pt/C electrocatalyst.

The average electron-transfer (n) number and the percentage production of HO_2^- (%HO_2^-) of the composite electrocatalysts were calculated along the reaction potential (with a measured collecting efficiency of 0.37) and the profiles are provided in Figure 5B.5b. The Mn_3O_4, Mn_3O_4-GONR composites and Pt/C had n numbers that stabilized at ~3.9 and with %HO_2^- values of less than 5.4%. This is a direct indication of four-electron ORR. Moreover, these electrocatalysts reached an n number of 3.8 at − 0.20 V, –0.11 V and –0.09 V, respectively, for Mn_3O_4 composite, Mn_3O_4-GONR composite and Pt/C. In other words, a high-level activity can be attained by the hybrid composite at only small potential difference to 20% Pt/C. In contrast, both the GONR composite and CNT only afforded n numbers less than 3.0 at –0.6 V with significant production of peroxide. This suggests the peroxide production rather than complete ORR dominated on these materials. Certainly, the Mn_3O_4-GONR hybrid composite delivers highly efficient four-electron ORR at a comparable activity to a commercial Pt/C electrocatalyst.

For the stability of hybrid composite towards methanol poisoning, constant potential amperometry in a hydrodynamic system was carried out to examine the current response in the system when 1.0 wt% methanol (MeOH) was injected (Figure 5B.5c). The 20% Pt/C electrocatalyst showed ~10% current reduction upon the addition of methanol. The Mn_3O_4-GONR hybrid composite, however, maintained a stable current profile over the course of the experiment. This indicates that the hybrid composite is chemically insensitive to the methanol in the alkaline electrolyte. Indeed, our hybrid composite electrocatalyst not only has excellent ORR activity, but also displays great chemical robustness against poisoning.

5B.5 Conclusion

In conclusion, we demonstrated that a rational combination of electrocatalytic components for each elementary ORR process can lead to highly efficient four-electron ORR. In the case of the Mn_3O_4-GONR hybrid composite, the dual electrocatalytic functions inherent in the hybrid together with the synergistic coupling were the true origins of the excellent performance that was observed. Through extensive electrochemical experiments, we have revealed that the GONR component facilitated oxygen reduction to peroxide, while the decorated Mn_3O_4 nanoparticles accelerated the electro-reduction of the peroxide for ORR completion when electron transport was expedited. Furthermore, we showed that the rate-determining step for the hybrid composite and of Pt/C electrocatalyst may be similar, and that our hybrid composite has good chemical stability through methanol-poisoning test. Overall, it is anticipated that this rational design principle can ultimately provide a logical path towards a functional all-in-one electrocatalyst.

Chapter VI.

Manganese-Oxygen Nanoclusters on Carbon Nanotube as Directly Bound Active Sites for Oxygen Reduction Reaction

A manuscript to be published

6.1 Abstract

Synergistic coupling in metal oxide/carbon hybrid can lead to effective catalytic interfaces for highly efficient oxygen reduction electrocatalysis. However, direct examination of the unexposed interfaces is difficult because of the on-site growth of metal oxide nanocrystals. In this report, we demonstrate that manganese-oxygen nanoclusters bound on carbon nanotube imitate the coupled interface found in manganese oxide/carbon hybrids and are the direct active sites for promoted oxygen reduction reaction (ORR). The nanometer size-scale and the amorphous nature of the nanoclusters were characterized by high-resolution transmission electron microscopy and extended X-ray absorption fine structure (EXAFS). Using differential pulse voltammetry, we observed improved activation of both peroxide generation and reduction reactions at the bare C–O–Mn domains in the nanoclusters as compare to Mn_3O_4 nanocrystals. Importantly, the nanocluster-decorated carbon nanotubes can directly promote more efficient four-electron ORR on the exposed amorphous active domains.

6.2 Introduction

The pursuit for high performance non-platinum electrocatalysts for oxygen reduction reaction (ORR) has been an important on-going research topic for fuel cell industries.[15,16,229] The goal is to accelerate the sluggish ORR process in order to enhance the energy efficiency and to maximize the output power at low cost. Currently, two major classes of developing electrocatalyst are represented by heteroatom-doped carbons and non-precious metal oxide/carbon hybrids.[21,95,108,123,138,156,157] The heteroatom-doped carbons include the nitrogen-doped

148

carbons and other metal-free phosphorus, sulfur, oxygen and halogen-doped carbon materials.[35,42,152,214,223] However, the origin of activity remains elusive in these non-metal electrocatalysts, and most of them have not been able to demonstrate Pt-level ORR activity without nitrogen. However, the metal oxide/carbon hybrids have been quite extensively studied for their unusual synergistic effect for ORR, as a result of which a level of activity close to that of Pt can be achieved.[95,156,157] This has stimulated the search for better combinations of metal oxide (e.g., Mn, Fe, Co, Cu or mixtures) and carbon support,[95,108,156,157,230-234] and raised interest in understanding the origin of the hybrid synergy.[156,231] In particular, unravelling the origin of the synergistic effect could show the way towards rational development of highly efficient ORR electrocatalysts. Although the actual mechanism is still unclear, the current opinion is that the synergistic effect is the result of the covalently coupled metal oxide/carbon interface. For example, facilitated electron transport across the bridging interface is a likely cause of the reduced ORR activation overpotential.[156] Furthermore, our recent study suggests that the synergistic result is a direct consequence of the promoted oxygen-to-peroxide reduction at the exposed interface periphery, with the help of highly efficient peroxide reduction by the neighbouring metal oxide nanocrystals.[227] Since the central synergistic effect revolves around the covalent C–O–M (or C–N–M) interfaces, gaining further mechanistic insight will require direct investigation of C–O–M moieties on carbon surfaces, without covering metal oxide nanocrystals.
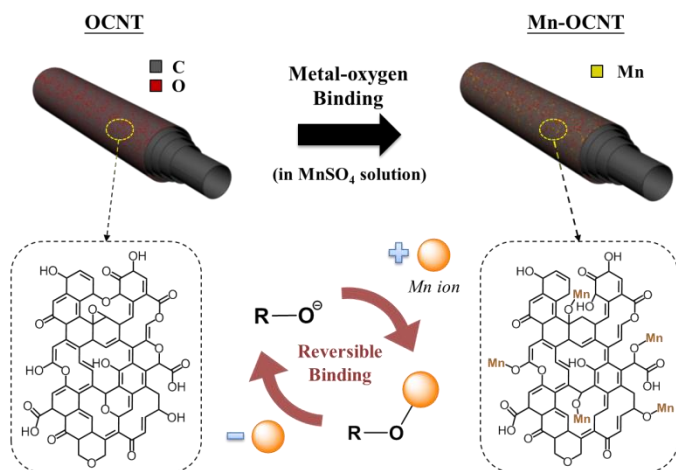
Figure 6.1 The preparation method of Mn-OCNT and the surface chemical structures of Mn-OCNT and OCNT.

With the aim of studying bare C–O–Mn moieties without the complicating effect of metal oxide nanocrystals that occur in typical hybrid catalysts, we introduced manganese-oxygen (Mn–O) nanoclusters to the surface of carbon nanotubes to imitate the interface configuration in the Mn_3O_4-GONR hybrid.[227] In our previous work, we showed that mildly oxidized CNTs (OCNTs, $KMnO_4$:CNT = 2:1) prepared using Hummer's method can preserve the electronic conductivity while incorporating a reasonable level of surface oxygen functionalities.**[223]** On such a system, we devised a protocol utilizing metal ion binding to the surface oxygen groups to develop directly connected Mn–O nanoclusters on OCNTs (Figure 6.1, see also Appendix E). Note that the reaction was carried out at pH ~6.0 to inhibit nanocrystal growth and the Mn-bound OCNTs (Mn-OCNTs) were subjected to dilute H_2O_2 treatment to stabilize the Mn–O nanoclusters from dissociation. The same procedure was applied to pristine CNTs as a reference to demonstrate the specific binding. A range of characterization methods, including high-resolution transmission electron microscopy (TEM) and X-ray absorption spectroscopy (XAS) were combined to elucidate the chemical nature of Mn–O nanoclusters on Mn-OCNT. We also assessed the ORR mechanism and the

activity of the Mn-OCNT by necessary voltammetry techniques.

6.3 Experimental Section

6.3.1 Preparation of OCNTs

The multi-walled carbon nanotubes (CNTs, purity > 95%) used in this work were kindly provided by Institute of Metal Research, Shengyang and were purified before use through extensive washing in 5.0 M HCl (Sigma), ethanol and water, separately for many times. In the preparation, 2.0 g of the purified CNT was used following a modified Hummer's method using 4.0 g of KMnO$_4$ (BDH Chem).[187] The resulting oxidized CNTs (OCNTs) were collected by filtration and extensively washed with water. OCNTs with different degrees of oxidation were prepared via the identical procedure with varying KMnO$_4$:CNT mass ratios.

6.3.2 Preparation of Mn-OCNT

Mn-OCNT was prepared through a simple Mn-binding protocol as follows. Typically 0.3 g of OCNTs was dispersed in a 60 mL of 0.4 M manganese sulfate (Ajax Chem) aqueous solution with the help of probe ultrasonic agitation. The solution was kept at its natural pH of about ~6.0. Note that Mn oxides do not precipitate at this pH. The mixture was magnetically stirred and maintained at 60 ℃ for 2 hours, followed by an addition of 5 mL 30% H$_2$O$_2$ (BDH Chemicals) to stabilize the as-formed Mn–O nanoclusters. After another half hour, Mn-OCNT was harvested by filtering and washing with water. The same procedure was applied to unmodified, purified CNTs as a control experiment and to different OCNTs to examine for selective binding. In the acid treatment, Mn-OCNT was suspended in a 3.0 M HCl solution and stirred for 4 hours before the sample was collected by filtration. For the

KOH treatment, an amount of Mn-OCNT was suspended in 1.0 M KOH for 20 minutes in air and then purified for an XAS measurement.

6.3.3 Preparation of Mn oxides

Pure MnO standard was provided on-site by National Synchrotron Radiation Research Center (NSRRC), Taiwan. Mn_3O_4 was synthesized by a one-pot method. An amount of manganese sulfate was dissolved in a H_2O_2 aqueous solution. 1.0 M KOH was then slowly dropped into the solution to precipitate brown Mn_3O_4 nanocrystals and the product was then purified by filtration and washing with water. Mn_2O_3 was prepared by heating $(CH_3COO)_2Mn.4H_2O$ (Sigma) at 550 °C for 4 hours in air. The α-MnO_2 synthesis employed a literature hydrothermal method.[235] The crystallinity of the Mn oxides was confirmed by XRD as shown in Figure S5.

6.3.4 Characterization

XPS was performed on a Kratos XPS spectrometer using a monochromated Al Kα source. The survey and high-resolution spectra were collected at pass energies of 160 eV and 20 eV, respectively. All spectra were charge-corrected against the C–C peak at 284.8 eV as reference and the full-width at half-maximum (FWHM) values were constrained to within 0.1 eV. ICP-OES for quantitative composition analysis was done on a Varian Vista Pro ICP-OES instrument, assisted by microwave digestion of samples on a Milestone Ethos-1 Advanced Microwave Digestion Labstation. High-resolution TEM was performed on a FEI-aberration-corrected Titan 80-300 transmission electron microscope at an accelerating voltage of 300 kV, using an ordinary transmission mode and high-angle annular dark-field (HAADF) mode (STEM). Powder X-ray diffraction (XRD) was carried out on a Bruker D8 Advance X-ray diffractometer with a Cu Kα source; the step rate was 0.02 degrees per second.

The XAS measurements were performed at 16A1 station (Tender X-ray beamline) in NSRRC, a 1.5 GeV light source. The incident beam energy was calibrated with a Mn metal standard. The energy range was scanned from 6400 eV to 7200 eV and the energy intervals for pre-edge, near-edge and post-edge were set to be 2.0 eV, 0.5 eV and 0.05 eV, respectively.

6.3.5   *Electrochemical measurements*

The electrochemical measurements employed a three-electrode setup, which consisted of a rotating Pt ring/glassy carbon (GC) disk working electrode (ALS Co., Ltd.; GC diameter: 4.0 mm, Pt ring inner diameter: 5.0 mm and outer diameter: 7.0 mm), a Pt wire counter electrode and an HgO/Hg reference electrode stabilized in 0.1 M KOH. The modified CNT electrocatalysts were prepared into liquid suspensions at 5 mg mL^{-1} in a 1.0 wt% Nafion (Sigma) solution, and a total of 75 μg of catalyst material was loaded onto the GC electrode. All voltammograms were measured in gas-saturated 0.1 M KOH electrolyte, on a CHI920D bipotentiostat instrument coupled with RRDE-3A apparatus (ALS Co., Ltd.). Gas saturation was achieved by bubbling O_2 gas at a flow rate of 15 mL min^{-1} for at least one hour before the measurements, while de-oxygenation was carried out by bubbling Ar gas under similar conditions.

The LSV-RRDE experiments were carried out in an O_2-saturated electrolyte, measured at a sweep rate of 10 mV s^{-1}. The electrode was rotated at 1600 rpm and the ring potential held at +0.5 V versus the reference electrode. The LSV-RDE experiment for H_2O_2 reduction activity was measured using the same parameters in an Ar-deaerated electrolyte containing 20 mM H_2O_2, except a ring potential was not applied. The DPV profiles were collected at an equivalent rate of 8 mV s^{-1} with a pulse width of 0.2 s for every 0.5 s, and at a 1600 rpm rotation rate. The Tafel plot

measurements employed stair-case voltammetry (SCV) in an O_2-saturated electrolyte at a constant electrode rotation rate of 1600 rpm in order to ensure steady-state conditions. The voltammograms were taken at a step size of 20 mV and 10 s dwell time was allowed before each data points was collected.

6.4 Results and Discussion
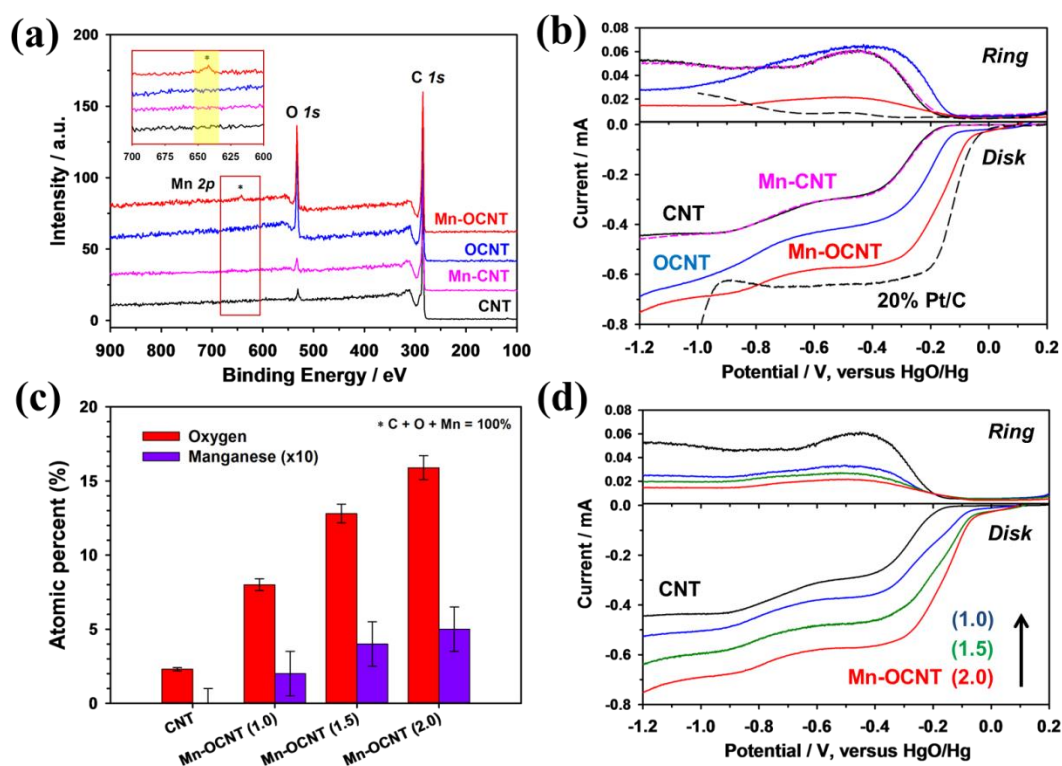
Figure 6.2 (a) XPS survey spectra and (b) LSV-RRDE profiles of Mn-OCNT and the controls. (c) The Mn and O contents (based on XPS quantitative analysis) of the Mn-OCNTs using OCNTs at varying oxidation degree and (d) the LSV-RRDE profiles of the Mn-OCNTs. All voltammograms were collected in an O_2-saturated 0.1 M KOH electrolyte using an electrode rotation rate of 1600 rpm.

X-ray photoelectron spectroscopy (XPS) was firstly employed to study the composition of the modified CNTs. The survey spectra in Figure 6.2a show that the

mild oxidation was successful, demonstrated by the intense O *1s* peaks in the oxidized CNTs. After the Mn-binding, the small signal at the Mn *2p* position (642 eV) for Mn-OCNT confirms the residual presence of Mn. It was noted that the surface oxygen is at a much higher content than Mn, probably due to efficient reversible binding. The Mn binding is also evident in the XPS O *1s* spectra of the OCNTs before and after binding (Figure E1, Appendix E). In contrast, the pristine CNT after the same Mn-binding procedure (Mn-CNT) exhibited no Mn signature, which suggests the Mn ions do not bind to the bare carbon surface. These observations were also supported by our inductively coupled plasma optical emission spectroscopy (ICP-OES) measurements, in which all except Mn-OCNT has negligible Mn content (< 0.01 wt%); Mn-OCNT had a Mn content of 9.45 wt% (Supporting Information). Note that most of the bound Mn on Mn-OCNT can be removed by an acid treatment, which means this material is vulnerable in an acidic environment. Nonetheless, these composition analyses evidently support the reality of Mn–O binding.

Next, we employed linear sweep voltammetry on a rotating ring-disk electrode (LSV-RRDE) to confirm the Mn–O binding as well as to assess the ORR activity on each modification. In Figure 6.2b, Mn-OCNT performed a very efficient ORR starting from an onset potential of –0.05 V (versus HgO/Hg reference electrode), which is very close to that of 20% Pt/C electrocatalyst (0.00 V). The large ORR disk current together with a small ring current indicates an apparent four-electron ORR with little peroxide production. These features resemble the superb ORR activity found in the Mn_3O_4-GONR hybrid,[236] even though Mn-OCNT only has a minute amount of Mn. On the other hand, the OCNT exhibited inferior ORR activity with a more negative onset potential (–0.11 V) and significant ring current, suggesting predominant peroxide generation and retarded ORR activation. It should be mentioned that the

ORR activity of OCNT is distinguished from original CNT by a finite improvement. This means that the activity of OCNT is further improved by the Mn binding. In a cross-checking experiment, the superb activity of Mn-OCNT degraded to the level of OCNT once the bound Mn ions were removed by an acid treatment (Figure E3, Appendix E). In any explanation, the Mn ions from the salt solution must be associated with the surface oxygen groups on OCNT to give rise to the superior electrocatalytic activity in Mn-OCNT. In addition, the Mn-CNT displayed an overlapping LSV-RRDE profile to the unmodified CNT. This signifies a selective binding of Mn ions to the surface oxygen groups, since a thorough wash with water on Mn-OCNT could not remove the bound metal ions.

The selectivity of Mn binding to the surface oxygen groups was further inspected on different OCNTs. A series of Mn-OCNTs were prepared using OCNTs of varying oxidation degree, represented by the $KMnO_4$:CNT mass ratios (1.0, 1.5 and 2.0). The composition of the resulting Mn-OCNT is provided in Figure 6.2c. There is a direct correlation between the Mn content and the oxygen level, even after extensive rinsing with water, which is a supporting evidence for the selective binding of Mn ions to the surface oxygen groups. Figure 6.2d shows the LSV-RRDE profiles of the as-prepared Mn-OCNTs. The consequences of the selective binding can be observed from the convergence of the ORR onset potentials and the progressive increase of the disk currents due to the growing Mn content. Moreover, the gradual decrease of the measured ring currents may suggest a facilitated consumption of peroxide intermediate with an increasing amount of Mn. Clearly, these results imply that the presence of bound Mn ions plays a key role in promoting the four-electron ORR.
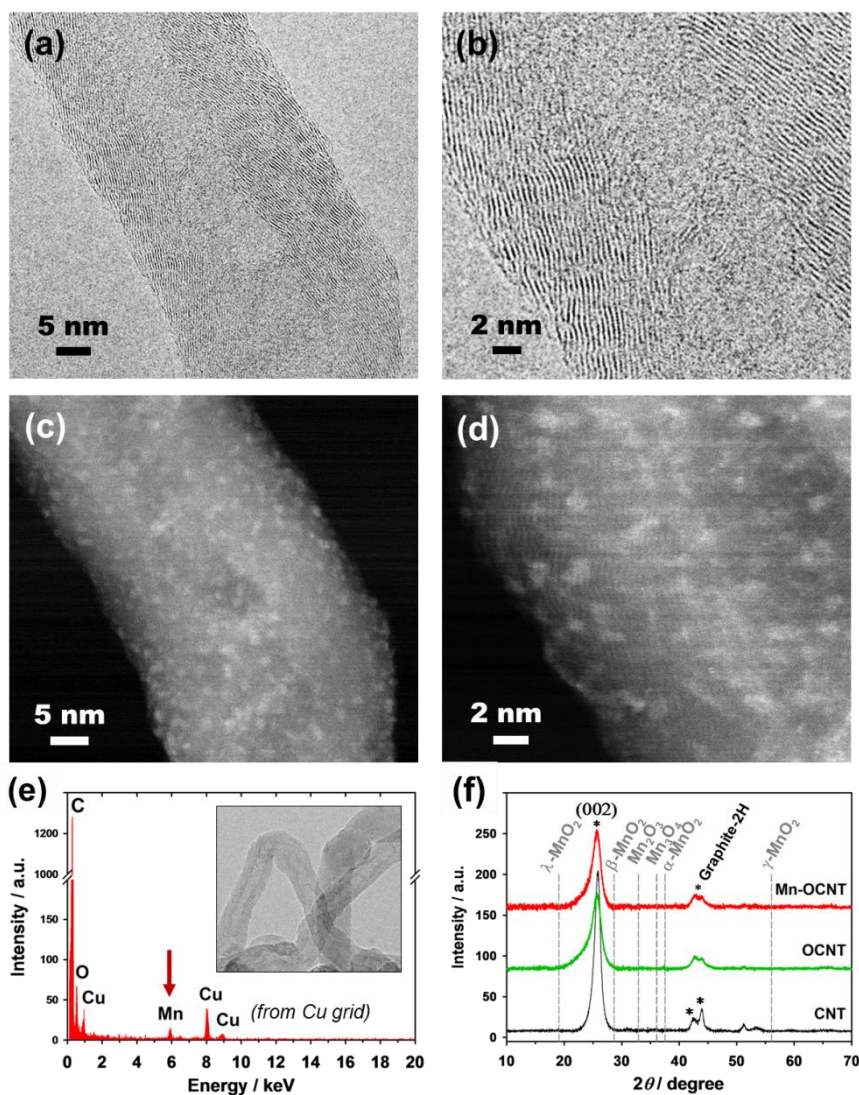
Figure 6.3 High-resolution TEM images of Mn-OCNTs in (a, b) normal mode and (c, d) HAADF mode; (e) the EDX spectrum of Mn-OCNT. (f) The XRD patterns of Mn-OCNT, OCNT and pristine CNT; the grey dashed lines indicate the strongest signal from possible manganese oxides (Mn_2O_3, Mn_3O_4 and MnO_2).

High-resolution TEM enables visualization of tiny Mn–O nanoclusters on Mn-OCNT. We performed this technique in different modes to validate the physical existence of Mn–O nanoclusters, as well as to check for any unexpected growth of nanocrystals. Ordinary high-resolution TEM images of Mn-OCNT are shown in Figure 6.3(a, b). The multi-walled nature of the nanotube is reflected by the graphitic lattice fringes, and the impact of mild oxidation can be seen from the minute

roughness of the outer surface. No nanoparticles could be observed on the nanotube or elsewhere under normal microscopy mode. Another important feature is the lack of lattice fringes for metal oxide nanocrystals, if they existed. In order to visualize the amorphous Mn–O nanoclusters, TEM images under high-angle annular dark-field (HAADF) mode were also taken to contrast for the heavy elements, as shown in Figure 6.3(c, d). Quite remarkably, there are in fact many small Mn–O nanoclusters of ~1.0 nm size adhered to the surface of nanotube. The local composition of the modified nanotubes was again checked by energy dispersive X-ray (EDX) spectroscopy. The metal content of the nanoclusters can be picked up by the Mn signature in the spectrum of Figure 6.3e; the Cu signals are sourced from the TEM grid. We further employed powder X-ray diffraction (XRD) to identify possible crystalline Mn oxide phases, if formed on Mn-OCNT. The XRD patterns of Mn-OCNT and its precursors are shown in Figure 6.3f, and the most intense diffraction peaks for the crystalline oxides are also listed in the pattern. All diffraction patterns possess identical characteristic peaks (labelled by asterisks), relating to graphite-2H crystal structure. The strong diffraction at ~26° (2θ) indicates the (002) crystal plane from the interlayers of the multi-walled OCNT. Not surprisingly, no diffraction peaks associate with any Mn oxide could be found. In other words, the Mn–O nanoclusters are amorphous and no growth of Mn oxide nanocrystals has occurred during the Mn-binding process.
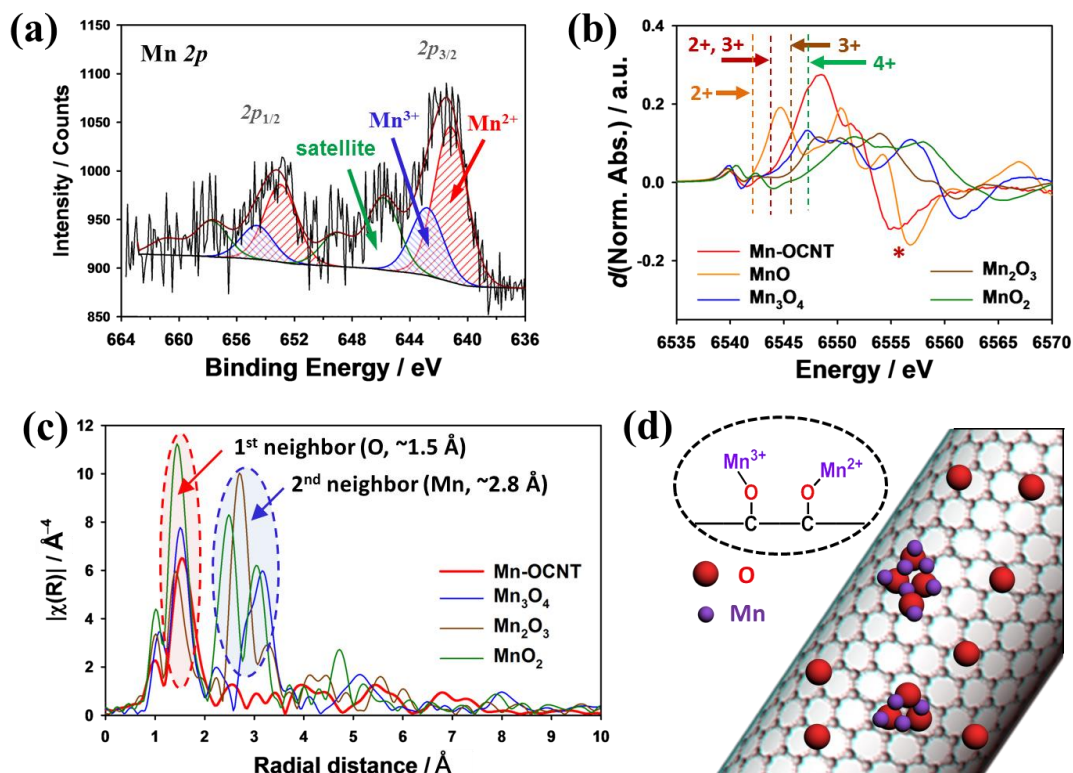
Figure 6.4. (a) High-resolution XPS Mn *2p* spectra of Mn-OCNT. (b) The first derivative of Mn *K*-edge XANES spectra and (c) the Fourier transforms of Mn *K*-edge EXAFS spectra of Mn-OCNT and crystalline Mn oxide standards. (d) A model surface configuration of Mn-OCNT.

We also investigated the chemical nature of the Mn–O nanoclusters using XPS and XAS. XPS at high spectral resolution can reveal the valence state of the bound Mn species. Figure 6.4a is the Mn *2p* spectra of Mn-OCNT. In the deconvolution analysis, we only resolved the principal peaks for the valence states, since the spectral features at higher binding energies could be complicated by the shake-up satellites.[237] The two characteristic $2p_{3/2}$ peaks at 641.2 eV and 642.8 eV reveal the presence of both divalent and trivalent states of the Mn species in Mn-OCNT.[238] The area of the shaded peaks additionally suggests that a small portion of the bound Mn^{2+} wasoxidized into Mn^{3+} during the H_2O_2 treatment. The edge feature in the X-ray

absorption near-edge structure (XANES) spectrum also agrees with the multivalent state of the bound Mn. The first derivative XANES spectra of Mn-OCNT and Mn oxide standards are shown in Figure 6.4b. The position of the main edge (indicated by the dashed lines) for the oxide standards suggests that the single-valent Mn^{2+} (MnO), Mn^{3+} (Mn_2O_3) and Mn^{4+} (MnO_2) species are located at 6542.2 eV, 6545.5 eV and 6547.0 eV, respectively.[239] For mixed-valent Mn^{2+}/Mn^{3+} oxide (Mn_3O_4), the main edge position is at 6543.7 eV. Clearly, Mn-OCNT (6543.5 eV) also has a mixed Mn^{2+}/Mn^{3+} state. Additionally, the presence of a characteristic trough for Mn^{2+} at ~6555 eV probably suggests a higher Mn^{2+} population in Mn-OCNT.[239,240] We further examined the chemistry of the Mn-OCNT treated in an alkaline solution in order to ensure that the mixed-valent chemistry will be preserved in the ORR. The XANES spectrum in Figure E7 (Appendix E) shows that the treated Mn-OCNT shares a similar valence nature with Mn_3O_4, which has a larger Mn^{3+} population in the crystal structure. In other words, the alkaline treatment merely increases the Mn^{3+} population in Mn-OCNT, and does not alter the mixed valence state overall. Certainly, there is a mixed $Mn^{2+/3+}$–O configuration in the nanoclusters, which is somewhat similar to the coupled interface structure (Mn^{3+}–O) in the Mn_3O_4-GONR hybrid.[227]

The diverse oscillation feature in the post-edge region in XANES profiles inspired us to study the subtle structural chemistry by extended X-ray absorption fine structure (EXAFS). The Fourier-transform EXAFS spectra can reveal the atomic neighbours to a central Mn ion at approximate radial distances. Figure 6.4c shows that the Mn oxide references have two well-defined closest neighbours, which can be ascribed to the first adjacent oxygen (~1.48 Å) and the first Mn neighbour (~2.8 Å).[241,242] This means that these crystalline Mn oxides have distinct local crystal structures around their Mn species. In contrast, Mn-OCNT only has one oxygen

neighbour located at 1.55 Å and no obvious second closest neighbour. In comparison to crystalline Mn oxides, the adjacent oxygen is slightly farther away from the Mn in the nanoclusters, perhaps due to a lack of crystalline order. The absence of the second closest neighbour in the profile suggests that the Mn species on Mn-OCNT are not at a fixed position relative to another Mn neighbour. Again, this strongly suggests the amorphous nature of the Mn–O nanoclusters, even down to a sub-nanometer scale.

On the basis of these observations, we constructed a model surface configuration for Mn-OCNT, as illustrated in Figure 6.4d. Firstly, the nanoclusters are attached to CNT in a $C–O–Mn^{2+}$ or $C–O–Mn^{3+}$ configuration, suggested by the Mn-binding experiments and the spectroscopy studies. Our composition analysis shows that there is much more oxygen than the bound Mn on Mn-OCNT, which means most of the surface oxygen groups remain unbound to Mn ions. Through TEM and XRD investigations, we know that there is no development of Mn oxide nanocrystals. The EXAFS study further emphasizes the amorphous nature of the Mn–O nanoclusters. It is likely that the nanoclusters have organized into small planar domains, without any crystalline development along the c-axis with respect to the graphitic planes.
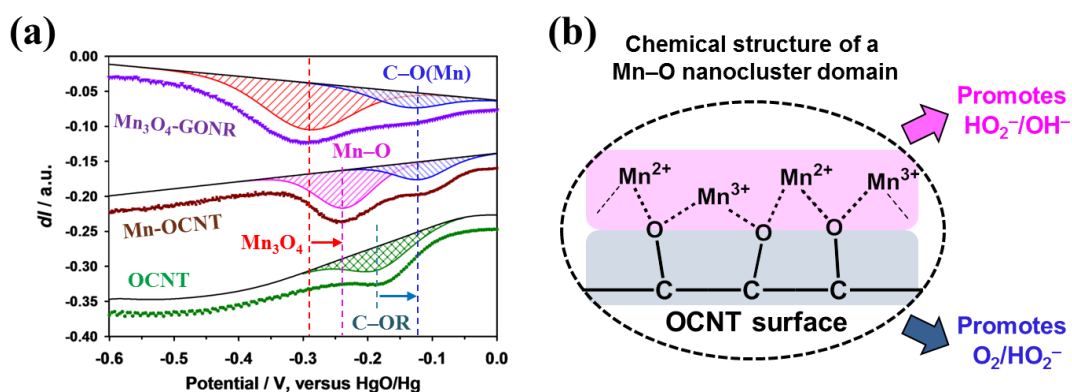
Figure 6.5 (a) DPV profiles of Mn-OCNT, OCNT and the Mn_3O_4-GONR hybrid composite in an O_2-saturated 0.1 M KOH electrolyte. (b) A Mn–O nanocluster domain, labelled with particular electrocatalytic functions for the ORR.

With uncovered Mn–O active domains decorated on conductive nanotubes, we are able to examine the ORR on this surface, which mimics the Mn oxide/carbon interface. Differential pulse voltammetry was carried out to resolve the sequential ORRs occurring on Mn-OCNT, as shown in Figure 6.5a. The Mn_3O_4-GONR hybrid composite (as reported in our previous work)[236] and OCNT are included for comparison. Without bound Mn ions, the peroxide generation ($O_2 \rightarrow HO_2^-$) on OCNT occurred at –0.188 V. Where electrocatalysts possess Mn–O domains in the form of hybrid interface or nanoclusters, there is a common improvement in the reaction potential for the hybrid composite (–0.128 V) and Mn-OCNT (–0.120 V). It is worthy to note the slightly higher reaction potential for the fully exposed Mn–O nanoclusters. This may be due to the more efficient access to the C–O–Mn sites for the primary reduction.[236] More interestingly, we observed a substantial improvement in the reaction potential for peroxide reduction ($HO_2^- \rightarrow OH^-$) on Mn-OCNT (–0.238 V) as compared to that of Mn_3O_4-GONR hybrid composite (–0.292 V). This means that the active sites in metal oxide/carbon hybrid are obscured by the covering nanocrystals. From our result, the exposed nanoclusters in an amorphous form are capable of accelerating the peroxide reduction at the Mn–O domains more effectively than the crystalline form. This is remarkable and highly significant because current knowledge of the high activity in metal oxide/carbon hybrid is usually attributed to the intrinsic activity of metal oxide nanocrystals, aided by the synergistic effect of the coupled interface, rather than to the interface directly.[156]

It is fairly obvious that the C–O–Mn moiety can catalyse two independent reduction reactions. If we must split the functional domains to describe their roles, then the C–O and $Mn^{2+/3+}$–O sub-domains should be ascribed for the peroxide generation and reduction, respectively, as shown in Figure 6.5b. Since the C–O

sub-domains (inclusive of carbonyl, carboxyl and epoxide) in oxidized carbons are known to facilitate peroxide generation, an activity enhancement is probably due to a change in the local electron density by the Mn binding. Similarly, the Mn–O sub-domain merely resembles an amorphous Mn oxide surface and its advanced activity is perhaps a result of the amorphous nature or the unusual coordination environment.
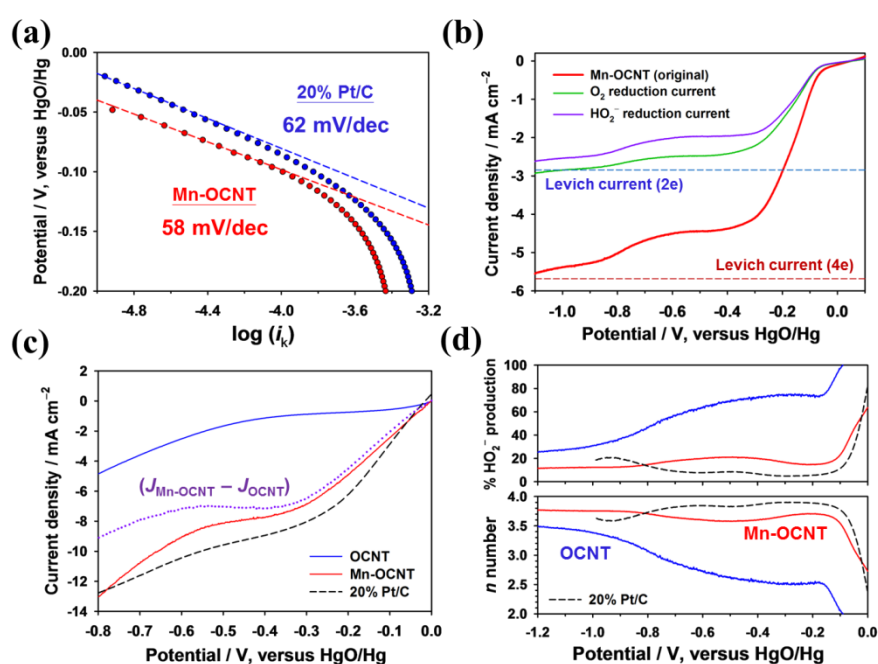
Figure 6.6 (a) Tafel plots for Mn-OCNT and 20% Pt/C. (b) A transformed LSV-RRDE profile for Mn-OCNT with separated reduction current densities. (c) LSV-RDE profiles of Mn-OCNT, OCNT and 20% Pt/C in Ar-deaerated 0.1 M KOH electrolyte containing 20 mM H_2O_2. (d) The calculated n numbers and %HO_2^- at –0.5 V from the corresponding LSV-RRDE profiles (Figure 6.2b).

The ORR mechanism of activation was further verified by Tafel analysis. The Tafel plots of Mn-OCNT and Pt/C are shown in Figure 6.6a. Both electrocatalysts exhibit a slope of ~60 mV dec^{-1}, which suggests the rate-determining step is likely a two-electron transfer process in a stepwise electrochemical reaction.[96] This supports

the sequential reduction mechanism on Mn-OCNT. On the basis of the stepwise ORR mechanism, we evaluated the electrocatalytic activity of Mn-OCNT. A mathematical treatment using both disk and ring currents was applied to derive the individual reduction currents for O_2 reduction and HO_2^- reduction (Supporting Information). Figure 6.6b is the transformed profile for Mn-OCNT. It is clear that the O_2 reduction current density almost approaches the diffusion-limiting current density for a two-electron transfer reaction described by the Levich relation. However, the HO_2^- reduction current density is lower than that of the primary reduction. This means some peroxide intermediate avoids being reduced at the Mn–O sub-domains. In other words, the amount of Mn may simply be insufficient to support the simultaneous reduction of the as-produced peroxides, although the Mn–O sub-domains are efficient for the reduction activation. We also directly assessed the peroxide-reducing ability of Mn-OCNT in a deaerated electrolyte containing 20 mM H_2O_2. The LSV on a rotating disk electrode (LSV-RDE), as shown in Figure 6.6c, demonstrates improved H_2O_2 reduction activity for Mn-OCNT in comparison to OCNT. If we take away the current density of OCNT, the dashed purple line is essentially the current density contributed by the Mn–O nanoclusters. Clearly, the enhanced peroxide reduction activity must be associated with the presence of Mn–O active centres.

Figure 6.6d is the calculated electron transfer (n) number and the percentage production of peroxide intermediate ($\%HO_2^-$) of Mn-OCNT and its precursors for comparison. As expected, Mn-OCNT performed an apparent four-electron ORR, given by its n number at ~3.7. This is very close to the n number of 20% Pt/C. In the $\%HO_2^-$ profile, the amount of peroxide produced on Mn-OCNT is ~17% as compared to ~6.0% on 20% Pt/C. As discussed earlier, this may be due to a deficiency in the

Mn–O active sub-domains for reducing peroxide. Nevertheless, this is a significant improvement from the activity level of OCNT by developing Mn–O nanoclusters.

6.5 Conclusion

In conclusion, we developed Mn–O nanoclusters on modified CNT in order to study the intrinsic activity of the coupled interface in Mn oxide/carbon hybrid. The selective formation of amorphous Mn–O nanoclusters on OCNT was extensively validated by comparative electrochemical experiments, high-resolution TEM and X-ray absorption/photoelectron spectroscopy. All results demonstrated that the chemical configuration of the nanoclusters is in agreement with the expected coupled hybrid junction without any covering Mn oxide nanocrystals and the Mn species are in a mixed Mn^{2+}/Mn^{3+} state. Our electrochemical measurements revealed that the Mn–O nanoclusters can act as direct active sites for an apparent four-electron ORR without any nanocrystals. Furthermore, the amorphous C–O–Mn domain can not only activate the peroxide generation more efficiently, but also effectively promote the peroxide reduction. These outcomes have led to recognition of the functional roles and the capability of Mn–O nanoclusters for ORR in an alkaline medium. We believe this knowledge will prompt rational innovation in non-precious ORR electrocatalysts.

Chapter VII.

Concluding Remarks

7.1 Conclusions

7.1.1 Optimizing Graphene Porous Electrodes for ORR

Optimizing the electrode structure for gas-diffusion is important to the ORR as opposed to selecting an appropriate electrocatalyst. As the reaction occurs at an electrode/electrolyte interface, efficient conduction for both electrons and ions is crucial to support fast reaction kinetics. Carbon-based electrocatalysts can have various forms and can self-assemble into different morphologies in a composite with an electrode binder. The morphology and composition of a carbon composite electrode essentially determine the capability for simultaneous electron/ion transport and therefore the observed performance for the ORR electrocatalysis. In the example of graphene/chitosan composite electrode (Chapter II), we demonstrated that the reaction overpotential can rise upon inefficient reactant-product inter-diffusion (trapped in the binder matrix) and poor electron conduction when there is an absence of connected carbon channels. To circumvent such situations, the composite electrode should have a high loading of conductive, active material to ensure densely connected electron conduction channels and a minimal binder content to facilitate the reactant-product inter-diffusion. In this way, the composite electrode can deliver a high reaction current density, at intrinsic reaction overpotential with respect to the electrocatalytic material.

7.1.2 The ORR on Heteroatom-doped Carbon Electrocatalysts

Heteroatom-doped carbon materials are believed to exert high electrocatalytic activity for the ORR when a particular electronic configuration is achieved. The N-doped carbons prepared at elevated temperatures have been excellent examples of the idea, although the origin of activity is still unclear because the N dopant can adopt

complex configurations and are usually formed with the help of transition metals. Current speculation is that the breaking of electro-neutrality at the carbon-dopant moiety may be the origin of the high activity in the N-doped carbons. The validation of such hypothesis requires the use of non-nitrogen dopants with less complex bonding configurations. For this reason, we have revisited the oxygen dopant as a more electronegative element (χ = 3.44) than nitrogen (χ = 3.04) (Chapter III) and systematically studied the halogen dopants as elements from the same group with decreasing electronegativity (Chapter IV). In addition, sulfur, as an unexpected dopant from using concentrated sulfuric acid was also investigated (Chapter IV).

Oxygen-modified carbons can provide a higher ORR activation potential as compare to unmodified carbons, but remain inferior to N-doped carbons and the reaction mechanism is a two-electron dominated pathway at low overpotential. Our study confirms that the electrocatalysis has to occur at the surface oxygen groups of an oxidized carbon nanotube and not the edge (sp^3) defects on the nanotube. For mildly oxidized carbons, the facilitated ORR occurs at the carbonyl and/or carboxyl groups, rather than at the hydroxyl groups. When the carbons are deeply oxidized via a modified Hummer's method, epoxide groups are introduced with different levels of carbonyl groups (and the carbon lattice is highly compromised). These epoxide groups are among the most active oxygen groups for the ORR only when in the absence of carbonyl groups and supported with conductive fillers, although it is a small +20 mV difference in the onset potential as compared to carbonyl group-rich carbons. In short, the oxygen groups in alternative bonding configurations displayed different ORR activation properties and none of them exhibited comparable activity to N-doped carbons. Clearly, a more electronegative dopant to nitrogen in a carbon lattice does not give rise the high activity.

Halogen group elements have a simple single bonding configuration and electronegativity which decreases with increasing period in the periodic table. Chlorine, bromine and iodine were selected as dopants to study the effect of reducing electronegativity contrast relative to carbon. We have demonstrated a solution-phase synthesis of halogen-doped RGO in both organic solvent and concentrated sulfuric acid, and confirmed the presence of C–X groups by XPS analysis. In general, our results suggest that Cl-doping does not enhance the ORR activity, whereas Br-doping and I-doping can provide substantial improvement in the reaction onset potential. This is interesting in that Cl is the most electronegative dopant in the system, but only those with lower electronegativity showed better activity. Again, the hypothesis of "breaking electro-neutrality at carbon-dopant moiety for better ORR activity" is not supported by the halogen-doped carbons.

Sulfur only has a small electronegativity difference relative to carbon ($\Delta\chi = 0.03$) and is in the same group as oxygen (although their chemical nature is very different). In our study with I-doped RGO, sulfur can be incorporated into the carbon material by substituting the carbon-bound iodide (C–I) through a complex redox reaction in concentrated sulfuric acid. The C–S configuration in the carbon was confirmed by XPS. In the tests that followed, the S-doped RGO exhibited very poor ORR activity even when compared to the original RGO. Certainly, sulfur, a weakly electronegative dopant, does not form the active site required for an efficient ORR.

Collectively, our experiments do not support the idea that electronegativity contrast is the sole origin of ORR activity in heteroatom-doped carbon materials. Rather, it appears more likely that the complex bonding/electronic configuration of the dopant is the true origin of the electrocatalytic activity, if the heteroatom-doped carbons are exclusively metal-free.

7.1.3 The ORR on Metal Oxide/Carbon Hybrid Electrocatalysts

The synergistic effect on metal oxide/carbon hybrid electrocatalysts describes an improved ORR activity when metal oxide nanocrystals are covalently attached to a carbon substrate. However, the origin of the synergistic effect is unclear − it could be a result of facilitated charge transport through the covalent connection or a more efficient active site at the covalent junction. Furthermore, the electrocatalytic role of each component of the hybrid (metal oxide, carbon substrate and the covalent interface) has not been clearly explained. To elucidate the origin of the synergistic effect, a hybrid system comprised of Mn_3O_4 nanocrystals and GONRs was carefully examined at the hybrid covalent interface (Chapter V-A). Using the same system, we separately studied and identified their functional roles of each component for the ORR (Chapter V-B). In the validation of the electrocatalytic hybrid interface, amorphous Mn–O nanoclusters were decorated at the surface of mildly oxidized carbon nanotubes to imitate an exposed hybrid interface, as the direct active site for the ORR (Chapter VI).

The covalent interface in the Mn_3O_4-GONR hybrid is responsible for a promoted ORR at the periphery of the attachment. Through detailed characterizations and various comparative experiments, the presence of C–O–Mn covalent junctions is evident in between the attached Mn_3O_4 nanocrystals and GONR. The nanocrystals grew upon consuming the epoxide groups on GONR (and thus a mild reduction had occurred) and remained connected to the GONR substrate after the growth through an oxygen bridge anchored to the octahedral Mn^{3+} site of the Mn_3O_4 nanocrystal. Since the majority of the interface is covered by the nanocrystals, any improved activity is attributed to the exposed peripheral sites. The DPV measurements showed that the Mn_3O_4-GONR hybrid promoted O_2 reduction to peroxide as compared to GONR, and

the activity for the subsequent peroxide reduction at the attached nanocrystals was similar to that of free-standing Mn_3O_4 nanocrystals. This means that the covalent C–O–Mn interface directly participates in the primary reduction of O_2, rather than assisting in the charge transport mechanism.

The second part focused on elucidating the role of the nanocrystals and carbon substrate in the hybrid for the ORR. We demonstrated that the GONR component in the hybrid facilitates the primary reduction of O_2, while the Mn_3O_4 nanocrystals facilitate the simultaneous electro-reduction of the peroxide intermediate rather than the possible alternative catalytic decomposition of peroxide. With the hybrid interface at the periphery, the primary O_2 reduction was further accelerated and therefore a higher reaction onset potential could be attained. In the activity evaluation, the hybrid composite exhibited superior ORR performance, at a level almost equivalent to the commercial Pt/C standard, and with good tolerance against methanol poisoning.

Further exploitation of the hybrid interface requires fully exposed C–O–Mn moieties at the surface of a conductive carbon support. For this purpose, we developed amorphous Mn–O nanoclusters on carbon nanotubes (Mn-OCNT) to imitate a hybrid interface, without the covering crystalline nanoparticles. The specific Mn–O binding and the physical presence of the nanoclusters were confirmed by the electrochemical experiments and high-resolution TEM. The chemical nature of the nanoclusters was elucidated by XPS and XAS characterizations; the covalent connections were in the forms of C–O–Mn^{2+} and C–O–Mn^{3+}. Our DPV experiments on the Mn-OCNT showed that the interface not only assisted in facilitating the primary O_2 reduction at the C–O(Mn) domain, but it also helped in the subsequent electro-reduction of the peroxide intermediate at the amorphous Mn–O(C) domains. The ORR activity of the Mn-OCNT also resembled that of the Mn_3O_4-GONR hybrid,

except for the slightly inferior peroxide reduction current due to the very low level of Mn–O nanoclusters. Nevertheless, it is clear that the hybrid interface is a direct active site for the generally promoted ORR.

In summary, the source of the commonly observed synergistic effect in metal oxide/carbon hybrid comes from the unique covalent interface between the nanocrystal and the carbon substrate and the cooperative electrocatalytic functions. Although the covalent interface facilitates the ORR by reducing the activation barrier for the stepwise reductions, the hindered exposure of the interface in conventional hybrid electrocatalysts greatly hinders their electrocatalytic output.

7.2 Future Prospects

There are still many challenges in developing low-cost, high-performance ORR electrocatalysts for fuel cells and metal-air batteries. Carbon-based materials, especially the heteroatom-doped carbons and metal oxide/carbon hybrids, have been considered potential candidates for replacing platinum-class materials. Unfortunately the poor structure of carbon composite electrodes and the lack of understanding of the activity origin in carbon-based materials and the reaction mechanism represent the two major obstacles retarding the electrocatalyst development. Solving these key problems is the most urgent task in the near future.

The first problem usually encountered in the exploitation of carbon-based electrocatalysts is the poor electrode structure of composite electrodes for the ORR occurring at complex phase boundaries. This could provide masked electrocatalytic activity of a material and thus result in misleading interpretations. In many cases, the problem of poor electron and ion transport has not been carefully considered in the preparation of a composite electrode. As such, further systematic studies should be

conducted on rational optimization of composite electrode structure to optimise the ORR kinetics.

While it is tempting to achieve high electrocatalytic activity by integrating all beneficial empirically-determined elements (e.g., N-doping and high-temperature treatment) into an electrocatalyst, grasping the knowledge of the activity origin is important for the rational design of advanced electrocatalysts. At present, there are still controversies regarding the origin of activity in heteroatom-doped carbons and metal oxide/carbon hybrids. For heteroatom-doped carbons, there is an underlying belief that the dopant can alter the chemical nature of a carbon framework in a way that is not unique to a particular doping element. The aspect of high electronegativity contrast at the carbon-dopant moiety for better ORR activity has been discouraged by the works presented in the thesis. More work needs to be done on clarifying the influence of trace metal impurities and the particular bonding configuration in N-doped carbons (i.e., the graphitic nitrogen); using other elements does not seem to help in clarifying the origin of the effect. For metal oxide/carbon hybrids, there appear to be numerous possibilities for chemical modification. With the basic understanding of the synergistic effect and its origin, different combinations of metal oxide and carbon substrate may be examined for the applicability of the theory, as well as for screening purposes. Other transition metal compounds (e.g., metal chalcogenides) may also be investigated in a hybrid configuration with carbon. All of this should shed some light on the development of highly effective ORR electrocatalysts.

In conclusion, there is a promising future for carbon-based electrocatalysts as they present versatile approaches for tailoring the physical, chemical and electronic properties of carbon materials. The increased understanding as a result of the studies described herein will hopefully be of benefit in helping fine-tune these properties for

optimal activity for the ORR. It is expected that these carbon-based materials will play a major role in massive energy storage and conversion systems in commercial markets.

References

1   Winter, M. & Brodd, R. J. What are batteries, fuel cells, and supercapacitors? *Chemical Reviews* **104**, 4245-4269, (2004).

2   Cheng, F. & Chen, J. Metal-air batteries: from oxygen reduction electrochemistry to cathode catalysts. *Chemical Society Reviews* **41**, 2172-2192, (2012).

3   Cairns, E. J. & Albertus, P. Batteries for electric and hybrid-electric vehicles. *Annual Review of Chemical and Biomolecular Engineering* **1**, 299-320, (2010).

4   Meinshausen, M. *et al.* Greenhouse-gas emission targets for limiting global warming to 2 degrees. *Nature* **458**, 1158-1162, (2009).

5   Boden, T. A., Marland, G. & Andres, R. J.   (ed U.S. Department of Energy) (Information Analysis Center, Oak Ridge National Laboratory, Oak Ridge, Tenn., U.S.A., 2010).

6   Zhang, J. & Song, C. in *PEM Fuel Cell Electrocatalysts and Catalyst Layers* 89-134 (Springer, 2008).

7   Debe, M. K. Electrocatalyst approaches and challenges for automotive fuel cells. *Nature* **486**, 43-51, (2012).

8   Li, Y. *et al.* Advanced zinc-air batteries based on high-performance hybrid electrocatalysts. *Nature Communication* **4**, 1805, (2013).

9   Girishkumar, G., McCloskey, B., Luntz, A. C., Swanson, S. & Wilcke, W. Lithium−Air battery: Promise and challenges. *The Journal of Physical Chemistry Letters* **1**, 2193-2203, (2010).

10   Lee, J.-S. *et al.* Metal–Air batteries with high energy density: Li–Air versus Zn–Air. *Advanced Energy Materials* **1**, 34-50, (2011).

11   Yang, L. *et al.* Boron-doped carbon nanotubes as metal-free electrocatalysts for the oxygen reduction reaction. *Angewandte Chemie International Edition* **50**, 7132-7135, (2011).

12   Chen, Z., Higgins, D., Tao, H., Hsu, R. S. & Chen, Z. Highly active nitrogen-doped carbon nanotubes for oxygen reduction reaction in fuel cell applications. *The Journal of Physical Chemistry C* **113**, 21008-21013, (2009).

13   Read, J. *et al.* Oxygen transport properties of organic electrolytes and performance of lithium/oxygen battery. *Journal of The Electrochemical Society* **150**, A1351-A1356, (2003).

14   Hoogers, G. in *Fuel Cell Technology Handbook   Handbook Series for Mechanical Engineering* (ed Gregor Hoogers)   (CRC Press, 2002).

15   Yang, L. *et al.* A mini review on carbon-based metal-free electrocatalysts for oxygen reduction reaction. *Chinese Journal of Catalysis* **34**, 1986-1991, (2013).

16   Wang, B. Recent development of non-platinum catalysts for oxygen reduction reaction. *Journal of Power Sources* **152**, 1-15, (2005).

17   Vasudevan, P., Santosh, S., Mann, N. & Tyagi, S. Transition metal complexes of porphyrins and phthalocyanines as electrocatalysts for dioxygen reduction. *Transition Metal Chemistry* **15**, 81-90, (1990).

18   Kiros, Y. Metal porphyrins for oxygen reduction in PEMFC. *International Journal of Electrochemical Science* **2**, 285-300, (2007).

19   Alonso-Vante, N., Tributsch, H. & Solorza-Feria, O. Kinetics studies of oxygen reduction in acid medium on novel semiconducting transition metal chalcogenides. *Electrochimica Acta* **40**, 567-576, (1995).

20   Collman, J. P. *et al.* Electrode catalysis of the four-electron reduction of oxygen to water by dicobalt face-to-face porphyrins. *Journal of the American Chemical Society* **102**, 6027-6036, (1980).

21   Wang, D.-W. & Su, D. Heterogeneous nanocarbon materials for oxygen reduction reaction. *Energy & Environmental Science* **7**, 576-591, (2014).

22   Daems, N., Sheng, X., Vankelecom, I. F. J. & Pescarmona, P. P. Metal-free doped carbon materials as electrocatalysts for the oxygen reduction reaction. *Journal of Materials Chemistry A* **2**, 4085-4110, (2014).

23   Sun, X. *et al.* A class of high performance metal-free oxygen reduction electrocatalysts based on cheap carbon blacks. *Scientific Report* **3**, 2505, (2013).

24   Zhu, Y. *et al.* Graphene and graphene oxide: Synthesis, properties, and applications. *Advanced Materials* **22**, 3906-3924, (2010).

25   Geim, A. K. & Novoselov, K. S. The rise of graphene. *Nature Materials* **6**, 183-191, (2007).

26   Castro Neto, A. H., Guinea, F., Peres, N. M. R., Novoselov, K. S. & Geim, A. K. The electronic properties of graphene. *Reviews of Modern Physics* **81**, 109-162, (2009).

27   Terrones, M. Science and technology of the twenty-first century: Synthesis, Properties, and Applications of Carbon Nanotubes. *Annual Review of Materials Research* **33**, 419-501, (2003).

28   Stoller, M. D., Park, S., Zhu, Y., An, J. & Ruoff, R. S. Graphene-based ultracapacitors. *Nano Letters* **8**, 3498-3502, (2008).

29   Gong, K. P., Du, F., Xia, Z. H., Durstock, M. & Dai, L. M. Nitrogen-doped carbon nanotube arrays with high electrocatalytic activity for oxygen reduction. *Science* **323**, 760-764, (2009).

30   Qu, L. T., Liu, Y., Baek, J. B. & Dai, L. M. Nitrogen-doped graphene as efficient metal-free electrocatalyst for oxygen reduction in fuel cells. *Acs Nano* **4**, 1321-1326, (2010).

31   Feng, Y. *et al.* Tuning the catalytic property of nitrogen-doped graphene for cathode oxygen reduction reaction. *Physical Review B* **85**, 155454, (2012).

32   Wang, H., Maiyalagan, T. & Wang, X. Review on recent progress in nitrogen-doped graphene: synthesis, characterization, and its potential applications. *ACS Catalysis* **2**, 781-794, (2012).

33   Bezerra, C. W. B. *et al.* A Review of Fe-N/C And Co-N/C Catalysts For The Oxygen Reduction Reaction. *Electrochimica Acta* **53**, 4937-4951, (2008).

34   Wu, G., More, K. L., Johnston, C. M. & Zelenay, P. High-performance electrocatalysts for oxygen reduction derived from polyaniline, iron, and cobalt. *Science* **332**, 443-447, (2011).

35   Liu, Z.-W. *et al.* Phosphorus-doped graphite layers with high electrocatalytic activity for the O$_2$ reduction in an alkaline medium. *Angewandte Chemie International Edition* **50**, 3257-3261, (2011).

36   Maruyama, J., Fukui, N., Kawaguchi, M. & Abe, I. Use of purine and pyrimidine bases as nitrogen sources of active site in oxygen reduction catalyst. *Journal of Power Sources* **194**, 655-661, (2009).

37   Hu, C. *et al.* One-step preparation of nitrogen-doped graphene quantum dots from oxidized debris of graphene oxide. *Journal of Materials Chemistry B* **1**, 39-42, (2013).

38   Liu, R. L., Wu, D. Q., Feng, X. L. & Mullen, K. Nitrogen-doped ordered mesoporous graphitic arrays with high electrocatalytic activity for oxygen reduction. *Angewandte Chemie-International Edition* **49**, 2565-2569, (2010).

39   Ma, G. *et al.* Nitrogen-doped hollow carbon nanoparticles with excellent oxygen reduction performances and their electrocatalytic kinetics. *The Journal of Physical Chemistry C* **115**, 25148-25154, (2011).

40   Wu, G. *et al.* Nitrogen-doped graphene-rich catalysts derived from heteroatom polymers for oxygen-reduction in nonaqueous lithium-O$_2$ battery cathodes. *Acs Nano* **6**, 9764-9776, (2012).

41   Sun, L. *et al.* Nitrogen-doped graphene with high nitrogen level via a one-step hydrothermal reaction of graphene oxide with urea for superior capacitive energy storage. *RSC Advances* **2**, 4498-4506, (2012).

42   Yang, Z. *et al.* Sulfur-doped graphene as an efficient metal-free cathode catalyst for oxygen reduction. *Acs Nano* **6**, 205-211, (2012).

43   Vasudevan, D. & Wendt, H. Electroreduction of oxygen in aprotic media. *Journal of Electroanalytical Chemistry* **392**, 69-74, (1995).

44   Shao, Y., Sui, J., Yin, G. & Gao, Y. Nitrogen-doped carbon nanostructures and their composites as catalytic materials for proton exchange membrane fuel cell. *Applied Catalysis B: Environmental* **79**, 89-99, (2008).

45   Kruusenberg, I., Leis, J., Arulepp, M. & Tammeveski, K. Oxygen reduction on carbon nanomaterial-modified glassy carbon electrodes in alkaline solution.

Journal of Solid State Electrochemistry **14**, 1269-1277, (2010).

46   Chen, Z., Higgins, D. & Chen, Z. W. Electrocatalytic activity of nitrogen doped carbon nanotubes with different morphologies for oxygen reduction reaction. *Electrochimica Acta* **55**, 4799-4804, (2010).

47   Schmidt, T. J., Paulus, U. A., Gasteiger, H. A. & Behm, R. J. The oxygen reduction reaction on a Pt/carbon fuel cell catalyst in the presence of chloride anions. *Journal of Electroanalytical Chemistry* **508**, 41-47, (2001).

48   Padbury, R. & Zhang, X. Lithium-oxygen batteries: Limiting factors that affect performance. *Journal of Power Sources* **196**, 4436-4444, (2011).

49   Peng, Y. & Liu, H. Effects of oxidation by hydrogen peroxide on the structures of multiwalled carbon nanotubes. *Industrial & Engineering Chemistry Research* **45**, 6483-6488, (2006).

50   Ramaswamy, N., Hakim, N. & Mukerjee, S. Degradation mechanism study of perfluorinated proton exchange membrane under fuel cell operating conditions. *Electrochimica Acta* **53**, 3279-3295, (2008).

51   Inaba, M. *et al.* Impacts of air bleeding on membrane degradation in polymer electrolyte fuel cells. *Journal of Power Sources* **178**, 699-705, (2008).

52   Yu, L., Pan, X., Cao, X., Hu, P. & Bao, X. Oxygen reduction reaction mechanism on nitrogen-doped graphene: A density functional theory study. *Journal of Catalysis* **282**, 183-190, (2011).

53   Yeager, E. Electrocatalysts for O_2 reduction. *Electrochimica Acta* **29**, 1527-1537, (1984).

54   Nørskov, J. K. *et al.* Origin of the overpotential for oxygen reduction at a fuel-cell cathode. *The Journal of Physical Chemistry B* **108**, 17886-17892, (2004).

55   Wroblowa, H. S., Yen Chi, P. & Razumney, G. Electroreduction of oxygen: A new mechanistic criterion. *Journal of Electroanalytical Chemistry and Interfacial Electrochemistry* **69**, 195-201, (1976).

56   Olson, T. S., Pylypenko, S., Fulghum, J. E. & Atanassov, P. Bifunctional oxygen reduction reaction mechanism on non-platinum catalysts derived from pyrolyzed porphyrins. *Journal of The Electrochemical Society* **157**, B54-B63, (2010).

57   Hasan, M. A., Zaki, M. I., Pasupulety, L. & Kumari, K. Promotion of the hydrogen peroxide decomposition activity of manganese oxide catalysts. *Applied Catalysis A: General* **181**, 171-179, (1999).

58   Lin, S.-S. & Gurol, M. D. Catalytic decomposition of hydrogen peroxide on iron oxide: Kinetics, mechanism, and implications. *Environmental Science & Technology* **32**, 1417-1423, (1998).

59   Mezour, M. A., Cornut, R., Hussien, E. M., Morin, M. & Mauzeroll, J. Detection of hydrogen peroxide produced during the oxygen reduction reaction at self-assembled thiol−porphyrin monolayers on gold using SECM and nanoelectrodes. *Langmuir* **26**, 13000-13006, (2010).

60   Jaouen, F. O_2 reduction mechanism on non-noble metal catalysts for PEM fuel cells. Part II: A porous-electrode model to predict the quantity of H_2O_2 detected by rotating ring-disk electrode. *The Journal of Physical Chemistry C* **113**, 15433-15443, (2009).

61   Jaouen, F. & Dodelet, J.-P. O2 reduction mechanism on non-noble metal catalysts for PEM fuel cells. Part I: Experimental rates of O_2 electroreduction, H_2O_2 electroreduction, and H_2O_2 disproportionation. *The Journal of Physical Chemistry C* **113**, 15422-15432, (2009).

62   Bard, A. J. & Faulkner, L. R. *Electrochemical methods: Fundamentals and applications, 2nd Edition*. 2nd edn,   (Wiley, 2000).

63   Schneider, A. *et al.* Transport effects in the oxygen reduction reaction on nanostructured, planar glassy carbon supported Pt/GC model electrodes. *Physical Chemistry Chemical Physics* **10**, 1931-1943, (2008).

64   Strelko, V. V., Kuts, V. S. & Thrower, P. A. On the mechanism of possible influence of heteroatoms of nitrogen, boron and phosphorus in a carbon matrix on the catalytic activity of carbons in electron transfer reactions. *Carbon* **38**, 1499-1503, (2000).

65   Strelko, V. V. *et al.* Mechanism of reductive oxygen adsorption on active carbons with various surface chemistry. *Surface Science* **548**, 281-290, (2004).

66   Li, R. *et al.* Insights into the adsorption of oxygen and water on low-index Pt surfaces by molecular dynamics simulations. *New Journal of Chemistry* **38**, 683-692, (2014).

67   Dai, J. & Yuan, J. Adsorption of molecular oxygen on doped graphene: Atomic, electronic, and magnetic properties. *Physical Review B* **81**, 165414, (2010).

68   Hu, X., Wu, Y., Li, H. & Zhang, Z. Adsorption and activation of O_2 on nitrogen-doped carbon nanotubes. *The Journal of Physical Chemistry C* **114**, 9603-9607, (2010).

69   Mustain, W. E. & Prakash, J. Kinetics and mechanism for the oxygen reduction reaction on polycrystalline cobalt–palladium electrocatalysts in acid media. *Journal of Power Sources* **170**, 28-37, (2007).

70   Duan, Z. & Wang, G. A first principles study of oxygen reduction reaction on a Pt(111) surface modified by a subsurface transition metal M (M = Ni, Co, or Fe). *Physical Chemistry Chemical Physics* **13**, 20178-20187, (2011).

71   Wang, G., Ramesh, N., Hsu, A., Chu, D. & Chen, R. Density functional theory

study of the adsorption of oxygen molecule on iron phthalocyanine and cobalt phthalocyanine. *Molecular Simulation* **34**, 1051-1056, (2008).

72   Tielens, F., Andrés, J., Van Brussel, M., Buess-Hermann, C. & Geerlings, P. DFT study of oxygen adsorption on modified nanostructured gold pyramids. *The Journal of Physical Chemistry B* **109**, 7624-7630, (2005).

73   Radovic, L. R. in *Carbons for Electrochemical Energy Storage and Conversion Systems*   (eds François Béguin & Elzbieta Frackowiak) Ch. 5, 203-210 (2010).

74   Radovic, L. R., Suarez, A., Vallejos-Burgos, F. & Sofo, J. O. Oxygen migration on the graphene surface. 2. Thermochemistry of basal-plane diffusion (hopping). *Carbon* **49**, 4226-4238, (2011).

75   Yeager, E. Dioxygen electrocatalysis: mechanisms in relation to catalyst structure. *Journal of Molecular Catalysis* **38**, 5-25, (1986).

76   Garten, V. & Weiss, D. The quinone-hydroquinone character of activated carbon and carbon black. *Australian Journal of Chemistry* **8**, 68-95, (1955).

77   Okamoto, Y. First-principles molecular dynamics simulation of O_2 reduction on nitrogen-doped carbon. *Applied Surface Science* **256**, 335-341, (2009).

78   Kim, H., Lee, K., Woo, S. I. & Jung, Y. On the mechanism of enhanced oxygen reduction reaction in nitrogen-doped graphene nanoribbons. *Physical Chemistry Chemical Physics* **13**, 17505-17510, (2011).

79   Wang, S., Yu, D., Dai, L., Chang, D. W. & Baek, J.-B. Polyelectrolyte-functionalized graphene as metal-free electrocatalysts for oxygen reduction. *Acs Nano* **5**, 6202-6209, (2011).

80   Radovic, L. R. in *Carbons for Electrochemical Energy Storage and Conversion Systems*   (eds François Béguin & Elzbieta Frackowiak) Ch. 5, 163-219 (CRC Press, 2010).

81   Batchelor-McAuley, C. & Compton, R. G. Thin-film modified rotating disk electrodes: Models of electron-transfer kinetics for passive and electroactive films. *The Journal of Physical Chemistry C* **118**, 30034-30038, (2014).

82   Hepburn, W. G. *et al.* Diffusional transport to and through thin-layer nanoparticle film modified electrodes: capped CdSe nanoparticle modified electrodes. *Physical Chemistry Chemical Physics* **16**, 18034-18041, (2014).

83   Cha, Q. in *Introduction to Kinetics of Electrode Processes*   (ed Quanxing Cha) Ch. 9, (Science Press, 2002).

84   Lawson, D. R., Whiteley, L. D., Martin, C. R., Szentirmay, M. N. & Song, J. I. Oxygen reduction at Nafion film-coated platinum electrodes: Transport and kinetics. *Journal of The Electrochemical Society* **135**, 2247-2253, (1988).

85   Wu, K.-H., Wang, D.-W. & Gentle, I. R. The value of mixed conduction for

oxygen electroreduction on graphene–chitosan composites. *Carbon* **73**, 234-243, (2014).

86   Zhao, Q., Majsztrik, P. & Benziger, J. Diffusion and interfacial transport of water in Nafion. *The Journal of Physical Chemistry B* **115**, 2717-2727, (2011).

87   Trasatti, S. & Petrii, O. A. Real surface area measurements in electrochemistry. *Journal of Electroanalytical Chemistry* **327**, 353-376, (1992).

88   Lu, Y.-C., Gasteiger, H. A. & Shao-Horn, Y. Method development to evaluate the oxygen reduction activity of high-surface-area catalysts for Li-Air batteries. *Electrochemical and Solid-State Letters* **14**, A70-A74, (2011).

89   Mayrhofer, K. J. J. *et al.* Measurement of oxygen reduction activities via the rotating disc electrode method: From Pt model surfaces to carbon-supported high surface area catalysts. *Electrochimica Acta* **53**, 3181-3188, (2008).

90   Nicholson, R. S. Theory and application of cyclic voltammetry for measurement of electrode reaction kinetics. *Analytical Chemistry* **37**, 1351-1355, (1965).

91   Suntivich, J., Gasteiger, H. A., Yabuuchi, N. & Shao-Horn, Y. Electrocatalytic measurement methodology of oxide catalysts using a thin-film rotating disk electrode. *Journal of The Electrochemical Society* **157**, B1263-B1268, (2010).

92   Du, C., Tan, Q., Yin, G. & Zhang, J. in *Rotating Electrode Methods and Oxygen Reduction Electrocatalysts* (eds Jiujun Zhang, Wei Xing, & Geping Yin) 171-198 (Elsevier, 2014).

93   Jia, Z., Yin, G. & Zhang, J. in *Rotating Electrode Methods and Oxygen Reduction Electrocatalysts* (eds Jiujun Zhang, Geping Yin, & Wei Xing) 199-229 (Elsevier, 2014).

94   Collman, J. P. & Decreau, R. A. Functional biomimetic models for the active site in the respiratory enzyme cytochrome c oxidase. *Chemical Communications*, 5065-5076, (2008).

95   Liang, Y. *et al.* Co3O4 nanocrystals on graphene as a synergistic catalyst for oxygen reduction reaction. *Nature Materials* **10**, 780-786, (2011).

96   Fletcher, S. Tafel slopes from first principles. *Journal of Solid State Electrochemistry* **13**, 537-549, (2009).

97   Kear, G. & Walsh, F. C. The characteristics of a true Tafel slope. *Corrosion and Materials* **30**, 51-55, (2005).

98   Voet, D. & Voet, J. G. in *Biochemistry, 4th Edition* Ch. 22, 841-846 (Wiley, 2011).

99   Kjaergaard, C. H., Rossmeisl, J. & Nørskov, J. K. Enzymatic versus inorganic oxygen reduction catalysts: comparison of the energy levels in a free-energy scheme. *Inorganic Chemistry* **49**, 3567-3572, (2010).

100   Vu, C., Han, K. N. & Lawson, F. Leaching behaviour of cobaltous and

cobalto-cobaltic oxides in ammonia and in acid solutions. *Hydrometallurgy* **6**, 75-87, (1980).

101   Momade, F. W. Y. & Momade, Z. G. A study of the kinetics of reductive leaching of manganese oxide ore in aqueous methanol–sulphuric acid medium. *Hydrometallurgy* **54**, 25-39, (1999).

102   Hubli, R. C., Mittra, J. & Suri, A. K. Reduction-dissolution of cobalt oxide in acid media: a kinetic study. *Hydrometallurgy* **44**, 125-134, (1997).

103   Collman, J. P. Functional analogs of Heme protein active sites†. *Inorganic Chemistry* **36**, 5145-5155, (1997).

104   Morozan, A., Campidelli, S., Filoramo, A., Jousselme, B. & Palacin, S. Catalytic activity of cobalt and iron phthalocyanines or porphyrins supported on different carbon nanotubes towards oxygen reduction reaction. *Carbon* **49**, 4839-4847, (2011).

105   Cheng, N., Kemna, C., Goubert-Renaudin, S. & Wieckowski, A. Reduction reaction by porphyrin-based catalysts for fuel cells. *Electrocatalysis*, 1-14, (2012).

106   Choi, J.-Y., Hsu, R. S. & Chen, Z. Highly active porous carbon-supported nonprecious metal−N electrocatalyst for oxygen reduction reaction in PEM fuel cells. *The Journal of Physical Chemistry C* **114**, 8048-8053, (2010).

107   Zheng, Y. *et al.* Nanoporous graphitic-C_3N_4@Carbon metal-free electrocatalysts for highly efficient oxygen reduction. *Journal of the American Chemical Society*, (2011).

108   Wu, Z.-S. *et al.* 3D nitrogen-doped graphene aerogel-supported Fe_3O_4 nanoparticles as efficient electrocatalysts for the oxygen reduction reaction. *Journal of the American Chemical Society* **134**, 9082-9085, (2012).

109   Choi, B. G., Yang, M., Hong, W. H., Choi, J. W. & Huh, Y. S. 3D macroporous graphene frameworks for supercapacitors with high energy and power densities. *Acs Nano* **6**, 4020-4028, (2012).

110   Eda, G., Fanchini, G. & Chhowalla, M. Large-area ultrathin films of reduced graphene oxide as a transparent and flexible electronic material. *Nature Nanotechnology* **3**, 270-274, (2008).

111   Tao, Y., Endo, M., Inagaki, M. & Kaneko, K. Recent progress in the synthesis and applications of nanoporous carbon films. *Journal of Materials Chemistry* **21**, 313-323, (2011).

112   Zheng, Y. *et al.* Nanoporous graphitic-C3N4@Carbon metal-free electrocatalysts for highly efficient oxygen reduction. *Journal of the American Chemical Society* **133**, 20116-20119, (2011).

113   Liang, J. *et al.* Facile oxygen reduction on a three-dimensionally ordered

macroporous graphitic C_3N_4/Carbon composite electrocatalyst. *Angewandte Chemie International Edition* **51**, 3892-3896, (2012).

114   Jiang, Z., Jiang, Z.-j., Tian, X. & Chen, W. Amine-functionalized holey graphene as a highly active metal-free catalyst for the oxygen reduction reaction. *Journal of Materials Chemistry A* **2**, 441-450, (2014).

115   Lai, L. *et al.* Exploration of the active center structure of nitrogen-doped graphene-based catalysts for oxygen reduction reaction. *Energy & Environmental Science* **5**, 7936-7942, (2012).

116   Biddinger, E. J., von Deak, D. & Ozkan, U. S. Nitrogen-containing carbon nanostructures as oxygen-reduction catalysts. *Topics in Catalysis* **52**, 1566-1574, (2009).

117   Yu, D., Xue, Y. & Dai, L. Vertically aligned carbon nanotube arrays Co-doped with phosphorus and nitrogen as efficient metal-free electrocatalysts for oxygen reduction. *The Journal of Physical Chemistry Letters* **3**, 2863-2870, (2012).

118   Zhang, C., Hao, R., Yin, H., Liu, F. & Hou, Y. Iron phthalocyanine and nitrogen-doped graphene composite as novel non-precious catalyst for oxygen reduction reaction. *Nanoscale* **4**, 7326-7329, (2012).

119   Chen, S. *et al.* Nitrogen-doped carbon nanocages as efficient metal-free electrocatalysts for oxygen reduction reaction. *Advanced Materials* **24**, 5593-5597, (2012).

120   Yang, W., Fellinger, T.-P. & Antonietti, M. Efficient metal-free oxygen reduction in alkaline medium on high-surface-area mesoporous nitrogen-doped carbons made from ionic liquids and nucleobases. *Journal of the American Chemical Society* **133**, 206-209, (2010).

121   Geng, D. *et al.* High oxygen-reduction activity and durability of nitrogen-doped graphene. *Energy & Environmental Science* **4**, 760-764, (2011).

122   Masa, J. *et al.* Trace metal residues promote the activity of supposedly metal-free nitrogen-modified carbon catalysts for the oxygen reduction reaction. *Electrochemistry Communications* **34**, 113-116, (2013).

123   Wang, D.-W. *et al.* The examination of graphene oxide for rechargeable lithium storage as a novel cathode material. *Journal of Materials Chemistry A* **1**, 3607-3612, (2013).

124   Scherson, D. A. *et al.* Cobalt tetramethoxyphenyl porphyrin—emission Mossbauer spectroscopy and O2 reduction electrochemical studies. *Electrochimica Acta* **28**, 1205-1209, (1983).

125   Maldonado-Hódar, F. J., Moreno-Castilla, C., Rivera-Utrilla, J., Hanzawa, Y. & Yamada, Y. Catalytic graphitization of carbon aerogels by transition metals. *Langmuir* **16**, 4367-4373, (2000).

126 Lefèvre, M., Dodelet, J. P. & Bertrand, P. Molecular oxygen reduction in PEM fuel cells: Evidence for the simultaneous presence of two active sites in Fe-based catalysts. *The Journal of Physical Chemistry B* **106**, 8705-8713, (2002).

127 Cao, R. *et al.* Promotion of oxygen reduction by a bio-inspired tethered iron phthalocyanine carbon nanotube-based catalyst. *Nature Communication* **4**, 2076, (2013).

128 van Wingerden, B., van Veen, J. A. R. & Mensch, C. T. J. An extended X-ray absorption fine structure study of heat-treated cobalt porphyrin catalysts supported on active carbon. *Journal of the Chemical Society, Faraday Transactions 1: Physical Chemistry in Condensed Phases* **84**, 65-74, (1988).

129 Matter, P. H., Zhang, L. & Ozkan, U. S. The role of nanostructure in nitrogen-containing carbon catalysts for the oxygen reduction reaction. *Journal of Catalysis* **239**, 83-96, (2006).

130 Sidik, R. A., Anderson, A. B., Subramanian, N. P., Kumaraguru, S. P. & Popov, B. N. O_2 reduction on graphite and nitrogen-doped graphite: Experiment and theory. *The Journal of Physical Chemistry B* **110**, 1787-1793, (2006).

131 Jaouen, F. d. r. *et al.* Cross-laboratory experimental study of non-noble-metal electrocatalysts for the oxygen reduction reaction. *ACS Applied Materials & Interfaces* **1**, 1623-1639, (2009).

132 Luo, Z. *et al.* Pyridinic N doped graphene: synthesis, electronic structure, and electrocatalytic property. *Journal of Materials Chemistry* **21**, 8038-8044, (2011).

133 Iwazaki, T., Obinata, R., Sugimoto, W. & Takasu, Y. High oxygen-reduction activity of silk-derived activated carbon. *Electrochemistry Communications* **11**, 376-378, (2009).

134 Sharifi, T., Hu, G., Jia, X. & Wågberg, T. Formation of active sites for oxygen reduction reactions by transformation of nitrogen functionalities in nitrogen-doped carbon nanotubes. *Acs Nano* **6**, 8904-8912, (2012).

135 Kundu, S. *et al.* Electrocatalytic activity and stability of nitrogen-containing carbon nanotubes in the oxygen reduction reaction. *Journal of Physical Chemistry C* **113**, 14302-14310, (2009).

136 Zheng, B., Wang, J., Wang, F.-B. & Xia, X.-H. Synthesis of nitrogen doped graphene with high electrocatalytic activity toward oxygen reduction reaction. *Electrochemistry Communications* **28**, 24-26, (2013).

137 Paliteiro, C., Hamnett, A. & Goodenough, J. B. The electroreduction of oxygen on pyrolytic graphite. *Journal of Electroanalytical Chemistry and Interfacial Electrochemistry* **233**, 147-159, (1987).

138 Wang, S. *et al.* Oxygen-enriched carbon material for catalyzing oxygen reduction towards hybrid electrolyte Li-air battery. *Journal of Materials Chemistry* **22**, 21051-21056, (2012).

139 Dreyer, D. R., Park, S., Bielawski, C. W. & Ruoff, R. S. The chemistry of graphene oxide. *Chemical Society Reviews* **39**, 228-240, (2010).

140 Wang, D.-W., Du, A., Taran, E., Lu, G. Q. & Gentle, I. R. A water-dielectric capacitor using hydrated graphene oxide film. *Journal of Materials Chemistry* **22**, 21085-21091, (2012).

141 Yang, D.-S., Bhattacharjya, D., Inamdar, S., Park, J. & Yu, J.-S. Phosphorus-doped ordered mesoporous carbons with different lengths as efficient metal-free electrocatalysts for oxygen reduction reaction in alkaline media. *Journal of the American Chemical Society* **134**, 16127-16130, (2012).

142 Zhang, C., Mahmood, N., Yin, H., Liu, F. & Hou, Y. Synthesis of phosphorus-doped graphene and its multifunctional applications for oxygen reduction reaction and lithium ion batteries. *Advanced Materials* **25**, 4932-4937, (2013).

143 Li, R., Wei, Z., Gou, X. & Xu, W. Phosphorus-doped graphene nanosheets as efficient metal-free oxygen reduction electrocatalysts. *RSC Advances* **3**, 9978-9984, (2013).

144 Yang, Z. *et al.* Sulfur-doped graphene as an efficient metal-free cathode catalyst for oxygen reduction. *Acs Nano* **6**, 205-211, (2012).

145 Park, J.-e. *et al.* Sulfur-doped graphene as a potential alternative metal-free electrocatalyst and Pt-catalyst supporting material for oxygen reduction reaction. *Physical Chemistry Chemical Physics* **16**, 103-109, (2014).

146 Wang, H., Bo, X., Zhang, Y. & Guo, L. Sulfur-doped ordered mesoporous carbon with high electrocatalytic activity for oxygen reduction. *Electrochimica Acta* **108**, 404-411, (2013).

147 Seredych, M., Idrobo, J.-C. & Bandosz, T. J. Effect of confined space reduction of graphite oxide followed by sulfur doping on oxygen reduction reaction in neutral electrolyte. *Journal of Materials Chemistry A* **1**, 7059-7067, (2013).

148 Karlický, F., Kumara Ramanatha Datta, K., Otyepka, M. & Zbořil, R. Halogenated graphenes: Rapidly growing family of graphene derivatives. *Acs Nano* **7**, 6434-6464, (2013).

149 Poh, H. L., Šimek, P., Sofer, Z. & Pumera, M. Halogenation of graphene with chlorine, bromine, or iodine by exfoliation in a halogen atmosphere. *Chemistry – A European Journal* **19**, 2655-2662, (2013).

150 Simek, P. *et al.* Towards graphene iodide: iodination of graphite oxide. *Nanoscale* **7**, 261-270, (2015).

151 Jeon, I.-Y. *et al.* Facile, scalable synthesis of edge-halogenated graphene nanoplatelets as efficient metal-free eletrocatalysts for oxygen reduction reaction. *Scientific Report* **3**, 1810, (2013).

152 Yao, Z. *et al.* Catalyst-free synthesis of iodine-doped graphene via a facile thermal annealing process and its use for electrocatalytic oxygen reduction in an alkaline medium. *Chemical Communications* **48**, 1027-1029, (2012).

153 Sheng, Z.-H., Gao, H.-L., Bao, W.-J., Wang, F.-B. & Xia, X.-H. Synthesis of boron doped graphene for oxygen reduction reaction in fuel cells. *Journal of Materials Chemistry* **22**, 390-395, (2012).

154 Yano, T., Tryk, D. A., Hashimoto, K. & Fujishima, A. Electrochemical behavior of highly conductive boron-doped diamond electrodes for oxygen reduction in alkaline solution. *Journal of The Electrochemical Society* **145**, 1870-1876, (1998).

155 Wang, S. *et al.* Vertically aligned BCN nanotubes as efficient metal-free electrocatalysts for the oxygen reduction reaction: A synergetic effect by Co-doping with boron and nitrogen. *Angewandte Chemie International Edition* **50**, 11756-11760, (2011).

156 Liang, Y. *et al.* Covalent hybrid of spinel manganese–cobalt oxide and graphene as advanced oxygen reduction electrocatalysts. *Journal of the American Chemical Society* **134**, 3517-3523, (2012).

157 Feng, J. *et al.* Engineering manganese oxide/nanocarbon hybrid materials for oxygen reduction electrocatalysis. *Nano Research* **5**, 718-725, (2012).

158 Ge, X. *et al.* Dual-phase spinel $MnCo_2O_4$ and spinel $MnCo_2O_4$/Nanocarbon hybrids for electrocatalytic oxygen reduction and evolution. *ACS Applied Materials & Interfaces* **6**, 12684-12691, (2014).

159 Wang, J., Zhou, J., Hu, Y. & Regier, T. Chemical interaction and imaging of single Co_3O_4/graphene sheets studied by scanning transmission X-ray microscopy and X-ray absorption spectroscopy. *Energy & Environmental Science* **6**, 926-934, (2013).

160 Gewirth, A. A. & Thorum, M. S. Electroreduction of dioxygen for fuel-cell applications: materials and challenges. *Inorganic Chemistry* **49**, 3557-3566, (2010).

161 Adler, S. B. Factors governing oxygen reduction in solid oxide fuel cell cathodes. *Chemical Reviews* **104**, 4791-4844, (2004).

162 Aricò, A. S., Antonucci, V., Alderucci, V., Modica, E. & Giordano, N. A.c.-impedance spectroscopy study of oxygen reduction at Nafion® coated gas-diffusion electrodes in sulphuric acid: Teflon loading and methanol cross-over effects. *Journal of Applied Electrochemistry* **23**, 1107-1116, (1993).

163   Deng, D. H. *et al.* Size effect of graphene on electrocatalytic activation of oxygen. *Chemical Communications* **47**, 10016-10018, (2011).

164   Sheng, Z. H. *et al.* Catalyst-free synthesis of nitrogen-doped graphene via thermal annealing graphite oxide with melamine and its excellent electrocatalysis. *Acs Nano* **5**, 4350-4358, (2011).

165   Lai, L. F. *et al.* Exploration of the active center structure of nitrogen-doped graphene-based catalysts for oxygen reduction reaction. *Energy & Environmental Science* **5**, 7936-7942, (2012).

166   Zheng, Y., Jiao, Y., Ge, L., Jaroniec, M. & Qiao, S. Z. Two-step boron and nitrogen doping in graphene for enhanced synergistic catalysis. *Angewandte Chemie-International Edition* **52**, 3110-3116, (2013).

167   Xu, J. X., Dong, G. F., Jin, C. H., Huang, M. H. & Guan, L. H. Sulfur and nitrogen co-doped, few-layered graphene oxide as a highly efficient electrocatalyst for the oxygen-reduction reaction. *ChemSusChem* **6**, 493-499, (2013).

168   Yang, Z. *et al.* Sulfur-doped graphene as an efficient metal-free cathode catalyst for oxygen reduction. *Acs Nano* **6**, 205-211, (2012).

169   Liang, Y. Y. *et al.* Co3O4 nanocrystals on graphene as a synergistic catalyst for oxygen reduction reaction. *Nature Materials* **10**, 780-786, (2011).

170   Wan, Y., Creber, K. A. M., Peppley, B. & Bui, V. T. Ionic conductivity of chitosan membranes. *Polymer* **44**, 1057-1065, (2003).

171   Ozarkar, S., Jassal, M. & Agrawal, A. Improved dispersion of carbon nanotubes in chitosan. *Fibers and Polymers* **9**, 410-415, (2008).

172   Yang, D. *et al.* Chemical analysis of graphene oxide films after heat and chemical treatments by X-ray photoelectron and micro-Raman spectroscopy. *Carbon* **47**, 145-152, (2009).

173   Ferrari, A. C. *et al.* Raman spectrum of graphene and graphene layers. *Physical Review Letters* **97**, 187401, (2006).

174   Kudin, K. N. *et al.* Raman spectra of graphite oxide and functionalized graphene sheets. *Nano Letters* **8**, 36-41, (2007).

175   Ferrari, A. C. Raman spectroscopy of graphene and graphite: Disorder, electron–phonon coupling, doping and nonadiabatic effects. *Solid State Communications* **143**, 47-57, (2007).

176   Lawrie, G. *et al.* Interactions between Alginate and Chitosan Biopolymers Characterized Using FTIR and XPS. *Biomacromolecules* **8**, 2533-2541, (2007).

177   Kinoshita, K. *Carbon: electrochemical and physicochemical properties*. (1988).

178   Menshykau, D. & Compton, R. G. Influence of electrode roughness on stripping

voltammetry: Mathematical modeling and numerical simulation. *The Journal of Physical Chemistry C* **113**, 15602-15620, (2009).

179   Nugent, J. M., Santhanam, K. S. V., Rubio, A. & Ajayan, P. M. Fast electron transfer kinetics on multiwalled carbon nanotube microbundle electrodes. *Nano Letters* **1**, 87-91, (2001).

180   Miyasaka, K. *et al.* Electrical conductivity of carbon-polymer composites as a function of carbon content. *Journal of Materials Science* **17**, 1610-1616, (1982).

181   Vargas-Bernal, R., Herrera-Pérez, G., Calixto-Olalde, M. E. & Tecpoyotl-Torres, M. Analysis of DC electrical conductivity models of carbon nanotube-polymer composites with potential application to nanometric electronic devices. *Journal of Electrical and Computer Engineering* **2013**, 179538, (2013).

182   Lefèvre, M., Proietti, E., Jaouen, F. & Dodelet, J.-P. Iron-based catalysts with improved oxygen reduction activity in polymer electrolyte fuel cells. *Science* **324**, 71-74, (2009).

183   Stankovich, S. *et al.* Synthesis of graphene-based nanosheets via chemical reduction of exfoliated graphite oxide. *Carbon* **45**, 1558-1565, (2007).

184   Pantea, D., Darmstadt, H., Kaliaguine, S., Sümmchen, L. & Roy, C. Electrical conductivity of thermal carbon blacks: Influence of surface chemistry. *Carbon* **39**, 1147-1158, (2001).

185   Yang, S., Feng, X., Wang, X. & Müllen, K. Graphene-based carbon nitride nanosheets as efficient metal-free electrocatalysts for oxygen reduction reactions. *Angewandte Chemie International Edition* **50**, 5339-5343, (2011).

186   Sarapuu, A., Helstein, K., Vaik, K., Schiffrin, D. J. & Tammeveski, K. Electrocatalysis of oxygen reduction by quinones adsorbed on highly oriented pyrolytic graphite electrodes. *Electrochimica Acta* **55**, 6376-6382, (2010).

187   Kosynkin, D. V. *et al.* Longitudinal unzipping of carbon nanotubes to form graphene nanoribbons. *Nature* **458**, 872-876, (2009).

188   Gerber, I. *et al.* Theoretical and experimental studies on the carbon-nanotube surface oxidation by nitric acid: Interplay between functionalization and vacancy enlargement. *Chemistry – A European Journal* **17**, 11467-11477, (2011).

189   Acik, M. *et al.* The role of intercalated water in multilayered graphene oxide. *Acs Nano* **4**, 5861-5868, (2010).

190   Li, H., Yang, C. & Liu, F. Novel method for determining stacking disorder degree in hexagonal graphite by X-ray diffraction. *Science in China Series B: Chemistry* **52**, 174-180, (2009).

191   Venezuela, P., Lazzeri, M. & Mauri, F. Theory of double-resonant Raman spectra in graphene: Intensity and line shape of defect-induced and two-phonon

bands. *Physical Review B* **84**, 035433, (2011).

192   López, G. P., Castner, D. G. & Ratner, B. D. XPS O 1s binding energies for polymers containing hydroxyl, ether, ketone and ester groups. *Surface and Interface Analysis* **17**, 267-272, (1991).

193   Rosenthal, D., Ruta, M., Schlögl, R. & Kiwi-Minsker, L. Combined XPS and TPD study of oxygen-functionalized carbon nanofibers grown on sintered metal fibers. *Carbon* **48**, 1835-1843, (2010).

194   Figueiredo, J. L., Pereira, M. F. R., Freitas, M. M. A. & Órfão, J. J. M. Modification of the surface chemistry of activated carbons. *Carbon* **37**, 1379-1389, (1999).

195   Lerf, A., He, H., Forster, M. & Klinowski, J. Structure of graphite oxide revisited. *The Journal of Physical Chemistry B* **102**, 4477-4482, (1998).

196   Hontoria-Lucas, C., López-Peinado, A. J., López-González, J. d. D., Rojas-Cervantes, M. L. & Martín-Aranda, R. M. Study of oxygen-containing groups in a series of graphite oxides: Physical and chemical characterization. *Carbon* **33**, 1585-1592, (1995).

197   Hoogers, G. *Fuel cell technology handbook*.   (CRC Press, 2002).

198   Zhou, X. *et al.* Synergistically enhanced activity of graphene quantum dot/multi-walled carbon nanotube composites as metal-free catalysts for oxygen reduction reaction. *Nanoscale* **6**, 2603-2607, (2014).

199   Zheng, J. *et al.* Production of graphite chloride and bromide using microwave sparks. *Scientific Report* **2**, 662, (2012).

200   Wu, J. *et al.* Controlled chlorine plasma reaction for noninvasive graphene doping. *Journal of the American Chemical Society* **133**, 19668-19671, (2011).

201   Lee, W. H. *et al.* Selective-area fluorination of graphene with fluoropolymer and laser irradiation. *Nano Letters* **12**, 2374-2378, (2012).

202   Marcano, D. C. *et al.* Improved synthesis of graphene oxide. *Acs Nano* **4**, 4806-4814, (2010).

203   Seery, D. J. & Britton, D. The continuous absorption spectra of chlorine, bromine, bromine chloride, iodine chloride, and iodine bromide. *The Journal of Physical Chemistry* **68**, 2263-2266, (1964).

204   Doskocil, E. J., Bordawekar, S. V., Kaye, B. G. & Davis, R. J. UV−Vis spectroscopy of iodine adsorbed on alkali-metal-modified zeolite catalysts for addition of carbon dioxide to ethylene oxide. *The Journal of Physical Chemistry B* **103**, 6277-6282, (1999).

205   Park, C. D., Choi, W. Y. & Kang, H. Ion and X-ray induced decomposition of alkali halates. A comparative study of the radiation induced reaction paths. *Radiation Effects and Defects in Solids* **115**, 65-72, (1990).

206 Zhou, X. L., Solymosi, F., Blass, P. M., Cannon, K. C. & White, J. M. Interactions of methyl halides (Cl, Br and I) with Ag(111). *Surface Science* **219**, 294-316, (1989).

207 Crist, B. V. KBr crystal: cleaved in air. *Surface Science Spectra* **1**, 292-296, (1992).

208 Solymosi, F. & Révész, K. Spectroscopic study on the adsorption and dissociation of CH_3I on Pd(100): thermal and photo effects. *Surface Science* **280**, 38-49, (1993).

209 Morgan, W. E., Van Wazer, J. R. & Stec, W. J. Inner-orbital photoelectron spectroscopy of the alkali metal halides, perchlorates, phosphates, and pyrophosphates. *Journal of the American Chemical Society* **95**, 751-755, (1973).

210 Kelemen, S. R., George, G. N. & Gorbaty, M. L. Direct determination and quantification of sulphur forms in heavy petroleum and coals: 1. The X-ray photoelectron spectroscopy (XPS) approach. *Fuel* **69**, 939-944, (1990).

211 Yu, X.-R., Liu, F., Wang, Z.-Y. & Chen, Y. Auger parameters for sulfur-containing compounds using a mixed aluminum-silver excitation source. *Journal of Electron Spectroscopy and Related Phenomena* **50**, 159-166, (1990).

212 Dillard, J. G. *et al.* An x-ray photoelectron and Auger electron spectroscopic study of the adsorption of molecular iodine on uranium metal and uranium dioxide. *The Journal of Physical Chemistry* **88**, 4104-4111, (1984).

213 Tan, Y. *et al.* Facile synthesis of manganese-oxide-containing mesoporous nitrogen-doped carbon for efficient oxygen reduction. *Advanced Functional Materials* **22**, 4584-4591, (2012).

214 Liang, J., Jiao, Y., Jaroniec, M. & Qiao, S. Z. Sulfur and nitrogen dual-doped mesoporous graphene electrocatalyst for oxygen reduction with synergistically enhanced performance. *Angewandte Chemie International Edition* **51**, 11496-11500, (2012).

215 Liang, H.-W., Zhuang, X., Brüller, S., Feng, X. & Müllen, K. Hierarchically porous carbons with optimized nitrogen doping as highly active electrocatalysts for oxygen reduction. *Nature Communication* **5**, 4973, (2014).

216 Ganguly, A., Sharma, S., Papakonstantinou, P. & Hamilton, J. Probing the thermal deoxygenation of graphene oxide using high-resolution in situ X-ray-based spectroscopies. *The Journal of Physical Chemistry C* **115**, 17009-17019, (2011).

217 Park, S. *et al.* Graphene oxide papers modified by divalent ions—Enhancing mechanical properties via chemical cross-linking. *Acs Nano* **2**, 572-578, (2008).

218 Szabó, T. *et al.* Evolution of surface functional groups in a series of progressively oxidized graphite oxides. *Chemistry of Materials* **18**, 2740-2749,

(2006).

219 Hwang, Y. S. & Lenhart, J. J. Adsorption of C_4-dicarboxylic acids at the hematite/water interface. *Langmuir* **24**, 13934-13943, (2008).

220 Zhou, G. *et al.* Oxygen bridges between NiO nanosheets and graphene for improvement of lithium storage. *Acs Nano* **6**, 3214-3223, (2012).

221 Nesbitt, H. W. & Banerjee, D. Interpretation of XPS Mn(2p) spectra of Mn oxyhydroxides and constraints on the mechanism of MnO_2 precipitation. *American Mineralogist* **83**, 305-315, (1998).

222 Ishii, M., Nakahira, M. & Yamanaka, T. Infrared absorption spectra and cation distributions in $(Mn, Fe)_3O_4$. *Solid State Communications* **11**, 209-212, (1972).

223 Wu, K.-H., Wang, D.-W. & Gentle, I. R. Revisiting oxygen reduction reaction on oxidized and unzipped carbon nanotubes. *Carbon* **81**, 295-304, (2015).

224 Malkhandi, S. *et al.* Electrocatalytic activity of transition metal oxide-carbon composites for oxygen reduction in alkaline batteries and fuel cells. *Journal of The Electrochemical Society* **160**, F943-F952, (2013).

225 Zhao, A. *et al.* Spinel Mn–Co oxide in N-doped carbon nanotubes as a bifunctional electrocatalyst synthesized by oxidative cutting. *Journal of the American Chemical Society* **136**, 7551-7554, (2014).

226 Olson, T. S. *et al.* Anion-exchange membrane fuel cells: Dual-site mechanism of oxygen reduction reaction in alkaline media on cobalt−polypyrrole electrocatalysts. *The Journal of Physical Chemistry C* **114**, 5049-5059, (2010).

227 Wu, K.-H. *et al. Resolving electrocatalytic interfaces in graphene oxide/Spinel oxide hybrids for synergistic oxygen reduction reaction* (The University of Queensland, Unpublished, 2015).

228 Katsounaros, I., Meier, J. C. & Mayrhofer, K. J. J. The impact of chloride ions and the catalyst loading on the reduction of H_2O_2 on high-surface-area platinum catalysts. *Electrochimica Acta* **110**, 790-795, (2013).

229 Jaouen, F. *et al.* Recent advances in non-precious metal catalysis for oxygen-reduction reaction in polymer electrolyte fuel cells. *Energy & Environmental Science* **4**, 114-130, (2011).

230 Lee, J.-S. *et al.* Ketjenblack carbon supported amorphous manganese oxides nanowires as highly efficient electrocatalyst for oxygen reduction reaction in alkaline solutions. *Nano Letters* **11**, 5362-5366, (2011).

231 Liang, Y. *et al.* Oxygen reduction electrocatalyst based on strongly coupled cobalt oxide nanocrystals and carbon nanotubes. *Journal of the American Chemical Society* **134**, 15849-15857, (2012).

232 Cao, Y. *et al.* Reduced graphene oxide anchoring $CoFe_2O_4$ nanoparticles as an effective catalyst for non-aqueous lithium-oxygen batteries. *Faraday*

Discussions **172**, 215-221, (2014).

233   Guo, S., Zhang, S., Wu, L. & Sun, S. Co/CoO nanoparticles assembled on graphene for electrochemical reduction of oxygen. *Angewandte Chemie* **124**, 11940-11943, (2012).

234   Yan, X.-Y. *et al.* Cuprous oxide nanoparticles dispersed on reduced graphene oxide as an efficient electrocatalyst for oxygen reduction reaction. *Chemical Communications* **48**, 1892-1894, (2012).

235   Wang, X. & Li, Y. Selected-control hydrothermal synthesis of α- and β-MnO_2 single crystal nanowires. *Journal of the American Chemical Society* **124**, 2880-2881, (2002).

236   Wu, K.-H. *et al. Dual electrocatalytic roles in Mn_3O_4 bound graphene oxide nanoribbon hybrid promote highly efficient oxygen reduction reaction* (The University of Queensland, Unpublished, 2015).

237   Brisk, M. A. & Baker, A. D. Shake-up satellites in X-ray photoelectron spectroscopy. *Journal of Electron Spectroscopy and Related Phenomena* **7**, 197-213, (1975).

238   Nesbitt, H. W. & Banerjee, D. Interpretation of XPS Mn(2p) spectra of Mn oxyhydroxides and constraints on the mechanism of MnO 2 precipitation. *American Mineralogist* **83**, 305-315, (1998).

239   Manceau, A., Marcus, M. A. & Grangeon, S. Determination of Mn valence states in mixed-valent manganates by XANES spectroscopy. *American Mineralogist* **97**, 816-827, (2012).

240   Gunter, T. E. *et al.* Determination of the oxidation states of manganese in brain, liver, and heart mitochondria. *Journal of Neurochemistry* **88**, 266-280, (2004).

241   Kadoma, Y., Uchimoto, Y. & Wakihara, M. Synthesis and structural study on MnO_2 nanosheet material by X-ray absorption spectroscopic technique. *The Journal of Physical Chemistry B* **110**, 174-177, (2005).

242   Meng, M. *et al.* Structure, catalytic oxidation performance, and sulfur resistance of Mn-based catalysts supported on modified mesoporous Al_2O_3. *Chinese Journal of Catalysis* **31**, 106-111, (2010).

243   Ponsonnet, L. *et al.* EELS analysis of hydrogenated diamond-like carbon films. *Thin Solid Films* **319**, 97-100, (1998).

Appendix A

Supplementary to Chapter II

Synthesis of graphene oxide by a modified Hummer's method:

1.0 g of expandable graphite flakes (GrafGuard 160-50-N, Graftech, USA) was mixed with 6.0 g $KMnO_4$ (BJH Chemicals), followed by addition of concentrated H_2SO_4 (98%, Sigma Aldrich). The reaction mixture was maintained at 60 ℃ in a water bath with continuous stirring over 5 hours. The reaction mixture slowly turned from dark green to brown and finally to a pink-purple color. After cooling to room temperature, 100 mL of water and 3.0 mL H_2O_2 (30%, Merck Pty Ltd) were added to the mixture, turning the solution bright yellow. The reaction solution was centrifuged at 4400 rpm for 30 minutes and the resulting supernatant decanted away. This process was repeated several times until the solution pH reached 7. The resulting graphene oxide powder was collected after a thermal exfoliation and reduction at 1000 ℃ for a period of few seconds.

Chitosan saturation content in purified water

The preparation of chitosan-saturated aqueous solution is described in the corresponding manuscript. Five parallel experiments were performed to obtain an average result for the chitosan content in the saturated solution. Briefly, 10.0 mL of the chitosan-saturated supernatant in a 20 mL reaction bottle was placed into an 80 ℃ oven to remove water. The weights of the empty bottles before and after the addition of chitosan were recorded (Table S1), and an average result was calculated from the data. The weight percentage of chitosan in G/Chit1:1 composite (1 mg/mL) of graphene was calculated as follows:

$$\text{Chitosan wt\%} = \frac{0.18 \text{ (mg)}}{1.00 + 0.18 \text{ (mg)}} \times 100\% = 15.25 \text{ wt\%}$$

Due to the high sensitivity at a small mass, the error analysis was not rigorously

attempted and therefore the measured weight percentage should be regarded as a rough estimate.

Table A1. *Data from the solution drying method*

Weight of empty bottles (g)	Weight of dried bottles (g)	Weight of chitosan (mg/10mL)
13.3919	13.3936	1.7
13.3793	13.3815	2.2
13.4086	13.4101	1.5
13.3832	13.3852	2.0
13.3764	13.3780	1.6
Average ± (Standard Deviation)		**0.18 ±0.03 mg/mL**

TEM image of thermally exfoliated graphene nanosheets
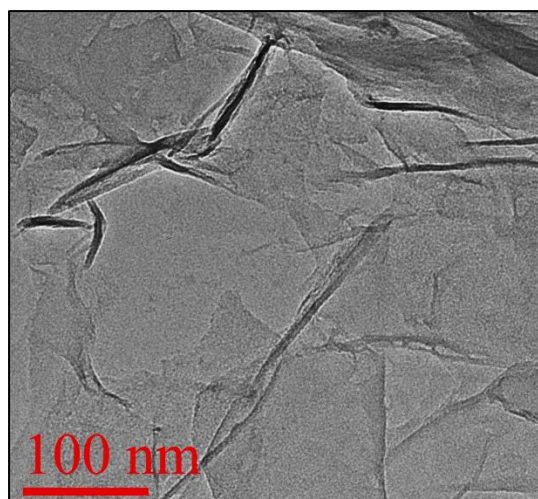
Figure A1. A TEM micrograph of thermally exfoliated graphene nanosheets. The lateral size of the nanosheets typically varies from 100 nm up to 600 nm.

Aqueous suspensions of graphene in chitosan-saturated solution
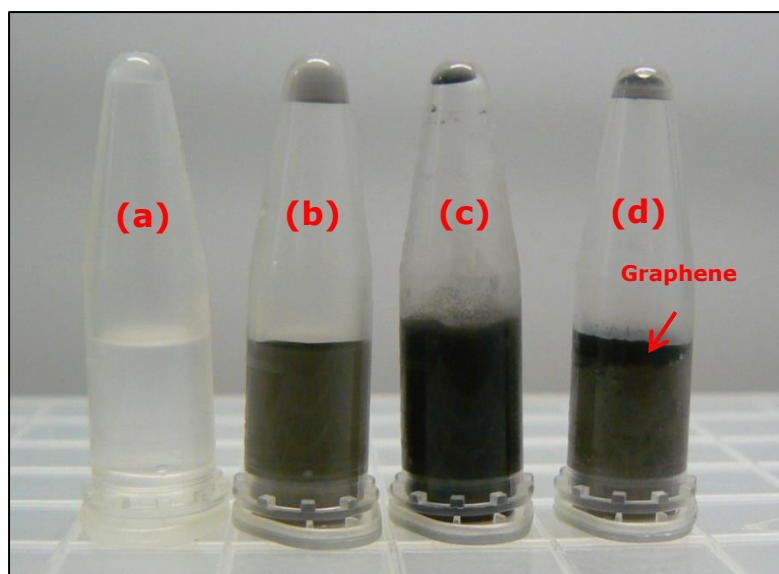
Figure A2. A photograph of G/Chit aqueous suspensions at different w/v ratios, and graphene nanosheets in purified water at 10 minutes after mixing. (a) Saturated chitosan solution [0.0 mg/mL], (b) G/Chit1:10 suspension [0.1 mg/mL], (c) G/Chit1:1 suspension [1.0 mg/mL] and (d) graphene suspension in purified water [1.0 mg/mL]. It was noticed that a strong aggregation of graphene nanosheets to the air-water interface within a short period.

Cyclic voltammetry on G/Chit1:1 composite in O_2 / N_2-saturated environment
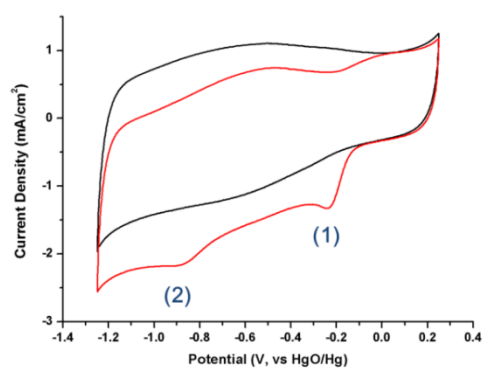
Figure A3. Cyclic voltammograms of G/Chit1:1 composite in O_2-saturated (red) and N_2-saturated (black) 0.1 M KOH electrolyte. The two reaction peaks appear only in the presence of O_2, suggesting they belong to ORR.
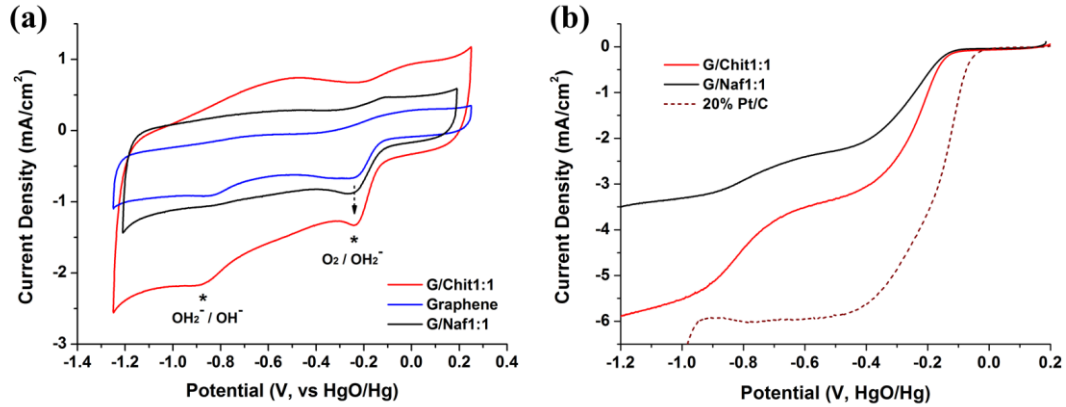
Figure A4. (a) Cyclic voltammogram (50 mV s^{-1}) and (b) LSV-RDE profile (10 mV s^{-1}, 1600 rpm) of graphene/Nafion composite at 1.0 mg/mL of 1 wt% Nafion solution (G/Naf1:1) in O$_2$-saturated 0.1 M KOH electrolyte. G/Chit1:1 composite, graphene film in the CV profile and Pt/C in the LSV-RDE profile are inserted for comparison purpose. In both figures, G/Chit1:1 composite displays the highest current density for all cases.

Koutecky-Levich Analysis on G/Chit1:1 Composite

The electron transfer (*n*) number of G/Chit1:1 composite was evaluated based on Koutecky-Levich (K-L) analysis (j^{-1} vs. $\omega^{-1/2}$) using linear sweep voltammetry on a rotating disk electrode (LSV-RDE). We have performed the analysis at a potential of –0.50 V by plotting the inverse current density (j^{-1}) against the inverse square-root of electrode rotation rate ($\omega^{-1/2}$), based on the K-L equation [Eq. (A1)],[35]

$$\frac{1}{j} = \frac{1}{j_K} + \frac{1}{0.2nFC_bD^{\frac{2}{3}}v^{-\frac{1}{6}}}\frac{1}{\sqrt{\omega}} \tag{A1}$$

where *j* is the measured current density (A cm^{-2}), j_K is the kinetic reaction current density for ORR, *n* is the average number of electrons transferred in ORR, *F* is the Faraday constant (*F* = *96,485 C mol^{-1}*), C_b is the bulk O$_2$ concentration, *D* is the diffusion coefficient of O$_2$ molecules in the electrolyte, *v* is the kinematic viscosity of the electrolyte, and ω is the

rotation rate of the disk electrode in rpm. We have used the parameters from the literature for 0.1 M KOH electrolyte system: $C_b = 1.2 \times 10^{-3}$ M, $D = 1.9 \times 10^{-5}$ cm^2 s^{-1}, and $v = 0.01$ cm^2 s^{-1}.[35] Figure A5 displays the LSV-RDE profiles for G/Chit1:1 composite at various rotation rates and an n number of 2.94 was calculated from the slope of the K-L plot.
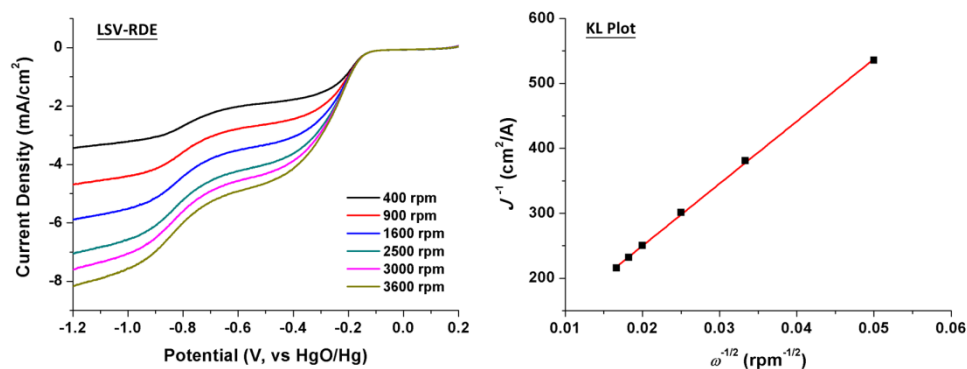
Figure A5. LSV-RDE profiles for G/Chit1:1 composite at various rotation rates in O$_2$-saturated 0.1 M KOH electrolyte (left) and the corresponding KL plot at –0.50 V (right).
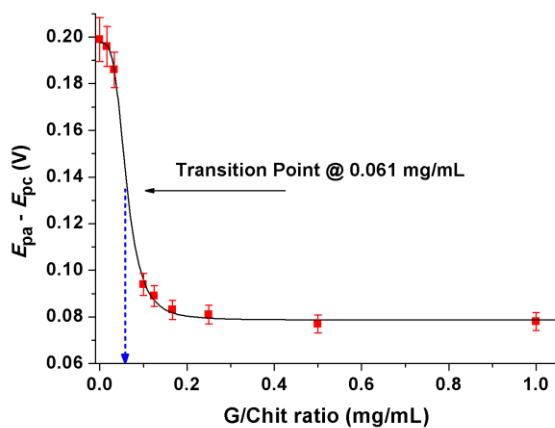
Figure A6. Graph of peak separation against G-Chit ratio in a linear scale. The peak separation data was obtained from the CV profiles in 10 mM K$_3$Fe(CN)$_6$/1.0 M KNO$_3$ system. Black line is the fitting and the transition point at 0.061 mg/mL is the "switching" point for electron conduction.

Appendix B

Supplementary to Chapter III

Hummer's oxidation of carbon nanotubes

0.6 g of the purified CNTs was mixed with 80 mL of concentrated H_2SO_4 and homogenized for 30 min under stirring. In a given mass ratio with CNT, an amount of $KMnO_4$ was slowly added into the mixture and the reaction temperature was raised to 60 °C. Once the target temperature was reached, the reaction mixture was maintained at constant stirring for 3.5 hours. After that, the solution was cooled down to ambient temperature, followed by an addition of 300 mL water solution containing 10 mL 30% H_2O_2 solution. In about 20 minutes, the oxidized CNTs (OCNTs) were filtered (or centrifuged), washed with water and ethanol extensively and finally dried in air at 60 °C. The mass ratio used: 1.0, 1.5, 2.0, 2.5, 3.0 and 5.0 for $KMnO_4$:CNT ratio

Synthesis of graphene oxide nanoribbon

The procedure is similar to the Hummer's oxidation of CNTs, except the synthesis started with 1.0 g of the purified CNTs and 120 mL of concentrated H_2SO_4. The $KMnO_4$ amount was increase to a mass ratio of 10 times the CNT mass and the reaction time was increased to 4.0 hours. After adding 300 mL of water/H_2O_2 solution, the solution was left for 2 days under stirring to stabilize the GONRs in the resulting solution. Through repeated centrifugation and extensive washing with water and ethanol, the final product was collected.

Oxidative acid etching of CNTs

Approximately 1.0 g of the purified CNTs was suspended in 150 mL solution of 70% HNO_3/ 98% H_2SO_4 in a volume-to-volume (v/v) ratio of 2:1 in a loosely capped glass bottle, wrapped by Al foil. The acid mixture was ultrasonically treated for 30 minutes in an ultrasonic bath before reaction. Next, the mixture was heated up to 85 °C in a water bath for a given period under magnetic stirring. Over a given time, 25

mL of the uniform solution was harvested from the bottle and diluted in 150 mL of water in order to filter and wash the surface oxidized CNTs (SOCNTs). Finally, the washed CNT was dried in air at 60 °C.

Thermal treatment of O-CNTs

This was performed in a tube furnace. Before the treatment, the tube chamber was purged with 5% H_2-containing N_2 gas for 30 minutes. The temperature was then raised to 800 °C and held for 2 hours, followed by natural cooling and sample collection.
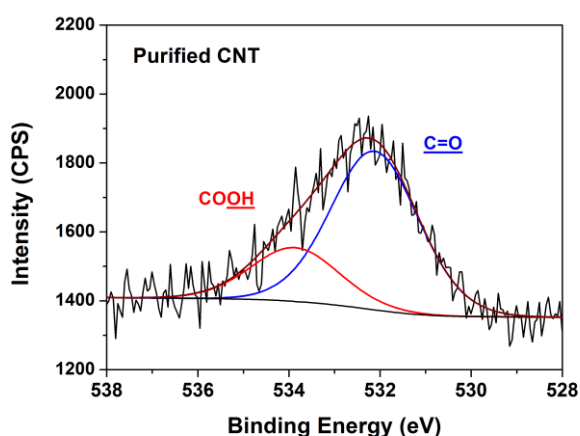

Figure B1. XPS O *1s* spectrum of purified CNT for reference. Note that the oxygen groups in CNT should not be compared with the OCNTs because they are most likely attributed to the adsorbed CO_2, hydrocarbons and hydrates (in the analytical chamber) when the oxygen is at a negligible level (C/O ratio = 70).
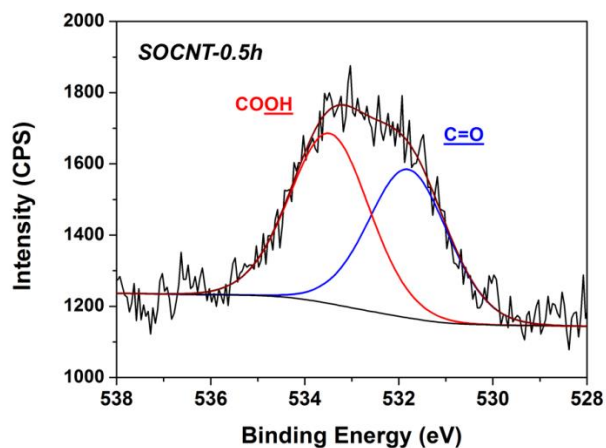
Figure B2. XPS O *1s* spectrum of SOCNT-0.5h for comparison with the spectral profile of SOCNT-48h in the manuscript.
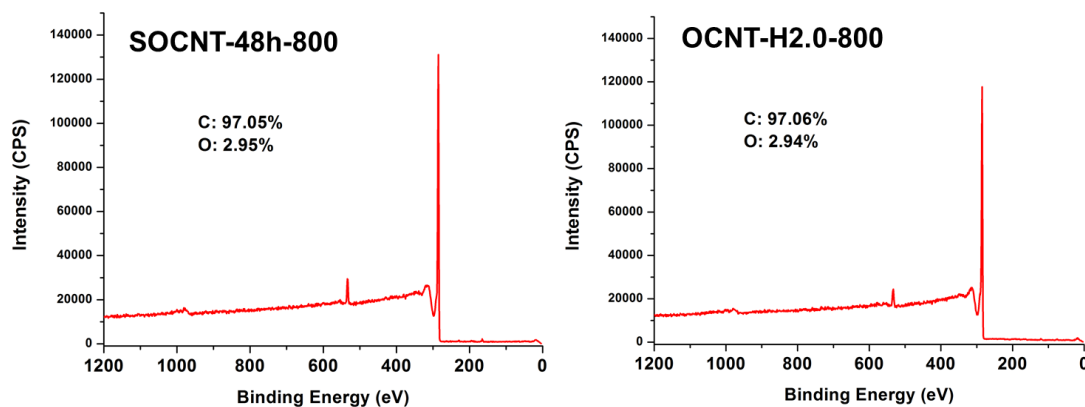
Figure B3. XPS survey spectra for the thermally treated O-CNTs and their respective contents are shown in the spectra.
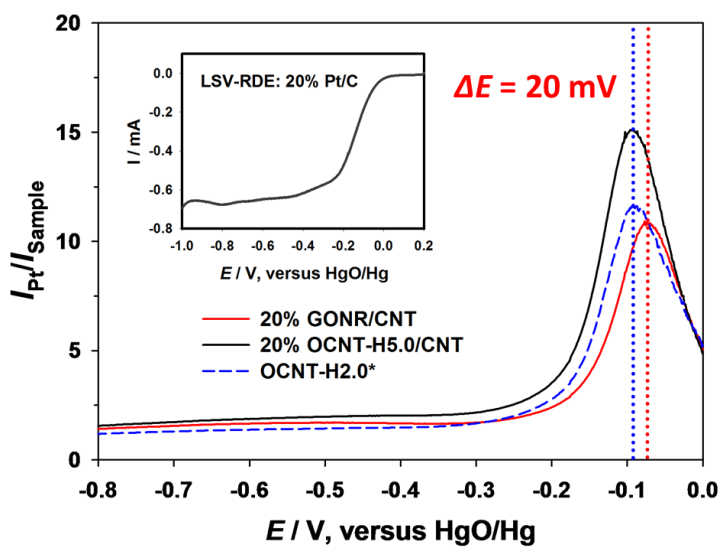
Figure B4. Modified linear sweep voltammetry on a rotating disk electrode (LSV-RDE) profiles for evaluating the reaction onset potential, using a Pt/C electrode as a reference. The peak effectively represents the reaction onset potential (it is in fact the point of deflection but since they share a similar profile shape, the peak can be used).

* the capacitive background was corrected to the background current of the blended samples at 0.0 V.

Appendix C

Supplementary to Chapter V-A
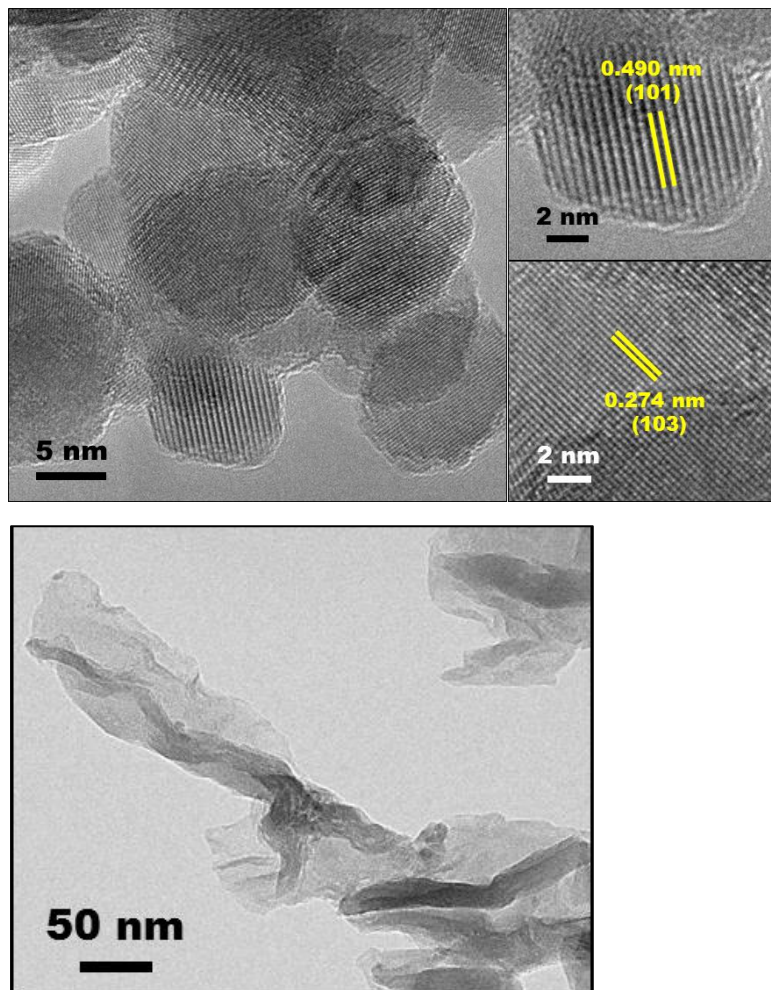
Figure C1. TEM micrographs of free-standing Mn_3O_4 nanoparticles (top) and pristine GONRs (bottom). The size of the particles is 10–30 nm, similar to that grown on GONR. The nanoparticles are highly crystalline and the interlayer spacing indicate the (101) and (103) crystal planes of spinel Mn_3O_4 structure.
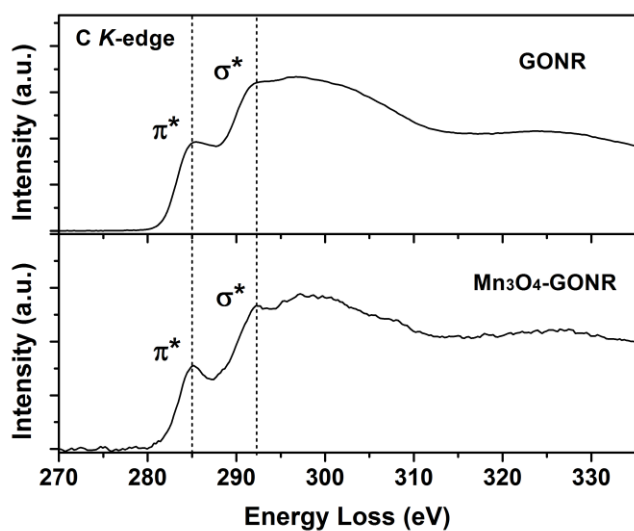
Figure C2. Electron energy loss spectra of Mn_3O_4-GONR hybrid and GONR. The feature at 285 eV and 292 eV signify the *1s* to π^* transition (sp^2 characteristic) and 1s to σ^* transition (sp^3 characteristic). The chemical reduction of GONR in the hybrid can be read from the augmented sp^2 characteristic of the sample.[243]
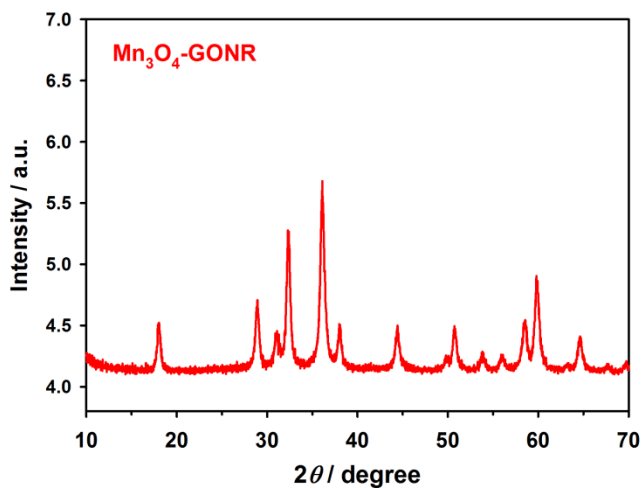
Figure C3. XRD pattern of Mn_3O_4-GONR hybrid. All diffraction peaks can be matched with Hausmannite (Mn_3O_4, PDF# 24-0734).
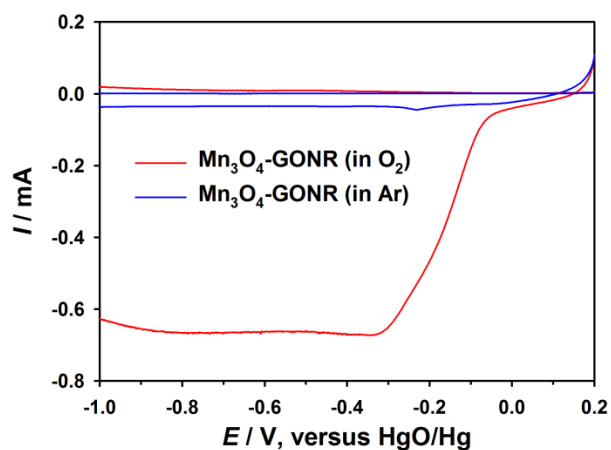
Figure C4. LSV-RRDE profiles of Mn$_3$O$_4$-GONR hybrid in Ar-deaerated or

O$_2$-saturated 0.1 M KOH electrolyte (@ 1600 rpm).
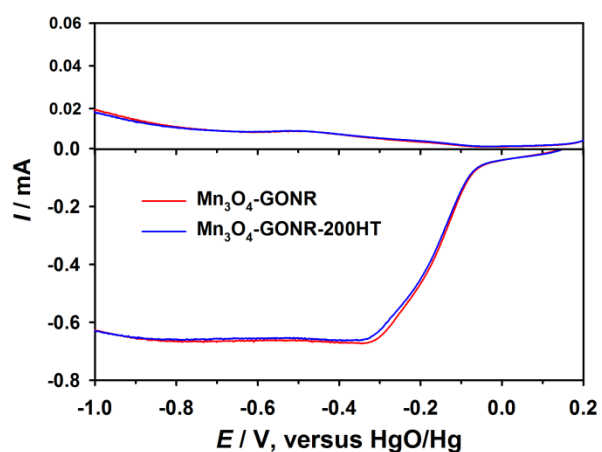
Figure C5. LSV-RRDE profiles of Mn$_3$O$_4$-GONR hybrid and the thermally treated

hybrid at 200 °C for 2 hours (Mn$_3$O$_4$-GONR-200HT) performed in an O$_2$-saturated

0.1 M KOH electrolyte (@ 1600 rpm). This indicates that the hybrid interface has a

good thermal stability.

Appendix D

Supplementary to Chapter V-B
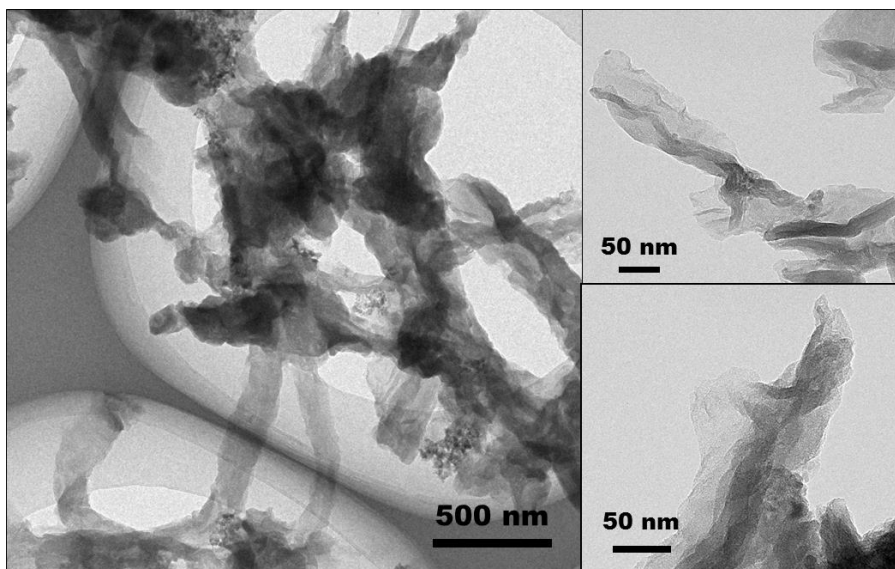
Figure D1. TEM micrographs of purified GONRs.
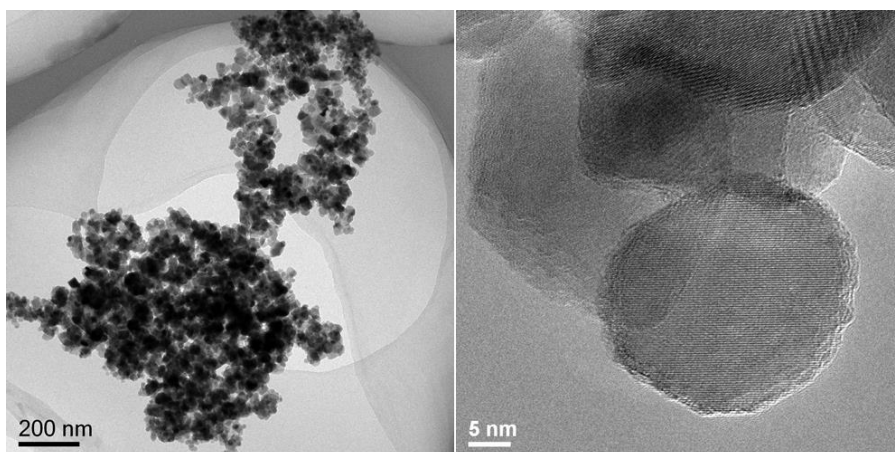
Figure D2. TEM micrographs of Mn$_3$O$_4$ nanoparticles.
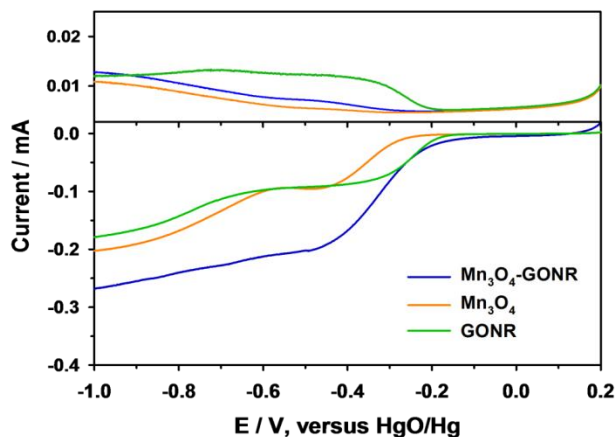
Figure D3. LSV-RRDE profiles of Mn_3O_4-GONR hybrid and the individual hybrid components, Mn_3O_4 nanoparticles and GONR, without CNTs for electron transport, in an O_2-saturated 0.1 M KOH electrolyte. The voltammograms were collected at a scan rate of 10 mV s^{-1}, at an electrode rotating rate of 1600 rpm.

In Figure D3, it is obvious that the impact of electron transport to ORR activity is significant as the reaction currents for both disk and ring were considerably lower than when CNTs were incorporated. Moreover, the ORR performance for each material was very different. Mn_3O_4 nanoparticles displayed a poor ORR activation potential relative to other materials. This suggests that Mn_3O_4 is perhaps not a good electrocatalyst for the initial oxygen reduction to peroxide. Also, there was not much ring current after ORR activation for Mn_3O_4 nanoparticles. This means the ORR immediately consumes any peroxide as generated. On the other hand, GONR shows a more positive ORR activation potential, although there is considerable ring current, signifying the generation of stable peroxide intermediates. The ring current for GONR was stable until -1.0 V, suggesting that this material hardly further reduce the peroxide into final product. From here, it is clear that each of the hybrid components carries a particular electrocatalytic role for ORR. When these components were combined together into a hybrid, the ORR behavior is a result of their mutual benefits:

an efficient ORR activation with a large disk reaction current and a minimal production of stable peroxide species.
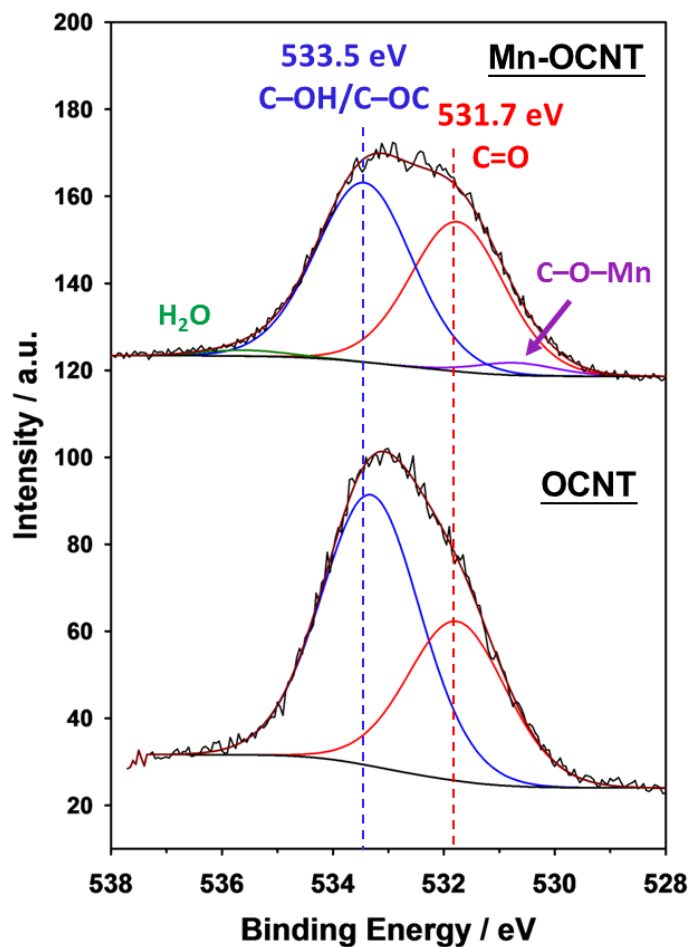
Appendix E

Supplementary to Chapter VI

Figure E1. XPS O *1s* spectra of Mn-OCNT (after binding) and OCNT (before binding); all FWHM values are fixed to 2.0. The Mn-attached oxygen is assigned to the peak at 530.7 eV. A decrease in the C–OH/C–OC feature should be due to the Mn-binding and the possible interaction between Mn ions and the surface oxygen.

Table E1. The Mn content of CNT and modified CNTs measured by inductively coupled plasma optical emission spectroscopy (ICP-OES).

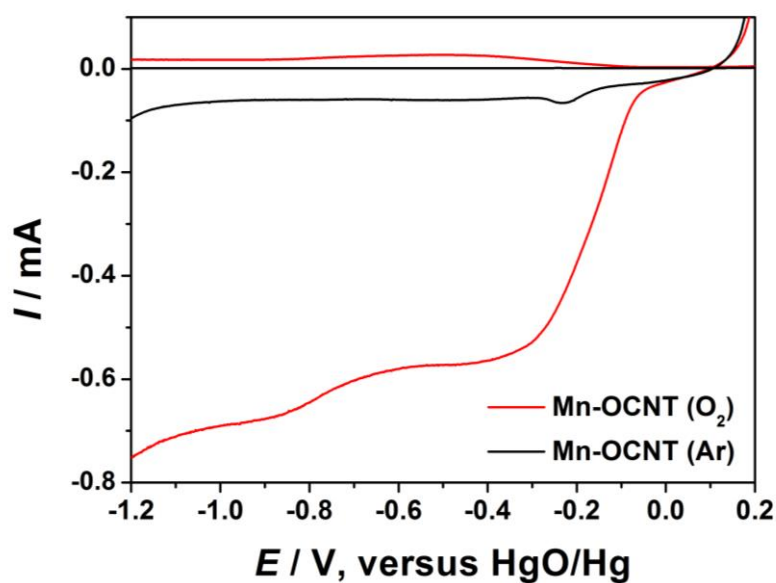| Sample	Mn content (wt% ±0.01)
CNT	0.00
Mn-CNT	0.01
OCNT	0.00
Mn-OCNT	9.45
Mn-OCNT (acid washed)	0.13

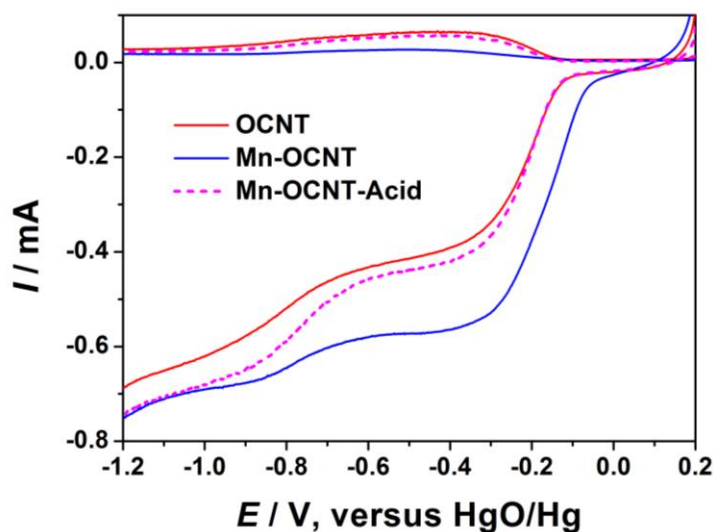**Figure E2.** LSV-RRDE profiles of Mn-OCNT in O_2-saturated and Ar-deaerated 0.1 M KOH electrolyte.

Figure E3. LSV-RRDE profiles of OCNT, Mn-OCNT and Mn-OCNT (acid washed) in O$_2$-saturated 0.1 M KOH electrolyte. The deprived ORR activity of Mn-OCNT after an acid treatment in 2.0 M HCl removes most of the bound Mn and therefore the activity degraded to the level of OCNT.
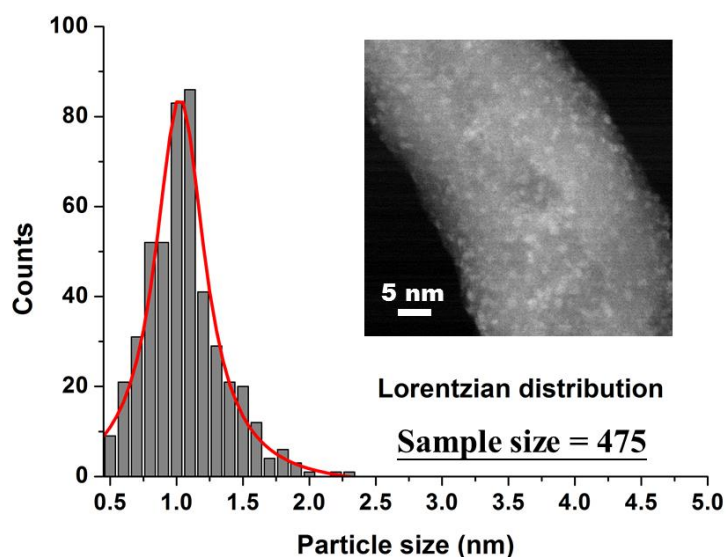

Figure E4. The size distribution of nanocluster domains on Mn-OCNT, as counted in HAADF TEM micrographs; the inset displays a sample HAADF TEM image of Mn-OCNT. A Lorentzian distribution was applied to the data and the median domain size is 1.02 nm.
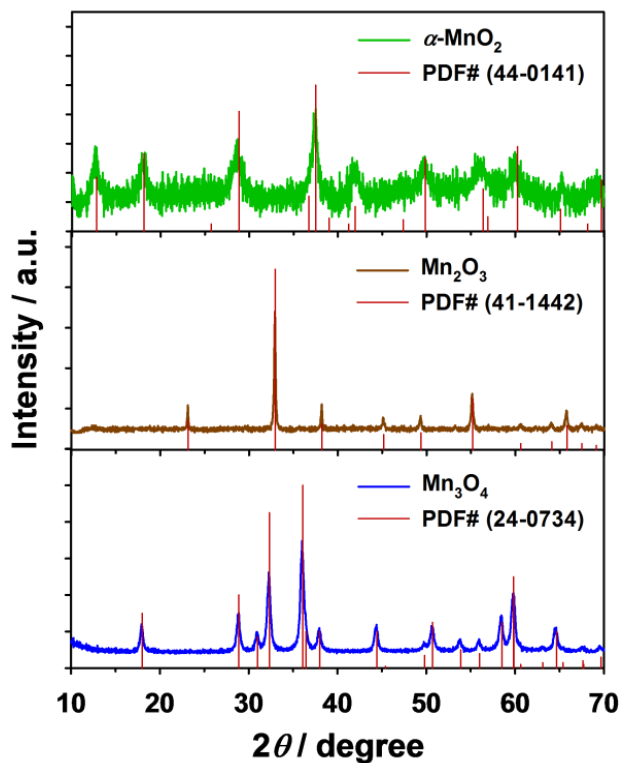
Figure E5. XRD patterns for the crystalline Mn oxide references. All Mn oxides are pure in their respective crystalline phases.
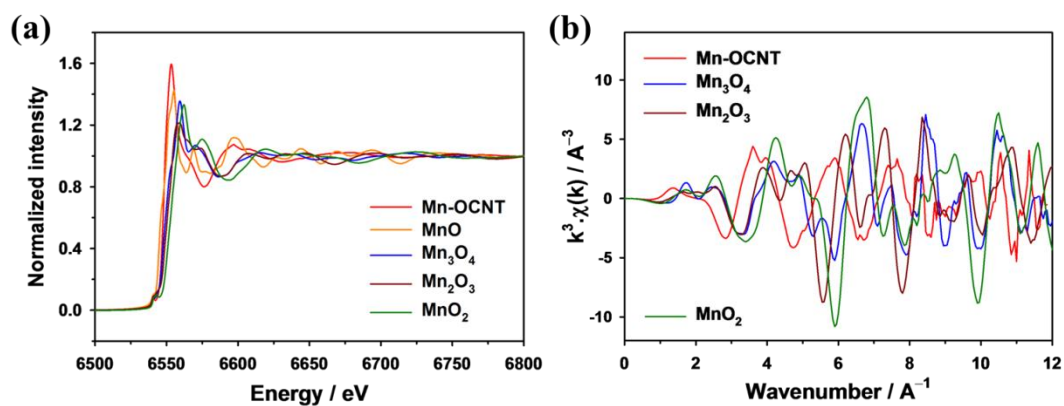

Figure E6. (a) The full Mn K-edge spectra for Mn-OCNT, crystalline Mn_3O_4, Mn_2O_3 and α-MnO_2 and (b) the transformed spectra in k-space using a k-weight of 3.0. Clearly the near-edge and post-edge features in the raw spectra are different and the oscillations in k-space are also distinguished from each other.
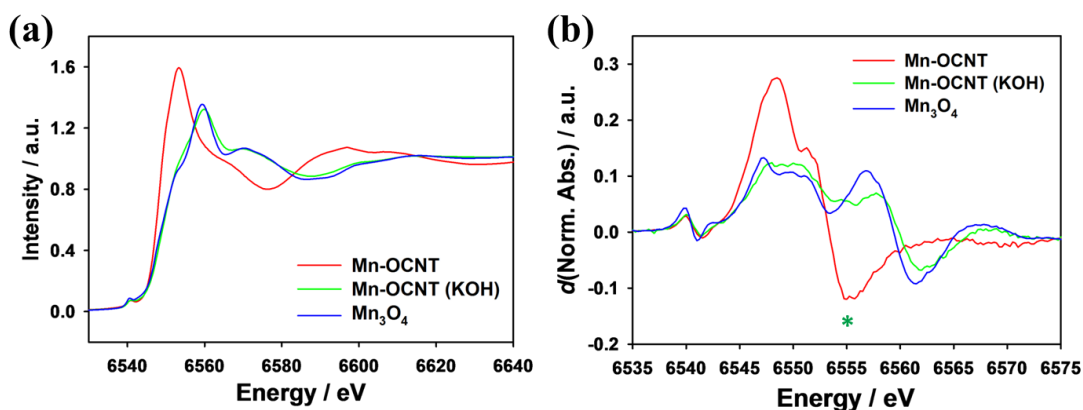
Figure E7. (a) The Mn *K*-edge XANES spectra and (b) the first derivative spectra of Mn-OCNT, KOH-treated Mn-CONT and Mn_3O_4. In the derivative spectrum of Mn-OCNT (KOH), the asterisk indicates the disappeared feature for mostly single-valent Mn^{2+} compound. Clearly the spectral profiles of KOH-treated Mn-OCNT become very similar to that of the mixed-valent Mn_3O_4 ($Mn^{2+}:Mn^{3+} = 1:2$); this suggests an increased Mn^{3+} population after the KOH treatment.

The mathematical treatment for ORR current separation.

The separation of O_2 reduction and peroxide reduction current densities employed the following equations by using both the disk and ring current in a LSV-RRDE profile:

$$j_{O2} = j_d \left(\frac{\sigma N + 1}{2\sigma N} \right) \qquad (E1)$$

$$j_{HO2} = j_d \left(\frac{\sigma N - 1}{2\sigma N} \right) \qquad (E2)$$

, where j_{O2} is the current density for O_2 reduction, j_{HO2} is the current density for peroxide reduction, j_D is the original disk current density, σ is the disk/ring current ratio, and *N* is the effective collecting efficiency. The derivations of Eq. E1 and E2 are shown below, and the detail will be published in another manuscript.

Basically the percentage completion for a full ORR reduction (if only sequential reduction mechanism is considered):

$$\%completion = \frac{v_{e2}}{v_{e2} + v_d} = \frac{j_{e2}}{j_{e2} + j_d}$$

, where v and j are reaction rate and current density, respectively, and the subscripts e2 means the peroxide reduction and d is the escape of peroxide intermediate from the disk electrode through diffusion. Since the escaped peroxide will be detected at the ring electrode such that:

$$j_d = \frac{j_r}{N}$$

Rearrange:

$$\frac{j_{e2}}{j_{e2} + j_r/N} = \frac{j_{e2}N}{j_{e2}N + j_r}$$

If we divide both side by j_d and let $\sigma = j_d/j_r$, we can yield:

$$\%completion = \frac{\frac{j_{e2}}{j_d}\sigma N}{\frac{j_{e2}}{j_d}\sigma N + 1}$$

Since the %completion can be described by the following equation, where γ is the selectivity for a complete ORR:

$$\%completion = \frac{\gamma}{1 + \gamma}$$

$$\gamma = \frac{\sigma N - 1}{2}$$

Thus,

$$\frac{\sigma N - 1}{2} = \frac{\frac{j_{e2}}{j_d}\sigma N}{\frac{j_{e2}}{j_d}\sigma N + 1}$$

An expression of j_{e2} is:

$$j_{e2} = j_d\left(\frac{\sigma N - 1}{2\sigma N}\right)$$

Since $j_d = j_{e1} + j_{e2}$,

$$j_{e1} = j_d\left(\frac{\sigma N + 1}{2\sigma N}\right)$$

The calculation of electron transfer (n) number and percentage production of peroxide ($\%HO_2^-$).

Similarly, the calculation for n number and $\%HO_2^-$ used the following equations:

$$n = \frac{4i_d}{i_d + i_r/N} \qquad\qquad (E3)$$

$$\%HO_2^- = \frac{200\,i_r}{i_d N + i_r} \qquad\qquad (E4)$$

, where i_d and i_r are the measured currents on disk and ring electrodes, respectively.